The Dissertation Committee for Ryosuke Okuno Certifies that this is the approved version of the following dissertation:

Modeling of Multiphase Behavior for Gas Flooding Simulation

Committee:

Russell T. Johns, Co-Supervisor

Kamy Sepehrnoori, Co-Supervisor

Chun Huh

Ekwere J. Peters

Keith P. Johnston

Modeling of Multiphase Behavior for Gas Flooding Simulation

by

Ryosuke Okuno, B.S.; M.S.

Dissertation

Presented to the Faculty of the Graduate School of
The University of Texas at Austin
in Partial Fulfillment
of the Requirements
for the Degree of

Doctor of Philosophy

The University of Texas at Austin
August 2009

To Yuki

Acknowledgements

I am grateful to my supervisors Dr. Russell T. Johns and Dr. Kamy Sepehrnoori for their guidance and continuous encouragement. Dr. Johns' insightful questions led me to a better understanding of complex problems. The discussions with Dr. Sepehrnoori improved practical significance of my research. I also thank the committee members, Dr. Ekwere J. Peters, Dr. Chun Huh, and Dr. Keith P. Johnston. Without learning from a wide variety of their knowledge, I would not have completed this dissertation.

I greatly acknowledge financial support from Japan Petroleum Exploration Co., Ltd. (JAPEX) and Japan Oil, Gas and Metals National Corporation (JOGMEC), along with the member companies of the Gas Flooding Joint Industry Project at the University of Texas at Austin.

I thank the staff in the Petroleum Engineering Department, Dr. Roger Terzian, Cheryl Kruzie, Schenck Nina, and Joanna Castillo for their help. I appreciate technical discussions with my colleagues, Dr. Yinghui Li, Gholamreza Garmeh, Meghdad Roshanfekr, Kaveh Ahmadi, Ashwin Venkatraman, and Gurpreet Singh.

Finally, I would like to express my deepest gratitude to my wife Yuki and my sons Haruki and Takumi for their love and support. I am also thankful for the encouragement from all of my family members.

Modeling of Multiphase Behavior for Gas Flooding Simulation

Publication No._____________

Ryosuke Okuno, Ph.D.
The University of Texas at Austin, 2009

Supervisors: Russell T. Johns and Kamy Sepehrnoori

Miscible gas flooding is a common method for enhanced oil recovery. Reliable design of miscible gas flooding requires compositional reservoir simulation that can accurately predict the fluid properties resulting from mass transfer between reservoir oil and injection gas. Drawbacks of compositional simulation are the efficiency and robustness of phase equilibrium calculations consisting of flash calculations and phase stability analysis.

Simulation of multicontact miscible gas flooding involves a large number of phase equilibrium calculations in a near-critical region, where the calculations are time-consuming and difficult. Also, mixtures of reservoir oil and solvent such as CO_2 and rich gas can exhibit complex phase behavior at temperatures typically below 120ºF, where three hydrocarbon-phases can coexist. However, most compositional simulators do not attempt to solve for three hydrocarbon-phases because three-phase equilibrium calculations are more complicated, difficult, and time-consuming than traditional two-phase equilibrium calculations. Due to the lack of robust algorithms for three-phase equilibrium calculations, the effect of a third hydrocarbon-phase on low-temperature oil displacement is little known.

We develop robust and efficient algorithms for phase equilibrium calculations for two and three phases. The algorithms are implemented in a compositional reservoir simulator. Simulation case studies show that our algorithms can significantly decrease the computational time without loss of accuracy. Speed-up of 40% is achieved for a reservoir simulation using 20 components, compared to standard algorithms. Speed-up occurs not only because of improved computational efficiency but also because of increased robustness resulting in longer time-step sizes. We demonstrate the importance of three-phase equilibrium calculations, where simulations with two-phase equilibrium approximations proposed in the literature can result in complete failure or erroneous simulation results.

Using the robust phase equilibrium algorithms developed, the mechanism is investigated for high efficiency of low-temperature oil displacements by CO_2 involving three hydrocarbon-phases. Results show that high displacement efficiency can be achieved when the composition path goes near the critical endpoint where the gaseous and CO_2-rich liquid phases merge in the presence of the oleic phase. Complete miscibility may not be developed for three-phase flow without considering the existence of a tricritical point.

Table of Contents

List of Tables

List of Figures

1. Introduction

This chapter describes the types of phase behavior problems to be solved in this dissertation. The objectives of the research are then listed. Last, an outline of the dissertation is described.

1.1 PROBLEM DESCRIPTION

Miscible gas flooding is a widely used method for enhanced oil recovery. Reliable design of miscible gas flooding requires a compositional model to predict the fluid properties resulting from mass transfer between reservoir oil and injection gas. The efficiency and reliability of the simulation depend significantly on the algorithms used for phase equilibrium calculations. Drawbacks of compositional simulation are the efficiency and robustness of flash calculations and phase stability analysis.

Compositional reservoir simulation typically uses a cubic equation of state to model the phase behavior of mixtures of reservoir oil and injection gas because of its simplicity and accuracy. Phase stability analysis determines the number of equilibrium phases, and flash calculations solve for intensive and extensive properties of the equilibrium phases. Those phase equilibrium calculations are performed in an iterative manner for all grid cells at every time step. Therefore, computational time of compositional simulation depends significantly on the efficiency of phase equilibrium algorithms used.

Robustness of phase equilibrium algorithms affects both computational time and reliability of compositional simulation. When a phase equilibrium calculation fails to converge to the correct solution, phase properties can discontinuously change over the time step. The discontinuity substantially decreases the subsequent time-step sizes and often stops the simulation from proceeding.

Several additional factors affect computational time, difficulty, and importance of phase equilibrium calculations. Computational time of phase equilibrium calculations increases with the degree of miscibility, the number of coexisting phases, and the number of components used in the simulation. Phase equilibrium calculations become more difficult and important, when multicontact miscibility is approached and/or when the number of phases increases.

Simulation of multicontact miscible gas flooding involves a large number of phase equilibrium calculations in a near-critical region, where the calculations are time-consuming and difficult, but important. Mixtures of reservoir oil and solvent such as CO_2 and rich gas can exhibit complex phase behavior at temperatures typically below 120ºF, where a third solvent-rich liquid phase can coexist with the oleic and gaseous phases. Reliable simulation of gas flooding involving such complex phase behavior requires robust phase equilibrium algorithms capable of handling at least three hydrocarbon-phases. However, most compositional simulators do not even attempt to solve for three hydrocarbon-phases because three-phase equilibrium calculations are more complicated, difficult, and time-consuming than traditional two-phase equilibrium calculations. Several authors proposed two-phase equilibrium approximations to avoid difficult three-phase equilibrium calculations in reservoir simulation. However, those approximations can result in complete failure of simulation or erroneous simulation results. Efficient and robust algorithms should be developed for three-phase equilibrium calculations.

The effect of a third hydrocarbon-phase on low-temperature oil displacement is little known owing to the lack of robust and efficient algorithms for three-phase equilibrium calculations. The existing theory for gas injection processes involving only two hydrocarbon-phases cannot explain why low-temperature oil displacements using CO_2 can achieve a high displacement efficiency of more than 95% when three hydrocarbon-phases are present. Understanding the displacements exhibiting three hydrocarbon-phases requires detailed knowledge of the complex three-phase behavior. Development of robust and efficient algorithms for three-phase equilibrium calculations for compositional simulation will significantly improve our knowledge for enhanced oil recovery involving complex phase behavior such as miscible gas flooding and steam flooding with solvents.

1.2 RESEARCH OBJECTIVES

Reliability and computational time of compositional simulation depend significantly on phase equilibrium algorithms used in the simulation. Although development of robust and efficient algorithms for phase equilibrium calculations has been an active research area for decades, prior studies only demonstrated robustness and/or efficiency of the algorithms in stand-alone calculations, instead of in compositional reservoir simulation. Robustness and efficiency of phase equilibrium algorithms are more important in simulation of multicontact miscible gas flooding than in stand-alone calculations. Phase equilibrium calculations become even more difficult when three hydrocarbon-phases coexist during the simulation. In this dissertation, we develop robust and efficient algorithms for phase equilibrium calculations, and implement them in a compositional reservoir simulator to demonstrate improved efficiency and robustness. Those practical results differentiate our research from others in the literature.

A compositional simulator capable of robust and efficient three-phase equilibrium calculations can be used to examine the effect of a third hydrocarbon-phase on the oil displacement. Using such a compositional simulator, we can obtain detailed information on the interaction between complex phase behavior and flow behavior during the displacement, which is difficult to obtain in an experimental study.

The objectives of this research are the following:

1. Develop robust and efficient algorithms for stability analysis and flash calculations for two and three phases.
2. Implement the algorithms in a compositional reservoir simulator to demonstrate the robustness and efficiency of the algorithms.
3. Demonstrate the importance of properly using three-phase equilibrium calculations for simulation involving three hydrocarbon-phases.
4. Understand the mechanism of high efficiency of oil displacements involving a third hydrocarbon-phase.

To achieve the first objective, we use a reduced method for stability analysis and flash calculations in compositional reservoir simulation. The reduced method can significantly decrease the number of equations to be solved in phase equilibrium calculations, resulting in improved efficiency and robustness of the simulation. We also solve the convergence problems of the multiphase constant-K flash calculation that is part of rigorous flash calculations using a cubic equation of state. Our algorithm for the multiphase constant-K flash calculation is a minimization of a non-monotonic convex function with a small feasible region. Mathematical proofs and example calculations are given to demonstrate that convergence to the correct solution is guaranteed.

For the second objective, we implement our algorithms for phase equilibrium calculations in UTCOMP, a multiphase compositional reservoir simulator (Chang *et al.* 1990). The updated UTCOMP with our algorithms is used to perform a number of simulation case studies for the third and forth objectives listed above.

1.3 OUTLINE OF DISSERTATION

This dissertation consists of seven chapters. Chapter 2 derives basics of phase equilibrium calculations from the first and second laws of thermodynamics. Basics of minimization algorithms and cubic equations of state are then described. After that, a literature review is given on phase equilibrium calculations and low-temperature oil displacements by CO_2.

In Chapter 3, we develop a new algorithm for constant-K flash calculations that is guaranteed to converge to the correct solution for any number of phases. The robustness of our algorithm is demonstrated by comparing with the standard algorithm. Our algorithm is implemented in a multiphase compositional simulator as part of rigorous flash calculations based on a cubic equation of state.

In Chapter 4, we improve an existing algorithm for two-phase flash calculations using a reduced method. A new algorithm for stability analysis using a reduced method is also developed. Our algorithms for two-phase flash and stability analysis using a reduced method are implemented in a compositional simulator to demonstrate the efficiency and robustness of our algorithms.

In Chapter 5, we demonstrate the importance of properly using three-phase equilibrium calculations in compositional reservoir simulation. We extend the algorithm for two-phase equilibrium calculations using the reduced method to three-phase calculations. The algorithm is then implemented in a multiphase compositional simulator to demonstrate conclusively the robustness and efficiency of our reduced method.

In Chapter 6, we investigate the mechanism for high efficiency of low-temperature oil displacements by CO_2 where three hydrocarbon-phases coexist at equilibrium. The key phase behavior for high displacement efficiency is identified in simulations of one-dimensional low-temperature oil displacements. To generalize the mechanism identified, quaternary fluid models are used to study the complex three-phase behavior and its effects on displacement efficiency.

Chapter 7 summarizes and concludes the research. Recommendations for future research are also presented.

2. Background

This chapter explains the required basics for phase equilibrium calculations, and gives a literature review. The first part of this chapter derives fundamental equations to be satisfied at phase equilibrium. The second part reviews various techniques to solve the phase equilibrium problems. Previous research on low-temperature oil displacements by CO_2 is also reviewed.

2.1 BASICS OF PHASE EQUILIBRIUM CALCULATIONS

This section first derives working equations for phase equilibrium calculations from the first and second laws of thermodynamics. Then, formulations for flash calculations and stability analysis are presented. Finally, cubic equations of state are described. We use one of the most popular cubic equations of state, the Peng-Robinson equation of state (Peng and Robinson 1976a) throughout this research, although any cubic equation of state can be used.

2.1.1 Phase Equilibrium Conditions

The first law of thermodynamics is the law of conservation of energy:

$$dU = dq + dw, \tag{2.1}$$

where U is internal energy, q is heat, and w is work. The signs of dq and dw are positive when they are transported from surroundings to a system. The first law states that heat q and work w are equivalent and internal energy U is constant for an isolated system. The second law of thermodynamics identifies a spontaneous change of state. The second law states that the total entropy for an isolated system S_{total} cannot decrease for a spontaneous change of state. That is, $dS_{total} = dS + dS' \geq 0$, where S and S' are entropies for a system and for surroundings within an isolated system, respectively. For a system and surroundings at the same temperature $T = T'$, using the definition of entropy $dS' \equiv dq'/T' = -dq/T$ leads to the Clausius inequality

$$dS \geq dq/T. \tag{2.2}$$

In equation (2.2), the equality holds only for reversible processes.

We can then derive a useful criterion for a spontaneous change of state in terms of the Gibbs free energy. Using equations (2.1) and (2.2) with an assumption of no non-expansion work results in

$$TdS - dU - PdV \geq 0, \tag{2.3}$$

where P is pressure and V is volume. From the definition of the Gibbs free energy $G \equiv U + PV - TS$,

$$dG = dU + PdV + VdP - TdS - SdT. \tag{2.4}$$

Equations (2.3) and (2.4) yield $dG - VdP + SdT \leq 0$, which becomes at a fixed temperature and pressure

$$dG \leq 0. \tag{2.5}$$

Equation (2.5) can identify a spontaneous change of state using only system properties. That is, equation (2.5) does not need properties for surroundings as does the second law of thermodynamics in the original form, $dS_{total} = dS + dS' \geq 0$. Equation (2.5) is useful also because phase equilibrium calculations are typically performed for a fixed temperature and pressure in compositional simulation. Equation (2.5) indicates that the solution for phase equilibrium calculations at a fixed temperature and pressure must be a minimum of the Gibbs free energy.

We now derive more specific phase equilibrium conditions for a multiphase, multicomponent, closed system at a fixed temperature and pressure. The total differential of the Gibbs free energy for a N_P-phase mixture consisting of N_C components is

$$dG = \left(\partial G/\partial T\right)_{P,\underline{n}} dT + \left(\partial G/\partial P\right)_{T,\underline{n}} dP + \sum_{j=1}^{N_P} \sum_{i=1}^{N_C} \overline{G}_{ij} dn_{ij},$$

where $\overline{G}_{ij}$ is the partial molar Gibbs free energy of component *i* in phase *j* and n_{ij} is the moles of component *i* in phase *j*. At a fixed temperature and pressure, the above equation becomes

$$dG = \sum_{j=1}^{N_P} \sum_{i=1}^{N_C} \overline{G}_{ij} dn_{ij} . \tag{2.6}$$

The first order necessary condition for a minimum of the Gibbs free energy is that the gradients of the Gibbs free energy with respect to independent mole numbers are zero. Because the system is closed, the moles of component *i* in phase N_P is dependent on the moles of component *i* in the other ($N_P - 1$) phases. That is,

$$n_{iN_P} = n_i - \sum_{j=1}^{N_P - 1} n_{ij} .$$

Therefore,

$$\begin{aligned} &\partial n_{ij}/\partial n_{ik} = 1 && \text{for } j = k \\ &\partial n_{ij}/\partial n_{ik} = 0 && \text{for } j \neq k \text{ and } j \neq N_P \\ &\partial n_{ij}/\partial n_{ik} = -1 && \text{for } j = N_P. \end{aligned} \tag{2.7}$$

Using equations (2.6) and (2.7), we obtain

$$\partial G/\partial n_{mn} = \sum_{j=1}^{N_P} \sum_{i=1}^{N_C} n_{ij}\, \partial \overline{G}_{ij} / \partial n_{mn} + \overline{G}_{mn} - \overline{G}_{mN_P} = \overline{G}_{mn} - \overline{G}_{mN_P} , \tag{2.8}$$

where $m = 1,\ldots,N_C$ and $n = 1,\ldots,(N_P - 1)$. In equation (2.8), the double-summation term is zero according to the Gibbs-Duhem equation. Then, the first-order necessary condition for a minimum of the Gibbs free energy becomes

$$\overline{G}_{ij} - \overline{G}_{iN_P} = 0, \text{ where } i = 1,\ldots,N_C \text{ and } j = 1,\ldots,\left(N_P - 1\right). \tag{2.9}$$

An equivalent expression in terms of fugacity is the following fugacity equations:

$$\ln f_{ij} - \ln f_{iN_P} = 0, \text{ where } i = 1,\ldots,N_C \text{ and } j = 1,\ldots,\left(N_P - 1\right). \tag{2.10}$$

In equations (2.10), f_{ij} is the fugacity of component i in phase j. In equations (2.9) and (2.10), phase N_P is the reference phase. The fugacity equations (2.10) are the working equations for flash calculations.

The derivation of the fugacity equations (2.10) from equations (2.9) needs a relation between fugacity of a component and partial molar Gibbs free energy of that component in a mixture. Because many textbooks do not present this important derivation, it will be shown below. Integration of a fundamental equation

$$\overline{V}_i = \partial \overline{G}_i / \partial P$$

from a reference pressure P^0 to a higher pressure P results in

$$\overline{G}_i\left(T, P, \underline{x}\right) - \overline{G}_i\left(T, P^0, \underline{x}\right) = \int_{P^0}^{P} \overline{V}_i dP, \tag{2.11}$$

where $\overline{V}_i$ is the partial molar volume of component i and $\underline{x}$ is a vector representing the composition of the phase mixture of interest. For ideal gas mixtures (IGM), the equation of state for ideal gas can be used with equation (2.11) to obtain

$$\overline{G}_i^{IGM}\left(T, P, \underline{x}\right) - \overline{G}_i^{IGM}\left(T, P^0, \underline{x}\right) = RT \ln\left(P / P^0\right), \tag{2.12}$$

where R is the gas constant. Fugacity is defined so that the form of equation (2.12) stays the same for non-ideal gas mixtures. That is,

$$\overline{G}_i\left(T, P, \underline{x}\right) - \overline{G}_i\left(T, P^0, \underline{x}\right) = RT \ln\left(f_i / f_i^0\right), \tag{2.13}$$

where f_i and f_i^0 are the fugacities at P and P^0, respectively. The fugacity f_i accounts for deviation from the partial pressure P_i in an ideal gas mixture caused by non-ideal behaviors of molecules such as repulsion and attraction. We subtract equation (2.12) from equation (2.13), and then consider $P^0 \rightarrow 0$. Considering that

$$f_i^0 = x_i P^0 \text{ and } \overline{G}_i\left(T, P^0, \underline{x}\right) = \overline{G}_i^{IGM}\left(T, P^0, \underline{x}\right) \text{ when } P^0 \rightarrow 0,$$

the following relation between fugacity and partial molar Gibbs free energy is obtained:

$$
\begin{aligned}
f_i &= x_i P \exp\left[\left(\overline{G}_i\left(T,P,\underline{x}\right)-\overline{G}_i^{IGM}\left(T,P,\underline{x}\right)\right)\Big/RT\right] \\
&= P \exp\left[\left(\overline{G}_i\left(T,P,\underline{x}\right)-\underline{G}^{IG}\left(T,P\right)\right)\Big/RT\right].
\end{aligned}
\tag{2.14}
$$

Equation (2.14) is given as a definition of fugacity in some textbooks (*e.g.*, Sandler 2006). The fugacity coefficient of component *i* is defined as $\varphi_i \equiv f_i/(x_iP)$, which is extensively used in phase equilibrium calculations.

2.1.2 Conventional Formulations for Flash Calculations

This section presents two basic formulations for flash calculations, minimization of the Gibbs free energy and solution of fugacity equations. Algorithms to solve the formulated problems will be discussed in section 2.2.

A flash calculation in this research is used to determine equilibrium phase compositions and phase amounts for a given temperature *T*, pressure *P*, and overall composition $\underline{z}$. The flash formulations to be developed in this section assume that split phases resulting from the flash calculation give a stable phase equilibrium state at lowest possible Gibbs free energy.

The most fundamental formulation for flash calculations at a given temperature and pressure is minimization of the Gibbs free energy. The molar Gibbs free energy of a multicomponent, multiphase system is given as

$$\underline{G} = \sum\nolimits_{j=1}^{N_P}\sum\nolimits_{i=1}^{N_C}\beta_j x_{ij}\overline{G}_{ij}\ , \tag{2.15}$$

where β_j is the mole fraction of phase *j* and x_{ij} is the mole fraction of component *i* in phase *j*. Considering material balance of each component,

$$\sum\nolimits_{j=1}^{N_P}\beta_j x_{ij} = z_i \quad \text{for } i = 1,...,N_C\ . \tag{2.16}$$

By definition, the following conditions must be satisfied:

$$\sum\nolimits_{i=1}^{N_C} z_i = 1.0, \tag{2.17}$$

$$\sum_{j=1}^{N_P} \beta_j = 1.0 \text{ and } \beta_j \geq 0 \text{ for } j = 1, \ldots, N_P, \tag{2.18}$$

$$\sum_{i=1}^{N_C} x_{ij} = 1.0 \text{ and } x_{ij} \geq 0 \text{ for } i = 1, \ldots, N_C \text{ and } j = 1, \ldots, N_P. \tag{2.19}$$

Use of equation (2.14) with equation (2.15) yields

$$\begin{aligned} \underline{G} &= RT\sum_{j=1}^{N_P}\sum_{i=1}^{N_C} \beta_j x_{ij} \ln\left(x_{ij}\varphi_{ij}\right) + \underline{G}^{IG}\sum_{j=1}^{N_P}\sum_{i=1}^{N_C} \beta_j x_{ij} \\ &= RT\sum_{j=1}^{N_P}\sum_{i=1}^{N_C} \beta_j x_{ij} \ln\left(x_{ij}\varphi_{ij}\right) + \underline{G}^{IG}. \end{aligned} \tag{2.20}$$

In equation (2.20), equations (2.16) and (2.17) were used. Molar Gibbs free energy for ideal gas $\underline{G}^{IG}$ depends on temperature and pressure, which are fixed in our flash calculations. Therefore, minimization of the Gibbs free energy given in equation (2.15) is equivalent to minimization of the following dimensionless function:

$$\underline{G}_R = \left(\underline{G} - \underline{G}^{IG}\right) / RT = \sum_{j=1}^{N_P}\sum_{i=1}^{N_C} \beta_j x_{ij} \ln\left(x_{ij}\varphi_{ij}\right). \tag{2.21}$$

The function $\underline{G}_R$ is minimized subject to equations (2.16), (2.18), and (2.19) using Newton's method. As demonstrated by Baker *et al.* (1982), the Gibbs free energy using a cubic equation of state can have local minima. The global minimum is the correct solution, and the other minima are false solutions. An important point is that minimization of $\underline{G}_R$ or $\underline{G}$ must satisfy the material balance equations (2.16) at every iteration step to fix a reference value of the function, which is $\underline{G}^{IG}/RT$ in equation (2.21).

The function $\underline{G}_R$ can be considered as the sum of two terms; $\underline{G}_R{}^I$ and $\underline{G}_R{}^E$ accounting for the ideal and excess term, respectively. That is,

$$\underline{G}_R = \underline{G}_R^I + \underline{G}_R^E, \tag{2.22}$$

where $\underline{G}_R^I = \sum_{j=1}^{N_P}\sum_{i=1}^{N_C} \beta_j x_{ij} \ln x_{ij}$ and $\underline{G}_R^E = \sum_{j=1}^{N_P}\sum_{i=1}^{N_C} \beta_j x_{ij} \ln \varphi_{ij}$. This separation is useful for analyzing convergence behavior of a flash algorithm as will be presented in section 2.2.1.

An alternative and conventional formulation is solution of fugacity equations (2.10) with equations (2.16), (2.18) and (2.19). Because fugacity equations are the first-order necessary conditions for a minimum of the Gibbs free energy, solution of fugacity equations converges to a stationary point of the Gibbs free energy, which can be a minimum, or a saddle point, or a maximum. However, robustness of flash calculations depends not only on the formulation but also on the algorithm used. Unlike minimization of the Gibbs free energy, solution of fugacity equations needs to satisfy the material balance equations (2.16) only when convergence is achieved. This flexibility leads to a robust and efficient algorithm to be developed in Chapters 4 and 5.

An isothermal-, isobaric-flash calculation has a solution because the number of unknowns equals the number of equations. For a given composition of $\underline{z}$, the unknowns are T_j, P_j, x_{ij}, and β_j, where $i = 1,\ldots,N_C$ and $j = 1,\ldots,N_P$. That is, the number of unknowns is $N_P(N_C + 3)$. Assuming no capillary pressure, the equations are $T_j = T_{N_P}$, $P_j = P_{N_P}$, where $j = 1,\ldots,(N_P - 1)$, and equations (2.10), (2.16), (2.18), and (2.19). In equations (2.16), only $(N_C - 1)$ equations are independent. Then, the number of equations is $N_P(N_C + 3) - 2$. When temperature and pressure for the system are specified, both the numbers of unknowns and equations are $N_P(N_C + 3) - 2$. This confirms that a flash calculation at a given temperature and pressure has a solution. This result is consistent with Duhem's theorem, which states that for any closed system formed initially from given amounts of prescribed chemical species, the equilibrium state is completely determined when any two independent variables are fixed (Smith *et al.* 2005).

2.1.3 Conventional Formulations for Stability Analysis

This section derives two basic formulations for stability analysis. Algorithms to solve the formulated problems will be discussed in section 2.2. In the previous section, flash calculations were formulated assuming that the number of equilibrium phases is known in advance. Stability analysis can detect whether a phase mixture is stable at a given temperature, pressure, and composition. If that phase is unstable, a flash calculation is performed to obtain multiphase properties.

Stability analysis can significantly affect the reliability and efficiency of compositional reservoir simulation. When the number of equilibrium phases is smaller than that assumed by stability analysis, the subsequent flash calculation, if converged, provides the correct solution by solving an unnecessarily large system of equations. If the number of equilibrium phases is greater than that assumed, the correct solution cannot be obtained and a false solution to be converged in the flash calculation depends on the initial estimate used. Chapter 5 demonstrates that use of only two-phase flash calculations in CO_2 flooding simulation involving three hydrocarbon-phases can result in a complete failure of the simulation due to discontinuous changes in physical properties. Knowing the correct number of equilibrium phases is important for robustness and efficiency of compositional reservoir simulation.

Baker *et al.* (1982) calculated the Gibbs free energy for several mixtures using a cubic equation of state to demonstrate that a stable equilibrium state must be the global minimum of the Gibbs free energy. They concluded that the tangent plane to the Gibbs free energy surface at a stable equilibrium state at a given temperature and pressure cannot lie above the Gibbs free energy surface at any composition. This condition is necessary and sufficient for phase stability. The conclusion of Baker *et al.* (1982) is consistent with the results from the original research by Gibbs (1873a, b).

Michelsen (1982a) developed a practical computational procedure for stability analysis based on the analysis of Baker *et al.* (1982). The procedure of Michelsen is used for a single-phase mixture or individual phases of a multiphase mixture. He defined the tangent plane distance (TPD) function. The TPD function is the difference between the Gibbs free energy and the tangent plane to the Gibbs free energy at a phase composition of interest. A phase is stable when the TPD function is always positive or zero.

The TPD function can be derived using the first-order Taylor series expansion of the Gibbs free energy around a phase composition of interest. A tangent plane $T(\underline{x})$ to the Gibbs free energy at a phase composition $\underline{z}$ is

$$\begin{aligned} T(\underline{x}) &= \underline{G}(\underline{z}) + \sum_{i=1}^{N_C} (x_i - z_i)\left(\partial \underline{G}(\underline{x})/\partial x_i\right)\Big|_{\underline{x}=\underline{z}} \\ &= \underline{G}(\underline{z}) + \sum_{i=1}^{N_C} (x_i - z_i)\left[\overline{G}_i(\underline{z}) - \overline{G}_{N_C}(\underline{z}) + \sum_{j=1}^{N_C} x_j \left(\partial \overline{G}_j/\partial x_i\right)\right] \\ &= \underline{G}(\underline{z}) + \sum_{i=1}^{N_C} x_i \overline{G}_i(\underline{z}) - \sum_{i=1}^{N_C} z_i \overline{G}_i(\underline{z}) \\ &= \sum_{i=1}^{N_C} x_i \overline{G}_i(\underline{z}). \end{aligned} \tag{2.23}$$

In equation (2.23), equations (2.16) were used, where component N_C is the reference component. The Gibbs-Duhem equation eliminated the summation term in the brackets in the second line of equation (2.23). Then, the TPD function $D(\underline{x})$ is obtained as

$$D(\underline{x}) = \underline{G}(\underline{x}) - T(\underline{x}) = \sum_{i=1}^{N_C} x_i \left(\overline{G}_i(\underline{x}) - \overline{G}_i(\underline{z})\right), \tag{2.24}$$

or in dimensionless form,

$$D_R(\underline{x}) = D/RT = \sum_{i=1}^{N_C} x_i \left(\ln x_i \varphi_i(\underline{x}) - \ln z_i \varphi_i(\underline{z})\right). \tag{2.25}$$

Stability analysis using the TPD function searches for a composition at which the TPD function is negative. If such a composition is found, the current phase with an overall composition of $\underline{z}$ is unstable. Otherwise, the current phase is assumed to be stable. If the global minimum of D or D_R is known, phase stability can be determined by the sign of that minimum. Therefore, one formulation for the stability analysis of Michelsen is minimization of the TPD function in composition space with the following equations:

$$\sum_{i=1}^{N_C} x_i = 1 \text{ and } x_i \geq 0 \text{ for } i = 1, \ldots, N_C . \tag{2.26}$$

An alternative and conventional procedure is to locate stationary points on the TPD function and check the sign of the TPD function to identify phase stability. This procedure is the stationary point method of Michelsen (1982a). At stationary points, the first-order derivatives of $D(\underline{x})$ given in equation (2.24) are all zero. That is,

$$\begin{aligned} \partial D\left(\underline{x}\right)/\partial x_i &= \left(\partial/\partial x_i\right)\left[\sum_{i=1}^{N_C} x_i\left(\bar{G}_i\left(\underline{x}\right) - \bar{G}_i\left(\underline{z}\right)\right)\right] \\ &= \left(\bar{G}_i\left(\underline{x}\right) - \bar{G}_i\left(\underline{z}\right)\right) - \left(\bar{G}_{N_C}\left(\underline{x}\right) - \bar{G}_{N_C}\left(\underline{z}\right)\right) = 0, \end{aligned}$$

or $$\bar{G}_i\left(\underline{x}\right) - \bar{G}_i\left(\underline{z}\right) = \bar{G}_{N_C}\left(\underline{x}\right) - \bar{G}_{N_C}\left(\underline{z}\right), \text{ where } i = 1, \ldots, \left(N_C - 1\right) . \tag{2.27}$$

In equations (2.27), the Gibbs-Duhem equation was used. Equations (2.16) were also used, where component N_C is the reference component. Substitution of equations (2.27) into equation (2.24) yields

$$\begin{aligned} D\left(\underline{x}\right) &= \sum_{i=1}^{N_C} x_i\left(\bar{G}_{N_C}\left(\underline{x}\right) - \bar{G}_{N_C}\left(\underline{z}\right)\right) \\ &= \bar{G}_{N_C}\left(\underline{x}\right) - \bar{G}_{N_C}\left(\underline{z}\right) \\ &= \bar{G}_i\left(\underline{x}\right) - \bar{G}_i\left(\underline{z}\right), \text{ where } i = 1, \ldots, N_C . \end{aligned} \tag{2.28}$$

Rearranging equations (2.28), we obtain

$$\ln X_i \varphi\left(\underline{x}\right) - \ln z_i \varphi\left(\underline{z}\right) = 0, \text{ where } X_i = x_i \exp\left(-D/RT\right) \text{ and } i = 1, \ldots, N_C . \tag{2.29}$$

Equations (2.29) are referred to as the stationarity equations. Equation (2.14) was used to obtain equations (2.29). The stationary point method locates stationary points using equations (2.26) and (2.29), and checks to see if $\sum_i X_i > 1.0$ ($i = 1, \ldots, N_C$). If a stationary point at which $\sum_i X_i > 1.0$ is found, then the current phase with a composition of $\underline{z}$ is unstable. Otherwise, the current phase is assumed to be stable.

Unlike flash calculations, stability analysis involves only one variable phase composition $\underline{x}$. This is true even for stability analysis for a multiphase mixture because stability analysis is performed for a single-phase mixture or individual phases of a multiphase mixture. For this reason, stability analysis is simpler than flash calculations in that material balance equations like equations (2.16) are not needed. However, it is difficult to ensure location of the global minimum of the TPD function or all stationary points using the stationary point method. Algorithms addressing this difficulty are discussed in section 2.2.3.

2.1.4 Basics of Minimization Algorithms

Minimization algorithms are used in multiple chapters in this dissertation. This section presents basics of minimization algorithms. We consider an unconstrained minimization problem

$$\text{minimize } F(x),$$
$$\text{where } x \in \mathrm{R}^n.$$

Function F is assumed to be twice continuously differentiable. The sufficient conditions for x^* to be a local minimum of F are that

$$\nabla F(x^*) = 0,$$
$$\nabla^2 F(x^*) \text{ is positive definite.}$$

An important class of minimization algorithms is gradient methods: $x^{k+1} = x^k + \alpha^k d^k$, where $k = 0,1,2,\ldots$ and the direction d^k is chosen so that

$$\nabla F(x^k)^T d^k < 0. \qquad (2.30)$$

It is easily proven that any direction d that satisfies equation (2.30) is a descent direction of F at x. Using a first-order Taylor series expansion,

$$\begin{aligned} F(x') = F(x+\alpha d) &= F(x) + \alpha \nabla F(x)^T d + o(\alpha \|d\|) \\ &= F(x) + \alpha \nabla F(x)^T d + o(\alpha). \end{aligned}$$

Rearranging the above,

$$F(x') - F(x) = \alpha\left[\nabla F(x)^T d + o(\|d\|)\right].$$

Equation (2.30) shows there exists $\alpha_u > 0$ such that

$$F(x') < F(x) \quad \forall\ \alpha\ \in (0, \alpha_u].$$

Two key ideas in gradient methods are the choice of the descent direction d^k and the step size α^k. Most gradient methods can be expressed as

$$x^{k+1} = x^k - \alpha^k D^k \nabla F\left(x^k\right), \text{ where } D^k \text{ is a positive definite matrix.}$$

For the steepest descent method, D^k is the identity matrix. For Newton's method, D^k is the inverse of the Hessian matrix of F at x^k. Newton's method minimizes the quadratic approximation of the original function around x^k given by

$$F_a^{\,k}(x) = F\left(x^k\right) + \nabla F\left(x^k\right)^T \left(x - x^k\right) + (1/2)\left(x - x^k\right)^T \nabla^2 F\left(x^k\right)\left(x - x^k\right).$$

We set the gradient of $F_a^{\,k}$ to zero and solve for x to obtain the next iterate,

$$x^{k+1} = x^k - \left[\nabla^2 F\left(x^k\right)\right]^{-1} \nabla F\left(x^k\right). \tag{2.31}$$

Equation (2.31) is the pure form of Newton's iteration. The generalized Newton's iteration is

$$x^{k+1} = x^k - \alpha^k \left[\nabla^2 F\left(x^k\right)\right]^{-1} \nabla F\left(x^k\right). \tag{2.32}$$

A method to determine the step size is univariate minimization along a given direction, also known as a line-search. That is,

$$\alpha^k \in \arg\min_{\alpha \in [0,s]} F\left(x^k + \alpha d^k\right). \tag{2.33}$$

The independent variable α is between 0.0 and s, and s is typically set to 1.0. This univariate minimization can be solved by Newton's method. This sub-problem for line-search does not need to be solved with exact accuracy for the quadratic convergence of the entire Newton's iteration.

Newton's method converges quadratically in the vicinity of a solution. A mathematical proof is given in a standard textbook (*e.g.*, Bertsekas 1999). There is no general criterion for how close the current iterate should be to exhibit a quadratic convergence rate. Newton's method may require a large number of iterations to exhibit eventually quadratic convergence.

Newton's method in the pure form, equation (2.31), can fail because the Hessian matrix may not be positive definite and because $F(x^{k+1})$ may be greater than $F(x^k)$. A line-search can fix the step-size for the latter situation. For the former situation, the modified Cholesky decomposition is widely used (Gill and Murray 1974, Gill *et al.* 1986). The modified Cholesky decomposition is used to modify efficiently the Hessian matrix to be positive definite when the Hessian matrix is not positive definite. This method is also used for a nearly singular Hessian matrix that is still positive definite. However, when the Hessian matrix is nearly singular, use of the modified Cholesky decomposition can result in an overly large step-size (Dennis and Schnabel 1996). A line-search technique often fails to find the next iterate for that case. This problem occurs in a near-critical region for phase equilibrium calculations, where accuracy and robustness is important for simulation of multicontact miscible gas flooding.

Newton's method for minimization can be viewed as a special case of that for root-finding of equations (Bertsekas 1999). Newton's method for root-finding of n equations is

$$x^{k+1} = x^k - \left[\nabla f\left(x^k\right)\right]^{-T} f\left(x^k\right), \text{ where } f : \mathrm{R}^n \to \mathrm{R}^n . \tag{2.34}$$

The transpose of the gradient matrix of f is the Jacobian matrix. If and only if the Jacobian matrix is symmetric, there exists a function F: $\mathrm{R}^n \to \mathrm{R}$ for which the gradient vector corresponds to f. This relation is used to develop a new algorithm for constant-K flash calculations in Chapter 3.

2.1.5 Cubic Equations of State

There are generally two methods for modeling vapor-liquid equilibrium; the equation of state (EOS) method and the activity coefficient method. The former is typically used for high pressure mixtures of hydrocarbons and inorganic gases. The vapor and liquid phases are described through fugacity coefficients using an EOS. The latter can be used for more complex molecules at low pressures. An activity coefficient is used for the liquid phase and an EOS is used for the vapor phase. Although they are two different methods, both can be derived from statistical mechanics (Vera and Prausnitz 1972, Sandler and Prausnitz 1982, Sandler 1985). For the accuracy and simplicity, we use the EOS method for phase behavior modeling for gas flooding in this dissertation.

Sandler (1985) showed that most cubic EOSs can be derived by plugging different approximations into a generalized form of the canonical partition function, which is referred to as the generalized van der Waals partition function. The generalization significantly improved the understanding of the relationship between the molecular theory and thermodynamic models used in engineering. The most important assumption in a cubic EOS or a van der Waals type EOS is that molecules are spherically symmetric. Although this assumption does not allow for complex molecules such as polar molecules and hydrogen bonding molecules, it enables us to separate the total energy of molecules into five independent terms; translation, rotation, vibration, electronic excitation, and interaction energy. The assumption of separable energies leads to the separation of the effects of free volume and molecular interactions, which originated with van der Waals (1873). The van der Waals EOS is

$$P = RT/(\underline{V} - b) - a/\underline{V}^2, \qquad (2.35)$$

where $\underline{V}$ is the molar volume and R is the gas constant. The first term of the right hand side of equation (2.35) is the free volume term and the second is the interaction term. The parameter a is referred to as the attraction parameter. The parameter b is often called the covolume parameter after Dupré (1869).

A large number of variations of the van der Waals EOS have been developed. Based on the comparisons of results from molecular simulation with those from widely used EOSs such as the Redlich-Kwong EOS and the Peng-Robinson EOS, Lee (1986) concluded that those cubic EOSs have little molecular level basis. The reasonable accuracy of those cubic EOSs would come from the empirically determined parameters and cancellation of errors between the attraction and covolume parameters.

To extend a cubic EOS to mixtures of N_C components, the following van der Waals mixing rules are widely used:

$$a_m = \sum\nolimits_{i=1}^{N_C} \sum\nolimits_{j=1}^{N_C} x_i x_j a_{ij} \text{ and } b_m = \sum\nolimits_{i=1}^{N_C} \sum\nolimits_{j=1}^{N_C} x_i x_j b_{ij}. \tag{2.36}$$

Parameters a_m and b_m are used in the same EOS as a pure fluid. Those quadratic mixing rules are justified by considering the virial form of a cubic EOS, where the second virial coefficient is linear in parameters a and b as shown in Abbott (1979). On the other hand, the n^{th} virial coefficient is related to interactions between n bodies (Hill 1986). That is, the second virial coefficient should be quadratic in composition as a consequence of pair-wise additive interaction energies. For hard spheres, b_m in equations (2.36) becomes simpler, resulting in the following mixing rules:

$$a_m = \sum\nolimits_{i=1}^{N_C} \sum\nolimits_{j=1}^{N_C} x_i x_j a_{ij} \text{ and } b_m = \sum\nolimits_{i=1}^{N_C} x_i b_i. \tag{2.37}$$

The combining rule for a_{ij} is

$$a_{ij} = \sqrt{a_i a_j}\left(1 - k_{ij}\right) = a_{ji},$$

where k_{ij} is the binary interaction coefficient (BIC) between components i and j.

The Peng-Robinson EOS is used with the van der Waals mixing rules, equations (2.37), for phase behavior modeling for compositional reservoir simulation throughout this dissertation. The Peng-Robinson EOS is

$$P = RT/\left(\underline{V} - b\right) - a\left(T\right)/\left[\underline{V}\left(\underline{V} + b\right) + b\left(\underline{V} - b\right)\right], \tag{2.38}$$

where $a\left(T\right) = 0.45724 R^2 T_C^2 \alpha\left(T\right)/P_C$

$$b = 0.07780 RT_C/P_C$$

$$\alpha\left(T\right) = 1 + \kappa\left(1 - \sqrt{T/T_C}\right)$$

$$\kappa = 0.37464 + 1.54226\omega - 0.26992\omega^2 \text{ for } \omega < 0.49$$

$$\kappa = 0.37964 + \omega\left(1.48503 + \omega(-0.16442 + 0.01667\omega)\right) \text{ for } \omega > 0.49.$$

The fugacity coefficient of component *i* in a mixture using the Peng-Robinson EOS is

$$\begin{aligned} \ln\varphi_i = {} & \frac{B_i}{B_m}\left(Z - 1\right) - \ln\left(Z - B_m\right) \\ & - \frac{A_m}{\left(\delta_1 - \delta_2\right)B_m}\left(\frac{2\sum_{j=1}^{N_C} x_j A_{ij}}{A_m} - \frac{B_i}{B_m}\right)\ln\left[\frac{Z + \delta_1 B_m}{Z + \delta_2 B_m}\right], \end{aligned} \tag{2.39}$$

where $\delta_1 = 1 + 2^{0.5}$ and $\delta_2 = 1 - 2^{0.5}$. The attraction and covolume parameters are dimensionless in equation (2.39); *e.g.*, $A_m = a_m P/(RT)^2$, $A_{ij} = a_{ij} P/(RT)^2$, and $B_m = b_m P/RT$.

2.2 LITERATURE REVIEW

This section presents various algorithms for phase equilibrium calculations for two and three phases. Three-phase equilibrium calculations are important for simulation of low-temperature oil displacements using CO_2 or rich gas. A review of low-temperature oil displacement by CO_2 is also presented in terms of multiphase behavior of mixtures of oil with CO_2 or rich gas, displacement characteristics, experimental observations on displacement mechanisms, and two-phase approximations proposed in the literature.

2.2.1 Flash Calculations

Flash calculations determine phase properties and amounts of equilibrium phases for a given temperature, pressure, and overall composition. The previous sections derived two conventional formulations for flash calculations, minimization of the Gibbs free energy and solution of fugacity equations. This section presents algorithms to solve the formulated problems.

The number of independent variables used is important for development of an algorithm. Considering implementation in a compositional reservoir simulator, the number of independent variables or equations to be solved should be minimized because computational efforts rapidly increase with the number of equations to be solved. This is true especially when the algorithm involves solution of a system of equations because a direct solver requires operation counts on the order of the cube of the number of equations. Use of more independent variables can also result in more iterations required to converge.

For conventional formulations, the minimum number of independent variables or equations to be solved is $N_C(N_P - 1)$ for a N_P-phase flash calculation using N_C components. Although there are algorithms in the literature that solve for more than $N_C(N_P - 1)$ independent variables (*e.g.*, Asselineau *et al.* 1979, Varotsis 1989, Teh and Rangaiah 2002), we do not discuss those algorithms. In Chapters 4 and 5, we develop a flash algorithm that solves for $6(N_P - 1)$ independent variables, which can be significantly fewer than $N_C(N_P - 1)$ for conventional flash algorithms.

2.2.1.1 Minimization of the Gibbs Free Energy

Many different algorithms to minimize the Gibbs free energy have been proposed and compared in the literature (*e.g.*, Gautam and Seider 1979, Ohanomah and Thompson 1984, Trangenstein 1985, Trangenstein 1987, Lucia *et al.* 1985, Ammar and Renon 1987, Litvak 1994, Teh and Rangaiah 2002). The standard type of algorithm for minimization of $\underline{G}_R$ given in equation (2.21) is the algorithms of Michelsen (1982b) and Perschke *et al.* (1989). This type of algorithm is based on Newton's method with a line-search technique, where the modified Cholesky decomposition algorithm of Gill and Murray (1974) provides a search direction if the Hessian matrix is not positive definite.

The standard minimization is performed in terms of $N_C(N_P - 1)$ independent variables,

$$w_{ij} \equiv \beta_j x_{ij}, \text{ where } i = 1,\ldots,N_C \text{ and } j = 1,\ldots,(N_P - 1). \tag{2.40}$$

Because $\sum_j w_{ij} = z_i$ from equations (2.16), w_{iN_P} are dependent on the others and arbitrarily selected as the reference values. Phase component mole fractions x_{ij} can be expressed as $x_{ij} = w_{ij}/\sum_i w_{ij}$ because $\sum_i w_{ij} = \beta_j$. The minimization problem can be written as follows:

$$\begin{aligned}
&\underset{\underline{w}}{\text{minimize}} \quad \underline{G}_R = \sum_{j=1}^{N_P} \sum_{i=1}^{N_C} \beta_j x_{ij} \ln\left(x_{ij}\varphi_{ij}\right) \\
&\text{subject to } \; w_{mn} = \beta_n x_{mn} \geq 0 \; \text{ and } \; \sum_{n=1}^{N_P} w_{mn} = z_m, \\
&\text{where } m = 1,\ldots,N_C \text{ and } n = 1,\ldots,N_P.
\end{aligned} \tag{2.41}$$

For a function F to be a local minimum at x^*, the sufficient condition is that $\nabla F\left(x^*\right) = 0$ and $\nabla^2 F\left(x^*\right)$ is positive definite. The first derivatives of $\underline{G}_R$ with respect to the independent variables, w_{mn} ($m = 1,\ldots,N_C$ and $n = 1,\ldots,N_P - 1$), are

$$\begin{aligned}
\partial \underline{G}_R / \partial w_{mn} &= \partial\left[\sum_{j=1}^{N_P} \sum_{i=1}^{N_C} w_{ij} \ln\left(x_{ij}\varphi_{ij}\right)\right] \Big/ \partial w_{mn} \\
&= \ln\left(x_{mn}\varphi_{mn}\right) - \ln\left(x_{mN_P}\varphi_{mN_P}\right) \\
&\quad + \sum_{i=1}^{N_C} w_{in}\left[\partial \ln\left(x_{in}\varphi_{in}\right)/\partial w_{mn}\right] + \sum_{i=1}^{N_C} w_{iN_P}\left[\partial \ln\left(x_{iN_P}\varphi_{iN_P}\right)/\partial w_{mn}\right] \\
&= \ln f_{mn} - \ln f_{mN_P} + \left[\sum_{i=1}^{N_C} x_{in}\left(\partial \overline{G}_{in}/\partial x_{mn}\right) + \sum_{i=1}^{N_C} x_{iN_P}\left(\partial \overline{G}_{iN_P}/\partial x_{mN_P}\right)\right] \Big/ RT \\
&= \ln f_{mn} - \ln f_{mN_P}.
\end{aligned} \tag{2.42}$$

In equation (2.42), the Gibbs-Duhem equation was used in the final step. Equation (2.42) indicates that the working equations for the minimization are the fugacity equations. The Hessian matrix is analytically derived from equation (2.42). The gradient vector and Hessian matrix are used in the Newton's iteration as given in equation (2.32).

As mentioned in section 2.1.2, minimization of $\underline{G}_R$ or $\underline{G}$ must satisfy the material balance equations (2.16) at every iteration step to fix a reference value of the function. The selection of independent variables given in equations (2.40) results in the easiest way to satisfy the material balance equations at every iteration step. After updating the $N_C(N_P - 1)$ independent variables at an iteration step, the dependent variables for the remaining phase can be calculated as

$$w_{iN_P} = z_i - \sum_{j=1}^{N_P-1} w_{ij}, \text{ where } i = 1, ..., N_C. \tag{2.43}$$

The algorithm of Perschke *et al.* (1989) is the following:

1. Obtain initial estimates for the $N_C(N_P - 1)$ independent variables w_{ij}, where i = 1,…,N_C and j = 1,…,(N_P − 1).
2. Calculate the dependent variables w_{iN_P} using equations (2.43).
3. Calculate compressibility factors and fugacity coefficients for N_P phases using an EOS. When the cubic EOS has multiple roots of the compressibility factors, the correct root is selected that results in the lowest Gibbs free energy (Evelein *et al.* 1976).
4. Calculate the gradient vector using equation (2.42) and the Hessian matrix analytically.
5. Decompose the Hessian matrix using the modified Cholesky decomposition algorithm. The positive definiteness is checked during the decomposition.
6. If the Hessian matrix is confirmed to be positive definite in step 5, check the convergence using the max norm of the gradient vector. If convergence is achieved, then stop. Otherwise, continue to step 7 below.

7. Obtain a search direction by solving the system of equations that is already decomposed in step 5.
8. Calculate a step length using the line search algorithm given in equation (2.33). This step must satisfy the positivity constraints given in equations (2.41), and also result in a lower value of the Gibbs free energy than that in the previous iteration step. Otherwise, stop.
9. Update the $N_C(N_P - 1)$ independent variables and go back to step 2.

Because the above algorithm is based on Newton's method, the convergence rate is quadratic in the vicinity of a solution. Perschke (1988) implemented the above algorithm for two and three phases in UTCOMP (Chang 1990, Chang *et al.* 1990), a multiphase compositional reservoir simulator. As will be mentioned in the next section, Perschke (1988) used an accelerated successive substitution algorithm to provide initial estimates for the independent variables.

Minimization algorithms can fail to converge to the correct solution for the following reasons: existence of multiple minima, a non-positive definite Hessian matrix, and a nearly singular Hessian matrix. When multiple minima exist, minimization algorithms can converge to a local minimum that is not the correct solution (Michelsen 1993). Multiple minima frequently occur for more than two phases. The best way to avoid convergence to such a false solution is to provide good initial estimates to start the minimization. Good initial estimates are often available from the previous time step in compositional reservoir simulation except when the number of equilibrium phases changes over the time step.

A non-positive definite Hessian matrix can occur when the current iteration point is not close to the solution. When the Hessian matrix is not positive definite, the resulting search direction is not a descent direction. In the above algorithm of Perschke *et al.* (1989), the modified Cholesky decomposition algorithm forces the Hessian matrix to be positive definite with minimal changes of diagonal entries.

When the Hessian matrix is significantly ill-conditioned, the modified Cholesky decomposition makes it safely positive definite. However, it can give an overly large step-size along the calculated direction (Dennis and Schnabel 1996) and that direction can be significantly affected by round-off errors due to the nearly singular Hessian matrix (Trangenstein 1987). A line-search technique often fails to find a point of lower Gibbs free energy for such a case. The ill-conditioned Hessian matrix frequently occurs during simulation of multicontact miscible gas flooding because of a large number of flash calculations in near-critical regions (Trangenstein 1987). As will be presented in Chapter 5, this ill-conditioning problem becomes more severe when more components are used in the simulations because of smaller values for independent variables. Trangenstein (1987) proposed a variable transformation procedure to overcome the ill-conditioning problem.

An issue in flash calculations is convergence to a false solution where multiple phases have the same composition and density. For two phases, this kind of false solution is called the trivial solution. Minimization of the Gibbs free energy can avoid the trivial solution because the trivial solution will have a higher Gibbs free energy than the correct solution (Trangenstein 1987).

Local minimization algorithms, such as the ones of Trangenstein (1987), Michelsen (1982b), and Perschke *et al.* (1989), have difficulties with existence of multiple minima. The solution for a flash calculation must be the global minimum of the Gibbs free energy. Although global minimization algorithms can have a greater possibility to find the global minimum than local minimization algorithms, they are not suitable for use in compositional simulation due to their computational inefficiency.

Also, Teh and Rangaiah (2002) presented example calculations where a global minimization algorithm based on a stochastic method cannot converge to the global minimum even for two-phase calculations, which are in general easier than three-phase calculations.

Newton's method has a quadratic convergence rate in the vicinity of a solution exploiting curvature information captured by the Hessian matrix. However, it can be computationally expensive to compute the Hessian matrix and solve the system of equations at each iteration step. Quasi-Newton methods use first derivative information at a sequence of iteration steps to capture curvature information, instead of computing second derivatives. A popular quasi-Newton method is based on the Broyden-Fletcher-Goldfarb-Shanno (BFGS) method (Broyden 1970ab, Fletcher 1970, Goldfarb 1970, Shanno 1970, Goldfarb 1976) for an inverse of the Hessian matrix approximation. The BFGS quasi-Newton method is super-linearly convergent at best, and can avoid solution of the system of equations at the expense of curvature information used in the iteration. That is, the BFGS quasi-Newton method can take more iterations than Newton's method at less computational effort per iteration. Ammar and Renon (1987) compared various algorithms for minimization of the Gibbs free energy including Newton's and BFGS quasi-Newton methods. Their comparisons showed that Newton's method requires shorter execution time than the BFGS quasi-Newton method in all cases studied in their paper. In this research, we do not consider the BFGS quasi-Newton method.

2.2.1.2 Solution of Fugacity Equations

Successive substitution (SS) is the traditional flash algorithm based on solution of the fugacity equations. SS is widely used because of its simplicity and robustness. In flash calculations using SS, the independent variables are *K*-values, which are defined as

$$K_{ij} = x_{ij} / x_{iN_P}, \text{ where } i = 1,\ldots,N_C \text{ and } j = 1,\ldots,(N_P - 1). \tag{2.44}$$

The N_Pth phase is arbitrarily selected as the reference phase in equations (2.44). K-values represent the tendency of components to partition among phases. SS solves equations (2.10) for K_{ij} (i = 1,…,N_C and j = 1,…,N_P − 1) with the material balance equations (2.16), (2.18), and (2.19). Rearrangement of equations (2.10) yields the following iteration scheme:

$$\ln K_{ij}^{k+1} = \ln \varphi_{iN_P}^{k} - \ln \varphi_{ij}^{k}, \text{ where } i = 1,\ldots,N_C \text{ and } j = 1,\ldots,(N_P - 1). \tag{2.45}$$

In equations (2.45), the superscripts indicate iteration steps.

As shown in equations (2.45), fugacity coefficients for phase components are calculated to update K-values in every iteration step. Because a fugacity coefficient of component i in phase j at a given temperature and pressure is a function of the composition of phase j, we need to calculate phase compositions for a given set of K-values. The standard procedure is a constant-K flash calculation as originally proposed by Rachford and Rice (1952). The goal of a constant-K flash calculation is to determine the phase mole fractions and phase compositions for a fixed overall composition and set of specified K-values.

The equations for a constant-K flash calculation are derived using equations (2.16), (2.18), (2.19), and (2.44). Substitution of equations (2.18) and (2.44) into equations (2.16) eliminates the dependent phase mole fraction and phase compositions resulting in

$$x_{iN_P} = z_i / t_i, \text{ where } t_i = 1 - \left[\sum\nolimits_{j=1}^{N_P - 1} \left(1 - K_{ij}\right) \beta_j \right] \text{ for } i = 1,\ldots,N_C. \tag{2.46}$$

Using equations (2.19) and (2.44), we obtain

$$\sum\nolimits_{i=1}^{N_C} \left(1 - K_{ij}\right) x_{iN_P} = 0 \quad \text{for } j = 1,\ldots,N_P - 1. \tag{2.47}$$

Substitution of equations (2.46) into equations (2.47) results in the final form of

$$f_j(\beta) = \sum_{i=1}^{N_C} \left(1-K_{ij}\right) z_i \big/ t_i = 0 \quad \text{for } j = 1,\ldots,N_P - 1, \tag{2.48}$$

where β is a vector with elements β_j (j = 1,…,N_P − 1). Rachford and Rice (1952) originally developed a special case of equations (2.48) for two phases, which is called the Rachford-Rice equation. Equations (2.48) are called the multiphase Rachford-Rice equations.

In each SS, K-values are updated in the outer iteration loop using equations (2.45) and a selected EOS. A constant-K flash calculation solves equations (2.48) in the inner iteration loop to determine phase compositions and phase mole fractions. To provide initial estimates for the independent variables, the Wilson's correlation (1969) is commonly used for two phases (Heidemann 1983), although other correlations have also been proposed by Whitson and Torp (1983), Chien (1983), and Varotsis (1989). The Wilson's correlation is given as

$$K_i = P_{Ri} \exp\left[5.373\left(1+\omega_i\right)\left(1-T_{Ri}\right)\right], \text{ where } P_{Ri} = P/P_{Ci} \text{ and } T_{Ri} = T/T_{Ci}\ , \tag{2.49}$$

where ω_i is the acentric factor of component i, and P_{Ci} and T_{Ci} are the critical pressure and temperature of component i, respectively. The Wilson's correlation assumes that molecules are similar to each other in size and electrical characteristics, and the phases form ideal solutions (Peng and Robinson 1976b, Michelsen 1993). Equation (2.49) is a good estimate only at low pressures. For more than two phases, better initial estimates are provided by stability analysis.

Steps for the SS algorithm are

1. Obtain initial estimates for (N_P − 1) sets of N_C K-values.
2. Calculate phase mole fractions and phase compositions by solving equations (2.48) (see section 2.2.2 and Chapter 3).

3. Calculate compressibility factors and fugacity coefficients for N_P phases using a cubic EOS.
4. Check for convergence based on the residuals of the fugacity equations, equations (2.10). If convergence is achieved, stop. Otherwise, continue to step 5 below.
5. Update the (N_P − 1) sets of *K*-values using equations (2.45).
6. Go to step 2.

The SS algorithm is linearly convergent for non-ideal mixtures, and its convergence becomes significantly slow in a near-critical region (Michelsen 1982b). To enhance convergence, several authors proposed different acceleration procedures (Boston and Britt 1978, Mehra *et al.* 1982, Mehra *et al.* 1983, Nghiem and Heidemann 1982, Michelsen 1982b). Perschke (1988) implemented the algorithm of Mehra *et al.* (1983) in the UTCOMP simulator (Chang *et al.* 1990) for two- and three-phase calculations. Michelsen (1998), however, pointed out that the typical speed-up of about a factor of three is still much slower than second-order methods. Also, these methods accelerate the convergence rate at the expense of the robustness of the original SS (Pan and Firoozabadi 2003, Michelsen and Mollerup 2004).

The robustness of SS is related to the fact that it can be considered as a gradient method for minimization of the Gibbs free energy (Mehra *et al.* 1983, Ammar and Renon 1987, Kaul 1992). Rearrangement of equations (2.45) results in

$$\left(\ln K\right)^{k+1} = \left(\ln K\right)^{k} - d_{\ln K}{}^{k}, \tag{2.50}$$

where ln$K$ = {lnK_{ij}} and $d_{\ln K} = \left\{\ln f_{ij} - \ln f_{iN_P}\right\}$ for i = 1,…,N_C and j = 1,…,(N_P − 1). Using equations (2.42) and (2.50), we obtain

$$d_{\ln K} = -\nabla_w \underline{G}_R \, . \tag{2.51}$$

A first-order approximation of $d_{\ln K}$ can be expressed as

$$d_{\ln K} \approx U dw, \tag{2.52}$$

where $U = \{\partial \ln K_{ij}/\partial w_{mn}\}$ and $dw = \{w_{ij}\}$ for i, $m = 1,\ldots,N_C$ and j, $n = 1,\ldots,(N_P - 1)$. Substitution of equation (2.51) into equation (2.52) results in

$$dw = -U^{-1}\nabla_w \underline{G}_R . \tag{2.53}$$

Kaul (1992) showed that matrix U is the same as the ideal mixing part of the Hessian matrix for the Gibbs free energy, H^I (see equation (2.22)). Therefore, equation (2.53) can be rewritten as

$$dw = -\left(H^I\right)^{-1} \nabla_w \underline{G}_R . \tag{2.54}$$

Equation (2.54) indicates that the SS algorithm is a gradient method for minimization of the Gibbs free energy if the Hessian matrix H^I is positive definite. Mehra *et al.* (1983) and Ammar and Renon (1987) proved for two phases that the Hessian matrix H^I is positive definite except at the trivial solution and the phase boundary, where it becomes semi-positive definite.

A difference between the SS algorithm and the minimization algorithm presented in section 2.2.1.1 is that the descent direction from the SS algorithm accounts only for the ideal mixing part of the Gibbs free energy. The poor convergence behavior of the SS algorithm in a near-critical region results from not considering the excess part of the Gibbs free energy. Another difference is that, unlike the minimization algorithm, the SS algorithm always takes a unit step size (*i.e.*, α in equation (2.32) is always 1.0). The robustness of the SS algorithm can be improved by confirming that the SS step results in a lower Gibbs free energy at each iteration step. If the Gibbs free energy is not decreased by that step, the step size is reduced to properly decrease the Gibbs free energy. However, reducing SS step sizes tends to increase the number of iterations required with little improvement of the robustness (Michelsen 1982b). The SS algorithm is very robust although it requires a large number of iterations in a near-critical region.

Because of the robustness, the SS algorithm is commonly used in phase equilibrium calculations to provide good initial estimates for higher order methods like Newton's method (Mehra *et al.* 1982, Nghiem *et al.* 1983, Michelsen 1982b, Ammar and Renon 1987, Pan and Firoozabadi 2003). The use of SS first and Newton's method next is commonly applied in compositional reservoir simulation, because Newton's method is quadratically convergent only when a good initial estimate of the parameters is given. SS is linearly convergent with a much larger region of convergence compared to Newton's method.

Heidemann and Michelsen (1995) reported that the SS algorithm may not converge for mixtures that exhibit a large negative deviation from an ideal solution. This suggests that use of negative BICs for the attraction term in a cubic EOS fluid model can adversely affect the robustness or number of iterations required for the SS algorithm.

The fugacity equations can be solved using higher-order methods like Newton's method for root-finding (see equation (2.34)). Conventional independent variables are *K*-values or the logarithm of *K*-values (Michelsen 1982b, Abhvani and Beaumont 1987), although other selections are possible (Fussell and Yanosik 1978, Fussell 1979, Fussell and Fussell 1979). Those root-finding algorithms for the fugacity equations are efficient only for two phases and not reliable for three phases (Michelsen 1982b). As the number of phases increases, there can be more critical points and more stationary points of the Gibbs free energy to which those algorithms converge. Because the root-finding algorithms do not necessarily decrease the Gibbs free energy at each iteration step, they can convergence to a false solution where multiple phases have the same composition and density (*i.e.*, the trivial solution for two phases). For three phases, Michelsen (1982b) recommended a minimization algorithm of the Gibbs free energy similar to the one presented in section 2.2.1.1.

2.2.2 Constant-*K* Flash Calculations

As mentioned in the previous section, flash calculations initially use successive substitution (SS) to provide better *K*-value estimates for final convergence of the equilibrium phase compositions using Newton's iterations. SS iterations and, depending on the choice of independent variables, Newton's iterations involve two loops; the outer iteration loop containing the inner iteration loop. *K*-values are updated based on fugacity equations in the outer iteration loop. Phase compositions and mole fractions are calculated to satisfy material balance equations in the inner iteration loop. Constant-*K* flash calculations are commonly performed in the inner loop as originally proposed by Rachford and Rice (1952). The goal of constant-*K* flash calculations is to determine the phase mole fractions and phase compositions for a fixed overall composition and set of specified *K*-values. Chapter 3 focuses on the constant-*K* flash calculation (inner iteration) as part of a rigorous EOS flash (outer iteration) for compositional reservoir simulation for any number of phases.

There are two different possibilities for a constant-*K* flash calculation within the framework of compositional simulation. The first, a positive flash, is a N_P-phase flash where the overall composition lies within the N_P-phase region, resulting in positive phase mole fractions. The second, a negative flash, is a flash where the overall composition is not within the N_P-phase region resulting in one or more negative phase mole fractions. In compositional simulation, the algorithm must be capable of successfully performing both types of flash calculations. Since a flash calculation is performed only when phase instability is detected based on the tangent plane criterion (Baker *et al.* 1982), phase mole fractions must be positive once the outer iteration correctly achieves the convergence. However, phase mole fractions calculated in a constant *K*-flash calculation can be negative prior to convergence, depending on the K-values provided by the most recent outer iteration (Nghiem and Li 1984, Pan and Firoozabadi 2003).

Another type of negative flash that is not considered in this dissertation is one where the overall composition lies in negative composition space. This kind of negative flash can be used for minimum miscibility pressure calculations (Yuan and Johns 2005), but is not needed in compositional reservoir simulation.

For two phases, several different formulations and solution techniques were proposed (Leibovici and Neoschil 1992, Warren and Adewumi 1993, Li and Johns 2007) and used in compositional reservoir simulation (Wang *et al.* 1997). However, the robustness of two-phase constant-K flash calculations is not an issue because it is a root-finding problem for a univariate monotonic function, which can be safely solved by a combination of bisection and Newton's method coupled with underrelaxation. The solution lies in the feasible region as identified previously by Whitson and Michelsen (1989). Bisection is performed to make the region narrower, while underrelaxation is used to avoid the Newton's iteration jumping out of the region of interest.

For more than two phases, the increase in the number of independent variables to be solved makes the behavior of the Rachford-Rice equations (2.48) more implicit and complicated. There are several attempts to solve this multiphase K-value problem, which are generally of two types; root-finding and minimization. The root-finding approach is more commonly used and typically solves a system of ($N_P - 1$) Rachford-Rice equations with Newton's method (Nelson 1987, Bünz *et al.* 1991, Eubank 2006). An exception is Deam and Maddox (1969), who proposed a different set of equations to be solved. None of them consider constraints for negative flash calculations. Leibovici and Neoschil (1995) extended the feasible region of Whitson and Michelsen (1989) to multiphase calculations and used Newton's method with underrelaxation.

However, Leibovici and Nichita (2008) stated that the algorithm does not work for some situations, and we demonstrate in Chapter 3 a case where the method cannot converge. Haugen *et al.* (2007) proposed a two-dimensional bisection algorithm to provide a good initial estimate for Newton's iterations for three-phase calculations. However, their procedure can take numerous iterations, and it likely does not always converge especially when an overall composition is in a near-critical region. This is consistent with the statement by Dennis and Schnabel (1996) that the bisection method does not extend naturally to multiple dimensions.

Michelsen (1994) developed a novel approach to multiphase constant-*K* flash calculations by rewriting the Rachford-Rice equation solution as the minimization of a convex function. Although no derivation of the function is given in his paper, his approach in our opinion is superior to the root-finding approach. The Michelsen's algorithm, however, considered only positive flash calculations. Leibovici and Nichita (2008) attempted to overcome this problem by formulating the minimization using the feasible region of Leibovici and Neoschil (1995), resulting in a minimization problem with an open constraint set. Their feasible region is confined by poles where the function cannot be defined, so that the feasible region is not sufficient and convergence problems can occur. Also, Leibovici and Nichita (2008) did not develop an algorithm to solve their minimization problem. Instead, they used a multipurpose minimization software. Robustness and efficiency of their minimization depend on the algorithm used because simple minimization algorithms cannot handle the open constraint set.

The importance of multiphase flash calculations for compositional simulation requires a robust and efficient algorithm for multiphase constant-*K* flash calculations that always converges. In Chapter 3, we develop an algorithm for which convergence can be analytically proven for any number of phases for both positive and negative constant-*K* flash calculations.

2.2.3 Stability Analysis

In section 2.1.3, we presented two conventional formulations for stability analysis, minimization of the tangent plane distance (TPD) function and stationary point method, although other formulations are possible (Nagarajan *et al.* 1991, Gupta *et al.* 1991, Eubank *et al.* 1992). We also mentioned a difficulty with the conventional stability analysis using a cubic EOS that location of the global minimum or all stationary points of the TPD function cannot be guaranteed. This is because a solution to be converged depends significantly upon the initial estimate used.

Attempting to improve the reliability of stability analysis, Michelsen (1982a) recommended use of multiple initial estimates. For two phases, the following two sets of initial estimates are used for the independent variables X_i ($i = 1,\ldots,N_C$) defined in equations (2.29):

$$X_i = K_i z_i \tag{2.55}$$

$$X_i = z_i / K_i, \tag{2.56}$$

where *K*-values are calculated using the Wilson's correlation, equation (2.49). Equations (2.55) attempt to search for a vapor-like phase, while equations (2.56) try to find a liquid-like phase.

For multiple phases, Michelsen (1982a) recommended using the lightest and heaviest components as pure phases for initial estimates. In addition, he used the following two sets of initial estimates:

$$X_i = z_i \varphi\left(\underline{z}\right) \tag{2.57}$$

$$X_i = \sum\nolimits_{j=1}^{N_P} y_{ij} \Big/ N_P\ , \tag{2.58}$$

where y_{ij} is a mole fraction of component i in phase j that is already known to exist. Equation (2.57) assumes an ideal gas mixture, and equation (2.58) provides the arithmetic mean of existing phase compositions.

There are four possible consequences of a local search for a minimum or stationary point of the TPD function; a positive value and a negative value of the TPD function, the trivial solution, and non-convergence. The trivial solution is where independent variable X_i at convergence is equal to the test phase composition or existing equilibrium phase compositions. That is, the trivial solution exists only at the overall composition for a single-phase stability analysis, but there are N_P trivial solutions for stability analysis for a N_P-phase mixture. The initial estimates given above are sequentially used until phase instability is detected by a negative value for the TPD function. Once phase instability is detected during a search for a minimum or stationary point, the stability analysis stops and the subsequent flash calculations are performed for split phase properties (Michelsen 1993). If stability analysis cannot find a negative value of the TPD function, the phase is assumed to be stable.

Successive substitution (SS) is widely used to locate a stationary point because of its robustness. Rearrangement of stationarity equations (2.29) results in the SS step,

$$X_i^{k+1} = z_i \varphi(\underline{z}) \Big/ \varphi(\underline{x})^k \text{, where } i = 1, \ldots, N_C \text{.} \tag{2.59}$$

In equations (2.59), the superscripts indicate iteration steps. The mole fractions are calculated as

$$x_i = X_i \Big/ \sum\nolimits_{j=1}^{N_C} X_j \text{, where } i = 1, \ldots, N_C \text{.} \tag{2.60}$$

The SS algorithm is as follows:

1. Calculate compressibility factors and fugacity coefficients for the phase with composition $\underline{z}$. When the cubic EOS has multiple roots in the compressibility factor,

the correct root is selected to result in the lowest Gibbs free energy (Evelein *et al.* 1976). This is also true for step 4 below.

2. Obtain initial estimates for X_i ($i = 1,\ldots,N_C$) from either equations (2.55), or (2.56), or (2.57), or (2.58).
3. Calculate mole fractions using equations (2.60).
4. Calculate compressibility factors and fugacity coefficients for the phase with composition $\underline{x}$.
5. Check for convergence based on the residuals of the stationarity equations (2.29). If convergence is achieved, stop. Otherwise, continue to step 6.
6. Update the N_C independent variables using equations (2.59).
7. Go to step 3.

The SS algorithm is linearly convergent, and the convergence is rapid when fugacity coefficients weakly depend upon the composition (Michelsen 1982a). Convergence of the SS algorithm, however, becomes significantly slow in a near-critical region.

For rapid convergence, Newton's method can be used to solve the stationarity equations (2.29) for independent variables X_i ($i = 1,\ldots,N_C$) (Perschke 1988). As in flash calculations, Newton's method can be initiated by the SS algorithm for good initial estimates. Perschke (1988) applied this use of SS followed by Newton's method in the UTCOMP simulator (Chang *et al.* 1990) because Newton's method is quadratically convergent only when a good initial estimate of the parameters is given. SS is linearly convergent with a much larger region of convergence compared to Newton's method.

Local minimization of the TPD function can be also used. Michelsen (1982a) recommended the BFGS quasi-Newton method, which is super-linear convergent near a solution (see section 2.2.1.1). The BFGS quasi-Newton method does not solve a system of equations at each iteration step. However, compared to Newton's method, it can take a larger number of iterations to converge because of less curvature information used for a descent direction. Perschke (1988) implemented the algorithm of Trangenstein (1987) in the UTCOMP simulator, which minimizes the TPD function. Perschke (1988) concluded that the minimization algorithm implemented is not as reliable as solution of stationarity equations using Newton's method.

As mentioned in section 2.1.3, stability analysis is performed for a single-phase mixture or individual phases of a multiphase mixture. For a N_P-phase mixture, the stability criterion based on the sign of the TPD function can be applied to all of the individual N_P phases (Michelsen 1982a). A standard algorithm performs stability analysis for only one of N_P phases for a multiphase mixture (Nghiem and Li 1984, Perschke *et al.* 1989, Nichita *et al.* 2002a, Nichita *et al.* 2006) because the existing N_P phases are on the same tangent plane to the Gibbs free energy. Stability analysis is needed for just one of the N_P phases if location of the global minimum or all stationary points of the TPD function is guaranteed. However, this is difficult to achieve for stability analysis using a cubic EOS. Stability analysis would be more reliable if more phases were tested because there would be more chances to locate the global minimum or all stationary points. However, efficiency and reliability should be balanced when implemented in a compositional simulator.

Michelsen (1982a) developed a method to detect whether or not the trivial solution is approached. If the method detects the trivial solution, the iteration is terminated. A different method was implemented in the UTCOMP simulator (version 3.8 2003). However, those methods must be carefully used because instability can be detected at a stationary point very close to the trivial solution for near-critical mixtures. This is particularly true in simulation of multicontact miscible gas flooding because stability analysis is frequently performed in a near-critical region.

Instead of performing a series of local searches for minima or stationary points of the TPD function, various global minimization approaches were proposed (*e.g.*, Trangenstein 1987, Sun and Seider 1995, Müller and Marquardt 1997, Pan and Firoozabadi 1998, Nichita *et al.* 2002b). Those algorithms are not guaranteed to converge to the global minimum. McDonald and Floudas (1995, 1997) developed a global minimization algorithm that always converges to the global minimum. However, their algorithm applies only when liquid phases are modeled using the NRTL, Wilson, modified Wilson, UNIQUAC, UNIFAC, or ASOG activity coefficient models, not a cubic EOS. We do not consider global minimization of the TPD function or the Gibbs free energy in this research because it is time-consuming and not suitable for use in compositional reservoir simulation.

The result from stability analysis can provide a good initial estimate for the subsequent flash calculation (Michelsen 1982a), except for stability analysis for a single-phase mixture. When stability analysis for a single-phase mixture with composition $\underline{z}$ identifies phase instability, we obtain composition $\underline{x}$ where the TPD function is negative. Using the two compositions $\underline{x}$ and $\underline{z}$, *K*-values (x_i/z_i or z_i/x_i for $i = 1,\ldots,N_C$) are calculated as the initial estimate for the subsequent two-phase flash calculation. However, composition $\underline{x}$ can be very close to composition $\underline{z}$ resulting in *K*-values that are near 1.0, whether or not composition $\underline{z}$ is near the critical point. If such *K*-values are used for a two-phase flash calculation for a non-critical mixture, the flash calculation will likely converge to the trivial solution. *K*-values from the Wilson's correlation (2.49) are safer to use in two-phase flash calculations for robust compositional simulation.

In stability analysis for two or more phases, a test phase composition is the composition of one of the known phases, instead of the overall composition. Therefore, stability analysis for N_P phases can provide a good estimate for the subsequent flash calculations for (N_P + 1) phases, where $N_P \geq 2$.

2.2.4 Efficient Flash Calculations for Compositional Simulation

Efficiency and reliability of compositional simulation depend significantly on the phase equilibrium algorithms used in the simulation. There are several factors affecting computational time and robustness of phase equilibrium calculations.

The total computational time of an iterative stand-alone algorithm is approximately a product of the computational time per iteration and the number of iterations. As discussed in the previous section on phase equilibrium algorithms, the number of iterations required to converge to a solution increases with the degree of miscibility between the equilibrium phases. The computational time per iteration, however, increases with N_P and N_C. Therefore, computational time of phase equilibrium calculations increases with the degree of miscibility, the number of coexisting phases, and the number of components used in the simulation.

Phase equilibrium calculations become more difficult and important, when multicontact miscibility is approached and/or when the number of phases increases. Convergence of phase equilibrium calculations becomes difficult to achieve in a near-critical region. The effect of errors in phase equilibrium calculations on compositional simulation is more significant in a near-critical region than in an immiscible region. This is because calculated phase properties are sensitive to the solution obtained in the flash calculations in a near-critical region.

An approach to efficient compositional simulation is to lump detailed components into fewer grouped components. This approach can speed-up the simulation by decreasing the number of components used in the calculations, but this often deteriorates the accuracy of phase behavior predictions, which is important in gas flooding simulations. Using more components in reservoir simulation is also suitable for reservoir–surface integrated modeling because surface process simulation typically requires 16-30 components (Leibovici *et al.* 2000).

Pedersen *et al.* (1985) reported fluid characterization examples where six pseudocomponents can reproduce the volumetric behavior of 40 ungrouped pseudocomponents. However, an EOS fluid model used in compositional simulation should provide accurate predictions of compositional behavior, which is more difficult to achieve compared to predictions of volumetric behavior.

The optimal number of pseudocomponents depends on operating conditions and processes to be simulated, such as depletion and miscible gas flooding (Kaul 1999). Therefore, determination of the optimal number of pseudocomponents requires sensitivity studies involving multiple fluid characterizations and simulation runs for each simulation project. Use of a small number of pseudocomponents without such time-consuming sensitivity studies would result in unreliable simulation results.

A non-iterative procedure to improve the efficiency of flash calculations in compositional simulation was developed by Stenby and Wang (1993) and Wang and Stenby (1994). The procedure is to linearly extrapolate phase component mole numbers with respect to pressure and overall component mole numbers from the previous time step. Their non-iterative procedure is part of Young’s flash algorithm (1991). Young’s flash algorithm uses the linear extrapolation to provide initial estimates for rigorous iterative flash calculations. Stenby and Wang concluded that their non-iterative procedure can decrease the computational time usually by a factor of two with reasonable accuracy. However, the accuracy of the simulation is problem-dependent because of the linear extrapolation. For example, the procedure could cause significant errors in simulation of miscible gas flooding with a large number of grid cells, large time steps, and a long simulation period. Such a difficult case for the non-iterative procedure was not tested in their paper.

Because approximate phase compositions and amounts from the non-iterative procedure can be far from the equilibrium state, simulations with the non-iterative procedure are not consistent with thermodynamics. Phase behavior predictions in simulations with the non-iterative procedure are not the same as those obtained through fluid characterization using an EOS. Therefore, reliability of simulation results cannot be confirmed without comparisons between the non-iterative and rigorous flash. The non-iterative procedure would be even more unreliable in three-hydrocarbon-phase simulation when the phase tracking algorithm uses phase compositions (Perschke 1988).

Another approach to efficient flash calculations for compositional simulation was proposed by Voskov and Tchelepi (2008) for two hydrocarbon-phases and by Gasmi *et al.* (2009) for three hydrocarbon-phases. Before starting a compositional reservoir simulation, they prepare tables that contain tie-simplex information (*i.e.*, tie-lines for two phases and tie-triangles for three phases) in composition space at temperature-pressure conditions to be simulated. Then, those tables are used to replace iterative stability analysis and to provide initial estimates for flash calculations during the simulation. Voskov and Tchelepi (2008) reported simulation examples where the simulations using their procedure were up to 3.6 times faster than those using conventional phase equilibrium calculations. Those speed-up results do not include time spent in the preparation of the tie-simplex tables used. Gasmi *et al.* (2009) used tie-simplex tables to replace flash calculations during the simulation, but predictions of the displacement front deviated from those with rigorous flash calculations. They presented no speed-up results for their three-hydrocarbon-phase simulations.

A drawback of using tie-simplex tables is that preparation of tie-simplex tables can be time-consuming. For N_C components exhibiting N_P phases at a fixed temperature and pressure, searches for tie-simplex must be performed in at least $\sum_j(N_C - j)$ directions, where $j = 2,\ldots,N_P$. For example, a system of 20 components forming three phases requires searches in at least 35 directions at a fixed temperature and pressure. Tie-simplex tables must be prepared to change reservoir oil, injection gas, the number of grid cells, and operating conditions (temperature and pressure). Also, speed-up from using tie-simplex tables depends on the amount of tie-simplex information prepared.

2.2.5 Reduced Method

A desirable approach to an efficient simulation is to reduce computational time without loss of accuracy. A reduced method that originated with Michelsen (1986) has been studied as a potential solution. In Chapters 4 and 5, we develop efficient and robust algorithms for flash calculations and stability analysis for two and three phases based on a reduced method. This section gives a literature review on reduced methods.

Michelsen (1986) demonstrated that flash calculations and stability analysis can be performed using only three and two independent variables, respectively. He assumed that all BICs are zero. His development was only for two-phase equilibrium calculations. The key idea was to consider fugacity coefficients as functions of the following two reduced parameters:

$$\begin{aligned} \theta_1 &= \sum\nolimits_{i=1}^{N_C} B_i x_i \\ \theta_2 &= \sum\nolimits_{i=1}^{N_C} \sqrt{A_i}\, x_i, \end{aligned} \tag{2.61}$$

where A_i and B_i are the EOS parameters for component i in dimensionless form (see section 2.1.5). x_i is the phase component mole fraction of component i in a phase.

From equation (2.39), a fugacity coefficient of component i in a mixture is given as

$$\ln \varphi_i = \frac{B_i}{B_m}\left(Z-1\right) - \ln\left(Z - B_m\right)$$
$$- \frac{A_m}{\left(\delta_1 - \delta_2\right) B_m}\left(\frac{2\sum_{j=1}^{N_C} x_j A_{ij}}{A_m} - \frac{B_i}{B_m}\right)\ln\left[\frac{Z + \delta_1 B_m}{Z + \delta_2 B_m}\right],$$

where $\delta_1 = 1 + 2^{0.5}$ and $\delta_2 = 1 - 2^{0.5}$. The fugacity coefficient is a function of the two reduced parameters for zero BICs because A_m, B_m, Z, and $\Sigma_j x_j A_{ij}$ can be expressed using those two parameters. That is,

$$A_m = \sum_{i=1}^{N_C}\sum_{j=1}^{N_C} x_i x_j \sqrt{A_i A_j}\left(1 - k_{ij}\right)$$
$$= \left(\sum_{i=1}^{N_C} x_i \sqrt{A_i}\right)^2 = \theta_2^2$$

$$B_m = \theta_1$$

$$Z = Z\left(A_m, B_m\right) = Z\left(\theta_1, \theta_2\right)$$

and,

$$\sum_{j=1}^{N_C} x_j A_{ij} = \sum_{j=1}^{N_C} x_j \sqrt{A_i A_j}\left(1 - k_{ij}\right)$$
$$= \sqrt{A_i}\sum_{j=1}^{N_C} x_j \sqrt{A_j} = \sqrt{A_i}\,\theta_2.$$

For reduced two-phase flash calculations, Michelsen (1986) used a phase mole fraction and two reduced parameters given in equations (2.61) as the independent variables. The following three equations are solved for those independent variables:

$$\begin{aligned} &\theta_1 - \sum_{i=1}^{N_C} B_i x_i = 0 \\ &\theta_2 - \sum_{i=1}^{N_C} \sqrt{A_i}\, x_i = 0 \\ &\sum_{i=1}^{N_C}\left(x_i - y_i\right) = 0, \end{aligned} \tag{2.62}$$

where x_i and y_i are the component mole fractions of component i in the liquid phase and the vapor phase, respectively. In equations (2.62), the liquid phase was arbitrarily selected as the independent phase. Newton's method for root-finding (see equation

(2.34)) was used to update the independent variables. The third equation in equations (2.62) is the Rachford-Rice equation.

In Michelsen's reduced stability analysis (1986), the following two equations are solved for two reduced parameters given in equations (2.61):

$$\begin{aligned} &\sum\nolimits_{i=1}^{N_C} \left(\theta_1 - B_i\right) X_i = 0 \\ &\sum\nolimits_{i=1}^{N_C} \left(\theta_2 - \sqrt{A_i}\right) X_i = 0, \end{aligned} \tag{2.63}$$

where X_i is defined in equations (2.29). Equations (2.63) are solved using Newton's method. The reduced method of Michelsen (1986) can offer significant savings in computational time because of fewer equations to be solved compared to N_C equations for conventional two-phase calculations.

Wang and Barker (1995) compared the non-iterative procedure (Stenby and Wang 1993) and the reduced flash of Michelsen (1986) in the UTCOMP simulator (Chang *et al.* 1990). They concluded that the reduced flash of Michelsen does not save significant computational time compared to the non-iterative procedure. However, they did not consider stability analysis using a reduced method to improve the efficiency of compositional simulation. They also did not compare the accuracy of simulations between the non-iterative and rigorous iterative flash. As mentioned in the previous section, the accuracy of the simulation with the non-iterative procedure is problem-dependent because of the linear extrapolation.

A drawback of Michelsen's reduced method is that the assumption of zero BICs is unsuitable for compositional reservoir simulation, especially for CO_2 flooding (Pedersen *et al.* 1985). Jensen and Fredenslund (1987) proposed a reduced method that can handle non-zero BICs for only one component. Hendriks (1988) proved that two-phase equilibrium calculations can be performed using a fewer number of independent variables than the number of components even for non-zero BICs. Hendriks and van Bergen

(1992) applied a reduced method to two-phase flash calculations with non-zero BICs. Their method approximates a BIC matrix using the spectral expansion. The minimum number of variables to obtain an accurate solution depends on the values of BICs.

After Hendriks and van Bergen (1992), many authors used the spectral expansion to handle non-zero BICs (Firoozabadi and Pan 2002, Nichita *et al.* 2002b, Pan and Firoozabadi 2003, Nichita *et al.* 2006, Hoteit and Firoozabadi 2006). However, the reduced parameters of Hendriks and van Bergen (1992) have a drawback when implemented in a compositional simulator. That is, the effect of truncated terms in the spectral expansion on the simulation results is unknown. Also, the number of reduced parameters becomes small only if the BIC matrix has few non-zero eigenvalues (Nichita *et al.* 2006).

Kaul and Thrasher (1996) presented an algorithm for minimization of the Gibbs free energy in reduced space for two-phase flash calculations. The number of independent variables is three for all zero BICs, and four for non-zero BICs. The independent variables in their method are not the reduced parameters because the ideal part of the Gibbs free energy contains phase component mole fractions (see section 2.1.2) which they were unable to calculate directly from the reduced parameters. As a result, their minimization algorithm has a non-symmetric matrix for the iteration equation, unlike the original form given in equation (2.32). This is a significant restriction because globally convergent methods cannot be applied, such as a line search technique and the modified Cholesky decomposition (Gill and Murray 1974, Gill *et al.* 1986) for the cases of a non-positive definite Hessian matrix. Also, they introduced approximations which become exact only for zero BICs. These approximations cause a significant sensitivity of convergence behavior to non-zero values of BIC because these approximations affect the search direction. Kaul and Thrasher (1996) showed an example where their minimization converges as slowly as successive substitution for non-zero BICs with the maximum value of 0.231.

Pan and Firoozabadi (2003) investigated the efficiency and robustness of two-phase flash calculations using the reduced parameters of Hendriks and van Bergen (1992). They compared root-finding of reduced flash equations with minimization of the Gibbs free energy in reduced space. The root-finding algorithm is an extension of that of Michelsen (1986) to non-zero BICs. The number of equations to be solved depends on the values of BICs. The minimization algorithm is similar to that of Kaul and Thrasher (1996). Pan and Firoozabadi (2003), however, did not use the approximations of Kaul and Thrasher that cause a sensitivity of convergence behavior to non-zero BICs.

Pan and Firoozabadi (2003) stated that root-finding of reduced flash equations is more efficient and robust than their minimization of the Gibbs free energy in reduced space. They reported difficulties of their minimization method that are caused by the non-symmetric matrix in the iteration equation as in Kaul and Thrasher (1996). Their difficulties arose because they were unable to calculate phase component mole fractions x_{ij} ($i = 1,\ldots,N_C$, $j = 1,\ldots,N_P$) directly from reduced parameters. However, phase component mole fractions can be easily calculated by performing one SS step for given reduced parameters as will be shown in sections 4.1.2 and 5.2.

Honami *et al.* (2000) presented reduced two-phase flash calculations capable of handling non-zero BICs. The number of their reduced parameters depends on the number of columns (or rows) including non-zero values. If a BIC matrix has m columns having non-zeros, the number of the reduced parameters is ($3 + 2m$). Unlike Hendriks and van Bergen (1992), their approach to non-zero BICs requires no pre-calculations because it allows for the original form of BICs. However, the number of the variables can be more than that of conventional flash depending on the number of columns having non-zeros in the BIC matrix. Their reduced flash algorithm was implemented in their compositional simulator to evaluate the efficiency of their reduced flash calculations. However, the simulation results using their reduced flash algorithm did not agree with those from a commercial simulator. Also, they did not use a reduced method for stability analysis in the simulations.

Li and Johns (2006) proposed a different approach to two-phase flash calculations with non-zero BICs. They introduced two sets of component-specific parameters to develop a BIC matrix. The number of independent variables in their flash calculations is three for zero-BICs, five for a BIC matrix with non-zero values only in one column, and six for the other cases. In this research, the reduced parameters of Li and Johns (2006) are used because of simplicity and flexibility.

The above studies on reduced methods assumed that only two hydrocarbon-phases exist. Nichita *et al.* (2006) extended a reduced method to more than two phases and reported calculation results and number of iterations in stand-alone calculations for three different fluids. They did not report the efficiency of their algorithm by comparing with other standard algorithms in terms of computational time.

Stability analysis using a reduced method was presented by Firoozabadi and Pan (2002). Their reduced parameters are based on Hendriks and van Bergen (1992). The stability analysis is formulated as minimization of the tangent place distance (TPD) function (Michelsen 1982a), where the algorithm is based on Kaul and Thrasher (1996). They observed that a surface of the TPD function is smoother in reduced space than in composition space. The smoothness of the TPD function in reduced space could eliminate unwanted local minima and improve the robustness of stability analysis. Nichita *et al.* (2002a) minimized the TPD function using a global minimization method attempting to find multiple minima. Hoteit and Firoozabadi (2006) used the stationary point method of Michelsen (1982a) using a reduced method.

Michelsen (1986) encountered poor convergence behavior in his reduced flash calculations, and he proposed a modified formulation to improve the problem. Pan and Firoozabadi (2003) reported convergence to a false solution using their reduced flash algorithm. As will be presented in Chapter 4, stability analysis using a standard reduced method can also exhibit poor convergence in a near-critical region. We improve this convergence problem in Chapters 4 and 5.

Prior to this research, no research reports the efficiency and robustness of reduced methods applied to both stability and flash calculations in compositional simulation. It is important to test algorithms in compositional simulation because requirements for robustness and efficiency are more severe in reservoir simulation than in stand-alone calculations. Phase equilibrium calculations in simulation of multicontact miscible gas flooding become difficult in critical regions, and small errors in phase equilibrium calculations can cause significant errors in phase property predictions. Simulation of low-temperature CO_2 flooding involving three hydrocarbon-phases is more difficult for phase equilibrium calculations because multiple critical points can be encountered during the displacement as will be presented in Chapter 6.

2.2.6 Low-Temperature Oil Displacement by CO_2

Mixtures of reservoir oil and solvent, such as CO_2 and rich gas, can exhibit complex phase behavior. A solvent-rich liquid phase can coexist with the oleic phase, or the oleic and gaseous phases at temperatures typically below 120ºF. The complex phase behavior results in displacements that behave differently from traditional gas flooding involving only vapor-liquid equilibrium. The complex phase behavior can also cause numerical issues in compositional simulation because three-phase equilibrium calculations are more complicated, difficult, and time-consuming than traditional two-phase equilibrium calculations. Several authors proposed two-phase equilibrium approximations that can be used to avoid three-phase equilibrium calculations in compositional reservoir simulation.

This section provides a review of studies on complex phase behavior of mixtures of oil and CO_2, and oil displacements by CO_2 involving such complex phase behavior. We also review two-phase equilibrium approximations for three-phase behavior proposed in the literature.

2.2.6.1 Multiphase Behavior of CO_2/Reservoir-Oil Mixtures

Phase behavior of mixtures of reservoir oil with CO_2 can significantly affect the oil recovery of CO_2 flooding. A key to successful gas flooding is an understanding of the phase behavior observed during the displacement. Because of the complexity, phase behavior of mixtures of reservoir oils with CO_2 has been studied in various ways, such as single- and multiple-contact measurements, slim-tube displacements, and numerical simulations using an EOS.

Multiple equilibrium-phases have been observed for mixtures of reservoir oils and CO_2 at temperatures typically below 120ºF (*e.g.*, Huang and Tracht 1974, Shelton and Yarborough 1977, Metcalfe and Yarborough 1979, Gardner *et al.* 1981, Henry and Metcalfe 1983, Orr and Jensen 1984, Turek *et al.* 1988, Khan *et al.* 1992, Creek and Sheffield 1993). Those phases include gaseous, oleic, CO_2-rich liquid, and asphaltenes. Asphaltene precipitation is important to consider if asphaltene precipitation and deposition significantly affect the oil recovery and if appearance of the solid phase increases flow resistivity of the permeable media (Hutchinson and Braun 1961). Creek and Sheffield (1993) observed that asphaltene precipitation little affected oil recoveries in their slim-tube displacements by CO_2 where the oils compared were significantly different in concentration of asphaltic components. We do not consider asphaltene precipitation in this research. We consider at most three hydrocarbon-phases; gaseous (V), oleic (L_1), and CO_2-rich liquid (L_2) phases.

Phase behavior of CO_2/reservoir-oil mixtures involving L_1-L_2-V equilibrium is conventionally presented on a *P*-*x* diagram. Figure 2.1 shows an example *P*-*x* diagram predicted using an EOS for the pseudo-binary system of a west Texas oil and CO_2 solvent. Three-phase equilibrium L_1-L_2-V typically occurs within a small pressure range at high CO_2 mole fractions on a *P*-*x* diagram at reservoir temperatures below 120ºF. Two liquid-phases can coexist at equilibrium at higher pressures above the three-phase region. The L_1-L_2 envelope tends to persist to higher pressures for heavier oils (Turek *et al.* 1988, Orr and Jensen 2007). Creek and Sheffield (1993) found no upper boundary of the L_1-L_2 envelope up to 18000 psia for the CO_2/reservoir-oil mixtures studied. Turek *et al.* (1988) observed no critical point for L_1-L_2 for the CO_2/west-Texas-oil systems studied in their paper. A L_2-V region, which cannot be seen in Figure 2.1, exists at pressures above the three-phase region at very high CO_2 mole fractions; *e.g.*, more than 99.0% in Turek *et al.* (1988). Creek and Sheffield (1993) reported that the L_2 phase became denser than the L_1 phase at pressures higher than 16500 psia in the L_1-L_2 region.

Effects of oil properties on the three-phase equilibrium were presented by several authors. Henry and Metcalfe (1983) reported that fractions of paraffinic, naphthenic, and aromatic components in a reservoir oil (PNA distribution) can significantly affect the occurrence of the three-phase region during the displacements. PNA distribution in oil can also affect efficiency of oil displacements by CO_2 (Holm and Josendal 1982). Turek *et al.* (1988) observed in their experiments that the pressure range of a three-phase region on a *P*-*x* diagram significantly varied with oil composition. Their experiments also indicate that the L_1-L_2 and L_1-L_2-V behavior on a *P*-*x* diagram depends on temperature and, to a lesser extent, oil composition.

A *P*-*x* diagram for solvent/reservoir-oil mixtures represents phase behavior only along the mixing line between the solvent and oil compositions at a fixed temperature. That is, a *P*-*x* diagram shows only a tiny portion of phase behavior that actually spans *P*-*T*-*x* space of (N_C + 1) dimension. Turek *et al.* (1988) observed in their single-contact measurements for CO_2 and west Texas oils that the L_2 phase has a similar composition to the V phase in the three-phase region. Based on this observation, they stated that the three-phase region exists within the narrow pressure range where the L_2 phase vaporizes with decreasing pressure. In *P*-*T*-*x* space, however, their observation only indicates that the mixing ratio of the oil and CO_2 happened to result in a composition that is close to a critical endpoint (CEP) for that system.

A CEP is where two of the three phases merge in the presence of the other phase (Uzunov 1993). There are two types of CEPs for mixtures of CO_2 and hydrocarbons. The first type of CEPs is where the two liquid phases L_1 and L_2 merge in the presence of the V phase (L_1=L_2-V). The second type of CEP is where the L_2 and V phases merge in the presence of the L_1 phase (L_1-L_2=V). That is, Turek *et al.* (1988) observed an overall composition near a CEP of type L_1-L_2=V. However, a composition within the three-phase region also can be near the other type of CEP or far from both CEPs. Three-phase behavior associated with CEPs is visually presented for CO_2/reservoir-oil mixtures in Chapter 6.

An issue in considering phase behavior on a *P*-*x* diagram is that the composition path actually observed during an oil displacement is not the mixing line between the oil and gas. Phase behavior along the composition path is more important to understand than that along the mixing line as explained in Chapters 5 and 6.

Orr and Jensen (1984) noticed that L_1-L_2 and L_1-L_2-V regions on *P*-*x* diagrams reported in the literature have marked differences in the shape and location. They explained the differences by using two ternary systems; $CO_2/C_3/C_{16}$ and $CO_2/C_1/C_{16}$. They concluded that *P*-*x* diagrams for CO_2/reservoir-oil systems can be qualitatively reproduced by the ternary systems. Larson *et al.* (1989) confirmed this conclusion in their paper. However, agreement on a *P*-*x* diagram does not necessarily mean agreement on phase behavior along the composition path encountered during an oil displacement. A serious problem associated with ternary representation is presented in Chapter 6. That is, three components do not have sufficient degrees of freedom to model critical points for more than two phases. For example, CEPs have only one degree of freedom in *P*-*T*-*x* space for three components. The tricritical point has no degree of freedom in *P*-*T*-*x* space for three components. Those critical points might be important for miscibility development, although miscibility development has not yet been found for a composition path that goes through a three-phase region (LaForce 2005).

An important, fundamental question on modeling the complex three-phase behavior for reservoir simulation is whether or not a cubic EOS can predict three-phase behavior for CO_2/reservoir-oil systems. van Konynenburg and Scott (1968, 1970, 1980) showed that most types of fluid phase behavior observed for binary mixtures can be qualitatively predicted by the van der Waals EOS using van der Waals mixing rules. The predictions include three-phase curves and critical curves. They proposed a classification of binary phase diagrams (*i.e.*, projections onto *P*-*T* diagrams), which is based on existence or non-existence of three-phase curves and how the three-phase curves are connected to critical curves. Similar investigations on the global phase diagrams, which show all possible fluid phase equilibria, were later performed for binary mixtures using the Redlich-Kwong EOS (Deiters and Schneider 1976, Deiters and Pegg

1989) and the Peng-Robinson EOS (Mushrif 2004, Yang 2006, Mushrif and Phoenix 2008). Phase behavior of ternary mixtures was predicted using the van der Waals EOS (Bluma and Deiters 1999), the Peng-Robinson EOS (Gauter 1999, Gauter *et al.* 1999), and the Soave-Redlich-Kwong EOS (Gregorowicz and de Loos 1996). Their results indicate that a cubic EOS is capable to predict three-phase behavior at least qualitatively. Even one of the simplest cubic equations of state, van der Waals EOS, never yields physically absurd predictions (van Konynenburg 1968).

Quantitatively accurate predictions of three-phase behavior using a cubic EOS require careful adjustments of parameters such as T_C, P_C, and acentric factors for heavy fractions. Those parameters have a significant influence on three-phase behavior predictions (Gregorowicz and de Loos 2001). BICs for CO_2 also significantly affect the phase behavior predictions because three-phase behavior typically occurs at high CO_2 mole fractions at reservoir pressures and temperatures. Larson *et al.* (1989), Khan *et al.* (1992), and Creek and Sheffield (1993) used the Peng-Robinson EOS to model three-phase equilibrium for mixtures of reservoir oil and CO_2. Chaback and Turek (1986) used a modified version of the Redlich-Kwong EOS, and Coutinho *et al.* (1995) used the Soave-Redlich-Kwong EOS. Khan *et al.* (1992) used the Peng-Robinson EOS fluid models for west Texas oils in their multiphase compositional simulations using UTCOMP (Chang *et al.* 1990). They successfully matched the slim-tube experimental data with the simulation results.

2.2.6.2 Displacement Characteristics

Three phase equilibrium L_1-L_2-V is observed at a wider pressure range during displacements than in single contact measurements (Henry and Metcalfe 1983, Creek and Sheffield 1993). This is because a mixing line between oil and gas, in general, is not the same as the actual composition path observed during a displacement. Single contact measurements provide phase behavior data only along a mixing line between oil and gas in composition space, which are used to construct a *P*-*x* diagram. Three-phase equilibrium L_1-L_2-V is observed during a displacement when the composition path goes through the three-phase region.

There are several characteristics of low-temperature oil displacements by CO_2 that are not observed in a typical oil displacement involving only L-V equilibrium. First, CO_2 breakthrough in those displacements can occur at more than 1.0 pore-volume injected (PVI) and in many cases well after 1.2 PVI (Orr *et al.* 1983, Khan 1992, Grigg and Siagian 1998, Creek and Sheffield 1993). Orr *et al.* (1983) stated that this late breakthrough is because CO_2 significantly increases its density on dissolution in the L_1 phase. Creek and Sheffield (1993) stated that this late breakthrough is a result of the large molar volume difference between the V and L_2 phases, and they called it the volume charging effect.

Second, reduced injectivity has been reported for low-temperature oil displacements by CO_2. Pontious and Tham (1978) reported reduced injectivity in continuous CO_2 flooding, which was attributed to formation of three phases within the transition zone. Henry and Metcalfe (1983) observed increased pressure drops across the cores in their displacement experiments involving three-hydrocarbon-phase flow. Based on those observations, several authors considered that the existence of three phases might improve sweep efficiency in CO_2 flooding because of a decreased mobility ratio at the displacement front (Henry and Metcalfe 1983, Mohanty *et al.* 1995). Orr *et al.* (1983) stated that it might be difficult to control reservoir pressure to stay within a range where three hydrocarbon-phases can coexist.

Third, slim-tube measurements reported in the literature show that low-temperature oil displacements by CO_2 involving three hydrocarbon-phases can result in high displacement efficiency of more than 90% (*e.g.*, Yellig and Metcalfe 1980, Gardner *et al.* 1981, Orr *et al.* 1981, Orr *et al.* 1983, Henry and Metcalfe 1983, Khan 1992, Creek and Sheffield 1993). High displacement efficiency of more than 90% can also result for oil displacements by rich gas exhibiting three hydrocarbon-phases (Shelton and Yarborough 1977, DeRuiter *et al.* 1994, Mohanty *et al.* 1995). Khan *et al.* (1992) simulated west Texas oil displacements by CO_2 using UTCOMP (Chang *et al.* 1990), an EOS compositional reservoir simulator capable of handling three hydrocarbon-phases. Their simulation results showed that those displacements can result in high displacement efficiency of more than 90% in spite of the immiscible three-hydrocarbon-phase flow. Nghiem and Li (1986) also observed high oil recovery with no miscible bank in their one-dimensional displacement simulations involving three hydrocarbon-phases.

2.2.6.3 Displacement Efficiency

A key parameter for designing gas flooding is the minimum miscibility pressure (MMP). In this dissertation, the thermodynamic MMP is defined as the minimum displacement pressure at which complete miscibility is developed along the composition path from injection gas through reservoir oil for one-dimensional flow in the absence of dispersion. The measured MMP is reported based on a series of slim-tube displacement measurements. The thermodynamic MMP is uniquely determined, but the measured MMP is not unique because there are multiple criteria for determining the MMP as mentioned below. These different kinds of MMPs in general do not have the same value.

A conventional way to determine the measured MMP is to find the lowest displacement pressure at which a recovery at 1.2 PVI is equal to or very near the maximum recovery at 1.2 PVI obtained in a series of displacements (Yellig and Metcalfe 1980). Several authors used different criteria for low-temperature oil displacements by

CO_2. Holm and Josendal (1974) used a criterion that the recovery factor is more than 80% at CO_2 breakthrough and more than 94% ultimately. Yellig and Metcalfe (1980) used another criterion that ultimate recovery is near the maximum recovery in a series of displacement measurements and sight-glass observations confirm the existence of transition zones from oil to CO_2. Creek and Sheffield (1993) recommended the criterion of Yellig and Metcalfe (1980) to allow for the volume charging effect mentioned in section 2.2.6.2. Negahban and Kremesec (1992) also used a criterion related to ultimate oil recovery. Orr *et al.* (1981) correctly pointed out that the measured MMP of Yellig and Metcalfe (1980) does not necessarily mean the thermodynamic MMP although it is likely sufficient to ensure an efficient displacement.

Several different correlations were proposed for experimentally measured MMPs for CO_2 flooding (CO_2-MMP). In the correlation of Holm and Josendal (1974), reservoir temperature and molecular weight for C_{5+} in the oil are the correlation parameters. Yellig and Metcalfe (1980) proposed another correlation, which used reservoir temperature as the correlation parameter and was independent of oil composition. Both correlations can be appreciably in error (Stalkup 1978, Holm and Josendal 1980). Orr and Jensen (1984) proposed to use vapor pressure of CO_2 (extrapolated if necessary) as a rough estimate of the CO_2-MMP for low-temperature oil reservoir. Their correlation is based on experimental results indicating that a L_2 phase extracts hydrocarbons efficiently and it appears as a L_1-L_2-V region on a P-x diagram at pressures near the extrapolated vapor pressure of CO_2. Creek and Sheffield (1993) observed in their displacement measurements that the measured CO_2-MMPs for Permian Basin oils always coincide with the lower boundary of the L_1-L_2-V regions on the P-x diagrams.

The correlation of Orr and Jensen (1984) and the observations of Creek and Sheffield (1993) indicate that existence of a three-phase region plays an important role for high efficiency of low-temperature oil displacements by CO_2. However, the thermodynamic MMP is not directly related to phase behavior on a *P-x* diagram because the thermodynamic MMP is determined by the interaction of flow with phase behavior.

Although measured CO_2-MMPs reported in the literature typically fall in a pressure range where three hydrocarbon-phases coexist during a displacement, it is little known whether or not the thermodynamic MMP is achieved within such a pressure range. The gas injection theory for oil displacements involving only L-V equilibrium shows that miscibility is developed at a two-phase critical point even when a composition path goes through a two-phase region (Johns 1992, Orr 2007). That is, existence of two-phase immiscible flow does not necessarily mean a partially miscible (or immiscible) displacement. LaForce (2005) studied analytical composition paths for displacements exhibiting three-phase immiscibility using ternary mixtures. She concluded that a composition path that goes through a three-phase region cannot develop multicontact miscibility. Thus, miscibility development has not been proven for displacements exhibiting three-phase flow.

A question then arises why low-temperature oil displacements by CO_2 can achieve high displacement efficiency in spite of three-phase immiscibility. Several authors attempted to explain mechanisms for the high displacement efficiency.

The most common explanation is that a L_2 phase can efficiently extract a certain range of hydrocarbons in the reservoir oil, *i.e.*, selectivity of a liquid CO_2 phase (Huie 1972). Creek and Sheffield (1993) stated that Permian Basin oil displacements by CO_2 result in high displacement efficiencies because of efficient extraction of midrange hydrocarbons into a L_2 phase. Holm and Josendal (1974, 1982) reported that a CO_2-rich vapor phase extracts C_6 and lighter and a L_2 phase can extract as heavy as C_{30}. They concluded that a CO_2-MMP is related inversely to the amount of extractable hydrocarbons (*i.e.*, C_5-C_{30} in their papers) present in the reservoir oil. Stewart and Nielsen (1953) reported that light components are extracted into a L_2 phase more than heavy components. Turek *et al.* (1988) reported that a L_2 phase can extract a significant portion of all but the heaviest hydrocarbon components in the reservoir oil. Orr *et al.* (1981) stated that a L_2 phase can extract as heavy as C_{24}, while Gardner *et al.* (1981) stated that it can extract hydrocarbons heavier than C_{35}. Orr *et al.* (1983) reported that a L_2 phase can contain 30wt% hydrocarbons and a CO_2-rich vapor phase at the same conditions extracts hydrocarbons less efficiently. Because of this selectivity of the L_2 phase, efficiency of low-temperature oil displacements by CO_2 can be rather high even for a L_1-L_2 partially miscible (or immiscible) displacement (Orr *et al.* 1981, Turek *et al.* 1988), depending on the oil properties.

In composition space, selectivity can be represented by the angularity of the tie-line (or a side of the tie-triangle) with respect to the coordinate of the component that is to be extracted selectively. That is, selective extraction depends on thermodynamic conditions such as temperature, pressure, and fluid properties. Extraction of hydrocarbons into the L_2 phase does not completely explain the mechanism of the high displacement efficiency. For example, heavy hydrocarbons cannot be extracted efficiently by the L_2 phase (Orr *et al.* 1981, DeRuiter *et al.* 1994).

The selective extraction is significant in a highly immiscible region (Spee and Schneider 1991, Joshi and Prausnitz 1984). As miscibility is approached, the selectivity becomes poor. As the tie-line (or a side of the tie-triangle) shrinks with increasing miscibility, the angularity of the tie-line (or a side of the tie-triangle) gradually looses its significance because the two phase-compositions become closer to each other.

Orr *et al.* (1981, 1983) and Gardner *et al.* (1981) simulated their slim-tube experiments for CO_2/low-temperature-oil systems using a simplified simulator. In their simulations, phase behavior predictions were based on simple polynomial representations for the pseudo-ternary diagrams (*e.g.*, CO_2, $C_{1\text{-}6}$, and C_{7+} in Gardner *et al.*, 1981) obtained from their single- and multi-contact measurements. A three-phase tie-triangle was invariant in their phase behavior predictions because it has zero degrees of freedom in a ternary diagram at a fixed temperature and pressure. Also, their tie-triangles were not directly measured, but they were assumed based on the measurements in two-phase regions. Based on the simplified simulations, Orr *et al.* (1981, 1983) and Gardner *et al.* (1981) concluded that significant extraction of hydrocarbons by the L_2 phase accounts for high displacement efficiency for CO_2/low-temperature-oil systems. However, their simulations did not fully describe three-phase behavior because of the ternary representation. This might be a reason for the deviations of oil recovery predictions from experimental results for three-hydrocarbon-phase displacements in Orr *et al.* (1983).

The common explanation based on the extraction of oil components by a L_2 phase cannot tell under what conditions the extraction becomes efficient. Extraction of oil components by a L_2 phase depends on thermodynamic conditions such as temperature, pressure, and composition. Also, the extraction of oil components by a L_2 phase is only a part of mass transfer among the three phases, L_1, L_2, and V. Complex three-phase behavior encountered during low-temperature oil displacements by CO_2 is little known.

Gardner *et al.* (1981) concluded that their low-temperature oil displacement by CO_2 is a vaporizing gas drive type, in which oil components are extracted (or "vaporized") into the L_2 phase. This is in contrast to Metcalfe and Yarborough (1979), who stated that low-temperature oil displacement by CO_2 is a condensing gas drive, where CO_2 is condensed into the L_1 phase. None of the authors fully describe complex mass transfer among the three phases. In Chapter 6, we show that CO_2 is simultaneously extracted from the V and L_1 phases into the L_2 phase within a three-phase region during low-temperature oil displacement by CO_2.

Other authors attributed the high efficiency of low-temperature oil displacements by CO_2 to near-miscibility between the L_1 and L_2 phases. Nghiem and Li (1986) performed one-dimensional simulations for low-temperature oil displacements by CO_2 using a 15-component EOS fluid model. A recovery factor of 87% was achieved at 1.2 PVI in their simulation involving three-hydrocarbon-phase flow. The L_1-L_2-V region exists in only one of the 40 grid cells used and flows behind the L_1-V region. The L_1-L_2 region follows the L_1-L_2-V region. They observed low interfacial tension between the L_1 and L_2 phases in the L_1-L_2 region and concluded that the high displacement efficiency is caused by near-miscibility between the two phases, L_1 and L_2, in the two-liquid-phase region, not in the three-phase region. The effect of the three-phase region would be marginal in their simulations because only one of 40 grid cells contains three hydrocarbon-phases.

Mohanty *et al.* (1995) studied the role of three-hydrocarbon-phase flow in low-temperature oil displacements by rich gas, where displacement efficiency of more than 90% was achieved for the cases of three-hydrocarbon-phase flow. They concluded that the efficient oil recoveries were caused by near-miscibility of two phases, the solvent-rich liquid and oleic phases, flowing ahead of the three-phase region at the displacement front.

In the displacements of Nghiem and Li (1986) and Mohanty *et al.* (1995), displacement efficiency is controlled by the miscibility in the L_1-L_2 two-phase region. That is, the high displacement efficiency observed by those authors is not unexpected considering the existing gas injection theory in which miscibility is developed at the critical point of two phases (Johns 1992, Dindoruk 1992, LaForce 2005, Orr 2007).

As will be presented in Chapter 6, high efficiency of displacements with three-hydrocarbon-phase flow can occur even when the two-phase regions are immiscible. We show that low-temperature oil displacements by CO_2 can achieve high displacement efficiency when the composition path goes near two CEPs.

2.2.6.4 Two-Phase Equilibrium Approximations

Reliable numerical simulation of rich gas or CO_2 floods in low-temperature oil reservoirs requires robust phase equilibrium algorithms capable of handling at least three hydrocarbon-phases. However, most compositional simulators do not attempt to solve for three hydrocarbon-phases because three-phase equilibrium calculations are more complicated, difficult, and time-consuming than traditional two-phase equilibrium calculations.

Nghiem and Li (1986) studied the importance of a third hydrocarbon-phase in multiphase compositional simulation by comparing simulation results with two-phase equilibrium calculations to those with three-phase equilibrium calculations. In their simulations with only two-phase equilibrium calculations, two-phase calculations are performed even in the three-phase region. They concluded that the two-phase equilibrium approximation can be used with little loss of accuracy because the three-phase region exists only over a small part of the reservoir. However, their conclusion was based on one-dimensional slim-tube simulations using only two recombined oils from the same field.

Several authors later demonstrated that the proper use of three-phase equilibrium calculations results in simulation results that are significantly different from those with two-phase equilibrium calculations (Khan *et al.* 1992, Wang and Strycker 2000, Guler *et al.* 2001). Also, as reported by Khan (1992) and Wang and Strycker (2000), convergence problems can occur when attempting to approximate such low-temperature gas floods using only two-phase equilibrium calculations, and in some cases the simulations cannot be completed. In Chapter 5, we explain one reason for convergence problems associated with the two-phase equilibrium approximation.

To overcome the drawbacks of simulation involving three hydrocarbon-phases, Fong *et al.* (1992) proposed another way to approximate three-hydrocarbon-phase simulations. They characterized fluids that exhibit three-phase equilibrium in such a way that the resulting EOS model predicts no three-phase region. They reported that simulation results with the two-phase equilibrium approximation agree well with the field data when the MMP simulated with the two-phase representation matches the experimentally determined MMP. However, as will be discussed in Chapter 5, the approximation procedure requires significant tuning of EOS parameters. Because their approximation procedure has no theoretical basis, there is no reason to expect accurate predictions of sweep efficiency, fluid injectivity, and phase properties, for example. If sweep and displacement efficiencies are not matched well using a two-phase equilibrium approximation, the simulated distribution of remaining oil after gas flooding will not be correct.

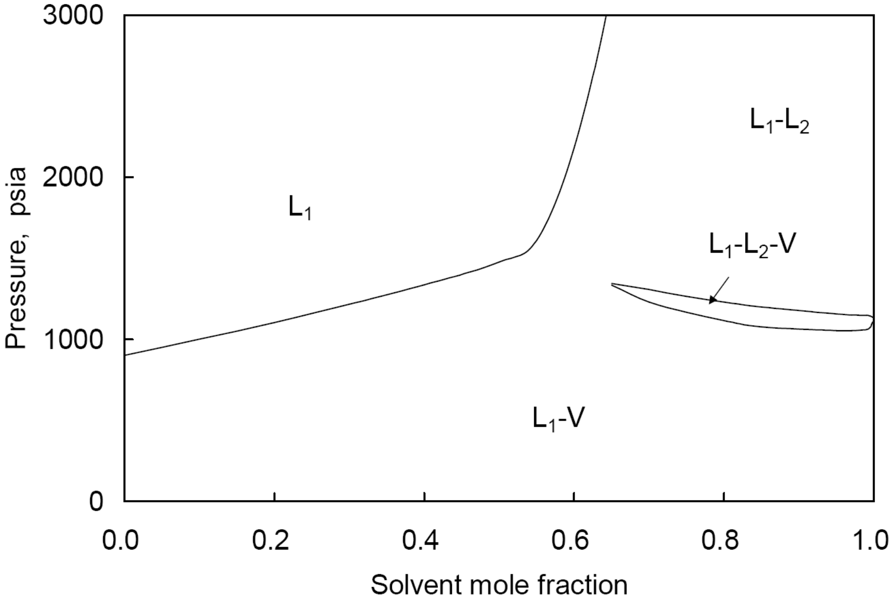

Figure 2.1 *P*-*x* diagram for the pseudo-binary mixture of a west Texas oil and CO_2 solvent.

3. Constant-*K* Flash Calculations

Multiphase flash algorithms typically use successive substitution (SS) followed by Newton's method. For N_P-phase flash calculations, ($N_P - 1$) Rachford-Rice (RR) equations are solved in every iteration step in SS, and depending on the choice of independent variables, in Newton's method. Solution of RR equations determines both compositions and amounts of phases for a fixed overall composition and set of *K*-values. A robust algorithm for RR is critical to obtain convergence in multiphase compositional simulation, and has not been satisfactorily developed unlike the traditional two-phase flash. In this chapter, we develop a robust and efficient algorithm for RR equations for multiphase compositional simulation that is guaranteed to converge to the correct solution independent of the number of phases for both positive and negative flash calculations.

First, we derive the convex function that we minimize to solve for the equilibrium phase mole fractions. This function is practically the same as Michelsen (1994), but we explicitly derive the function so that our algorithm can be clearly understood. The function is then analyzed in detail to develop a robust and efficient algorithm using Newton's method with a line search technique. After that, we present example stand-alone calculations for three and five phases. Last, our algorithm is implemented in a multiphase compositional simulator and used in an example simulation of a low-temperature oil displacement by CO_2 involving three-hydrocarbon-phase flow.

3.1 CONSTANT-*K* FLASH FORMULATION AND ALGORITHM

In this section, we derive a new algorithm for a N_P-phase constant-*K* flash calculation that is based on minimization of a convex function with N_C linear constraints. The convex function is similar to the one presented by Michelsen (1994). Unlike previous research, however, we derive and analyze the behavior of the function to develop a practical and robust algorithm for compositional simulation. We also provide a very small region in which the solution to the RR equations must exist.

3.1.1 Convex Function

The convex function is derived by exploiting a special structure of the RR equations. We begin by examining the common root-finding technique to solve equations (2.48) by constructing the Jacobian matrix, where the elements are given by

$$J_{jk} = \sum_{i=1}^{N_C} \left[\left(1-K_{ij}\right)\left(1-K_{ik}\right) z_i \right] \Big/ t_i^2 ,$$

where $t_i = 1 - \left[\sum_{j=1}^{N_P-1} \left(1-K_{ij}\right) \beta_j \right]$ for $i = 1,\ldots,N_C$ and $j,k = 1,\ldots,N_P-1$.

The Jacobian matrix is symmetric, indicating that there is a scalar function $F(\beta)$ for which the gradient vector consists of the RR equations. This is best explained by examining the relation between Newton's method for root-finding and that for minimization. That is, the iteration schemes for Newton's method are

$$\beta^{n+1} = \beta^n - \left[\nabla f\left(\beta^n\right)^T \right]^{-1} f\left(\beta^n\right) \text{ for root-finding,}$$

and

$$\beta^{n+1} = \beta^n - \left[\nabla^2 F\left(\beta^n\right) \right]^{-1} \nabla F\left(\beta^n\right) \text{ for minimization.}$$

Although the derivations of these schemes are different from each other, the latter can be viewed as a special case of the former. That is, f corresponds to the gradient of F if and only if the Jacobian matrix of f is symmetric (Bertsekas 1999). The function F to be minimized is then easily found by performing an indefinite integral of f_j with respect to β_j to obtain

$$F\left(\beta\right) = \sum_{i=1}^{N_C} \left[-z_i \ln\left|t_i\right| \right]. \tag{3.1}$$

In the above function, the constant of integration is set to zero without loss of generality. Equation (3.1) is identical to the one presented by Michelsen (1994), except that he retained the integration constant. The minimization function F defined by equation (3.1) is easily proven to be convex because its Hessian matrix is positive semidefinite as shown in the next section.

3.1.2 Convexity and Function Behavior

A gradient vector of the function F consists of the RR equations, while the Hessian matrix consists of the derivatives of the RR equations with respect to the independent variables. That is,

$$\nabla F = f = \left\{ f_j \right\} \in \mathrm{R}^{(N_P - 1)} \text{ and } \nabla^2 F = \left\{ H_{kj} \right\} = \left\{ \partial f_j / \partial \beta_k \right\} \in \mathrm{R}^{(N_P-1)\times(N_P-1)},$$

where

$$\partial f_j / \partial \beta_k = \sum_{i=1}^{N_C} \left[\left(1 - K_{ij}\right)\left(1 - K_{ik}\right) z_i \right] \Big/ t_i^2 = Y^T D Y$$

and,

$$D = diag\left(z_1, ..., z_{N_C}\right) \in \mathrm{R}^{N_C \times N_C}$$

$$Y = \left\{ Y_{ij} \right\} = \left\{ \left(1 - K_{ij}\right) \Big/ t_i \right\} \in \mathrm{R}^{N_C \times (N_P - 1)}.$$

The matrix D is positive definite because z_i ($i = 1,\ldots,N_C$) are all positive.

A constant K-flash problem requires that the number of components (N_C) is equal to or greater than the number of phases (N_P). The degree of freedom for a flash calculation at a given temperature and pressure must be at least two. That is, $F = N_C - N_P + 2 \geq 2$ to obtain $N_C \geq N_P$, according to the Gibbs phase rule. In addition, if the $N_C \times (N_P - 1)$ matrix Y is of full rank, we have $Yy \neq 0$ for any vector $y \neq 0$.

Considering the positive definiteness of D, we can prove the positive definiteness of the Hessian matrix Y^TDY as follows:

$$y^T \left(Y^T D Y \right) y = \left(Yy \right)^T D(Yy) > 0 \text{ for all vector } y.$$

The above proof holds for both positive flash and negative flash where one or more phase mole fractions are negative, but the phase compositions are positive. However, it does not hold for another kind of negative flash where an overall composition lies in negative composition space (*i.e.*, D is not positive definite). We do not consider this type of negative flash in this dissertation.

If Y is not of full rank, the Hessian matrix is only positive semidefinite, and there exists a vector along which the function value does not change. To see this, suppose that the p^{th} and q^{th} columns of the matrix Y or a $N_C \times (N_P - 1)$ matrix $\{1 - K_{ij}\}$ are linearly dependent. Then, there exists a constant α such that

$$\left(1-K_{ip}\right)=\alpha\left(1-K_{iq}\right) \text{ for all } i\,.$$

Then, the p^{th} and q^{th} columns of the Hessian matrix become linearly dependent as shown below.

$$\begin{aligned} H_{kp} &= \partial f_p \big/ \partial \beta_k = \sum\nolimits_{i=1}^{N_C}\left[\left(1-K_{ip}\right)\left(1-K_{ik}\right)z_i\right]\Big/t_i^2 \\ &= \sum\nolimits_{i=1}^{N_C}\left[\alpha\left(1-K_{iq}\right)\left(1-K_{ik}\right)z_i\right]\Big/t_i^2 = \alpha H_{kq}\,. \end{aligned}$$

The Hessian matrix, therefore, is only positive semidefinite for this case. This is also confirmed by the function values which are constant along a vector d with $(1 - K_{1q})$ for p^{th}, $-(1 - K_{1p})$ for q^{th}, and zeros for the other elements. That is,

$$\begin{aligned} d^T\nabla F &= \left(1-K_{1q}\right)\left[\sum\nolimits_{i=1}^{N_C}\left(1-K_{ip}\right)z_i\big/t_i\right]-\left(1-K_{1p}\right)\left[\sum\nolimits_{i=1}^{N_C}\left(1-K_{iq}\right)z_i\big/t_i\right] \\ &= \sum\nolimits_{i=1}^{N_C}\left(z_i/t_i\right)\left[\alpha\left(1-K_{1q}\right)\left(1-K_{iq}\right)-\alpha\left(1-K_{1q}\right)\left(1-K_{iq}\right)\right]=0\,. \end{aligned}$$

Therefore, for a $N_C \times (N_P - 1)$ matrix $\{1 - K_{ij}\}$ of full rank, the Hessian matrix of F is positive definite and the function is strictly convex. Otherwise, the Hessian matrix is only positive semidefinite. A semidefinite Hessian occurs for example at critical points, including critical endpoints (called bicritical points in Haugen *et al.*, 2007) where two of three phases are critical and at equilibrium with the other non-critical phase (see section 2.2.6.1).

Another important behavior of the function is that if the region $t_i > 0$ ($i = 1,\ldots,N_C$) is unbounded, then the function becomes monotonic. That is, the function does not have a minimum, and there is no solution to the constant-*K* flash with N_P phases. The proof of this statement is straightforward. If the region is unbounded, there exists a vector *d* such that

$$\sum_{j=1}^{N_P-1}\left(K_{ij}-1\right)d_j \geq 0 \text{ for all } i\,.$$

Thus, the function is always non-increasing along the vector *d* when

$$d^T\nabla F = \sum_{j=1}^{N_P-1}\sum_{i=1}^{N_C} -z_i\left(K_{ij}-1\right)d_j \big/ t_i \leq 0\,.$$

This result is in contrast to Leibovici and Nichita (2008) who incorrectly showed a case where the region is unbounded, but the function has a minimum (Figure 4 with their explanation in section 4.2 “Reservoir oil/CO_2 mixture”).

3.1.3 Constraints

The function has N_C poles defined when $t_i = 0$ ($i = 1,\ldots,N_C$) as for the traditional two-phase constant-*K* flash. Positive values of t_i ($i = 1,\ldots,N_C$) define the most simplistic feasible region for the solution of a multiphase constant-*K* flash calculation. This is the same type of the feasible region used in the root-finding technique of Leibovici and Neoschil (1995) and the minimization approach of Leibovici and Nichita (2008). To formulate a minimization of *F*, Leibovici and Nichita (2008) used the constraint set *L’* = $\{\beta \mid t_i > 0,\ i = 1,\ldots,N_C\}$. Care must be taken in handling this open set *L’*. When one simplifies the open set to be a closed set $L = \{\beta \mid t_i \geq 0,\ i = 1,\ldots,N_C\}$, iterations can lie on a pole ($t_i = 0$), where the function cannot be defined and the calculations will then cease. When an iteration point is near the pole, Newton’s iteration makes little improvement in minimizing the objective function, if any, because of the non-quadratic behavior along the poles. The convergence problem is significant because it can stop the simulation from proceeding.

To increase the robustness of the iterations, we develop a new feasible region of smaller size that also contains no poles. Our feasible region is derived based on non-negativity of phase component mole fractions, $0 \le x_{ij} \le 1$ ($i = 1,\ldots,N_C$ and $j = 1,\ldots,N_P$). To allow for a negative flash, we consider that phase mole fractions can be negative. This is important because as iterations proceed in EOS flash calculations, a few iterations may be outside of the multiphase region of interest, but with more iterations (if allowed) can move back into the multiphase region. Using equations (2.44) and (2.46), the non-negativity of phase component mole fractions requires the following inequalities:

$$0 \le z_i \le t_i = 1 - \left[\sum_{j=1}^{N_P-1} \left(1 - K_{ij}\right) \beta_j \right]$$

$$0 \le K_{ij} z_i \le t_i = 1 - \left[\sum_{j=1}^{N_P-1} \left(1 - K_{ij}\right) \beta_j \right].$$

The final form of constraints is easily derived as

$$a_i^T \beta \le b_i , \tag{3.2}$$

where $a_i = \{1 - K_{ij}\}$, $\beta = \{\beta_j\}$, $b_i = \min\{1 - z_i, \min_j\{1 - K_{ij} z_i\}\}$ for $i = 1,\ldots,N_C$, $j = 1,\ldots,(N_P - 1)$. The constraint set $S = \{\beta \mid a_i^T \beta \le b_i,\ i = 1,\ldots,N_C\}$ leads to a smaller feasible region than that based on the set $L = \{\beta \mid t_i \ge 0,\ i = 1,\ldots,N_C\}$. The new set S does not contain the region near the poles, where the minimization function exhibits poor convergence. The feasible region developed in this section is the primary, but important difference between our algorithm and Michelsen (1994) because this feasible region leads to robustness for both positive and negative flash calculations.

3.1.4 Algorithm

In this section we present a detailed algorithm that can be used to solve robustly the multiphase constant-*K* flash calculations. Our formulation for multiphase constant-*K* flash developed in the previous section is as follows:

$$\text{Minimize } F(\beta) = \sum_{i=1}^{N_C}\left[-z_i \ln|t_i|\right] \text{ subject to } a_i^T\beta \le b_i.$$

We only consider cases where the minimization has a unique solution. That is, the minimization function is convex and non-monotonic over the constraint set $S = \{\beta \mid a_i^T\beta \le b_i,\ i = 1,\ldots,N_C\}$. This is the case in compositional simulation because N_P-phase flash calculations are performed only when existence of a N_P-phase solution is ensured by stability tests. Stability analysis can fail, but when it does so it fails to predict the existence of an additional phase, not the other way around. The minimization of the convex function is safely solved using search directions and step sizes based on Newton's method coupled with a line search along that direction.

In multiphase compositional simulation, such as with UTCOMP (Chang *et al.* 1990), a good initial estimate may be available from the previous time step or from the previous iteration step in the flash calculation. Otherwise, we need to make an initial estimate of the β to start the iterations. Haugen *et al.* (2007) proposed two-dimensional bisection to initiate Newton's iterations for three-phase constant-*K* flash calculations. However, analysis of our minimization function explicitly generates good initial estimates for β with no iteration by considering N_P constraints for phase mole fractions, $\beta_j \ge 0$ ($j = 1,\ldots,N_P$), in addition to equations (3.2). A feasible initial estimate is then determined by an equally weighted mean of the vertices of the intersection of the sets S and $P = \{\beta \mid \beta_j \ge 0, j = 1,\ldots,N_P\}$.

An algorithm to solve the minimization is as follows:

1. Generate an initial estimate for the independent variables β_j ($j = 1,\ldots,N_P - 1$) based on the previous time step, the previous iteration step, or an equally weighted mean of the vertices of the S and P intersection.
2. Calculate the gradient of the convex function F and set an iteration index n to one.
3. Calculate the Hessian matrix and solve the system of equations to obtain the Newton's direction. That is, calculate

   $$d^n = -\left(\nabla^2 F^n\right)^{-1} \nabla F^n .$$

4. Calculate the maximum feasible step size λ_{max} along the Newton's direction d^n as shown below. If $\lambda_{max} \geq 1$, then set λ_{max} to 1.0 resulting in a unit Newton's step.

   $$\lambda_{max} = \min_i \left\{ \frac{b_i - a_i^T \beta^n}{a_i^T d^n} : a_i^T d^n > 0 \right\}$$

5. Determine a step size λ^n using a line search technique (given later in this section) applied over the range of $0 \leq \lambda^n \leq \lambda_{max}$.
6. Update the independent variables, $\beta_j^{n+1} = \beta_j^n + \lambda^n d^n$.
7. If the max norm of the gradient is less than a specified tolerance (*e.g.*, 10^{-8}), stop. Otherwise, continue to step 8.
8. Increase the iteration index ($n = n + 1$) and go back to step 3.

The Newton's direction is guaranteed to be a descent direction because the Hessian matrix is positive definite. In step 3, the Hessian matrix can be inverted inexpensively for three-phase cases. Step 4 calculates the maximum feasible step size λ_{max} along the Newton's direction. The value of λ_{max} less than one indicates that the full Newton's step would go out of the feasible region, so it is not allowed. The above procedure ensures that the Newton's iterations do not go out of the feasible region and the optimal step size is taken.

The line search used is based on the univariate Newton's method with a relatively large tolerance (*e.g.*, 10^{-3}) for the max norm of the gradient. The line search minimizes the following function over the region of $0 \le s \le 1$:

$$g(s) = F(\beta + s\lambda_{max} d).$$

Considering the convexity of the function, if the gradient is non-positive at the initial point $s = 1$, we do not perform the line search taking $s = 1$ as a solution. The procedure is

1. Set an initial estimate for s to one and an iteration index n to zero.
2. Calculate the first-order derivative of g as shown below. If the absolute value of the first-order derivative is less than a specified tolerance, then stop. Otherwise, continue to step 3.

   $$(dg/ds)^n = \lambda_{max} \left[\nabla F\left(\beta + s^n \lambda_{max} d\right)\right]^T d$$

3. Calculate the second-order derivative of g.

   $$\left(d^2 g/ds^2\right)^n = \left(\lambda_{max}\right)^2 d^T \left[\nabla^2 F\left(\beta + s^n \lambda_{max} d\right)\right] d$$

4. Update the iteration variable s.

   $$s^{n+1} = s^n - (dg/ds)^n \Big/ \left(d^2 g/ds^2\right)^n$$

5. Let $n = n + 1$, and go back to step 2.

3.2 COMPARISONS USING STAND-ALONE CALCULATIONS

In this section, we perform example calculations for three and five phases, although our algorithm can be applied with complete robustness for even more phases. Because five-phase calculations cannot be illustrated in a figure, three-phase calculations are discussed in more detail. For stand-alone calculations, there are no previous time steps or iteration steps to use as an initial guess. We compare two algorithms to perform stand-alone calculations; the minimization with the constraint set S (MS) developed in this research and the conventional root-finding algorithm with the constraint set $L = \{\beta \mid t_i \geq 0, i = 1,\ldots,N_C\}$ (RL) developed by Leibovici and Neoschil (1995). For underrelaxation in the RL algorithm, we use 0.9 as the underrelaxation parameter.

We cannot directly compare with Leibovici and Nichita (2008), because they did not provide the algorithm used in their paper. However, there is no practical difference between Leibovici and Neoshil (1995) and Leibovici and Nichita (2008) because Newton's methods for the root-finding of the former and the minimization of the latter result in the same search direction (see section 2.1.4 for the relationship between the two types of Newton's methods). A minor difference between Leibovici and Neoshil (1995) and Leibovici and Nichita (2008) is that the former uses bisection and the latter could use line search along the search direction. This difference can affect the number of iterations required to converge, but does not affect the possibility of non-convergence that results from their feasible region confined by poles. The important difference between our algorithm and the others is that our feasible region does not contain any region of non-convergence. This section shows that the feasible region can significantly affect the convergence behavior.

To compare the two methods, we randomly generated overall compositions and K-values according to the following procedure:

1. Randomly generate N_P positive phase compositions. K-values are calculated based on those compositions.
2. Randomly generate positive phase mole fractions, and calculate overall composition using equations (2.16).
3. Solve the generated problem using either MS or RL.
4. Go back to step 1.

Thus, we are solving only flash calculations here where the phase mole fractions are positive. This is the most frequently encountered situation in compositional simulation. Initial estimates for MS are generated as described in the previous section. For RL, initial estimates of β_j ($j = 1,\dots,N_P - 1$) are set to $1/N_P$. This initial estimate is always feasible for RL because it corresponds to an equally weighted mean of vertices of the set $P = \{\beta \mid \beta_j \geq 0, j = 1,\dots,N_P\}$, which is contained by the set L. Initial estimates generated for MS and RL are in general different from each other because they are based on the different feasible regions. The stopping criteria for MS and RL are 10^{-8} for the max norm of the gradient of F and for the maximum residual of the RR equations, respectively.

The results show that the average numbers of iterations per flash are almost the same; 3.5 for MS and 3.6 for RL for three phases, and 3.8 for MS and 3.7 for RL for five phases. However, the number of iterations per problem is more problem-dependent for RL than for MS as shown in Figure 3.1. The maximum number of iterations for the one-million flash calculations when three phases are present is seven for MS, compared to 20 for RL. For five phases, MS requires only six iterations at most, compared to 20 for RL.

We show four example calculations for three phases in detail. The overall composition and *K*-values for the first example are given as example 1 in Table 3.1. As shown in Figure 3.2, our algorithm converges in only four iterations compared to 20 for RL. Figure 3.3 shows the iteration path in β space for both methods, MS and RL. In this figure, the feasible region is the intersection of the zones above the solid lines and those below the dashed lines (*i.e.*, the shaded region). For RL, the first Newton's step does not go out of its feasible region, but goes very near one of the poles. Once an iteration approaches a pole, it takes many iterations for it to move away from the pole.

This is best understood by considering the behavior of the function to be minimized instead of a system of equations actually solved by RL. As the pole is approached, the function exhibits more planar shape, and the quadratic approximation, on which Newton's method is based, becomes less appropriate. Also, the nearly planar shape of the function results in a large condition number of the Hessian matrix. Figure 3.4 shows the condition numbers of the Hessian matrix for MS and the Jacobian matrix for RL during the iterations. Although the largest condition number for RL is 8.1 million for this case, the condition number can be much larger depending on how close the iteration point is to the pole. If the condition number is too large, the calculation cannot converge owing to round-off errors.

Example 2 in Table 3.1 shows a case where RL cannot converge. As shown in Figure 3.5, RL cannot decrease the residual of the RR equations, while MS converges in only four iterations. Figure 3.6 shows the iteration path in β space for each algorithm. For MS, a unit Newton's step for the first iteration moves out of its feasible region, and the line search is performed to determine the next iteration point. For RL, a unit Newton's step does not go out of its feasible region, but the resulting iteration point is located very near one of the poles. Because of the round off errors caused by a significantly large condition number of the Jacobian matrix, the iterations cannot move away from the pole. Figure 3.7 shows the condition number as a function of a step size along the Newton's direction for the first iteration for each algorithm. A unit step size for each algorithm corresponds to a point on the boundary of its feasible region. For RL, the Jacobian matrix can be significantly ill-conditioned in the vicinity of a pole resulting in poor convergence. The region of poor convergence is never encountered in our MS method.

Example 3 in Table 3.1 gives a case where thermodynamic conditions are close to a critical endpoint (called a bicritical point in Haugen *et al.*, 2007); *i.e.*, a point in *P*-*T*-*x* space at which two of the three phases merge in the presence of the other non-critical phase. The conditions near a critical endpoint are indicated by the two sets of *K*-values, which become equal to each other. The area of the feasible region is 25 times larger for RL than that for MS as shown in Figure 3.8. Figure 3.9 compares the convergence behaviors of MS and RL, where MS converges in four iterations compared to seven for RL. As shown in Figure 3.10, the smaller feasible region provides a better initial estimate for MS, and also reduces the number of iterations required for convergence. The correct solution to which MS converges is $(\beta_1, \beta_2) = (0.87, 2.2 \times 10^{-6})$, which is very near a phase boundary. This example also shows that our algorithm has no convergence problem in the vicinity of phase boundaries.

Example 4 in Table 3.1 also provides conditions near a critical endpoint for three components. This example is given, however, to demonstrate that our algorithm is capable of robust negative flash calculations even for near-critical conditions. Figure 3.11 shows the tie-triangle on the ternary diagram. The elongated tie-triangle indicates that two of the three phases are near-critical and at equilibrium with the other highly immiscible phase. We consider the negative flash calculation for this near-critical mixture at an overall composition located outside the tie-triangle as shown in Figure 3.11. Figure 3.11 shows that MS converges to the solution in five iterations, while RL does so in eight iterations. The iteration paths taken in β space are given in Figure 3.12. Figure 3.12 shows only part of the feasible region for clarity, but the feasible region is bounded as proven in section 3.1.2. The feasible region for RL results in a less accurate initial estimate and more iterations to convergence because the feasible region for RL is bigger and exhibits poor convergence near the poles.

MS occasionally performs several iterations for line search in the first iteration. In terms of computational effort, the line search is inexpensive taking only 20% of the computational time for one iteration of RL.

3.3 SIMULATION CASE STUDY

We implemented and tested our new algorithm in various simulation runs with UTCOMP to confirm that it is applicable to multiphase compositional simulation. We emphasize here that our constant-*K* flash algorithm works as part of rigorous EOS flash calculations within UTCOMP. That is, we do not assume constant *K*-values for our simulations. This section presents one simulation example, where the computations are performed using a Pentium 4 CPU at 3.0 GHz and 2.0 GB of RAM.

We consider gas injection (impure CO_2 injection) for one pore-volume in a quarter of a staggered-line-drive pattern. A permeability field is stochastically generated for a two-dimensional reservoir model, as shown in Figure 3.13. The reservoir oil used is the Bob Slaughter Block (BSB) west Texas oil, for which the minimum miscibility pressure for pure CO_2 injection was experimentally measured to be approximately 1200 psia at the reservoir temperature of 105°F (Khan *et al.* 1992). The reservoir and fluid properties are summarized in Tables 3.2 and 3.3. For the seven-component fluid model, the Peng-Robinson equation of state (Peng and Robinson 1976a) is used with the van der Waals mixing rules. The parameters for the relative permeability model for the CO_2-rich liquid phase are assumed to be the same as those for the gaseous phase. The aqueous phase is at its residual saturation. The initial, injection, and production pressures are set to 1100, 1250, and 1100 psia, respectively.

In the flash calculations, we use SS followed by minimization of the Gibbs free energy. Stability analysis uses the stationary point method (Michelsen 1982a) with SS followed by Newton’s method. The switching criteria from SS to the second-order convergence methods are 10^{-3} both for flash calculations and stability analysis. The stopping criteria for flash calculations and stability analysis are 10^{-8}, while that for the constant-*K* flash calculations is 10^{-10}. Stability analysis for a single phase is performed only for well cells and cells adjacent to two- or three-phase cells, as described by Young and Stephenson (1983), and implemented in UTCOMP by Chang (1990).

The resulting oil recovery is shown in Figure 3.14. Figures 3.15 and 3.16 show the saturation distributions of the oleic, gaseous, and CO_2-rich liquid phases, and the distribution of the number of phases both at the breakthrough time of 0.45 PVI. The three-phase region exists in 23% of the total number of grid cells. Nghiem and Li (1986) observed that a three-phase region exists only in a small part of grid cells in their one-dimensional simulations, and concluded that the three-phase region can be ignored by using only two-phase flash calculations with little loss of accuracy. However, as shown here the number of cells in a three-phase equilibrium state can be much larger when two-dimensional simulations are considered.

Three-phase constant-*K* flash calculations were performed approximately 0.7 million times. There were no failures in those calculations confirming the robustness of our algorithm for constant-*K* flash for this case. Table 3.4 shows the breakdown in computational time for phase equilibrium calculations. Three-phase constant-*K* flash calculations, which are not shown in the table, take only 0.38% of the total computational time. The phase equilibrium calculations take 70% of the total computational time, where 14% is for stability analysis and 56% for flash calculations. Table 5 also shows that when the method of Young and Stephenson is not used and stability analysis for a single phase is performed for all single-phase cells, the phase equilibrium calculations take 76% of the total computational time. Thus, there is a 6% savings in time by not always performing stability calculations in this example. In this example, there is only a small difference in the simulation results using the two methods.

The total computational time could be significantly increased due to the reduction in automatic time-step sizes that result when non-convergence occurs in phase equilibrium calculations as will be shown in Chapter 5. Simulations where convergence problems exist may not even be possible to complete to required injection times. There are a variety of problems that can occur in compositional simulation, but our algorithm eliminates convergence problems associated with multiphase constant K-flash calculations.

3.4 SUMMARY AND CONCLUSIONS

We formulated the constant-K flash calculation with N_P phases as a minimization of a non-monotonic convex function with N_C linear constraints. The behavior of the minimization function was investigated in detail. We developed a robust and practical K-flash algorithm that is guaranteed to converge to the correct solution independent of the number of phases for both positive and negative flash calculations. The algorithm was implemented in a stand-alone flash code and in UTCOMP, a multiphase compositional simulator, where K-values change with composition. The conclusions are as follows:

1. Our algorithm is guaranteed to converge because the minimization function is convex and because the small feasible region developed in this research does not contain zones near poles where the Hessian matrix is ill-conditioned.
2. Procedures for multiphase constant-K flash calculations developed prior to this research were shown not to converge for some situations or to converge slowly because of large feasible regions that are bounded by poles.
3. Our algorithm can improve the reliability and efficiency of multiphase compositional simulation as part of rigorous EOS flash calculations. Convergence within our K-

flash calculation is not dependent on the initial guess from a prior flash calculation as we ensure that the initial guess is in the feasible region.

4. Fewer iterations are required for convergence using our algorithm because the feasible region is significantly smaller than that proposed in prior research. We demonstrated that even for five equilibrium phases our algorithm requires only six iterations at most in one-million flash calculations with different *K*-values that were randomly generated.

Table 3.1 Example overall compositions and constant-K values for flash calculations

Example 1

Component	z	K_1	K_2
1	0.204322076984	1.23466988745	1.52713341421
2	0.070970999150	0.89727701141	0.02456487977
3	0.267194323384	2.29525708098	1.46348240453
4	0.296291964579	1.58954899888	1.16090546194
5	0.067046080882	0.23349348597	0.24166289908
6	0.062489248292	0.02038108640	0.14815282572
7	0.031685306730	1.40715641002	14.3128010831

Example 2

Component	z	K_1	K_2
1	0.132266176697	26.3059904941	66.7435876079
2	0.205357472415	1.91580344867	1.26478653025
3	0.170087543100	1.42153325608	0.94711004430
4	0.186151796211	3.21966622946	3.94954222664
5	0.111333894738	0.22093634359	0.35954341233
6	0.034955417168	0.01039336513	0.09327536295
7	0.159847699672	19.4239894458	12.0162990083

Example 3

Component	z	K_1	K_2
1	0.896646630194	1.64571122126	1.61947897153
2	0.046757914522	1.91627717926	2.65352105653
3	0.000021572890	0.71408616431	0.68719907526
4	0.000026632729	0.28582415424	0.18483049029
5	0.016499094171	0.04917567928	0.01228448216
6	0.025646758089	0.00326226927	0.00023212526
7	0.014401397406	0.00000570946	0.00000003964

(Table 3.1 Continued)

Example 4

Component	z_i	K_{i1}	K_{i2}	x_{i1}	x_{i2}	x_{i3}
1	0.08860	0.112359551	1.011235955	0.100	0.900	0.890
2	0.81514	13.72549020	0.980392157	0.700	0.050	0.051
3	0.09626	3.389830508	0.847457627	0.200	0.050	0.059

Table 3.2 Reservoir properties in simulation case study

Dimensions	1000 ft × 500 ft × 20 ft
Number of grid cells	40 × 20 × 1
Porosity	0.25
ln-mean permeability	102 mD
Dykstra-Parsons coefficient	0.58
Correlation length	x: 600 ft, y: 300 ft
Reservoir temperature	105ºF
Initial reservoir pressure	1100 psia
Relative permeability model	Corey
	W / L_1 / G / L_2*
Residual saturation	0.25 / 0.20 / 0.05 / 0.20
Endpoint relative permeability	0.21 / 0.70 / 0.35 / 0.35
Exponent	1.5 / 2.5 / 2.5 / 2.5
Initial saturation	0.25 / 0.75 / 0.0 / 0.0

* W: Aqueous phase, L_1: Oleic phase, G: Gaseous phase, L_2: CO_2-rich liquid phase

Table 3.3 Fluid properties used in simulation for BSB oil (from Khan *et al.* 1992)

	Oil (Mol %)	Gas (Mol %)	Molecular weight	*Tc* (°F)	*Pc* (psia)	Acentric factor	BIC*
							CO_2
CO_2	3.37	95.0	44.01	87.90	1069.87	0.225	0
C_1	8.61	5.0	16.04	−116.59	667.20	0.008	0.055
$C_{2\text{-}3}$	15.03	0.0	37.20	159.90	652.56	0.131	0.055
$C_{4\text{-}6}$	16.71	0.0	69.50	374.13	493.07	0.240	0.055
$C_{7\text{-}15}$	33.04	0.0	140.96	630.68	315.44	0.618	0.105
$C_{16\text{-}27}$	16.11	0.0	280.99	892.16	239.90	0.957	0.105
C_{28+}	7.13	0.0	519.62	1236.79	238.12	1.268	0.105

* All others are 0.0.

Table 3.4 Computational time required for simulation case study

		Limited use of one-phase stability analysis		One-phase stability analysis used for all one-phase cells	
		Time (sec)	Percentage	Time (sec)	Percentage
Overall simulation		1829	100	2209	100
Phase equilibrium		1277	70	1671	76
Stability analysis	1 phase	98	5	497	23
	2 phases	161	9	159	7
Flash calculations	2 phases	590	32	587	27
	3 phases	428	23	427	19

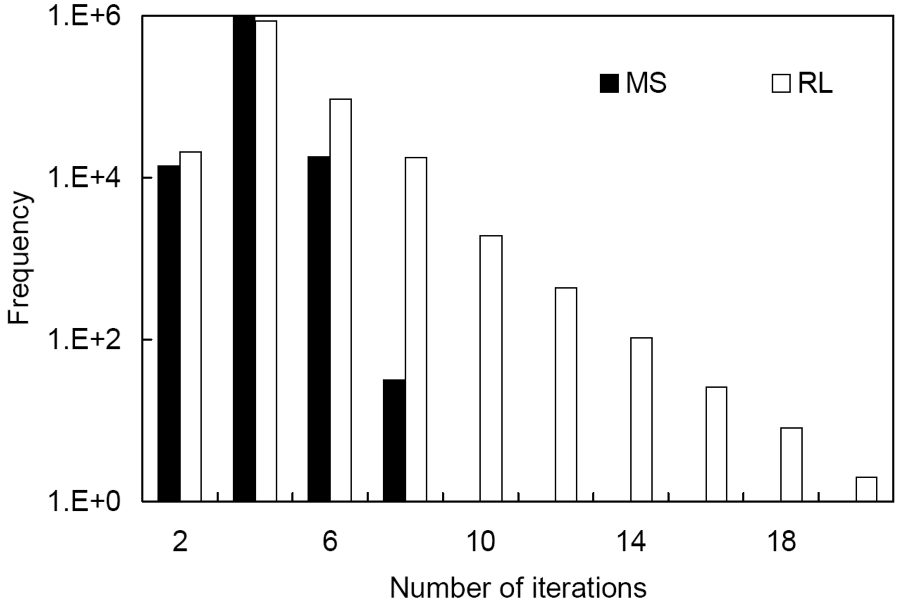

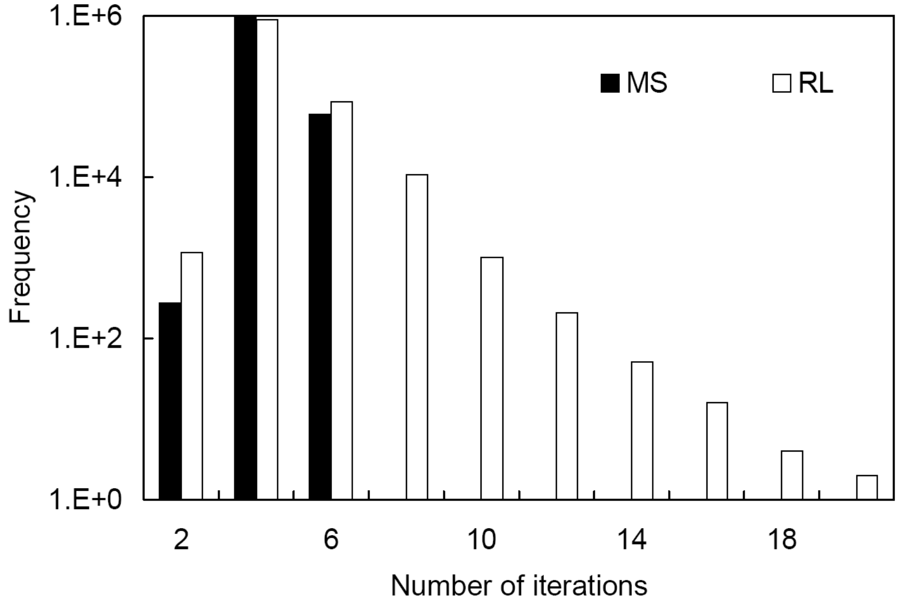

Figure 3.1 Frequency distribution of the numbers of iterations for one million flash calculations. Top: Three-phase calculations. Bottom: Five-phase calculations.

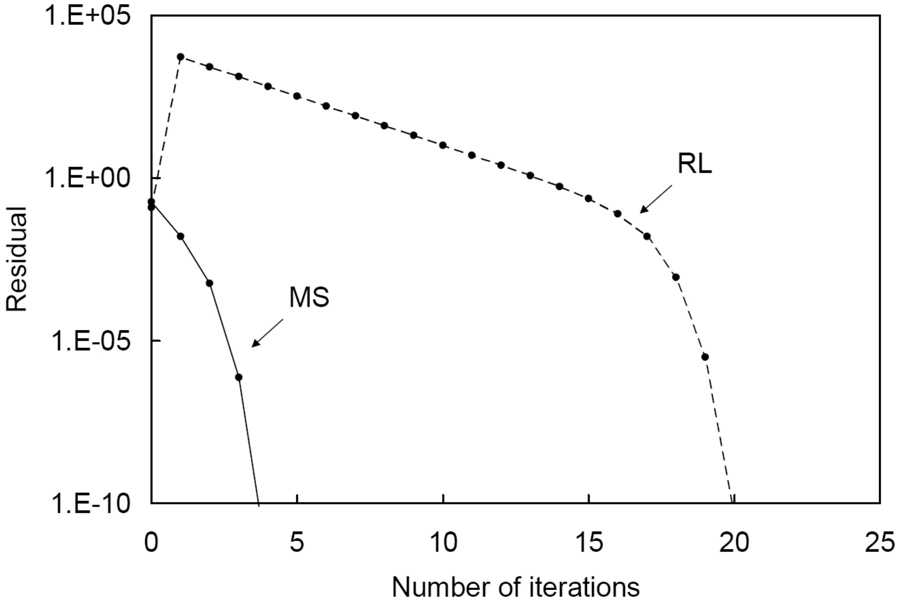

Figure 3.2 Convergence behaviors of the MS and RL algorithms for example 1 in Table 3.1. MS takes only four iterations compared to 20 for RL.

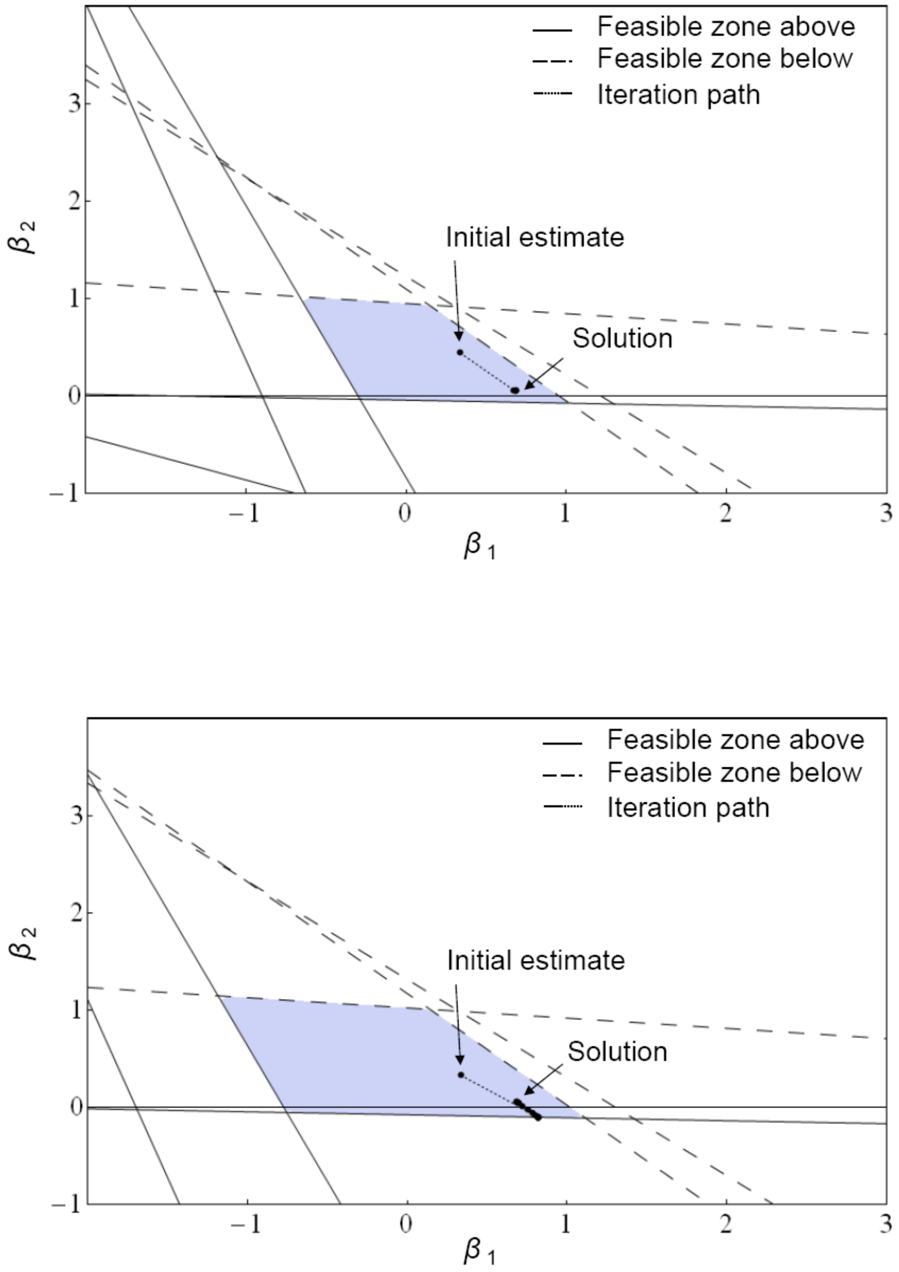

Figure 3.3 Iteration path for example 1 in Table 3.1. The shaded region is the feasible region, which is the intersection of the zones above the solid lines and those below the dashed lines. The constraints are defined in section 3.1.3. Top: The MS algorithm. Bottom: The RL algorithm.

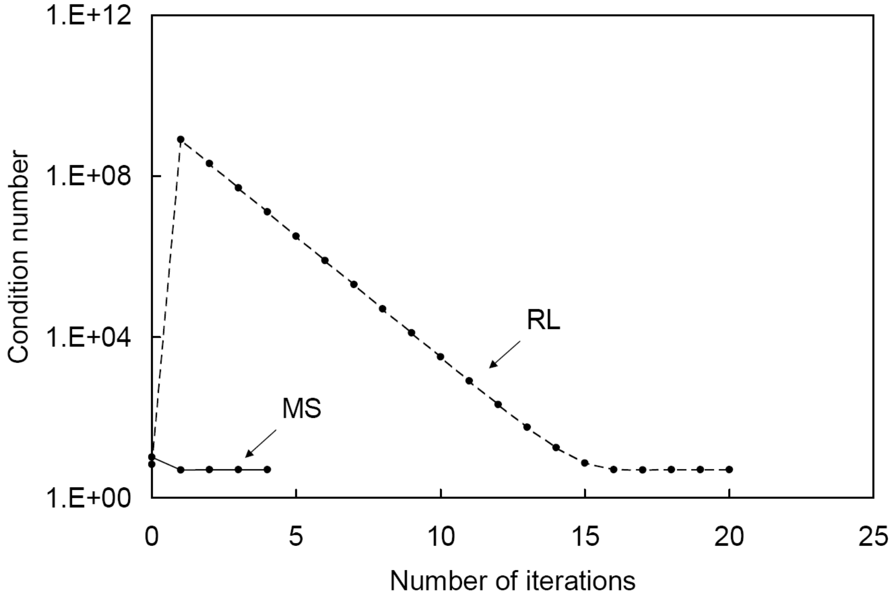

Figure 3.4 Condition number during the iteration for example 1 in Table 3.1. The condition number for RL becomes very large near the pole demonstrating the poor convergence properties of RL.

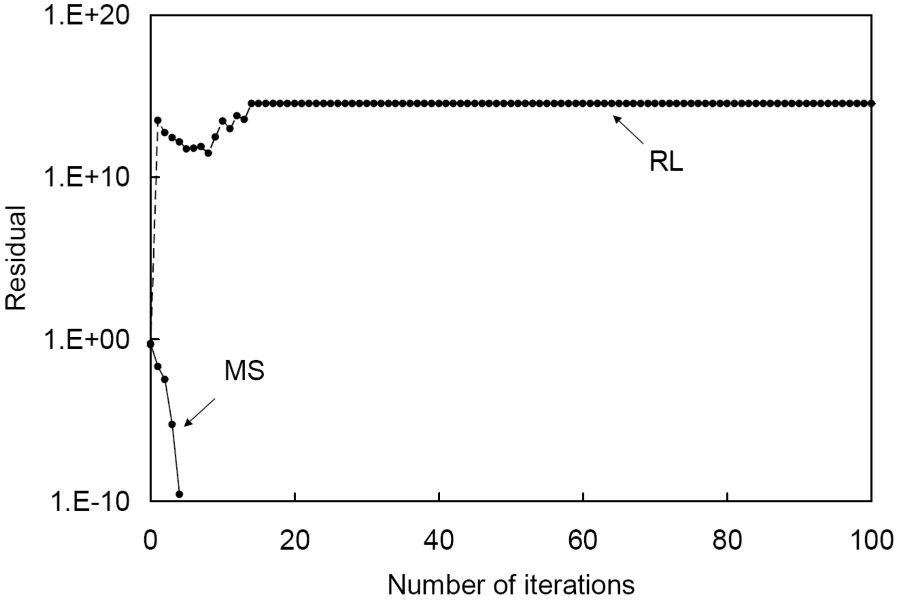

Figure 3.5 Convergence behaviors of the MS and RL algorithms for example 2 in Table 3.1. RL cannot converge, while MS converges in only four iterations.

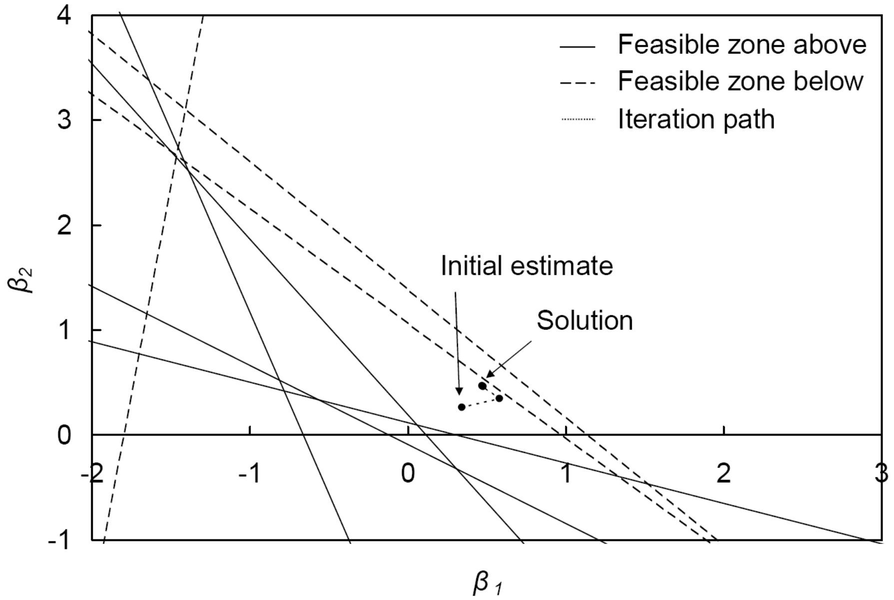

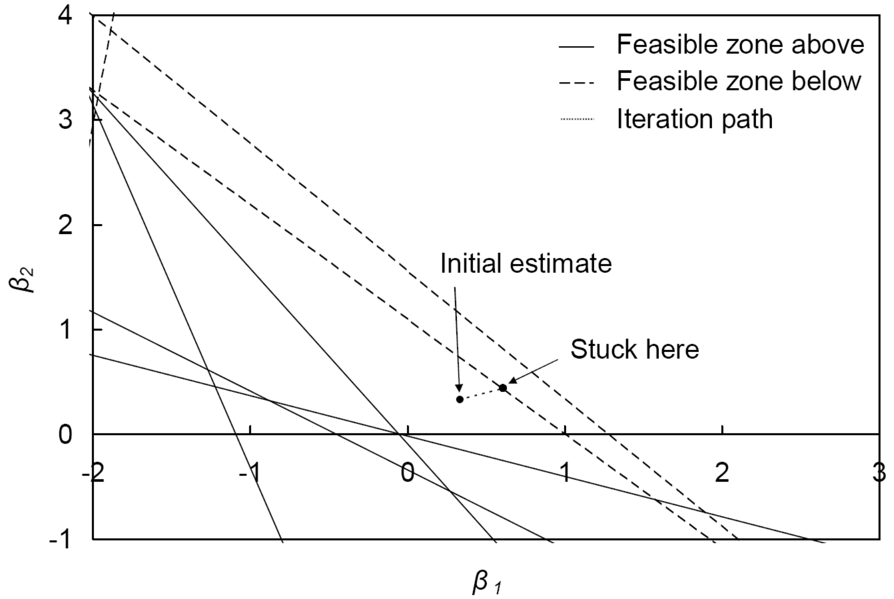

Figure 3.6 Iteration path for example 2 in Table 3.1. The feasible region is the intersection of the zones above the solid lines and those below the dashed lines. Top: The MS algorithm. Bottom: The RL algorithm. The iterations of RL become stuck very near the pole.

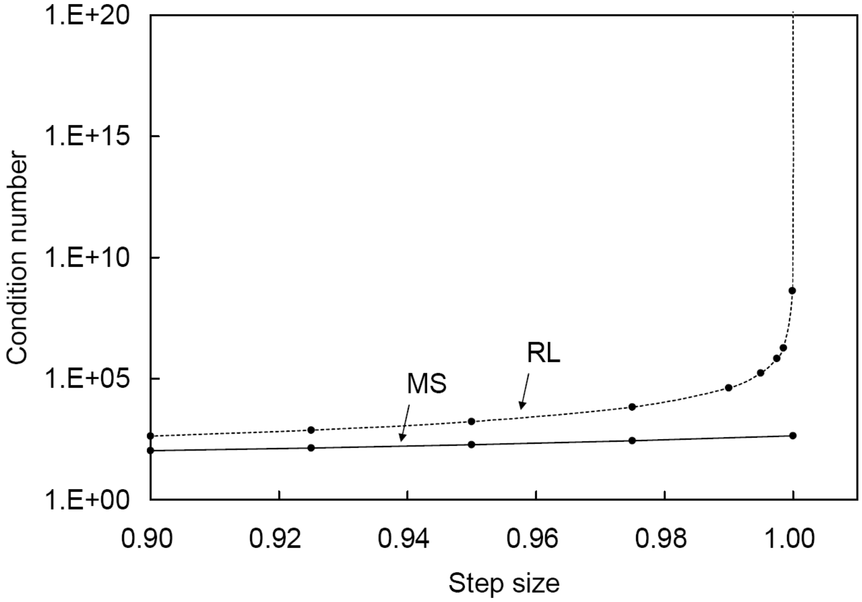

Figure 3.7 Condition number along Newton's direction for the first iteration step for example 2 in Table 3.1. The condition number for RL rapidly increases as the feasibility limit is approached, while that for MS increases only slightly.

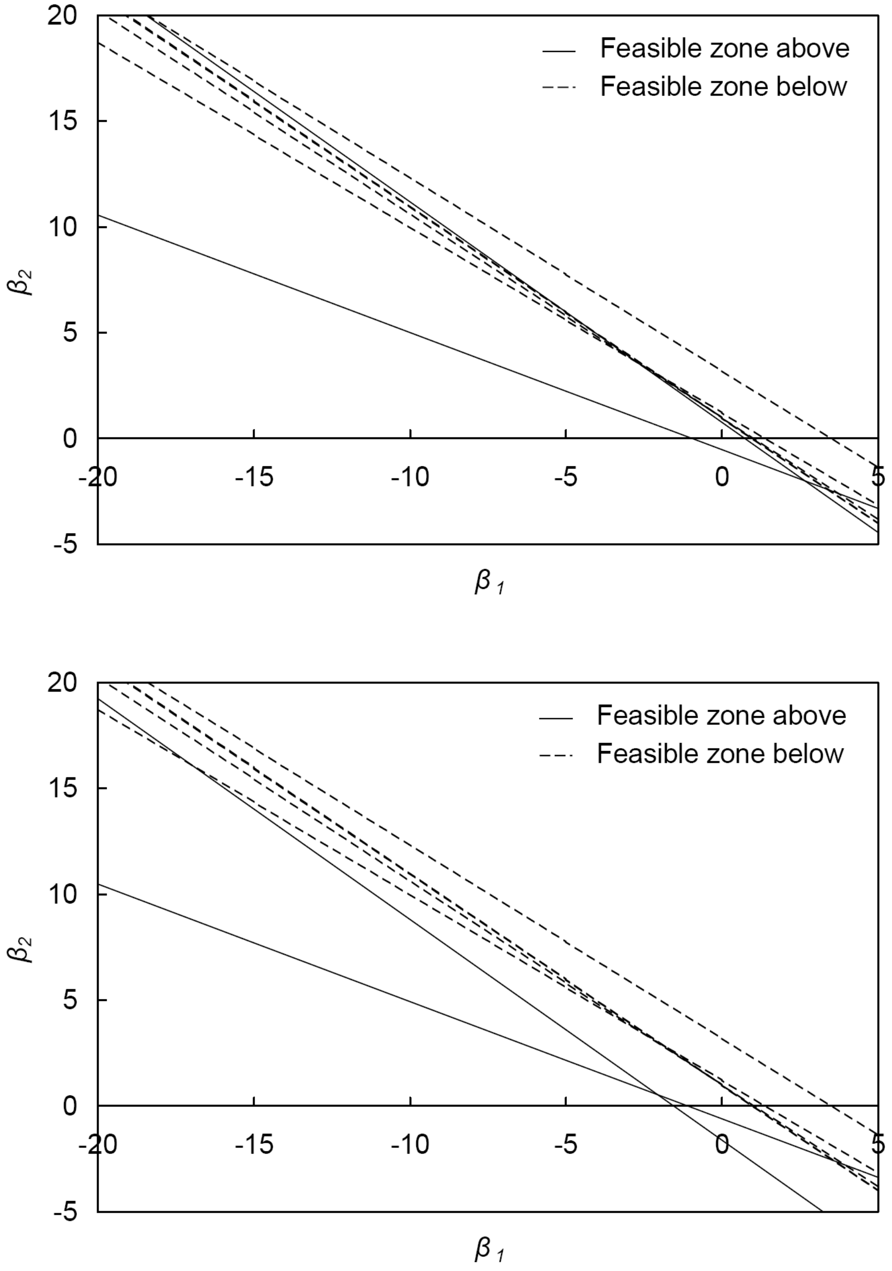

Figure 3.8 Feasible region for example 3 in Table 3.1 that is shown as the intersection of the zones above the solid lines and those below the dashed lines. Top: The MS algorithm. Bottom: The RL algorithm. The feasible region is 25 times larger for RL than that for MS.

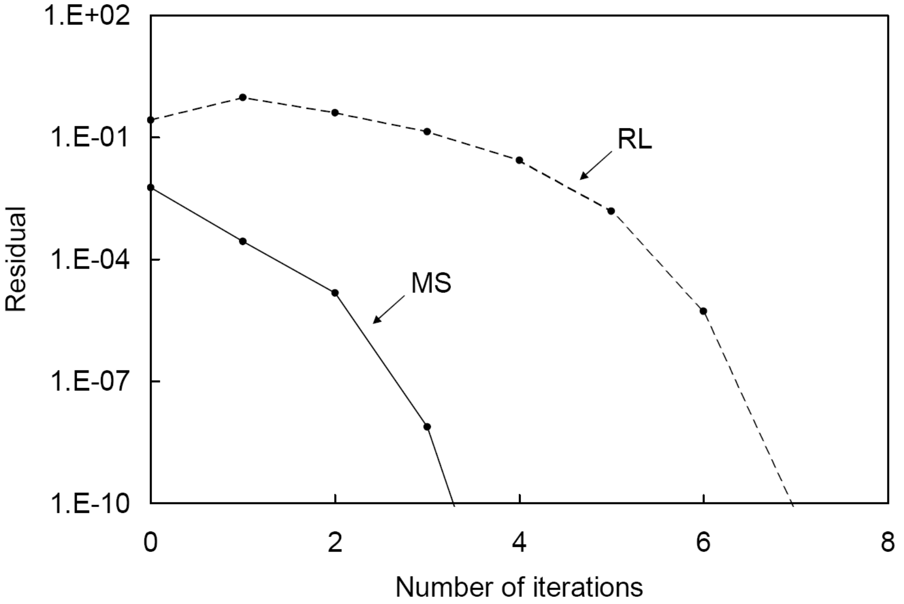

Figure 3.9 Convergence behaviors of the MS and RL algorithms for example 3 in Table 3.1.

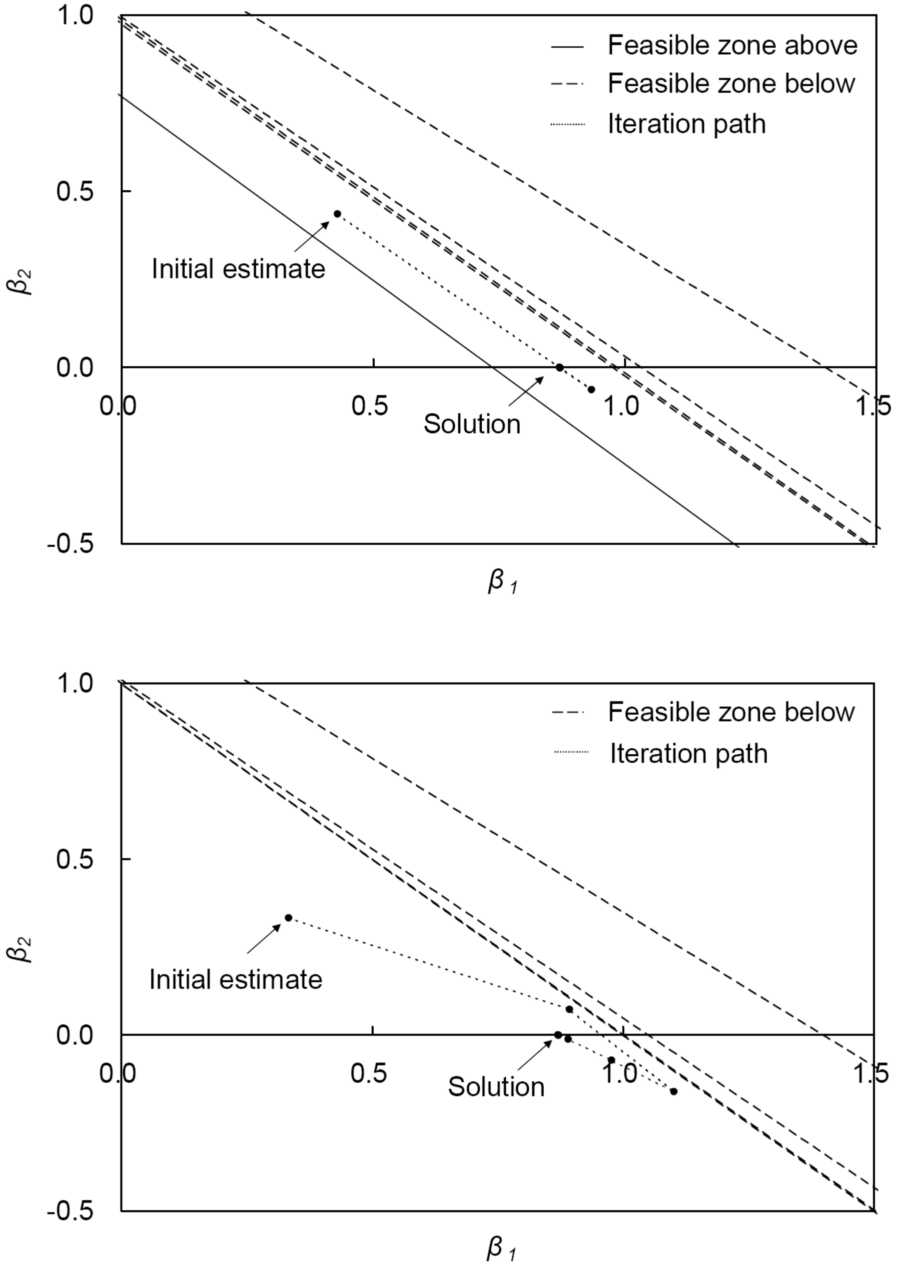

Figure 3.10 Iteration path for example 3 in Table 3.1. The feasible region is the intersection of the zones above the solid lines and those below the dashed lines. Top: The MS algorithm. Bottom: The RL algorithm.

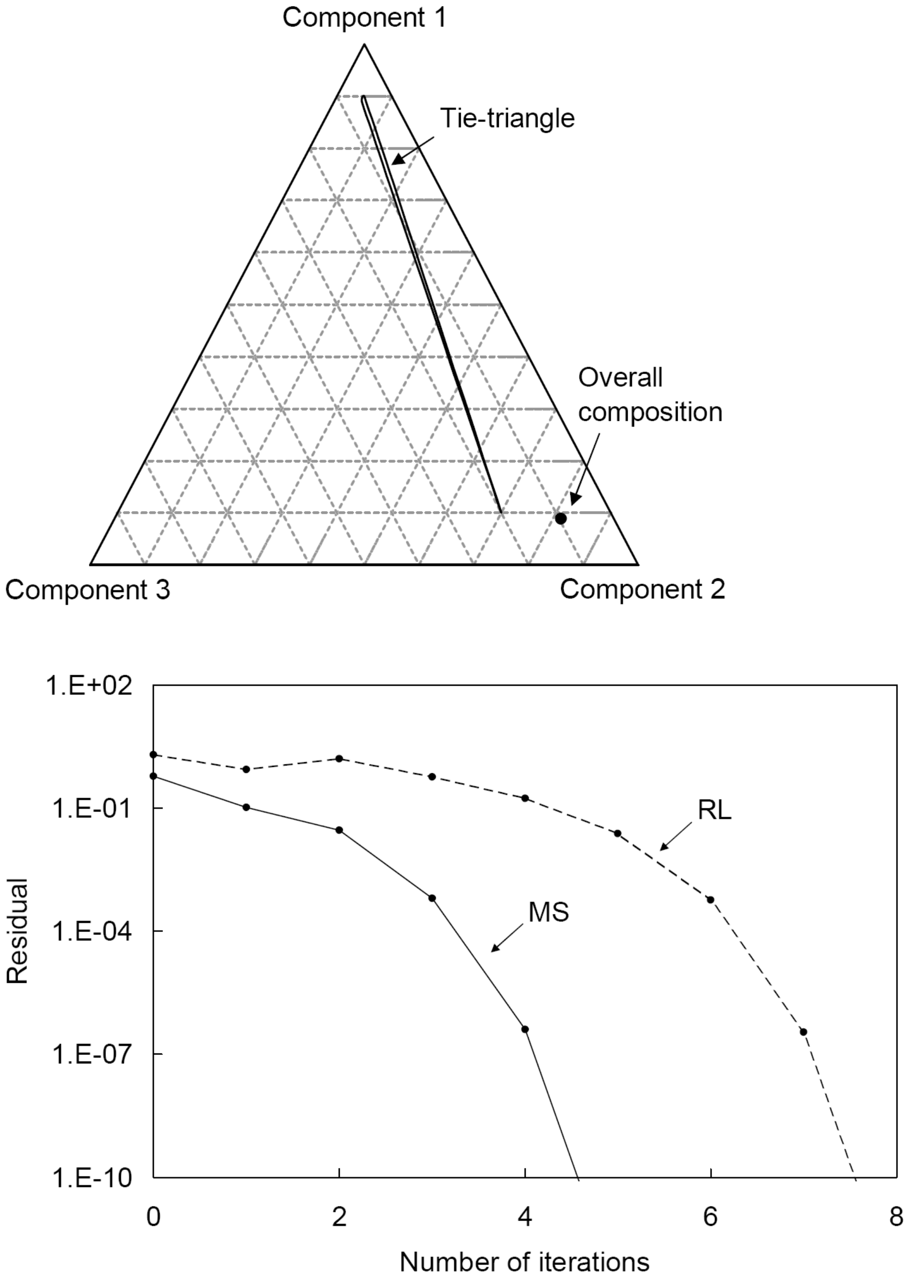

Figure 3.11 Top: Ternary diagram showing the tie-triangle and overall composition for the negative flash example 4 in Table 3.1. Bottom: Convergence behaviors of the MS and RL algorithms for example 4 in Table 3.1.

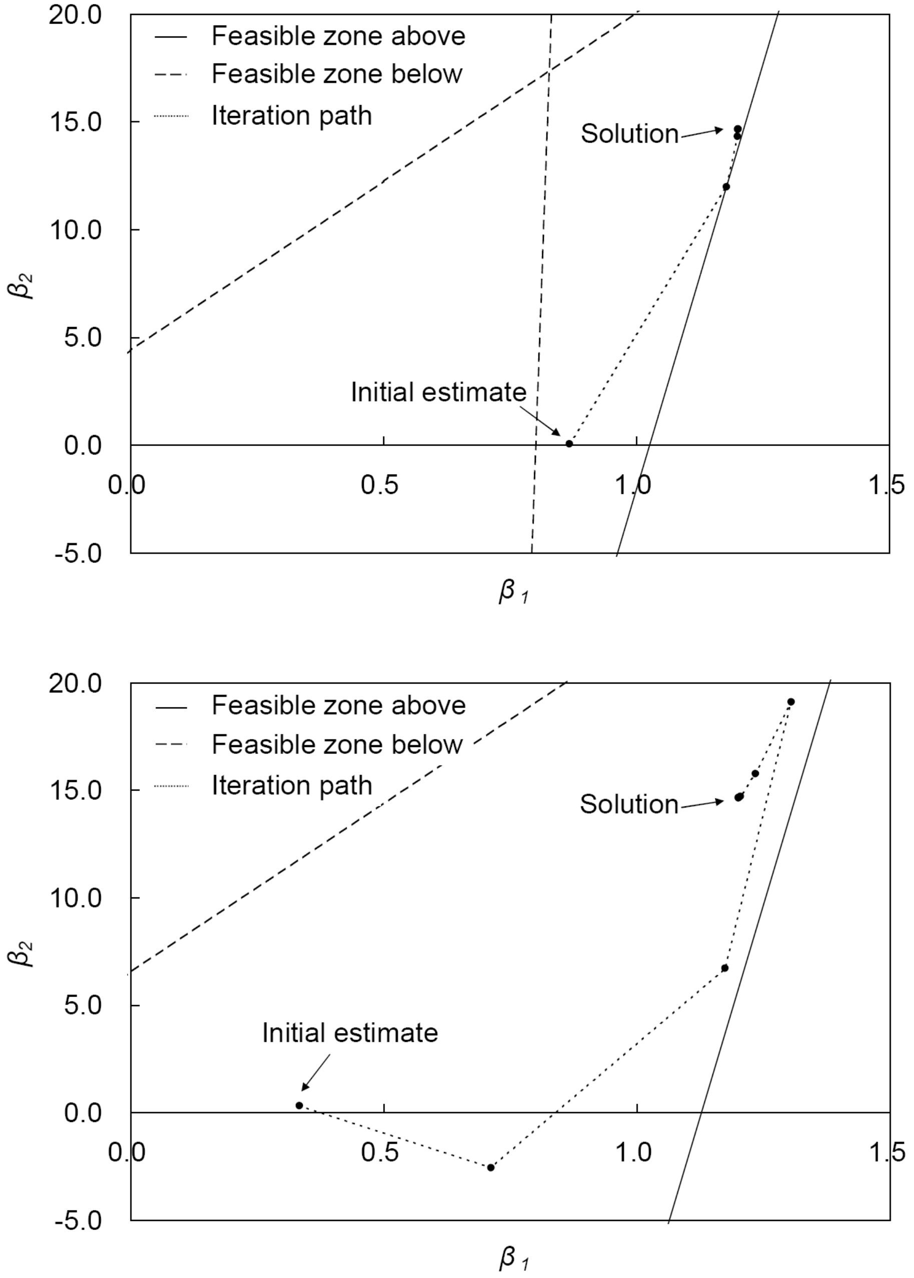

Figure 3.12 Iteration path for example 4 in Table 3.1. The feasible region is the intersection of the zones above the solid lines and those below the dashed lines. Top: The MS algorithm. Bottom: The RL algorithm.

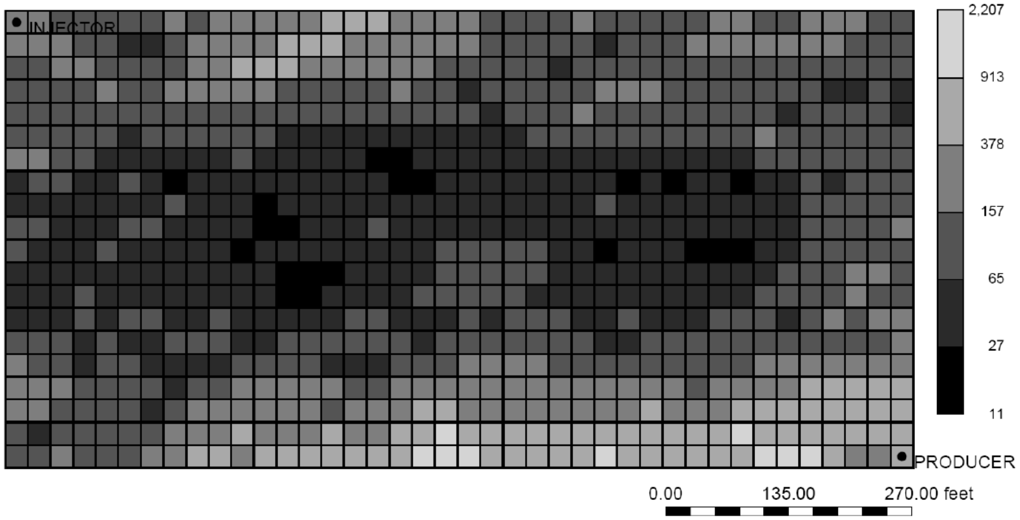

Figure 3.13 Randomly generated permeability field in mD.

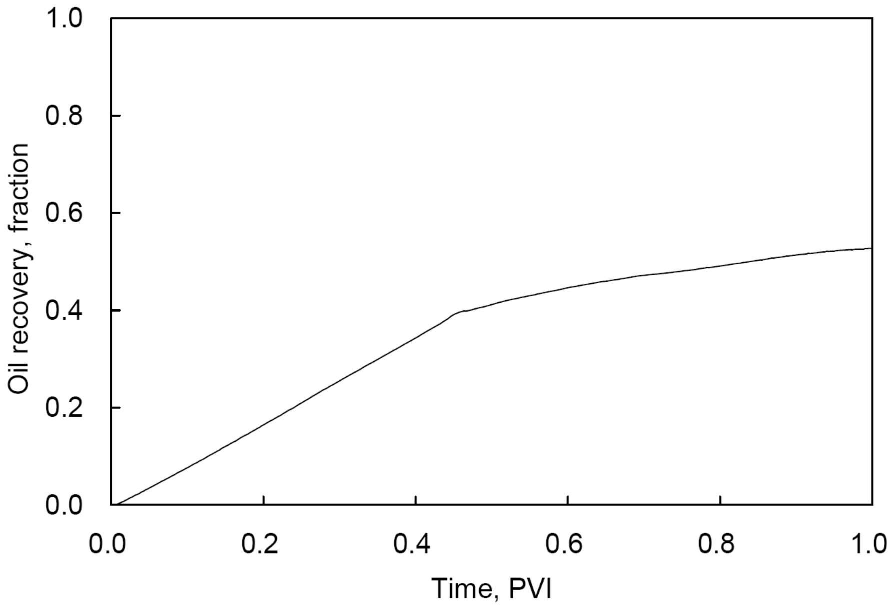

Figure 3.14 Oil recovery for the simulation case study.

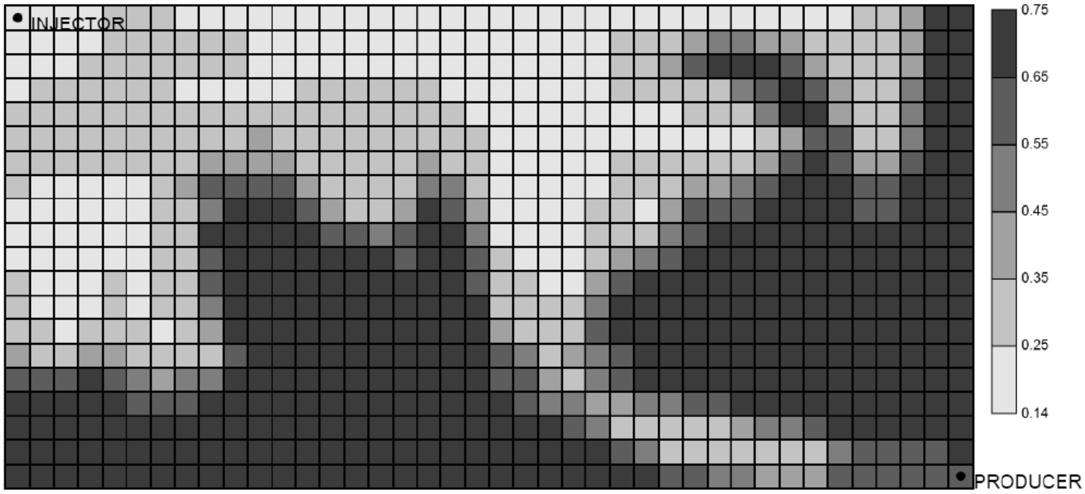

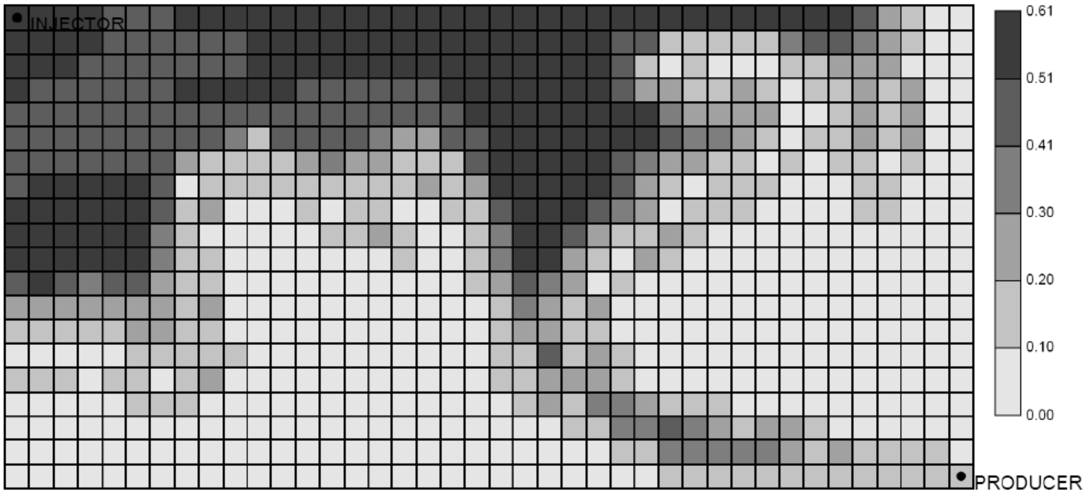

Figure 3.15 Top: Oleic phase distribution at 0.45 PVI. Bottom: Gaseous phase distribution at 0.45 PVI.

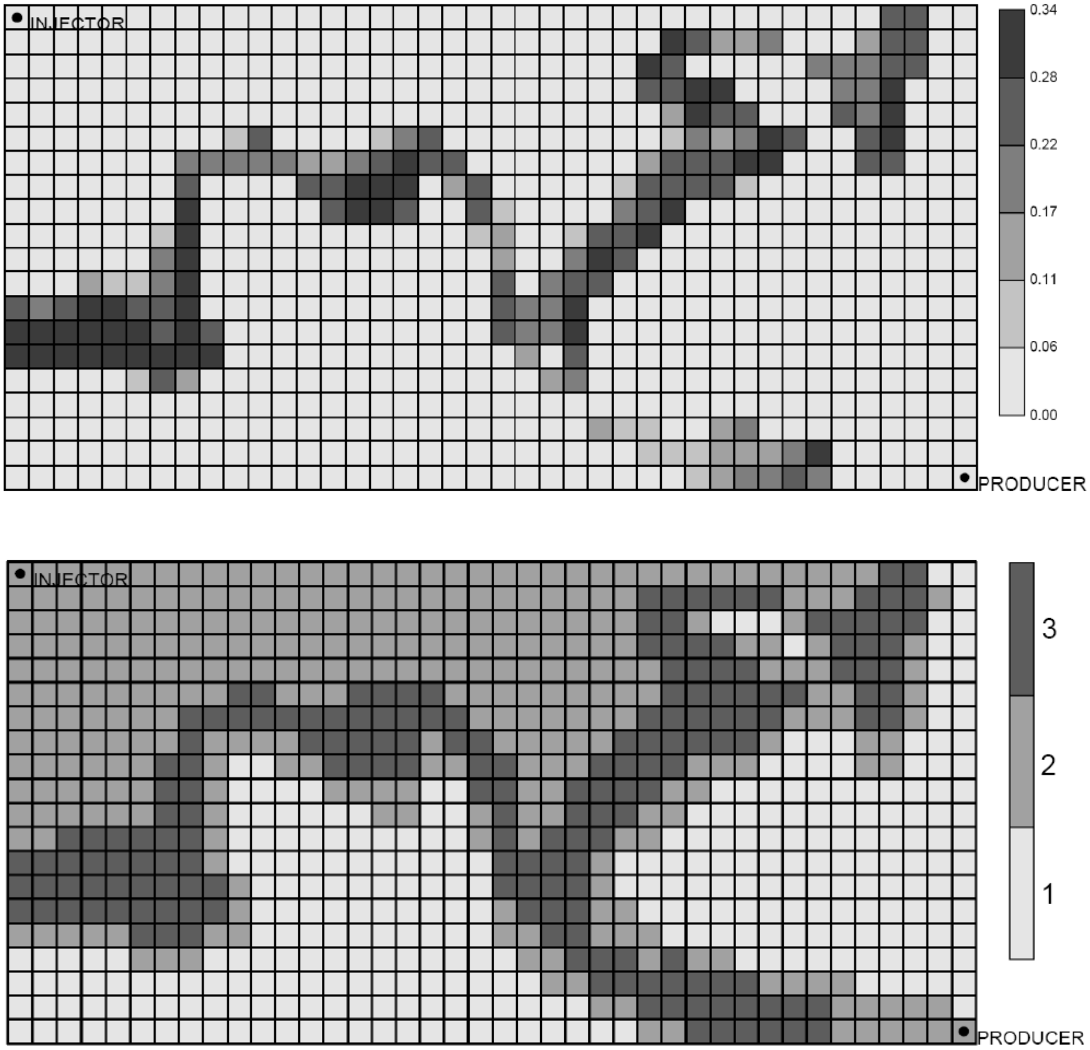

Figure 3.16 Top: CO_2-rich liquid phase distribution at 0.45 PVI. Bottom: Distribution of the number of hydrocarbon-phases at 0.45 PVI.

4. Two-Phase Equilibrium Calculations Using a Reduced Method

Simulating gas injection processes requires a compositional model to predict the fluid properties resulting from mass transfer between reservoir fluid and injection gas. A drawback of compositional simulation is the efficiency and robustness of phase equilibrium calculations. Reduced methods for phase equilibrium calculations have been studied as a potential solution to improve the efficiency of compositional simulation. However, most of those studies have been performed only in stand-alone calculations, and the robustness and efficiency of a reduced method has not been confirmed in compositional simulation. In this chapter, we develop robust and efficient algorithms for two-phase equilibrium calculations using a reduced method and implement them in a compositional reservoir simulator.

4.1 FORMULATIONS AND ALGORITHMS

In this section, we present the reduced parameters used in this research. We then derive formulations of the reduced flash and stability analysis and present practical algorithms to solve the formulated problems.

4.1.1 Reduced Parameters

The Peng-Robinson equation of state (Peng and Robinson 1976a) is used with the van der Waals mixing rules throughout this research, although any cubic equation of state can be used. To handle non-zero binary interaction coefficients (BICs), Li and Johns (2006) introduced two sets of component-specific parameters to replace BICs:

$$k_{ij} = \left(h_i - h_j\right) g_i g_j, \text{ where } i, j = 1, \ldots, N_C . \tag{4.1}$$

The parameters h_i and g_i can be considered as fitting parameters to represent the BICs, or better yet, to match *PVT* data directly; the parameters h_i and g_i could replace BICs during fluid characterization. As long as the characterized fluid model using the parameters h_i and g_i can accurately predict the phase behavior, the reduced phase equilibrium calculations are as accurate as the conventional calculations. The reduced parameters are defined as

$$\theta_{kj} = \sum_{i=1}^{N_C} \eta_{ki} x_{ij}, \tag{4.2}$$

where $\eta_i = \left(B_i,\ \sqrt{A_i},\ \sqrt{A_i} h_i g_i,\ \sqrt{A_i} h_i^2 g_i,\ \sqrt{A_i} g_i\right)$, $j = 1, \ldots, N_P$, and $k = 1, \ldots, 5.$

The key to obtaining an efficient algorithm is that fugacity coefficients for a phase can be expressed as functions of the five reduced parameters for the corresponding phase. The fugacity coefficient (see equation (2.39)) is a function of five reduced parameters because A_m, B_m, Z, and $\Sigma_j x_j A_{ij}$ can be expressed using those five parameters. That is,

$$\begin{aligned}
A_m &= \sum_{i=1}^{N_C} \sum_{j=1}^{N_C} x_i x_j \sqrt{A_i A_j} \left(1 - k_{ij}\right) \\
&= \sum_{i=1}^{N_C} \sum_{j=1}^{N_C} x_i x_j \sqrt{A_i A_j} \left[1 - \left(h_i - h_j\right)^2 g_i g_j\right] \\
&= \left(\sum_{i=1}^{N_C} x_i \sqrt{A_i}\right)^2 - 2\left(\sum_{i=1}^{N_C} x_i \sqrt{A_i} h_i^2 g_i\right)\left(\sum_{i=1}^{N_C} x_i \sqrt{A_i} g_i\right) + 2\left(\sum_{i=1}^{N_C} x_i \sqrt{A_i} h_i g_i\right)^2 \\
&= \theta_2^2 - 2\theta_4 \theta_5 + 2\theta_3^2
\end{aligned}$$

$$B_m = \theta_1$$

$$Z = Z\left(A_m, B_m\right) = Z\left(\theta_1, \theta_2, \theta_3, \theta_4, \theta_5\right)$$

and,

$$\begin{aligned}
\sum_{j=1}^{N_C} x_j A_{ij} &= \sum_{j=1}^{N_C} x_j \sqrt{A_i A_j} \left(1 - k_{ij}\right) \\
&= \sum_{j=1}^{N_C} x_j \sqrt{A_i A_j} \left[1 - \left(h_i - h_j\right)^2 g_i g_j\right] \\
&= \sqrt{A_i} \sum_{j=1}^{N_C} x_j \sqrt{A_j} - \sqrt{A_i} h_i^2 g_i \sum_{j=1}^{N_C} x_j \sqrt{A_j} g_j \\
&\quad - \sqrt{A_i} g_i \sum_{j=1}^{N_C} x_j \sqrt{A_j} h_j^2 g_j + 2\sqrt{A_i} h_i g_i \sum_{j=1}^{N_C} x_j \sqrt{A_j} h_j g_j \\
&= \sqrt{A_i} \theta_2 - \sqrt{A_i} h_i^2 g_i \theta_5 - \sqrt{A_i} g_i \theta_4 + 2\sqrt{A_i} h_i g_i \theta_3.
\end{aligned}$$

As described later, the numbers of independent variable for the reduced flash and stability analysis is $6(N_P - 1)$ compared to $N_C(N_P - 1)$ for the conventional flash calculations. For stability analysis, the number of independent variable is five for the reduced method and N_C for conventional methods. That is, the number of equations to be solved in the reduced method does not depend on N_C used in the calculations. Therefore, the reduced flash can decrease the number of equations to be solved when more than six components are used in the calculations. This is often the case in compositional simulation especially when the phase behavior is complex.

The reduced number of equations can be exploited when Newton's method is used as the solution technique. In this research, the reduced method is initiated by the conventional successive substitution (SS) both for stability analysis and flash calculations, and followed by Newton's method. Use of SS first and Newton's method next is commonly applied in compositional reservoir simulation, because Newton's method converges quadratically only when a good initial estimate of the parameters is given. As explained in section 2.2.1, SS is linearly convergent within a larger region of convergence compared to Newton's method.

An alternative procedure to obtain reduced parameters is to approximate a BIC matrix using the spectral expansion (Hendriks and van Bergen 1992). In a reduced method based on the spectral expansion, the minimum number of reduced parameters for accurate phase behavior predictions depends on the values of BICs as shown by Firoozabadi and Pan (2002). Nichita *et al.* (2006) stated that a reduced method using the spectral expansion is effective only if a BIC matrix has only few non-zero eigenvalues. The reduced method using the parameters of Li and Johns (2006) is more accurate than that using the spectral expansion because parameters h and g for the former can be directly used in EOS fluid characterization to match *PVT* data. Although we use the reduced parameters of Li and Johns (2006), the solution techniques for a reduced method presented in this dissertation can also be applied using reduced parameters from the spectral expansion.

4.1.2 Reduced Flash Calculations

We now derive a practical and robust algorithm for two-phase reduced flash calculations (RF). For a flash calculation at a given temperature and pressure, the solution must be the global minimum of the Gibbs free energy in composition space. The first-order necessary condition for a minimum of the Gibbs free energy leads to the fugacity equations (2.10) or

$$F_{ij} = \ln\left(x_{ij}\varphi_{ij}\right) - \ln\left(x_{iN_P}\varphi_{iN_P}\right) = 0, \quad \text{where } i = 1,\dots,N_C \text{ and } j = 1,\dots,\left(N_P - 1\right). \quad (4.3)$$

In equations (4.3), phase N_P is the reference phase. The fugacity equations must be satisfied with the material balance equations (2.16), (2.18), and (2.19). We define $K_{ij} = x_{ij} / x_{iN_P}$ for $i = 1,\dots,N_C$ and $j = 1,\dots,(N_P - 1)$. Nghiem and Li (1984) solved equations (4.3), (2.16), (2.18), and (2.19) for $2N_C$ independent variables, $\ln K_{i1}$ and $\ln K_{i2}$ ($i = 1,\dots,N_C$), for their three-phase flash calculations. Rearranging equations (4.3), K-values become functions of $5N_P$ reduced parameters.

$$K_{ij} = \varphi_{iN_P}\left(\underline{\theta}_{N_P}\right) \Big/ \varphi_{ij}\left(\underline{\theta}_j\right), \text{ where } i = 1,\dots,N_C \text{ and } j = 1,\dots,\left(N_P - 1\right). \quad (4.4)$$

Considering the material balance equations and given overall composition, the reduced parameters for the reference phase N_P can be expressed using reduced parameters and phase mole fractions for the other ($N_P - 1$) phases.

$$\theta_{kN_P} = \left(\theta_k^z - \sum\nolimits_{j=1}^{N_P-1} \beta_j \theta_{kj}\right) \Big/ \beta_{N_P}, \text{ where } \theta_k^z = \sum\nolimits_{i=1}^{N_C} \eta_{ki} z_i \text{ and } k = 1,\dots,5. \quad (4.5)$$

Then, K-values in equations (4.4) can be considered as functions of $6(N_P - 1)$ variables. Once K-values are calculated, phase compositions are computed directly as

$$x_{iN_P} = z_i / t_i \text{ and } x_{ij} = K_{ij} x_{iN_P}, \quad (4.6)$$

where $t_i = 1 - \left[\sum_{j=1}^{N_P - 1} \left(1 - K_{ij} \right) \beta_j \right]$, $i = 1, ..., N_C$, and $j = 1, ..., \left(N_P - 1 \right)$. This rearrangement of the original flash formulation confirms that both intensive and extensive phase properties can be viewed as functions of $6(N_P - 1)$ independent variables θ_{kj} and β_j, where $k = 1,\ldots,5$ and $j = 1,\ldots,(N_P - 1)$.

The reduced flash equations to be solved for the $6(N_P - 1)$ independent variables are

$$\begin{aligned} F_m^R &= \theta_{kj} - \sum_{i=1}^{N_C} \eta_{ki} x_{ij} = 0 \quad \text{for } m = k \times j \\ F_m^R &= \sum_{i=1}^{N_C} \left(x_{iN_P} - x_{ij} \right) = 0 \quad \text{for } m = 5\left(N_P - 1 \right) + j \end{aligned} \tag{4.7}$$

where $k = 1,\ldots,5$ and $j = 1,\ldots,(N_P - 1)$. Equations (4.7) include the multiphase Rachford-Rice equations (Rachford and Rice 1952, also see section 2.2.1.2) to satisfy the material balance equations. The Jacobian matrix is of size $6(N_P - 1) \times 6(N_P - 1)$, independent of N_C used in the calculation.

The algorithm developed for the reduced two-phase flash ($N_P = 2$) is as follows:

1. Calculate θ_k^z ($k = 1,...,5$) as defined in equations (4.5).
2. Obtain initial estimates for the six independent variables, θ_{kj} and β_j ($k = 1,\ldots,5$ and $j = 1$), based on the solution from successive substitution.
3. Calculate the reduced parameters for the reference phase N_P using equations (4.5).
4. Calculate compressibility factors and fugacity coefficients for the two phases using an EOS. When the cubic EOS has multiple roots of the compressibility factor, the correct root is selected that results in the lowest Gibbs free energy (Evelein *et al.* 1976).
5. If $\max\{|F_i|\} < \varepsilon$, then stop. Otherwise, continue to step 6.
6. Calculate K-values using equations (4.4) based on the fugacity coefficients in step 4.
7. Calculate compositions for the two phases using equations (4.6).

8. Calculate the residuals of equations (4.7).
9. Construct the 6×6 Jacobian matrix analytically (see Li and Johns 2006) and solve the system of equations.
10. Update the six independent variables θ_{kj} and β_j ($k = 1,\ldots,5$ and $j = 1$).
11. Repeat steps 3, 4, 6, and 7 and update the independent variables except for β_1.
12. Go to step 3.

The above algorithm is different from that of Li and Johns (2006), which uses the basic Newton's method to solve the system in the reduced space (*i.e.*, go to step 3 after step 10). As will be shown, the above algorithm improves the convergence behavior near critical points. Also, the stopping criterion is based on the fugacity equations alone in the above algorithm. This is an important issue in practice and will be discussed in section 4.4.

In step 9, one possibility is to use Gaussian elimination to solve the 6×6 system. Use of Cramer's rule (Strang 2006) is another possibility. Cramer's rule provides a symbolic form of the inverse Jacobian matrix. That form is fixed because our reduced method solves a fixed number of equations independent of the number of components. However, simple experimental calculations show that Gaussian elimination is 70% faster than Cramer's rule for a 3×3 system. The advantage of Gaussian elimination increases with the size of a system to be solved. Therefore, Gaussian elimination is used in step 9 in our algorithm. This is also true for our reduced stability analysis that is presented in the next section.

To demonstrate the improved convergence behavior of our algorithm for reduced flash calculations (improved RF), we compare it with the following three algorithms: the basic algorithm for reduced flash calculations (basic RF) (Li and Johns 2006) that does not include step 11, minimization of the Gibbs free energy with respect to component mole numbers in a phase (MG) (Perschke *et al.* 1989, also see section 2.2.1.1), and solution of fugacity equations with respect to K-values (FK) (Nghiem *et al.* 1983). Figure 4.1 shows the convergence behavior in terms of the residuals of the fugacity equations, equations (4.3), with different algorithms. The fluid used is oil A given by Li and Johns (2006) at 484°F and 1044.62 psia for a near-critical mixture (Table 4.1). The initial estimates are given by SS with a switching criterion for Newton's iteration when $\max\{|F_i|\} < 10^{-3}$. The convergence rate for each algorithm is linear for the first eight iterations indicating that the switching point from SS to Newton's method is not within the region of the quadratic convergence of Newton's method. Nevertheless, Newton's method should be used in the final iterations because using SS alone requires more than 78 thousands iterations to reduce $\max\{|F_i|\}$ from 10^{-3} to 10^{-8}, compared to 10 iterations for the improved RF.

The basic RF takes almost twice the number of iterations compared with the improved RF when a stopping criterion of $\max\{|F_i|\} < 10^{-6}$ is used. The behavior of the basic RF results from the fact that the reduced method solves the fugacity equations, equations (4.3), only indirectly. The improved RF also solves the fugacity equations indirectly, but the improved algorithm eliminates the undesirable convergence behavior. The convergence behavior of our improved RF is remarkable considering its simplicity because it can converge with a smaller number of iterations than MG, which uses a line search technique to enhance convergence.

FK is not shown in the figure because for this case it converges to the trivial solution where the vapor- and liquid-phase have the same composition and density. Although the improved RF requires 20% more computational time per iteration than the basic RF, the tradeoff is worth the increased robustness.

When implemented in a compositional reservoir simulator, we found that the improved RF rarely converged to the trivial solution for extremely difficult cases where overall compositions are very near the binodal curve in the critical region. For the few cases, the flash calculation is repeated where the Rachford-Rice equation (1952) is solved in step 11 to obtain phase compositions and mole fractions, and update the six independent variables. This procedure makes the summation conditions, equations (2.19), satisfied at each iteration and tends to avoid the trivial solution. Besides, one may avoid the trivial solution by selecting the independent variables between (θ_1^L, .., θ_5^L, L) and (θ_1^V, .., θ_5^V, V) based on the values of L and V (Fussell and Yanosik 1978).

The Newton's iteration containing one SS step mentioned above suggests a way to calculate phase component mole fractions x_{ij} ($i = 1,\ldots,N_C$, $j = 1,\ldots,N_P$) from reduced parameters. As mentioned in section 2.2.5, Kaul and Thrasher (1996) and Pan and Firoozabadi (2003) encountered difficulties in their minimization algorithms for the Gibbs free energy in reduced space. Their difficulties arose because they were unable to calculate phase component mole fractions directly from reduced parameters. However, phase component mole fractions can be easily calculated by performing one SS step for given reduced parameters. This relationship between phase component mole fractions and reduced parameters confirms that the Gibbs free energy is a function of reduced parameters because both ideal and excess parts of the Gibbs free energy are functions of reduced parameters (see section 2.1.2). Kaul and Thrasher (1996) and Pan and Firoozabadi (2006) did not use this relationship in their minimization algorithms for the Gibbs free energy in reduced space.

4.1.3 Reduced Stability Analysis

In this section, we derive an algorithm for stability analysis using the reduced method. A common numerical method for stability analysis is to search for a phase composition at which the tangent plane distance (TPD) function is negative (Michelsen 1982a). If such a phase composition is found, the current phase with composition $\underline{z}$ is unstable. Otherwise, the current phase is assumed to be stable. The stationary point method of Michelsen locates stationary points on the TPD function and checks the sign of the TPD function to identify phase stability.

For stability analysis of a single-phase mixture, the location of stationary points is performed using vapor- and liquid-like initial estimates based on *K*-values from the Wilson's correlation (1969), equation (2.49). If the first calculation with a vapor-like (or liquid-like) estimate converges either to the trivial solution or to a non-trivial solution with a positive value of the TPD function, then the second calculation starts with a liquid-like (or vapor-like) estimate searching for phase instability. If the two calculations do not identify phase instability, the current phase with composition $\underline{z}$ is assumed to be stable. If either set of the calculation identifies phase instability, the stability analysis is followed by a flash calculation to obtain a two-phase solution.

An integral part of the algorithm is to locate stationary points and the reduced method can be applied there. The following stationarity equations should be satisfied at a stationary point of the TPD function (see section 2.1.3):

$$S_i = \ln X_i + \ln \varphi_i\left(\underline{x}\right) - \ln \mathrm{z}_i \varphi_i\left(\underline{z}\right) = 0,\ \text{where } i = 1,\ldots,N_C. \tag{4.8}$$

In a conventional algorithm, equations (4.8) are solved with the independent variables of X_i (i = 1,…,N_C). The mole fractions are calculated using equations (2.60). Rearranging equations (4.8), all variables are functions of the five reduced parameters. That is,

$$X_i = \mathrm{z}_i \varphi_i\left(\underline{z}\right) / \varphi_i\left(\underline{\theta}\right),\ \text{where } i = 1,\ldots,N_C \tag{4.9}$$

and we need only five equations to solve the original problem of N_C dimension. The non-linear equations to be solved for reduced stability analysis are

$$S_k^R\left(\underline{\theta}\right)=\sum_{i=1}^{N_C}\left(\theta_k-\eta_{ki}\right)z_i\varphi_i\left(\underline{z}\right)/\varphi_i\left(\underline{\theta}\right)=0,\ \text{where } k=1,\ldots,5. \qquad (4.10)$$

The size of the Jacobian matrix is 5×5 regardless of N_C, which makes the solution of a system of equations faster and more robust for the reduced method than for the conventional method. The reduced method is switched from SS when a specified criterion is satisfied (*e.g.*, $\max\{|S_i|\} < 10^{-3}$). The algorithm for locating a stationary point using the reduced method is as follows:

1. Calculate compressibility factors and fugacity coefficients for the phase with composition $\underline{z}$. When the cubic EOS has multiple roots in the compressibility factor, the correct root is selected to result in the lowest Gibbs free energy (Evelein *et al.* 1976). This is also true for step 5 below.
2. Obtain initial estimates for X_i (i = 1,…,N_C) from successive substitution.
3. Calculate mole fractions using equations (2.60).
4. Calculate the five reduced parameters using equations (4.2).
5. Calculate compressibility factors and fugacity coefficients for the phase with composition $\underline{x}$ as functions of $\underline{\theta}$.
6. If $\max\{|S_i|\} < \varepsilon$, then stop. Otherwise, continue to step 7.
7. Calculate residuals of equations (4.10).
8. Construct the 5×5 Jacobian matrix analytically (see Appendix B) and solve the system of equations.
9. Update the five reduced parameters.
10. Repeat step 5 and calculate X_i (i = 1,…,N_C) using equations (4.9).
11. Go to step 3.

The algorithm presented here is different from the basic Newton's method to solve the system in reduced space (*i.e.*, go to step 5 after step 9). The main difference is that our algorithm takes one SS step inside the iteration loop, which improves the convergence behavior near critical points.

Figure 4.1 compares the convergence behaviors in terms of residuals of the stationarity equations, equations (4.8), with the following algorithms: the improved algorithm for reduced stability analysis (improved RSA), the basic Newton's method to solve the reduced system equations (4.10) (basic RSA), and the conventional stability analysis with direct solution of the stationarity equations with respect to the N_C independent variables (CSA). The fluid used in the comparison is oil A of Li and Johns (2006) for a near-critical mixture (Table 4.1). The initial estimate for the Newton's iteration of the stability analysis is given by SS with a switching criterion of $\max\{|S_i|\} < 10^{-3}$. Both the basic and improved RSA solve the stationarity equations only indirectly, but the improved RSA does not exhibit the undesirable convergence behavior of the basic RSA as shown in Figure 4.1. Although the improved RSA requires 30% more computational time per iteration than the basic RSA, the tradeoff is worth the increased robustness. The results show that the basic RSA can take almost twice the number of iterations compared with the improved RSA when a stopping criterion of $\max\{|S_i|\} < 10^{-6}$ is used. The improved RSA can converge in an even smaller number of iterations than CSA, which directly solves the stationarity equations with the N_C independent variables.

4.2 CONVERGENCE PROBLEM WITH STABILITY ANALYSIS

Hoteit and Firoozabadi (2006) reported that the minimum of the TPD function obtained by local minimization algorithms can be discontinuous in a single-phase region in pressure-temperature (*P*-*T*) space. They also reported that numerical algorithms for stationary points can exhibit poor convergence behavior near the discontinuity. However, they did not discuss what causes the discontinuity and convergence problems.

In this section, we demonstrate the appearance of the discontinuity for a binary mixture as the pressure changes at a fixed temperature. We also show that the poor convergence can result from a saddle point on the TPD function and can occur in the region slightly outside the “shadow-phase region” of Rasmussen *et al.* (2006). The shadow-phase region is where equations (4.8) have two solutions; the trivial solution and a non-trivial solution with a positive value for the TPD function.

We consider the stability analysis of a binary mixture consisting of 20% C_1 and 80% *n*-C_{20}. The critical point of the mixture is calculated to be at 911.73°F and 312.63 psia using the Peng-Robinson EOS. Figures 4.2, 4.3, and 4.4 show construction of the dimensionless TPD function (D/RT) at a fixed temperature 800°F and three different pressures 690, 633, and 575 psia, respectively. Those pressures are in the single-phase region in the P-T diagram because D/RT is non-negative in the entire x_{C1} space. The outer boundary of the shadow-phase region at this temperature is at 632.7 psia, where a saddle point exists on the TPD function.

For the case of 690 psia, D/RT has a unique minimum that corresponds to the trivial solution. For the case of 633 psia, D/RT also has the same unique minimum. However, the gradient becomes very close to zero at the inflection point around at x_{C1} = 0.67. For the case of 575 psia, D/RT has two minima; one is the trivial solution and the other is a non-trivial solution with a positive value of D/RT. When a local minimization algorithm is used with a vapor-like initial estimate, the algorithm obtains the local minimum at x_{C1} = 0.76. Therefore, when the local minimum of D/RT converged by using a vapor-like estimate as the initial guess is plotted as a function of pressure, there exists a discontinuity at 632.7 psia, the outer boundary of the shadow-phase region (Figure 4.5). This discontinuity is what Hoteit and Firoozabadi (2006) reported in their paper for different mixtures. The global minimum will not exhibit this kind of discontinuity because the global minimum of *D/RT* is always zero in a single-phase region (the trivial solution).

When the conditions are closer to the critical point, the location of the saddle point becomes closer to the trivial solution and the degree of discontinuity becomes smaller. Figure 4.6 shows *D/RT* at a temperature of 900°F and a pressure of 377 psia. The outer boundary of the shadow-phase region at this temperature is at 376.5 psia. When stability analysis is performed for this mixture with a vapor-like initial estimate, the improved RSA and CSA requires 21 and 33 iterations to decrease max$\{|S_i|\}$ from 10^{-3} to 10^{-10}, respectively. The poor convergence behavior arises from the existence of the inflection point with a very small value of the gradient, because it tends to attract the values for each subsequent iteration.

There are several approaches to improve the problem. The safest approach would be to take a larger number of SS steps to provide a better initial estimate for the Newton's method. Another approach is to use a global minimization algorithm for the TPD function. However, those time-consuming methods would not be justified to use in compositional simulation, because the standard stability analysis using the stationary point method assumes a stable single-phase when convergence cannot be achieved within a specified number of iterations. Therefore, a practical approach for compositional simulation would be to simply stop the iteration and assume a stable single-phase when the iterations do not sufficiently improve the objective function for a few consecutive iterations (*e.g.,* five iteration steps).

The procedure of Hoteit and Firoozabadi (2006) would be another practical approach. They set the maximum number of iterations to be 15 for the reduced method, and assume a stable single-phase when convergence cannot be achieved within the maximum number of iterations. We implement their procedure in this research. This simple procedure is practical for use in a compositional simulator, because it does not affect the simulation results whether or not convergence to the trivial solution can be correctly achieved for stability analysis of the stable single-phase mixture.

4.3 COMPARISONS USING STAND-ALONE CALCULATIONS

As described in section 4.1, the reduced method solves equations that are not directly related to the fugacity equations, equations (4.3), for flash calculations, and stationarity equations, equations (4.8), for stability analysis. Although Figure 4.1 demonstrated that the improved reduced method can converge in fewer iterations than other algorithms for the same initial estimate, we investigate further the robustness and efficiency of the reduced method. From this point on, we only consider the improved RF for reduced flash and the improved RSA for reduced stability analysis.

4.3.1 Robustness

For flash calculations, we compare the robustness of the algorithms, the reduced flash (RF) and solution of fugacity equations with respect to *K*-values (FK), both of which use a simple solution of the non-linear equations using Newton's method. The comparisons are based on the number of SS steps required for Newton's method to converge to the correct solution. A smaller number of SS steps required would indicate that the function behaves favorably for the Newton's method within a wider region around the solution.

Flash calculations for oil A (Table 4.1) are performed at different conditions along the line on the *P*-*T* diagram shown in Figure 4.7. The initial estimates used in the calculations are generated by the Wilson's correlation, equation (2.49). As shown in Figure 4.8, the number of SS steps required is a strong function of the distance from the critical point. RF requires a smaller number of SS steps than FK at all conditions studied here. The advantage of RF against FK becomes significant in the critical region, which is important in gas flooding simulation where the compositional path can go near or through the critical region.

For stability analysis, we compare the reduced stability analysis (RSA) with conventional stability analysis (CSA). The comparisons are based on the number of iterations taken by the Newton's method. The initial estimates are again generated by the Wilson's correlation. Figure 4.8 shows that the number of iterations increases as the conditions become close to the critical region. CSA converges in up to twice the number of iterations compared with RSA, indicating the robustness of the reduced method. Both algorithms need no SS step for the Newton's iteration to converge to a correct solution for all conditions studied here.

4.3.2 Efficiency

The total computational time of an iterative stand-alone algorithm is approximately a product of the computational time per iteration and the number of iterations. As shown in Figures 4.1 and 4.8, the reduced method generally takes fewer iterations than the others. Therefore, comparisons of computational time per iteration demonstrate the efficiency of the reduced method in stand-alone calculations. The computations are performed using a Pentium 4 CPU at 3.0 GHz and 2.0 GB of RAM throughout this research.

A significant part of computational time per iteration can be spent in construction of the Jacobian or Hessian matrix, and solution of the systems by the Newton's method. The reduced method decreases the computational time by decreasing the size of the Jacobian matrix. We again use oil A (see Table 4.1). Figure 4.9 shows that the computational time per iteration is much shorter for the reduced method than for the others. The advantage of the reduced method increases rapidly with N_C because the number of equations to be solved is fixed for the reduced method, while those for minimization of the Gibbs free energy (MG) and FK increase with N_C. The results are consistent with an algebraic fact that if a direct solver is used, the solution of the system of equations requires operation counts on the order of the cube of the number of equations.

The significant speed-up of the reduced method is not only because of the rapid solution of the system of equations, but also because of rapid construction of the Jacobian matrix. Rasmussen *et al.* (2006) stated that construction of the Jacobian matrix for a reduced method is cumbersome. Figure 4.10 compares the computational time spent in the construction of the Jacobian or Hessian matrix for different algorithms for flash and stability analysis. The computational time spent in the construction of such a matrix is shorter for the reduced method for all cases except for the seven-component stability analysis case.

The computational cost of construction of the Jacobian or Hessian matrix depends on how directly the functions are related to the independent variables. The reduced parameters explicitly express fugacity coefficients, which are important thermodynamic state functions in phase equilibrium calculations (see section 4.1.1). In Figure 4.10, the Jacobian matrix construction for FK is more time-consuming than those in the other algorithms. This is because *K*-values are related to fugacity in a significantly indirect manner. The construction of the Hessian matrix in MG is computationally inexpensive because the matrix is symmetric and because the function has a relatively direct relation to the independent variables.

4.4 SIMULATION CASE STUDIES

Stand-alone calculations are necessary, but not sufficient for the algorithms to be practical in a simulator. The algorithms developed in this research are implemented in

UTCOMP, which is a compositional reservoir simulator originally developed by Chang *et al.* (1990). Perschke *et al.* (1989) developed the phase behavior algorithms in the original UTCOMP. The algorithms consist of accelerated successive substitution (ASS) and minimization of the Gibbs free energy for flash calculations, and stationary point method and minimization of the TPD function for stability analysis. All the calculations are performed in conventional N_C space. In this research, we replaced the ASS with the normal SS to robustly initiate the second-order convergence method.

The main factors making phase equilibrium calculations time-consuming and difficult are the number of components and the degree of miscibility. To demonstrate the robustness and efficiency of the reduced method, simulation case studies are conducted using UTCOMP with three different combinations of the algorithms: (RSA, RF), (CSA, MG), and (CSA, FK). Gas flooding in a quarter five-spot pattern with a stochastically generated permeability field is simulated with a varying number of components and degree of miscibility using a two-dimensional reservoir model. The reservoir properties and fluid properties are summarized in Tables 4.2 and 4.3, respectively. Figure 4.11 shows the permeability field used and an oil saturation distribution before breakthrough. The number of components is varied from 7 to 20. When more than seven components are used, the heaviest pseudocomponent, C_{25+}, is split to as many components as needed with the same properties. The degree of miscibility is varied by changing reservoir pressure at a constant temperature of 260°F. The minimum miscibility pressure (MMP) calculated by the PVTsim software of Calsep is 3626 psia at the reservoir temperature. In each case, the injection gas is injected for one pore-volume.

For stability analysis and flash calculations, the second-order convergence methods are initiated by SS. The switching criteria are $\max\{|S_i|\} < 10^{-3}$ for stability analysis and $\max\{|F_i|\} < 10^{-3}$ for flash calculations. The stopping criteria of the Newton's methods are $\max\{|S_i|\} < 10^{-8}$ for stability analysis and $\max\{|F_i|\} < 10^{-8}$ for flash calculations. In addition, CSA, MG, and FK use a relative step size criterion, $\max\{|\delta\alpha_i/\alpha_i|\} < 10^{-8}$, where α_i is the i^{th} independent variable and $\delta\alpha_i$ is the updated amount for α_i. The stopping criteria for the reduced method are based neither on the residuals of the reduced equations, equations (4.7) and (4.10), nor on the relative step size. That is, the reduced flash uses residuals of fugacity equations alone as the stopping criterion. We observed a case where the max norm of the reduced flash equations is 10^{-9} while that of fugacity equations is 10^{-3}. Pan and Firoozabadi (2003) reported similar observations. Therefore, the residuals of the reduced equations should not be used for determination of convergence of the reduced method.

One popular algorithm for stability analysis is a quasi-Newton method to minimize the TPD function using the Broyden-Fletcher-Goldfarb-Shanno (BFGS) method for the inverse of the Hessian matrix approximation (Michelsen 1982a). The BFGS quasi-Newton method is super-linearly convergent at best, and can avoid solution of the system of equations at the expense of curvature information used in the iteration. That is, the BFGS quasi-Newton method can take more iterations than the Newton's method at less computational effort per iteration. Ammar and Renon (1987) compared various algorithms for minimization of the Gibbs free energy including the Newton's and BFGS quasi-Newton methods. Their comparisons showed that the Newton's method requires shorter execution time than the BFGS quasi-Newton method in all cases studied in their paper. In this research, we do not consider the BFGS quasi-Newton method both for stability analysis and flash calculations, although it can be applied to both conventional and reduced methods. We investigate the effect of the number of equations to be solved for phase equilibrium calculations on the efficiency of reservoir simulation, instead of the effect of the convergence rate near the solution or the curvature information used in the iteration.

In the simulation case studies, stability analysis for a single phase is performed only for well cells and cells adjacent to two-phase cells. Flash calculations are performed for grid cells where two phases existed at the previous time step or stability analysis indicates instability of a single phase.

4.4.1 Immiscible Case

For this case, the initial, injection, and production pressures are set to 2850, 2900, and 2400 psia, respectively. This case is relatively easy for phase equilibrium algorithms because the thermodynamic conditions are far from miscibility. All algorithms converge with no failures, and lead to exactly the same simulation results (Figure 4.12).

Location of a stationary point for stability analysis was performed approximately 100 thousand times, and flash calculations approximately 400 thousand times. Average numbers of iterations for RSA, CSA, RF, MG, and FK were 1.9, 2.0, 1.6, 1.6, and 1.8, respectively.

Table 4.4 shows a breakdown of computational time for the 10- and 20-component cases using the three different combinations of the algorithms. For example, use of the algorithms (CSA, FK) took 53% of the total computational time on the phase equilibrium calculations for the 10-component case, and 66% for the 20-component case.

Table 4.4 also shows that use of (RSA, RF) resulted in phase equilibrium calculations that were 63% and 85% faster than when (CSA, MG) and (CSA, FK) were used, respectively, for the 10-component case. For the 20-component case, the phase equilibrium calculations using (RSA, RF) were 2.4 and 4.2 times faster than when (CSA, MG) and (CSA, FK) were used, respectively. The speed-up comes from the decreased computational time using the Newton's method (shaded parts in Table 4.4), where the reduced method exploits the reduced number of equations to be solved. Figure 4.12 shows the total computational time for varying N_C and for different algorithms. Compared to the other algorithms, the reduced method offers more than 23% and 47% speed-up for the 10- and 20-component cases, respectively.

4.4.2 Multicontact Miscible Case

For this case, the initial, injection, and production pressures are set to 4550, 4600, and 4100 psia, respectively. This case is more difficult for phase equilibrium algorithms because the pressures are above the MMP and fluids are multicontact miscible.

Location of a stationary point for stability analysis was performed about 1.3 million times, and flash calculations about 2.3 million times. Average numbers of iterations for RSA, CSA, RF, MG, and FK were 1.9, 2.0, 1.3, 1.3, and 1.4, respectively.

The reduced flash converged to the trivial solution only four times, while the other two flash algorithms failed more than 20 times. Because of the increased failure rate with (CSA, MG) and (CSA, FK), the simulation results are not identical, although they are very similar (Figure 4.13). The non-convergence of MG and FK are consequences of the round-off errors caused by nearly singular Hessian and Jacobian matrices in the critical region (Trangenstein 1987). The four cases of a trivial solution with the reduced flash occur when compositions are located in the vicinity of the binodal curves very near the critical region. In fact, liquid phase mole fractions of the correct solutions are 0.999, 0.997, 0.997, and 0.998.

Table 4.5 shows a breakdown of computational time for 10- and 20-component cases using the three different combinations of the algorithms. When using the algorithms (CSA, FK), the phase equilibrium calculations spent 57% of the total computational time for the 10-component case, and 66% for the 20-component case.

Use of (RSA, RF) resulted in the phase equilibrium calculations that were 30% and 38% faster than when (CSA, MG) and (CSA, FK) were used, respectively, for the 10-component case. For the 20-component case, the phase equilibrium calculations using (RSA, RF) were 1.8 and 2.5 times faster than when (CSA, MG) and (CSA, FK) were used, respectively. The speed-up is a consequence of the reduced number of equations to be solved in the Newton's iteration using the reduced method (shaded parts in Table 4.5).

Figure 4.13 shows the total computational times with different numbers of components and different algorithms. The use of the reduced method results in simulations that are more than 15% and 35% faster than those with the other algorithms for 10- and 20-component cases, respectively. The speed-up factors of the total computational time are smaller than for the immiscible case because part of the computational time spent by the second-order convergence methods is smaller for this case.

Similarly, if a larger number of grid cells are used, the speed-up factors will decrease because solution of the pressure equations takes a larger part of the total computational time. Actual saved time, however, becomes more significant as the phase equilibrium problems become more difficult and the computational time becomes longer. For example, use of (RSA, RF) saved 1574 seconds compared to (CSA, FK) for the multicontact miscible case, and 317 seconds for the immiscible case. Also, the saved time would be even more significant if stability analysis for a single phase is performed for all cells unlike in these case studies.

4.5 SUMMARY AND CONCLUSIONS

We developed robust and efficient algorithms for two-phase equilibrium calculations using a reduced method. Those algorithms were implemented in a compositional simulator to demonstrate the efficiency and robustness in simulations with different numbers of components and degrees of miscibility. Key conclusions are

1. The simple algorithm developed in this research for the reduced method improves convergence behavior near the critical region. Reservoir simulations for multicontact miscible cases showed the improved robustness of our reduced method, compared to the standard algorithms used in this research..
2. Simulation case studies confirmed that the reduced method can significantly decrease computational time without loss of accuracy.
3. Because of the significant speed-up, use of the reduced method can allow for a larger number of components to be used in the simulation for improved accuracy of the fluid characterization.

Table 4.1 Fluid properties for oil A (from Li and Johns 2006)

	Mole fraction (Mol %)	*Tc* (°F)	*Pc* (psia)	Acentric factor	*h*	*g*	BIC*		
							CO_2	C_1	*n*-C_{10}
CO_2	5.0	87.90	1069.87	0.225	1.0	1.170	0.000	0.144	0.114
C_1	10.0	−116.59	667.20	0.008	0.3	0.250	0.144	0.000	0.071
C_2	12.0	90.05	708.35	0.098	0.0	0.103	0.120	0.002	0.040
C_3	12.0	205.97	615.76	0.152	0.0	0.103	0.120	0.002	0.040
n-C_4	15.0	305.69	551.10	0.193	0.0	0.103	0.120	0.002	0.040
n-C_5	17.0	385.61	489.38	0.251	0.0	0.103	0.120	0.002	0.040
n-C_{10}	29.0	652.01	305.68	0.490	2.0	0.098	0.114	0.071	0.000

* All others are 0.0.

Table 4.2 Reservoir properties in simulation case studies

Dimensions	1000 ft × 1000 ft × 20 ft
Number of grid cells	20 × 20 × 1
Porosity	0.25
ln-mean permeability	113 mD
Dykstra-Parsons coefficient	0.74
Correlation length	x: 300 ft, y: 300 ft
Reservoir temperature	260ºF
Relative permeability model	Corey
	W / O / G*
Residual saturation	0.25 / 0.20 / 0.05
Endpoint relative permeability	0.21 / 0.70 / 0.35
Exponent	1.5 / 2.5 / 2.5
Initial saturation	0.25 / 0.75 / 0.0

* W: Aqueous phase, O: Oleic phase, G: Gaseous phase

Table 4.3 Fluid properties used in simulation case studies

	Oil (Mol %)	Gas (Mol %)	Molecular weight	*Tc* (°F)	*Pc* (psia)	Acentric factor
CO_2	0.77	1.0	44.01	87.90	1071.60	0.225
C_1	20.25	65.0	16.04	−116.59	667.20	0.008
C_{2-3}	11.80	30.0	38.40	158.88	653.37	0.130
C_{4-6}	14.84	4.0	72.82	379.87	485.94	0.244
C_{7-14}	28.63	0.0	135.82	625.86	315.54	0.600
C_{15-24}	14.90	0.0	257.75	861.15	261.51	0.903
C_{25+}	8.81	0.0	479.95	1202.09	250.31	1.229

	h	*g*	BIC*
			CO_2
CO_2	1	1	0
C_1	0	0.1318	0.1318
C_{2-3}	0	0.1318	0.1318
C_{4-6}	0	0.1318	0.1318
C_{7-15}	0	0.09885	0.09885
C_{16-27}	0	0.09885	0.09885
C_{28+}	0	0.09885	0.09885

* All others are 0.0.

Table 4.4 Breakdown of computational time for immiscible case

		10 components		
		(RSA, RF)	(CSA, MG)	(CSA, FK)
Overall simulation (sec)		123.6	152.6	164.6
Phase equilibrium (sec)		47.5	77.3	87.7
Stability analysis (sec)	SS	12.2	12.8	12.1
	Newton	4.8	5.2	5.0
Flash calculations (sec)	SS	9.5	9.7	9.3
	Newton	21.1	49.7	61.3

		20 components		
		(RSA, RF)	(CSA, MG)	(CSA, FK)
Overall simulation (sec)		296.0	435.7	612.7
Phase equilibrium (sec)		96.6	236.3	406.0
Stability analysis (sec)	SS	28.5	27.0	30.0
	Newton	8.2	22.7	22.9
Flash calculations (sec)	SS	21.3	22.0	21.3
	Newton	38.6	164.5	331.9

Table 4.5   Breakdown of computational time for multicontact miscible case

		10 components		
		(RSA, RF)	(CSA, MG)	(CSA, FK)
Overall simulation (sec)		1010.8	1164.2	1214.1
Phase equilibrium (sec)		498.6	645.9	690.3
Stability analysis (sec)	SS	292.6	292.9	295.0
	Newton	58.2	65.4	64.2
Flash calculations (sec)	SS	32.9	34.3	34.2
	Newton	114.9	253.2	296.9

		20 components		
		(RSA, RF)	(CSA, MG)	(CSA, FK)
Overall simulation (sec)		2352.2	3186.3	3926.5
Phase equilibrium (sec)		1051.1	1867.4	2588.6
Stability analysis (sec)	SS	664.9	678.5	670.8
	Newton	105.5	281.0	278.8
Flash calculations (sec)	SS	74.7	77.1	73.0
	Newton	205.9	830.8	1566.0

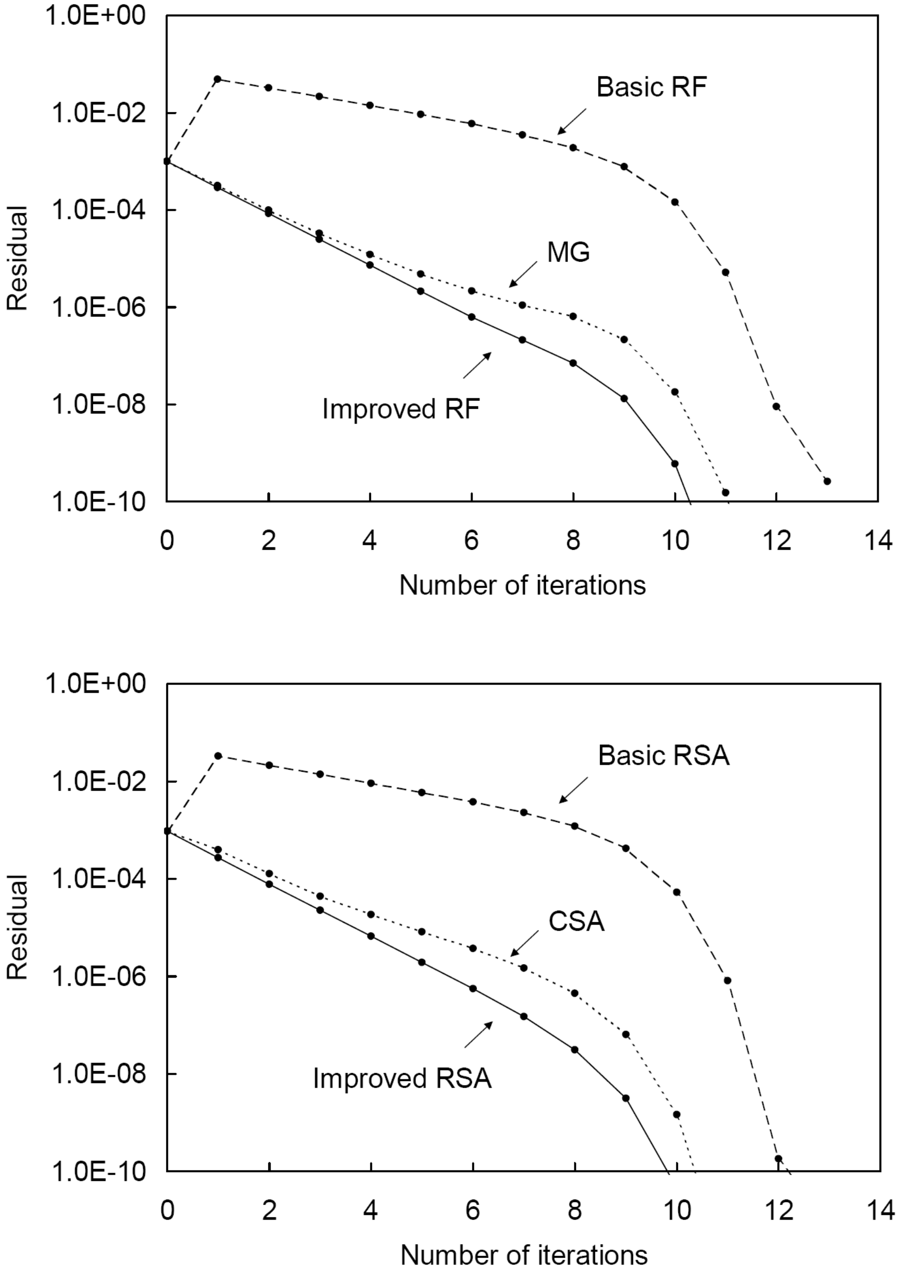

Figure 4.1 Comparisons of the convergence behaviors of different algorithms for a near-critical mixture. Top: Flash calculations. Bottom: Stability analysis.

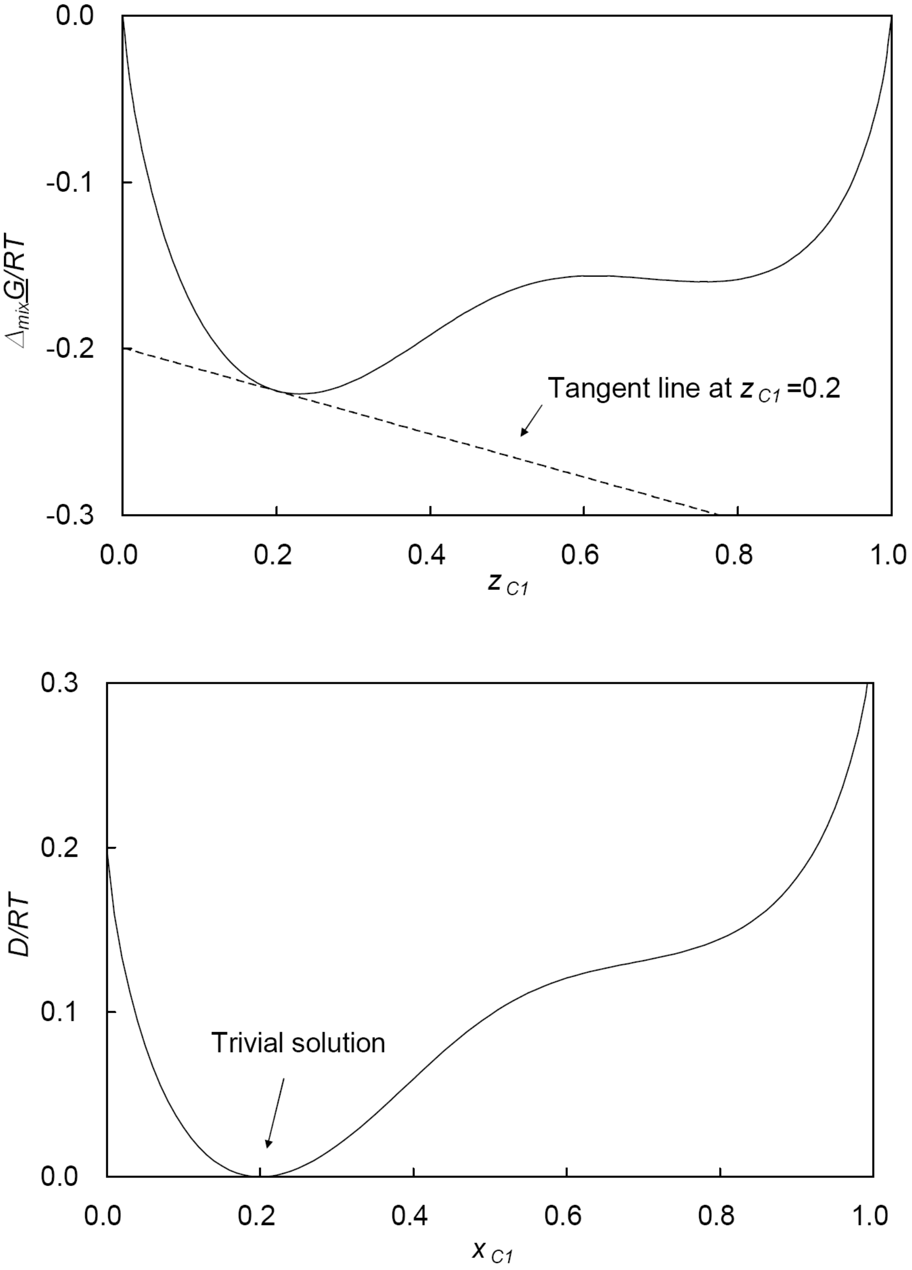

Figure 4.2 Construction of the TPD function for a mixture of 20% C_1 and 80% n-C_{20} at 800˚F and 690 psia. Top: The dimensionless molar Gibbs free energy of mixing. Bottom: The dimensionless TPD function.

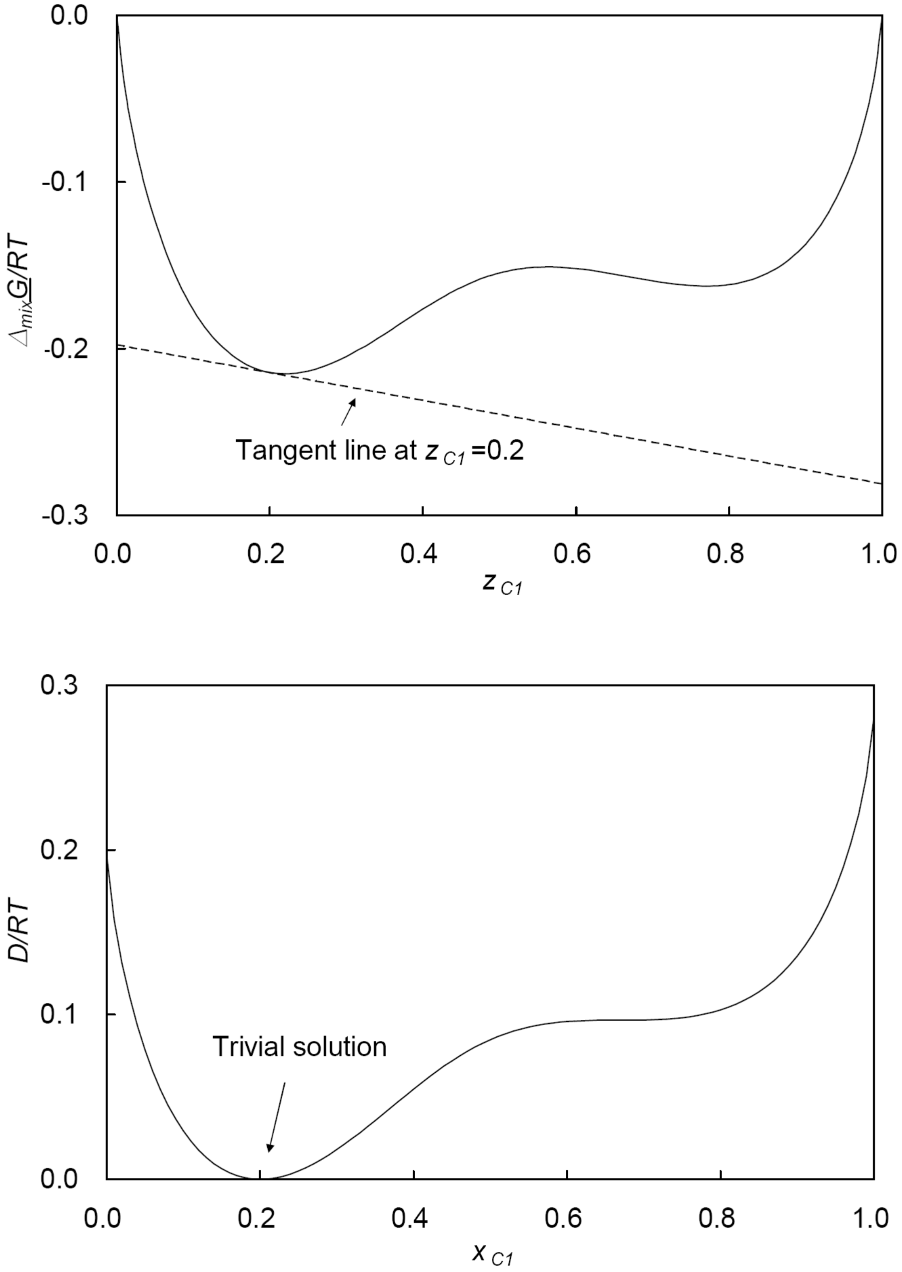

Figure 4.3 Construction of the TPD function for a mixture of 20% C_1 and 80% *n*-C_{20} at 800˚F and 633 psia. Top: The dimensionless molar Gibbs free energy of mixing. Bottom: The dimensionless TPD function.

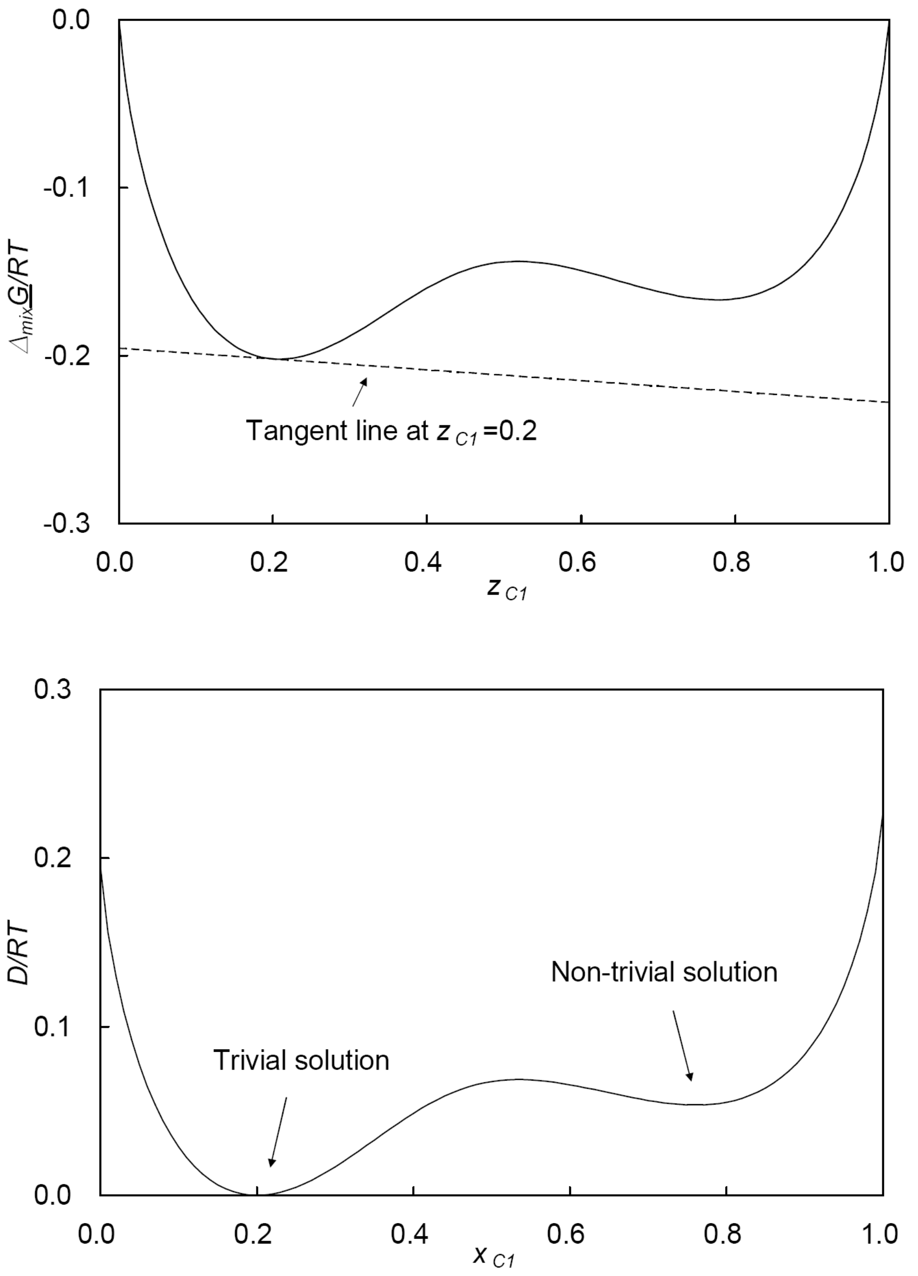

Figure 4.4 Construction of the TPD function for a mixture of 20% C_1 and 80% n-C_{20} at 800˚F and 575 psia. Top: The dimensionless molar Gibbs free energy of mixing. Bottom: The dimensionless TPD function.

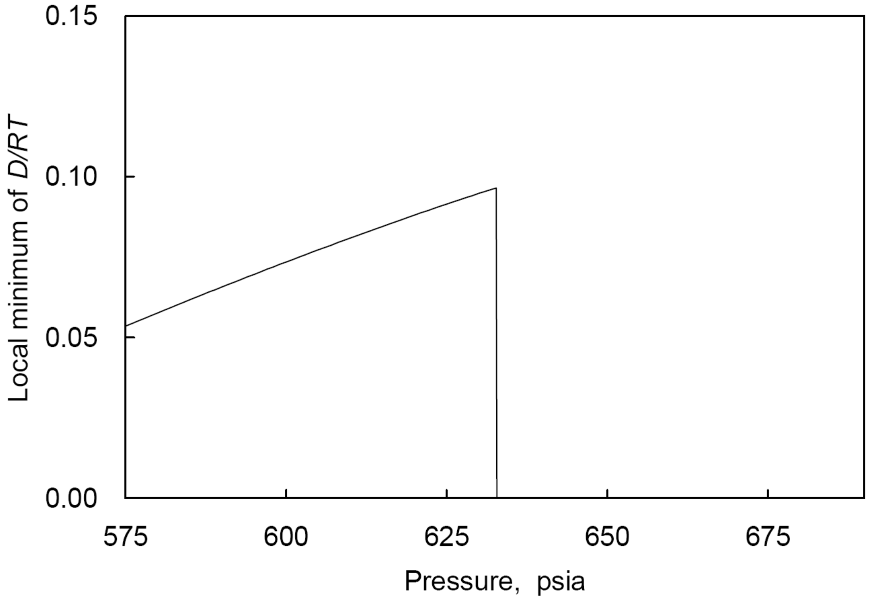

Figure 4.5 Local minimum of D/RT for a mixture of 20% C_1 and 80% n-C_{20} at 800˚F converged by starting with a vapor-like initial estimate. There is a discontinuity at 632.7 psia corresponding to the outer boundary of the "shadow-phase region".

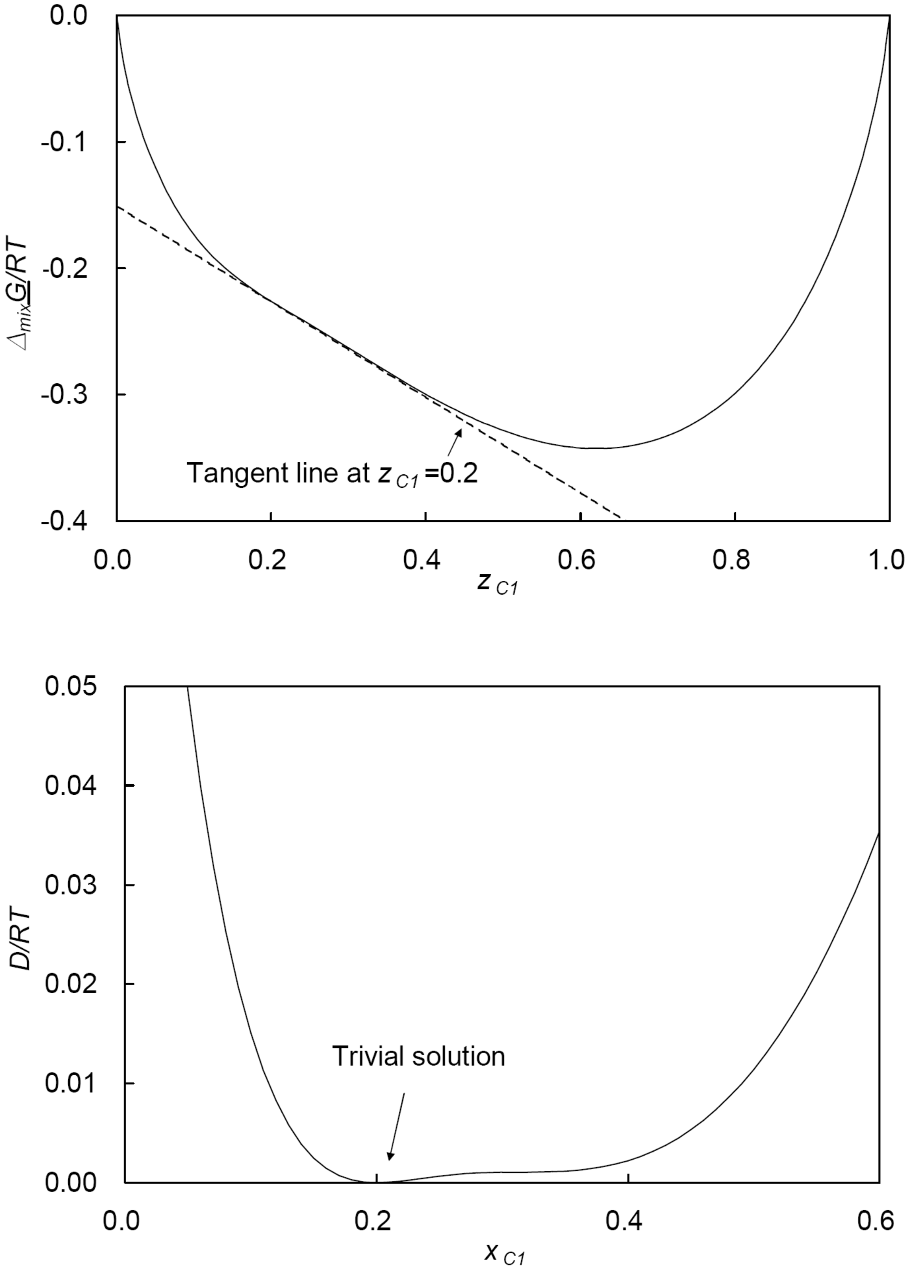

Figure 4.6 Construction of the TPD function for a mixture of 20% C_1 and 80% n-C_{20} at 900˚F and 377 psia. Top: The dimensionless molar Gibbs free energy of mixing. Bottom: The dimensionless TPD function.

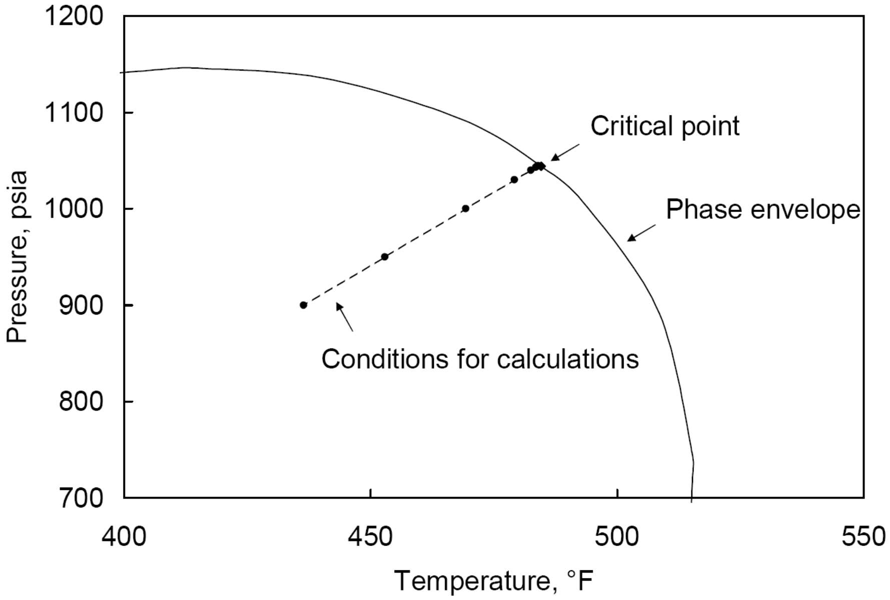

Figure 4.7 *P-T* diagram of oil A showing the conditions used in the comparisons.

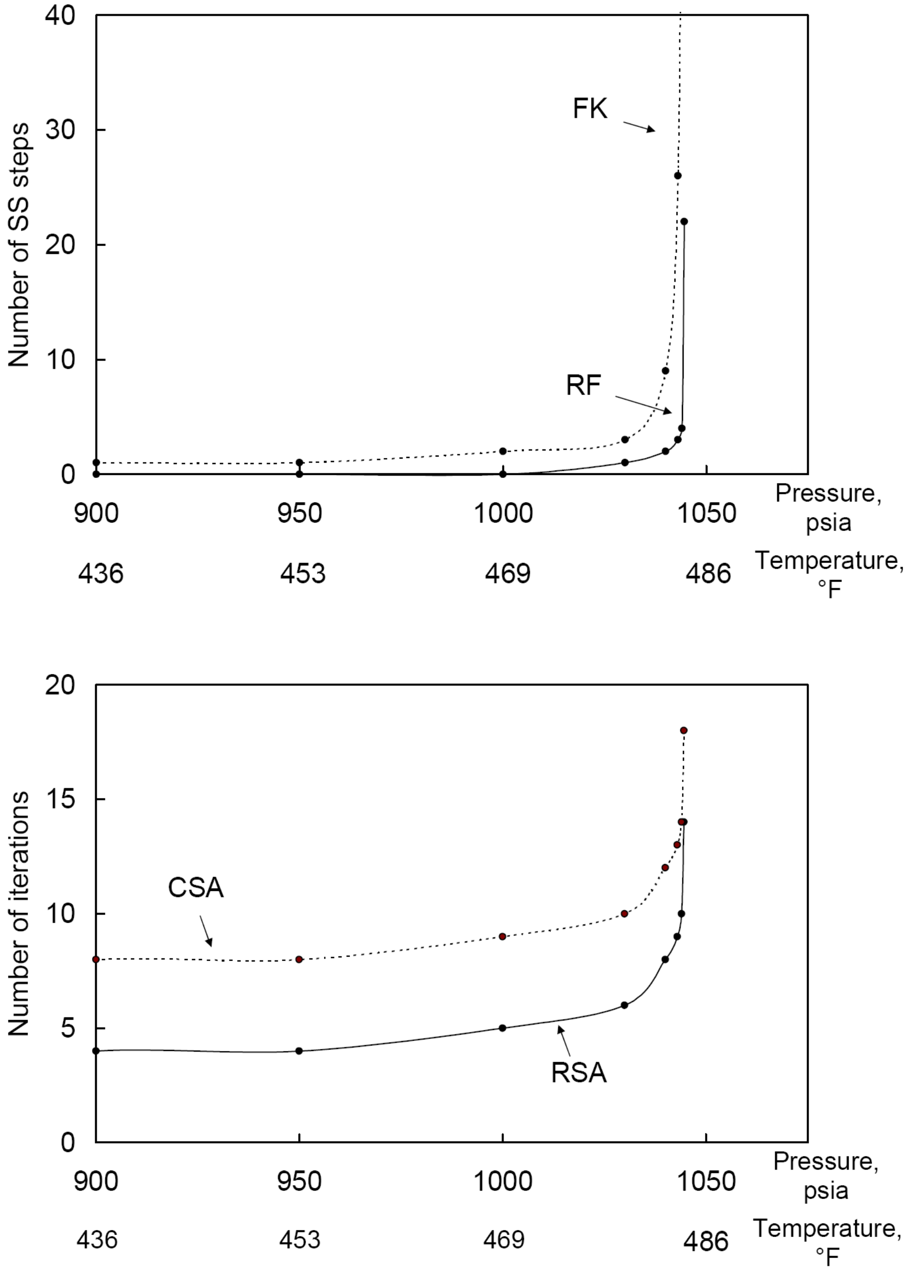

Figure 4.8 Top: The number of SS steps required for the second-order flash algorithms to converge. Bottom: The number of iterations taken by different second-order algorithms for stability analysis.

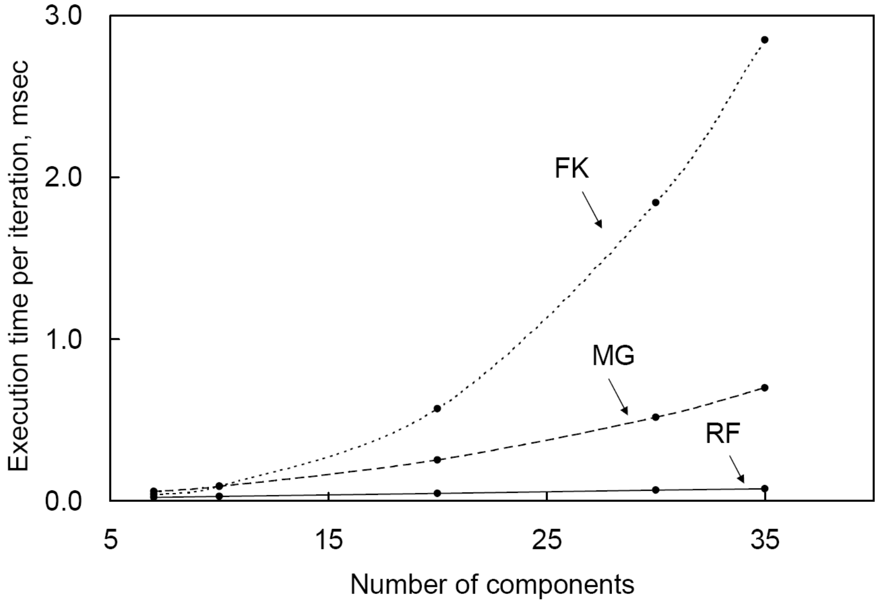

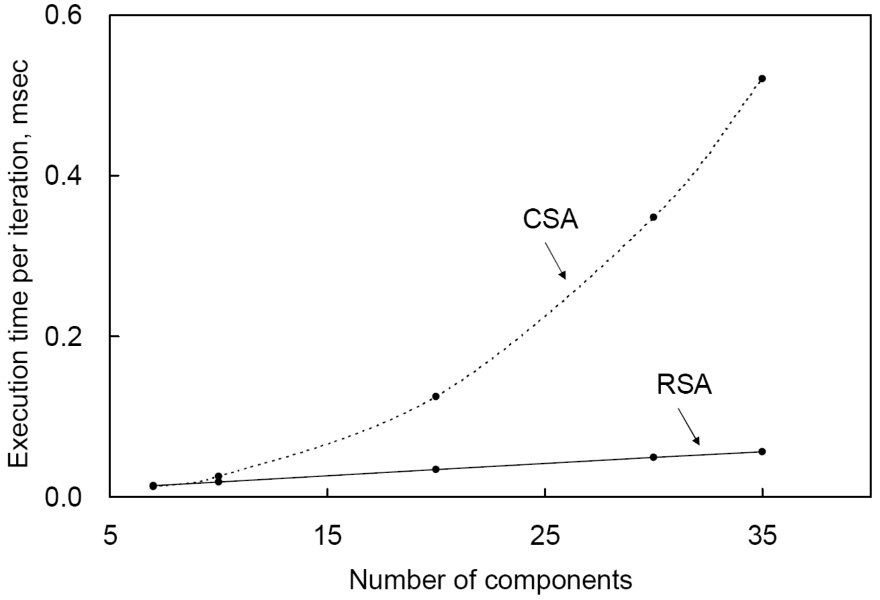

Figure 4.9 Execution time per iteration with different algorithms. Top: Flash calculations. Bottom: Stability analysis.

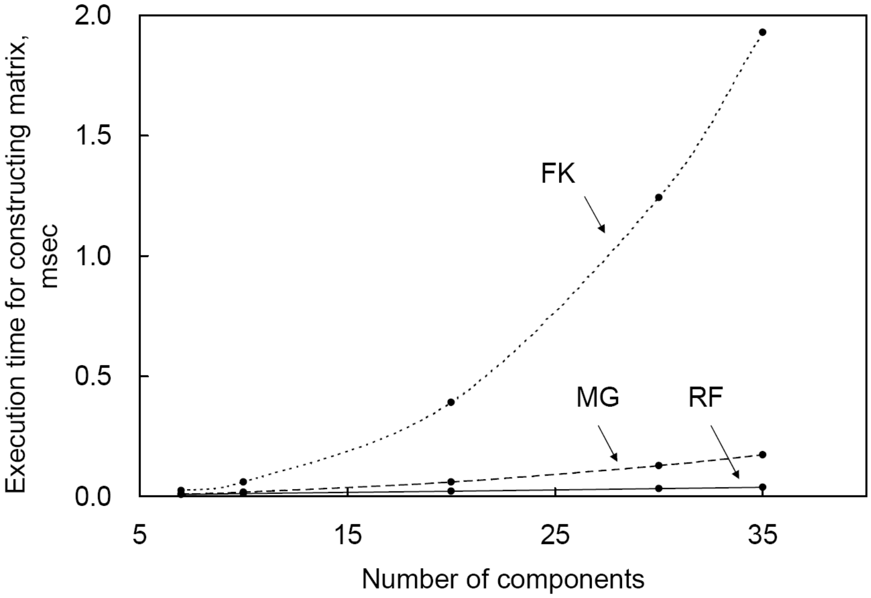

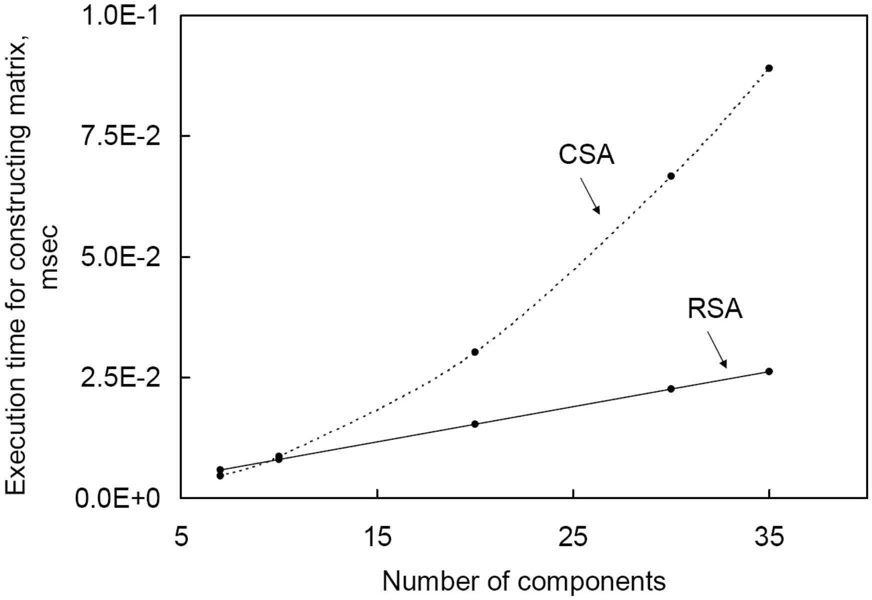

Figure 4.10 Execution time for constructing matrices with different algorithms. Top: Flash calculations. Bottom: Stability analysis.

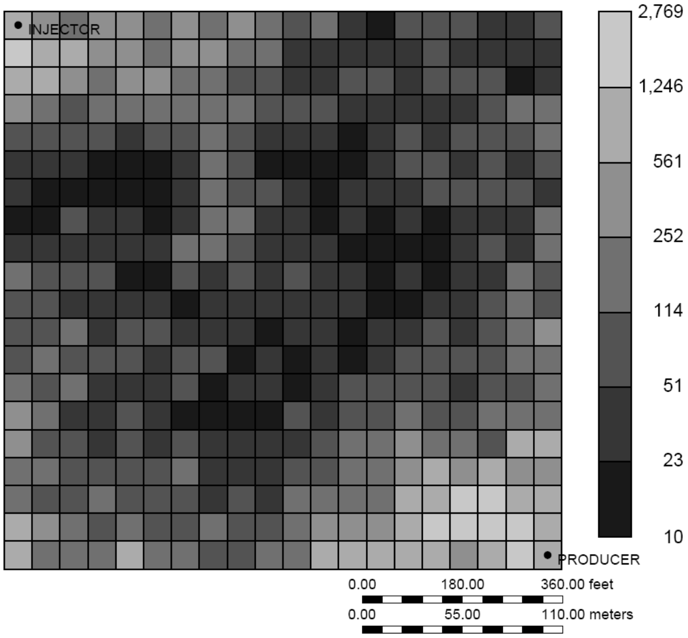

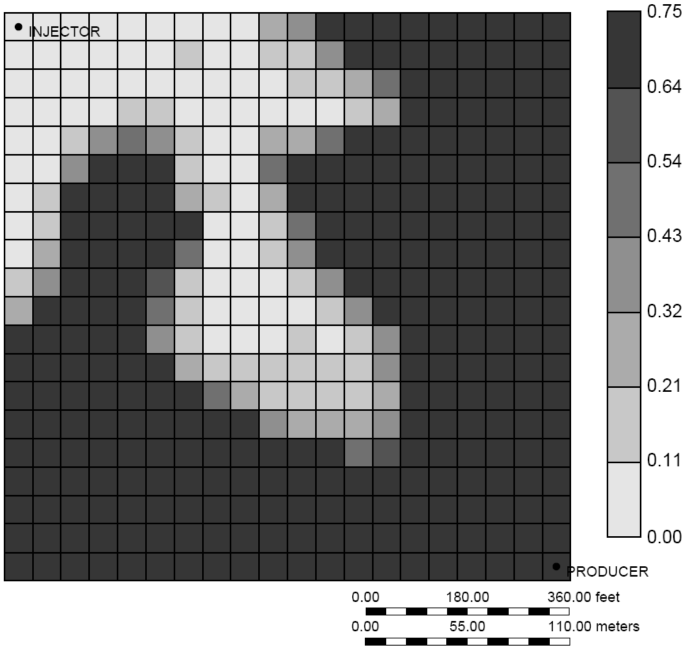

Figure 4.11 Top: Randomly generated permeability field in mD. Bottom: Oil saturation distribution at 0.25 PV for the immiscible case.

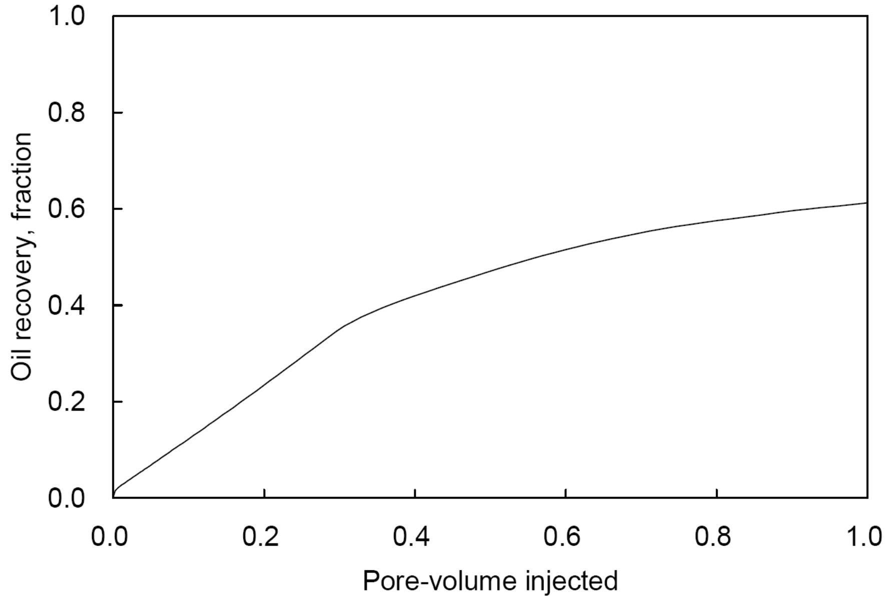

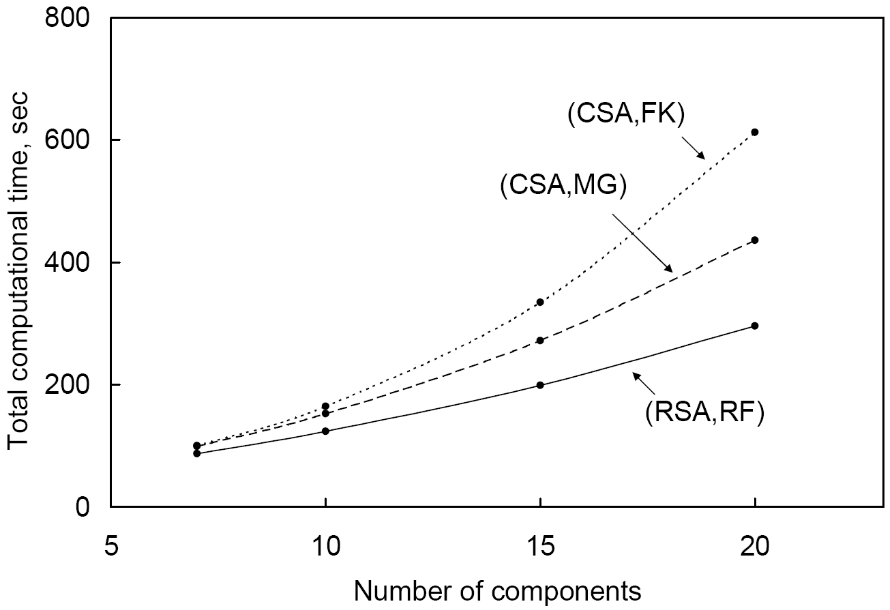

Figure 4.12 Comparisons for the immiscible case. Top: Oil recovery is identical for all algorithms. Bottom: Total computational time vs. N_C for the different combinations of flash and stability algorithms.

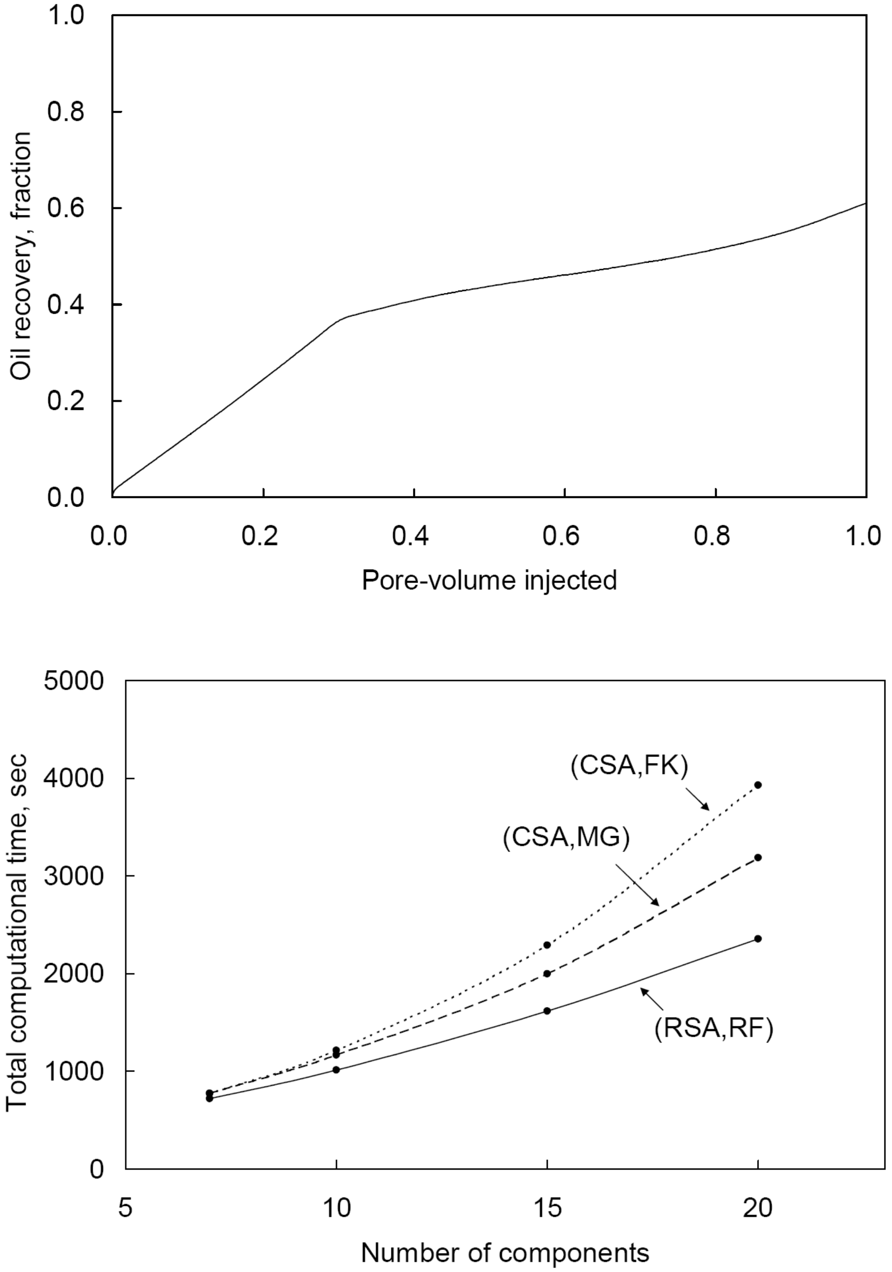

Figure 4.13 Comparisons for the multicontact miscible case. Top: Oil recovery is identical for all algorithms. Bottom: Total computational time vs. N_C for the different combinations of flash and stability algorithms.

5. Three-Phase Flash Using a Reduced Method

CO_2 flooding at low temperatures often results in three or more hydrocarbon-phases, including a CO_2-rich liquid phase and asphaltene precipitation. Multiphase compositional simulation must accurately simulate such gas floods, although most simulators do not consider more than two hydrocarbon-phases. Typical reasons for not modeling three or more hydrocarbon-phases are the increased computational time and robustness associated with flash calculations. Use of a reduced method is a potential solution to these problems.

Because of the drawbacks of three-hydrocarbon-phase reservoir simulation, several approximation procedures for complex three-phase behavior have been proposed in the literature. In this chapter, we demonstrate the importance of using three-phase flash calculations in compositional simulation by investigating difficulties with those approximations. We then extend our algorithm developed in Chapter 4 for reduced two-phase flash calculations to three-phase calculations. The algorithm is compared to a standard algorithm in terms of efficiency and robustness in stand-alone calculations. Last, we implement the algorithm in the UTCOMP simulator, and give simulation case studies that demonstrate conclusively the increased efficiency and robustness of our reduced method.

5.1 IMPORTANCE OF THREE-PHASE FLASH IN COMPOSITIONAL SIMULATION

In this section, we demonstrate the importance of three-phase equilibrium calculations in compositional simulation. We investigate difficulties with several procedures for two-phase equilibrium approximations that have been proposed in the literature to avoid performing three-phase calculations.

5.1.1 Use of Two-Phase Flash in a Three-Phase Region

Nghiem and Li (1986) proposed to use two-phase equilibrium calculations to approximate complex reservoir simulations where three hydrocarbon-phases can coexist. There are multiple solutions for a two-phase flash calculation in a three-phase region. For oleic (L_1), solvent-rich liquid (L_2), and gaseous (V) phases, a simple combinatorial analysis leads to three possible combinations; L_1-L_2, L_1-V, and L_2-V. However, the possibility of converging to L_2-V is small because L_2-V equilibrium occurs within a small region at very high solvent mole fractions on a pseudo-binary pressure-composition (P-x) diagram for oil and solvent. For example, L_2-V equilibrium occurs for solvent mole fractions greater than 0.99 on the P-x diagram studied by Turek *et al.* (1988). Therefore, a two-phase solution is likely L_1-L_2 or L_1-V.

Which of the two possible solutions is obtained by a two-phase flash calculation in the three-phase region depends on the overall composition. To see this, we consider a ternary mixture consisting of CO_2, C_1, and n-C_{20}. The properties of the ternary mixture are shown in Table 5.1. Figure 5.1 shows the tie-triangle at 40°F and 1000 psia calculated by using the Peng-Robinson EOS (Peng and Robinson 1976a). The three vertices represent fixed equilibrium compositions of the gaseous (V), oleic (L_1), and CO_2-rich liquid (L_2) phases. A false two-phase solution depends on the overall composition within the tie-triangle because there is one degree of freedom after temperature and pressure are specified.

We now perform a series of two-phase flash calculations with varying overall composition from point A (0.655, 0.219) to point C (0.737, 0.135) as shown in Figure 5.2. The tie-line found by two-phase flash calculations at point A must result in the L_1-V phases since it lies on the boundary of the tie-triangle. For the same reason, the two-phase flash at point C must result in L_1-L_2 phases. Considering the shape of the Gibbs free energy function for a three-phase mixture, for flash calculations from A to C, there must be a composition that discontinuously changes from the L_1-V tie-line to the L_1-L_2 tie-line. This is given by point B in Figure 5.2, where both intensive and extensive properties of the phases discontinuously change. For example, compressibility factors and phase mole fractions for the two phases are shown in Figure 5.3. The compressibility factor of the gaseous phase exhibits a significant change from 0.474 to 0.208.

To see the effect of the discontinuity on reservoir simulation, we calculate the saturation of phase j as $S_j = \beta_j Z_j / \sum_i \beta_i Z_i$, where $i = 1,\dots,N_P$ and β_j and Z_j are the phase mole fraction and compressibility factor of phase j, respectively. The variation of the oleic phase saturation for the fictitious two-phase system is shown in Figure 5.4. The oleic phase saturation discontinuously varies from 0.55 to 0.70. Oscillations in physical properties caused by the discontinuous changes of flash calculation solutions were observed by Khan *et al.* (1992) and Mohanty *et al.* (1995) in their simulations using only two-phase equilibrium calculations in the three-phase region. The discontinuity also causes substantial reductions in time-step sizes, and often stops the simulation from proceeding as shown in Figure 5.5.

Nghiem and Li (1986) attempted to select L_1-L_2 solutions during their simulations in the three-phase region by using initial estimates for K-values between the L_1 and L_2 phases from the previous time-step. However, if the overall composition is located between point A and a point (0.696, 0.177) near point B, the two-phase flash calculation converges to the L_1-V solution even if the K-values between L_1 and L_2 are provided as the initial estimate. That is, their procedure does not guarantee avoidance of this discontinuity.

The numerical behavior of two-phase flash calculations in a three-phase region presented above can explain the observations of Khan (1992) and Wang and Strycker (2000), who reported non-convergence of simulations with two-phase equilibrium calculations in the three-phase region. Two-phase flash calculations in a three-phase region can be also performed as a preconditioning step for three-phase flash calculations. However, stability analysis can provide a good initial estimate for subsequent three-phase flash calculations.

5.1.2 Two-Phase EOS Representation of Three-Phase Behavior

Fong *et al.* (1992) presented fluid characterization procedures for a two-phase EOS model that can be used in reservoir simulation to approximate three-phase behavior of mixtures of CO_2 and low-temperature reservoir oil. Their fluid characterization approach attempts to eliminate the three-phase region on the *P-x* diagram for the oil and CO_2. Their motivation was that the approximation could avoid long computational time spent in phase equilibrium calculations, convergence problems associated with three-phase flash calculations, and use of a four-phase relative permeability model (where one aqueous and three hydrocarbon phases are included).

They compared two characterization procedures, which are different only in what portion of the *P-x* diagram is matched by tuning binary interaction coefficients (BICs) of CO_2 to experimental data. Their first procedure A is to match the boundary between L_1-V and L_1 at low CO_2 mole fractions. Their second procedure B is to match the boundary between L_1-V and L_1 at high CO_2 mole fractions for a two-phase representation with the upper boundary of the L_1-L_2-V region. Procedure B eliminates not only the L_1-L_2-V region, but also the L_1-L_2 region. Based on the comparisons between procedures A and B and slim-tube data, they concluded that procedure B is superior to A for approximating three-hydrocarbon-phase simulation. However, their procedure, although novel, has little theoretical basis, and may provide inaccurate simulation results, such as sweep efficiency, fluid injectivity, and phase properties. For example, the recovery curves from their slim-tube simulations with the North Ward Estes oil using procedures A and B did not exhibit the sharp bend at breakthrough as observed in the slim-tube test.

We demonstrate the use of their characterization procedures by considering one-dimensional displacement of the North Ward Estes (NWE) oil with impure CO_2, for which the component properties are taken from Khan *et al.* (1992) as shown in Table 5.2. Figure 5.6 shows the predicted *P*-*x* diagram at the reservoir temperature of 83°F and the three-phase region on the pressure-temperature (*P*-*T*) diagram at several oil and gas mixtures. In the *P*-*x* diagram, a L_1-L_2-V region exists between 1050 and 1350 psia at solvent mole fractions greater than 0.65. The critical point of the injection gas is 81°F and 1115 psia, and there is no phase boundary at the reservoir temperature of 83°F for the injection gas, *i.e.*, at the solvent mole fraction of 1.0 in the *P*-*x* diagram. The *P*-*T* diagram shows that the maximum temperature for existence of the three-phase region is 93°F at a solvent mole fraction of 0.90.

Starting with the original fluid characterization shown in Table 5.2, we obtain the following BICs of CO_2 by using procedure A: 0.2 for CO_2-C_1, CO_2-$C_{2\text{-}3}$, CO_2-$C_{4\text{-}6}$, and CO_2-$C_{7\text{-}16}$ and 0.0 for CO_2-$C_{17\text{-}29}$ and CO_2-C_{30+}. The *P*-*x* diagram at 83°F using procedure A is compared with the original in Figure 5.7. The boundary between L_1-V and L_1 at low solvent mole fractions is almost identical with the original. Figure 5.7 also shows the three-phase region on the *P*-*T* diagram at different solvent mole fractions. Because the three-phase envelopes do not intersect the reservoir temperature of 83°F, there are no three-phase regions in the *P*-*x* diagram at 83°F. Changes in BICs of CO_2 affect little the phase behavior predictions of oil because CO_2 mole fraction is small in the oil. For example, Figure 5.8 shows that the *P-T* diagram from the original characterization coincides with that from procedure A.

Reservoir properties for the one-dimensional simulation are shown in Table 5.3. An injector at the first cell is operated at a constant injection rate of 750 SCF/D, and a producer at the last cell produces at a constant bottom-hole pressure of 900 psia. The total variation diminishing higher-order scheme of Liu *et al.* (1994) in UTCOMP is used to control numerical dispersion in our simulations.

Figure 5.9 shows the recoveries using the original fluid characterization of Khan *et al.* (1992) and procedure A. The former is 27% higher than the latter after 2.0 HCPVI. That is, displacement efficiency can be significantly underestimated when procedure A is used. Also, procedure A does not necessarily avoid the three-phase calculations as was originally assumed by Fong *et al.* (1992). When we allow for three-phase equilibrium calculations in the simulation with procedure A, three hydrocarbon-phases exist over a few consecutive grid cells near the displacement front during the simulation. This is because procedure A attempts to eliminate a three-phase region only on a *P-x* diagram, which represents phase behavior along the mixing line between the oil and injection gas, instead of the actual composition path observed during the displacement. This is consistent with Henry and Metcalfe (1983) and Creek and Sheffield (1993), who observed in their experiments that the dynamic L_1-L_2-V region is larger than one derived from static experiments. As long as three-phase regions exist and only two-phase equilibrium calculations are performed in simulations, convergence problems can stop simulations from proceeding as discussed in the previous section, even though convergence problems do not occur in this particular case. Therefore, procedure A leads to either a complete failure of simulation or erroneous simulation results.

We now consider procedure B by starting with the original characterization in Table 5.2. We could not, however, achieve a good match using procedure B. Although Fong *et al.* (1992) were able to apply the procedure starting with a different fluid characterization, there are no EOS parameters presented in their paper. Procedure B likely cannot be applied in some situations because, as described below, it requires a significant deviation from the original characterization for three-phase behavior.

Figure 5.10 shows projections of the *P*-*T*-*x* diagram onto *P*-*T* and *T*-*x* diagrams for the pseudo-binary mixture of the NWE oil and injection gas calculated by the PVTsim software of Calsep. On the *P*-*T* diagram, the binodal curve for 100% oil is shown, but that for 100% gas is not shown for clarity. On the *T*-*x* diagram, the critical locus up to 22938 psia at a solvent mole fraction of 0.85 is shown. This type of phase behavior in Figure 5.10 is analogous to that for binary systems CO_2+*n*-alkane from *n*-C_{14} through *n*-C_{21} in that L_1-L_2-V equilibrium exists and the critical locus of L=V critical points gradually changes its behavior to L_1=L_2 (*e.g.*, Alwani and Schneider 1976, Miller and Luks 1989).

Procedure B attempts to obtain phase behavior similar to binary systems CO_2+*n*-alkane from C_1 through *n*-C_6, which exhibit a continuous L=V critical locus between two critical points for the pure components with neither L_1-L_2-V nor L_1-L_2 equilibrium. The former type of phase behavior is categorized as type III and the latter as type I according to van Konynenburg and Scott (1980), who introduced the classification of fluid phase behavior for binary mixtures based on the van der Waals EOS. The difference between the phase behavior types for CO_2-*n*-alkane binary systems comes from the difference in the carbon number or chain length of the *n*-alkane molecule. Considering that the NWE oil contains a large amount of components with much larger carbon numbers than *n*-C_6, procedure B should be difficult to apply to the NWE oil.

5.2 REDUCED METHOD FOR THREE-PHASE FLASH CALCULATIONS

Three-phase equilibrium calculations are important in simulation of low-temperature gas floods. However, the computational time required and robustness of the calculations have led several authors to make two-phase equilibrium approximations. The use of a reduced method is a potential practical solution. For miscible gas simulations involving only L-V equilibrium, Chapter 4 demonstrated that a reduced method gives significant savings in computational time with improved robustness. In this section, we extend the reduced flash algorithm for two phases to three-phase calculations. We use the same stability analysis algorithm as in Chapter 4 since stability analysis is performed only on a single-phase mixture or one of the individual phases of a multiple-phase mixture (Perschke *et al.* 1989).

Reduced parameters used in our method are given in section 4.1.1. We use the formulation for N_P-phase flash calculations using the reduced method presented in section 4.1.2. This section presents an algorithm for the three-phase reduced flash calculations that is different from that for two phases.

The algorithm to solve equations (4.7) for three phases is an extension of the algorithm for two-phase calculations. The reduced flash starts with an initial estimate from the conventional successive substitution (SS). The algorithm is the following:

1. Calculate θ_k^z ($k = 1,...,5$) as defined in equations (4.5).
2. Obtain initial estimates for the $6(N_P - 1)$ independent variables, θ_{kj} and β_j ($k = 1,\ldots,5$ and $j = 1,\ldots,N_P - 1$), based on the solution from SS.
3. Calculate the reduced parameters for the reference phase N_P using equations (4.5).
4. Calculate compressibility factors and fugacity coefficients for the N_P phases using an EOS. When the cubic EOS has multiple roots of the compressibility factor, the

correct root is selected that results in the lowest Gibbs free energy (Evelein *et al.* 1976).

5. If $\max_{ij}\{|F_{ij}|\} < \varepsilon$, then stop. Otherwise, continue to step 6. F_{ij} are given in equations (4.3).
6. Calculate K-values using equations (4.4) based on the fugacity coefficients in step 4.
7. Calculate compositions for the N_P phases using equations (4.6).
8. Calculate the residuals of equations (4.7).
9. Construct the $6(N_P - 1) \times 6(N_P - 1)$ Jacobian matrix analytically (see Appendix B) and solve the system of equations.
10. Update the $6(N_P - 1)$ independent variables θ_{kj} and β_j ($k = 1,\ldots,5$ and $j = 1,\ldots,N_P - 1$).
11. Repeat steps 3, 4, and 6 to obtain a new set of K-values.
12. Solve the multiphase Rachford-Rice equations to obtain phase compositions, x_{ij}, and mole fractions, β_j ($i = 1,\ldots,N_C$ and $j = 1,\ldots,N_P$), using the algorithm given in Chapter 3.
13. Update the independent variables θ_{kj} and β_j ($k = 1,\ldots,5$ and $j = 1,\ldots,N_P - 1$) using equations (4.2).
14. Go to step 3.

The above algorithm updates the independent variables twice during one iteration. The first update is Newton's method, and the second is a SS step (steps 11-13). This additional SS step is also used only for extremely difficult cases for a two-phase flash where overall compositions are very near the binodal curve in the critical region. We recommend that it always be used for three-phase calculations.

The stopping criterion for the above algorithm is based on the fugacity equations, equations (4.3), instead of the reduced flash equations, equations (4.7), because the scale of the residual for equations (4.3) can be significantly different from that of equations

(4.7). The criterion based on the fugacity equations is thermodynamically more fundamental than that based on the reduced flash equations, equations (4.7).

5.3 STAND-ALONE THREE-PHASE FLASH CALCULATIONS

We now demonstrate the efficiency and robustness of the reduced flash algorithm (RF) for three-phase calculations. We compare RF with the method of minimization of the Gibbs free energy (MG) of Michelsen (1982b), which was implemented in UTCOMP by Perschke *et al.* (1989). MG minimizes the Gibbs free energy in terms of $N_C(N_P - 1)$ component mole numbers of the independent phases (see section 2.2.1.1). The algorithm is based on Newton's method with a line-search technique, where the modified Cholesky decomposition algorithm of Gill and Murray (1974) provides a search direction if the Hessian matrix is not positive definite.

Conventional two-phase flash calculations use root-finding of fugacity equations, instead of MG. MG, however, is used for our comparisons for three-phase flash calculations because of robustness and computational efficiency. MG is more robust than root-finding of fugacity equations because MG can ensure that the Gibbs free energy is decreased in each iteration step. In Chapter 4, we showed that MG can take shorter computational time per iteration than root-finding of fugacity equations for two-phase flash calculations using 10 or more components. Michelsen (1982b) recommended using MG for more than two phases, instead of root-finding of fugacity equations.

We consider a flash calculation for a mixture of the Bob Slaughter Block (BSB) oil and impure CO_2. A fluid model was developed by Khan *et al.* (1992) using the Peng-Robinson EOS as shown in Table 5.4, where the parameters h_i and g_i ($i = 1,\ldots,N_C$) for the reduced method are also given. For this example flash calculation, the temperature and pressure are 105°F and 1295 psia. Table 5.5 gives the overall composition, which is a mixture of the oil and injection gas given in Table 5.4.

The calculation starts with stability analysis for a single-phase mixture. After the stability analysis detects an instability, a two-phase flash calculation is performed to obtain an intermediate two-phase solution. Stability analysis is performed again for one of the two phases. The three-phase flash is performed when this stability analysis determines that the intermediate two-phase system is unstable. The stability analysis also provides an initial estimate for the following three-phase flash with the conventional SS. SS is switched to Newton's method for either RF or MG when $\max_{ij}\{|F_{ij}|\} < 10^{-3}$.

This example flash calculation is a difficult case where conditions are close to a critical point. Table 5.5 gives the three-phase solution for this problem. The resulting equilibrium compositions for the oleic and CO_2-rich liquid phases are near each other, indicating that the conditions are in a near-critical region. Figure 5.11 shows the convergence behaviors of RF and MG for this example calculation. MG takes 17 iterations to satisfy the stopping criterion of $\max_{ij}\{|F_{ij}|\} < 10^{-8}$ compared to 10 iterations for RF. The slow convergence of the initial iterations for both algorithms indicates that the switching point from SS is not sufficiently close to the solution to exhibit a second-order convergence rate. This convergence behavior is characteristic of phase equilibrium calculations near a critical point. The simple algorithm for RF exhibits remarkably improved convergence behavior compared to MG, which uses globally convergent techniques like line-search to enhance its convergence.

Total computational time of a flash calculation is determined by the number of iterations multiplied by the computational time per iteration. RF generally takes fewer iterations compared to MG as shown above and in Chapter 4.

We next compare computational time per iteration for RF with that for MG. Computations are performed using a Pentium 4 CPU at 3.0 GHz and 2.0 GB of RAM throughout this research. The computational time per iteration depends on how close the current iteration point is to the solution because both RF and MG contain an inner iteration loop; RF iteratively solves the Rachford-Rice equations, and MG performs line-search in an iterative manner inside the outer iteration loop. Figure 5.12 shows computational time per iteration for RF and MG for different N_C. When more than seven components are used, the heaviest component is split to as many components as needed with the same properties. This is also true for the simulation case studies to be presented later. The top and bottom plots of Figure 5.12 give the time per iteration when switched from SS with a criterion of 10^{-3} and 10^{-7}, respectively. For both cases, RF is faster than MG, and the advantage of RF over MG becomes more significant as N_C is increased. For the former case, the speed-up factor is 2.2 for 10 components and 6.3 for 20 components. For the latter case, the speed-up factor is 2.0 for 10 components and 4.7 for 20 components. Those speed-ups of RF come from the reduced number of equations to be solved. For three phases, the number of equations is always 12 for RF and $2N_C$ for MG.

As long as equations (4.1) hold, the reduced method gives exactly the same calculation results as a conventional method using binary interaction coefficients. This fact does not depend on the number of components used. Tables 5.2 and 5.4 show that the equality holds both for the NWE and BSB oils. That is, the calculation results from RF are the same as those from MG in the example calculations if the algorithms converge to the correct solution.

5.4 SIMULATION CASE STUDIES WITH THE REDUCED METHOD

We implemented and tested our algorithm for the reduced method in various runs with UTCOMP to confirm its robustness and efficiency. Two simulation examples are presented in this section.

UTCOMP is an IMPEC multiphase compositional simulator originally developed by Chang *et al.* (1990). Perschke *et al.* (1989) developed the phase equilibrium algorithms in the original UTCOMP. The multiphase equilibrium calculations in UTCOMP consist of stability analysis and flash calculations, for which a flow chart is given in Appendix A. The algorithms use accelerated successive substitution (ASS) and minimization of the Gibbs free energy for flash calculations, and the stationary point method and minimization of the tangent plane distance function for stability analysis (Michelsen 1982a). All the calculations with the original UTCOMP are performed in conventional N_C space, instead of reduced space. In this research, we replace the ASS with the normal SS to robustly start the second-order convergence method. We also replace the original Rachford-Rice algorithm in UTCOMP with that given in Chapter 3 since our algorithm is guaranteed to converge to the correct solution for any number of phases.

Stability analysis in UTCOMP is based on the procedure of Michelsen (1982a) as implemented by Perschke (1988). *K*-values from the Wilson's correlation (1969) are used to generate two-sided initial phase compositions (*i.e.*, vapor-like and liquid-like compositions) for stability analysis from one to two phases. For stability analysis from two to three phases, four initial estimates are used as is explained in Perschke (1988).

We compare the efficiency and robustness of the reduced method with those of the original code in UTCOMP for simulations with different fluids, numbers of components, and reservoir models. The reduced method uses the algorithms for reduced stability analysis (RSA) and reduced flash calculations (RF) developed in this chapter and Chapter 4. The original UTCOMP uses the conventional stability analysis (CSA) based on the stationary point method and minimization of Gibbs free energy (MG) for flash calculations, both in conventional N_C space. In those calculations, the conventional SS initiates the second-order convergence methods. The switching criteria from SS to the second-order convergence methods are $\max\{|S_i|\} < 10^{-3}$ for stability analysis and $\max_{ij}\{|F_{ij}|\} < 10^{-3}$ for flash calculations, where S_i are the stationarity equations defined in equations (4.8) and F_{ij} are the fugacity equations defined in equations (4.3). The stopping criteria are $\max\{|S_i|\} < 10^{-8}$ for stability analysis and $\max_{ij}\{|F_{ij}|\} < 10^{-8}$ for flash calculations. In addition, CSA and MG use a relative step size criterion, $\max\{|\delta\alpha_i/\alpha_i|\} < 10^{-8}$, where α_i is the i^{th} independent variable and $\delta\alpha_i$ is the updated amount for α_i.

Stability analysis for a single phase mixture is performed in all single-phase grid cells. Flash calculations are only performed for grid cells where phase instability is detected by stability analysis. The Corey model is used for the relative permeability function. The parameters for relative permeability of a solvent-rich liquid phase are assumed to be the same as those of a gaseous phase. An aqueous phase exists at its residual saturation. The total variation diminishing higher-order scheme of Liu *et al.* (1994) is used to control numerical dispersion.

5.4.1 North Ward Estes Oil With an Areal 2-D Reservoir Model

We consider an oil displacement with an injection gas consisting of 5% C_1 and 95% CO_2 for 1.2 HCPVI in a quarter of a staggered-line-drive pattern. The permeability field is stochastically generated for an areal, two-dimensional reservoir model as shown in Figure 5.13. The reservoir oil is the North Ward Estes (NWE) oil for which a fluid model using the Peng-Robinson EOS was developed by Khan *et al.* (1992). The properties of the oil and injection gas are shown in Table 5.2. The MMP with pure CO_2 was experimentally determined to be approximately 937 psia at the reservoir temperature of 83°F (Fong *et al.* 1992). Figure 5.6 shows the *P-x* diagram for the reservoir oil and injection gas at the reservoir temperature predicted by the EOS model. Table 5.6 gives the reservoir properties. The injection well is operated at a constant injection rate of 10^4

SCF/D, while the production well produces at a constant bottom-hole pressure of 930 psia.

Figures 5.14 and 5.15 show saturation distributions and the distribution of the number of hydrocarbon-phases at breakthrough near 0.5 HCPVI. At this time, three hydrocarbon-phases exist in 20% of the total grid cells, so that three-phase equilibrium calculations play an important role in the simulation results. Simulations using (CSA, MG) and (RSA, RF) are almost identical with each other (Figure 5.16). The computational time, however, depends significantly on the algorithm used. Table 5.7 gives a breakdown of the computational times for the 10- and 20-component cases. The computational time with different N_C is plotted in Figure 5.17 for each algorithm. Use of the reduced method results in simulations with shorter computational times than when (CSA, MG) is used for all cases studied here. The advantage of the reduced method against (CSA, MG) becomes more significant as N_C increases. For example, the speed-up of the simulations is 12% for the 10-component case, and 43% for the 20-component case. The speed-up is attributed to the decreased computational time in phase equilibrium calculations with the second-order convergence methods, where the reduced method can exploit the decreased number of equations to be solved (shaded parts in Table 5.7). Figure 5.17 shows that the Newton's iteration with (RSA, RF) is 1.6 times and 3.6 times faster than with (CSA, MG) for the 10- and 20-component cases, respectively.

We also simulate this oil displacement using (CSA, MG) with the fluid characterization from procedure A of Fong *et al.* (1992) described before (see Figure 5.7). Three-phase equilibrium calculations are not performed for this simulation. As expected, simulation results are significantly different from those with three-phase equilibrium representations. Figure 5.16 shows that breakthrough using fluid characterization procedure A occurs much earlier and the oil recovery can be underpredicted by up to 5%. The deviation in recovery for this two-dimensional reservoir simulation is much smaller than that for the one-dimensional reservoir simulation shown in Figure 5.9, indicating that the sweep efficiency is overpredicted using procedure A.

Figure 5.17 compares the computational times of simulations using (CSA, MG) with procedure A, and (RSA, RF) and (CSA, MG) with the three-phase characterization. The computational time for the three-hydrocarbon-phase simulation with (RSA, RF) is 68% longer for 10 components, and 31% longer for 20 components compared to the two-hydrocarbon-phase simulation with (CSA, MG). That is, the speed-up from using procedure A becomes less significant as more components are used in the simulation.

Figure 5.17 also shows that the Newton's iterations for phase equilibrium calculations with (RSA, RF) in the three-hydrocarbon-phase simulation are faster than those with (CSA, MG) in the two-hydrocarbon-phase simulation for more than 10 components. This is a consequence of the reduced number of equations to be solved for (RSA, RF). For example, when more than 12 components are used, two-phase calculations with (CSA, MG) solve more equations than three-phase calculations with (RSA, RF).

5.4.2 Bob Slaughter Block Oil With a 2-D Layered Reservoir Model

We next simulate an oil displacement with injection gas consisting of 5% C_1 and 95% CO_2 for 1.5 HCPVI in a two-dimensional layered reservoir model. The reservoir consists of three layers with different thickness, porosity, and permeability as given in Table 5.8. The production and injection wells are open from the top to the bottom layer. The reservoir oil is the Bob Slaughter Block (BSB) oil (Khan *et al.* 1992), and the properties are shown in Table 5.4. The MMP with pure CO_2 was experimentally determined to be approximately 1200 psia at the reservoir temperature of 105°F (Khan *et* *al.* 1992). The injection well is operated at a constant bottom-hole pressure of 1300 psia, and the production well produces at a constant bottom-hole pressure of 900 psia.

Three hydrocarbon-phases form over a relatively small portion of the reservoir compared to the previous example with the NWE oil. Figures 5.18 and 5.19 show phase saturations and the distribution of the number of phases at 0.4 HCPVI. At this time, three and two hydrocarbon-phases exist in 11% and 36% of the total grid cells, respectively. Simulation results using (CSA, MG) and (RSA, RF) are nearly identical with each other (Figure 5.20). Table 5.9 shows a breakdown of the computational time for the 10- and 20-component cases. As in the previous NWE oil case, the use of (RSA, RF) can significantly decrease the computational time without loss of accuracy. Figure 5.21 compares the computational times with (RSA, RF) and (CSA, MG) for different N_C. For example, the speed-up using (RSA, RF) is 17% and 39% for the 10- and 20-component cases, respectively. The speed-up mainly is attributed to the decreased computational time in the second-order convergence methods (shaded region in Table 5.9). Figure 5.21 compares the computational time spent in the Newton's iteration for the stability and flash calculations. The Newton's iteration with (RSA, RF) is 1.9 times and 4.2 times faster than that with (CSA, MG) for the 10- and 20-component cases, respectively.

Simulation with (RSA, RF) also exhibits significantly improved robustness compared to that with (CSA, MG). MG can fail to converge to a correct solution in the following three cases: 1) the line-search cannot find lower Gibbs free energy; 2) independent phase component mole numbers are updated to be negative; 3) convergence cannot be achieved within a specified number of iterations. RF can fail to converge to a correct solution in the following two cases: 1) it converges to a trivial solution; 2) it cannot converge within a specified number of iterations. RF contains an iterative solution of the Rachford-Rice equations, but our minimization algorithm developed in Chapter 3 guarantees convergence even for more than three phases. Figure 5.22 shows the number of failures with varying N_C for RF and MG. The failure rate of MG is much more sensitive to N_C compared to that of RF. MG can suffer significantly from round-off errors in near-critical regions (Trangenstein 1987). The round-off errors become more severe when more components are used because the independent variables have smaller values. RF also can suffer from round-off errors in near-critical regions, but the results show improved stability of the algorithm.

To see the effect of N_C on the condition number of the Hessian matrix for MG, we consider the mixture of the BSB oil and gas that is at the same conditions as in the example calculation in section 5.3. The condition number of the Hessian matrix for MG is 1.3×10^{10} for seven components, and 1.8×10^{11} for 20 components. The increase in the condition number by one order of magnitude can significantly affect the failure rate of MG because millions of flash calculations are typically performed in near-critical regions for simulation of multicontact miscible gas floods.

The increased failure rate of MG decreases the time-step size for the simulation using UTCOMP, because of discontinuous changes in physical parameters, such as saturation and density. The decreased time-step size in turn increases the frequency of the solution of the pressure equations for the IMPEC scheme. For that reason, the 20-component case solves the pressure equations 163 more times than the 7-component case. Figure 5.23 shows that the number of pressure equation solutions required increases as the failures in three-phase flash calculations increase.

Failures in flash calculations can substantially decrease the time-step sizes as shown in Figure 5.24, where for illustration time-steps are shown over a small portion of the total simulation time. Figure 5.24 also shows that the time-step size is more stable for simulations with (RSA, RF) than for simulations with (CSA, MG) due to the four failures of MG. Those results demonstrate that robustness of phase equilibrium algorithms can affect the efficiency of the simulation not only through phase equilibrium calculations themselves but also through a reduction of the time-step sizes. Also, if stability analysis fails to correctly predict that three hydrocarbon-phases exist, the resulting false two-phase solution could cause a reduction in the time-step sizes (see section 5.1.1). The speed-up as the result of improved time-step sizes would be more significant when more grid cells are used because the system of pressure equations becomes larger and pressure equation solutions are costly.

When a flash calculation fails to converge to the correct solution, UTCOMP in general does not repeat the same calculation using a different algorithm. UTCOMP continues the simulation, but a time-step size is decreased to alleviate a large change in physical properties over the time-step. There is another possible way to handle this. When the primary flash algorithm fails to converge to the correct solution, a simulator can attempt to solve the same flash problem using a more robust, but typically more time-consuming algorithm. For such a simulator, flash failures also directly increase the total computational time of the simulation.

5.5 SUMMARY AND CONCLUSIONS

We investigated the importance of three-phase equilibrium calculations in simulation of low-temperature gas floods. We then developed an efficient and robust algorithm for three-phase flash calculations using a reduced method. The algorithm was implemented in a multiphase compositional simulator UTCOMP to demonstrate the efficiency and robustness in simulations using different fluids, numbers of components, and reservoir models. The results show that

1. The two-phase equilibrium approximations proposed in the literature can lead to a complete failure of simulation or erroneous simulation results when three phases are present.
2. Use of the reduced method can significantly decrease the computational time without loss of accuracy. Simulations with the three-phase reduced method can take less computational time than conventional methods assuming only two phases exist.
3. Compared to the standard algorithms used in this research, the reduced method exhibits improved efficiency and robustness especially when more components are used in the simulation.
4. Based on the simulation case studies using UTCOMP, the robust three-phase flash with the reduced method decreases the computational time not only because of the flash calculations themselves but also because of improved time-step sizes.
5. Because of the significant speed-up, use of the reduced method can allow for more components to be used in the simulation. Using more components in reservoir simulation can improve accuracy of the fluid characterization and reservoir–surface integrated modeling.

Table 5.1 Properties of the ternary mixture

	Mole fraction (Mol %)	*Tc* (°F)	*Pc* (psia)	Acentric factor	BIC*
					CO_2
CO_2	70	87.89	1069.87	0.225	0.00
C_1	20	−116.59	667.20	0.008	0.12
n-C_{20}	10	920.93	161.66	0.907	0.10

* All others are 0.0.

Table 5.2 Fluid properties for simulations for NWE oil (from Khan *et al.* 1992)

	Oil (Mol %)	Gas (Mol %)	Molecular weight	*Tc* (°F)	*Pc* (psia)	Acentric factor
CO_2	0.77	95.0	44.01	87.89	1069.87	0.225
C_1	20.25	5.0	16.04	−116.59	667.20	0.008
$C_{2\text{-}3}$	11.80	0.0	38.40	158.88	653.37	0.130
$C_{4\text{-}6}$	14.84	0.0	72.82	379.87	485.94	0.244
$C_{7\text{-}14}$	28.63	0.0	135.82	625.86	351.54	0.600
$C_{15\text{-}24}$	14.90	0.0	257.75	861.15	261.51	0.903
C_{25+}	8.81	0.0	479.95	1202.09	250.31	1.229

	h	*g*	BIC*
			CO_2
CO_2	1.0	1.00	0.00
C_1	0.0	0.12	0.12
$C_{2\text{-}3}$	0.0	0.12	0.12
$C_{4\text{-}6}$	0.0	0.12	0.12
$C_{7\text{-}14}$	0.0	0.09	0.09
$C_{15\text{-}24}$	0.0	0.09	0.09
C_{25+}	0.0	0.09	0.09

* All others are 0.0.

Table 5.3 Reservoir properties for one-dimensional simulation for NWE oil

Dimensions	500 ft × 5 ft × 10 ft
Number of grid cells	100 × 1 × 1
Porosity	0.15
Permeability	30 mD
Initial pressure	1000 psia
Reservoir temperature	83ºF
Relative permeability model	Corey
	W / L_1 / G / L_2*
Residual saturation	0.40 / 0.20 / 0.05 / 0.05
Endpoint relative permeability	0.35 / 0.50 / 0.65 / 0.65
Exponent	3.0 / 3.0 / 3.0 / 3.0
Initial saturation	0.4 / 0.6 / 0.0 / 0.0

* W: Aqueous phase, L_1: Oleic phase, G: Gaseous phase, L_2: CO_2-rich liquid phase

Table 5.4 Fluid properties for simulations for BSB oil (from Khan *et al.* 1992)

	Oil (Mol %)	Gas (Mol %)	Molecular weight	Tc (°F)	Pc (psia)	Acentric factor
CO_2	3.37	95.0	44.01	87.89	1069.87	0.225
C_1	8.61	5.0	16.04	−171.67	667.20	0.008
C_{2-3}	15.03	0.0	37.20	159.90	652.56	0.131
C_{4-6}	16.71	0.0	69.50	374.13	493.07	0.240
C_{7-15}	33.04	0.0	140.96	630.68	315.44	0.618
C_{16-27}	16.11	0.0	280.99	892.16	239.90	0.957
C_{28+}	7.13	0.0	519.62	1236.79	238.12	1.268

	h	g
CO_2	1.0	1.00
C_1	0.0	0.055
C_{2-3}	0.0	0.055
C_{4-6}	0.0	0.055
C_{7-15}	0.0	0.105
C_{16-27}	0.0	0.105
C_{28+}	0.0	0.105

Table 5.5 Three-phase solution for an example flash calculation for BSB oil

		Overall composition	Oleic phase composition	Gaseous phase composition	CO_2-rich liquid phase composition
Phase mole fractions		-	0.62169	0.17728	0.20103
Component mole fractions					
	CO_2	0.57529	0.53522	0.74337	0.55099
	C_1	0.07305	0.05410	0.15894	0.05592
	C_{2-3}	0.10297	0.10873	0.07527	0.10957
	C_{4-6}	0.09088	0.10614	0.02086	0.10546
	C_{7-15}	0.10509	0.12903	0.00155	0.12236
	C_{16-27}	0.03792	0.04750	6.2515E−06	0.04173
	C_{28+}	0.01480	0.01928	9.0351E−10	0.01399

Table 5.6 Reservoir properties for simulation case study for NWE oil

Dimensions	400 ft × 200 ft × 10 ft
Number of grid cells	30 × 15 × 1
Porosity	0.15
ln-mean permeability	24.5 mD
Dykstra-Parsons coefficient	0.59
Correlation length	x: 200 ft, y: 100 ft, z: 10 ft
Reservoir temperature	83ºF
Initial reservoir pressure	1000 psia
Relative permeability model	Corey
	W / L_1 / G / L_2*
Residual saturation	0.40 / 0.20 / 0.05 / 0.05
Endpoint relative permeability	0.35 / 0.50 / 0.65 / 0.65
Exponent	3.0 / 3.0 / 3.0 / 3.0
Initial saturation	0.4 / 0.6 / 0.0 / 0.0

* W: Aqueous phase, L_1: Oleic phase, G: Gaseous phase, L_2: CO_2-rich liquid phase

Table 5.7 Breakdown of computational time for simulations for NWE oil

		10 components			
		(RSA, RF)		(CSA, MG)	
Overall simulation (sec)		578.5	100%	647.5	100%
Phase equilibrium (sec)		446.5	77%	514.5	79%
Stability analysis (sec)	SS	289.3	50%	291.5	45%
	Newton	54.5	9%	68.3	11%
Flash calculations (sec)	SS	43.5	8%	44.0	7%
	Newton	59.1	10%	110.6	17%

		20 components			
		(RSA, RF)		(CSA, MG)	
Overall simulation (sec)		1322.3	100%	1884.2	100%
Phase equilibrium (sec)		957.5	72%	1505.8	80%
Stability analysis (sec)	SS	663.7	50%	689.1	37%
	Newton	94.1	7%	306.0	16%
Flash calculations (sec)	SS	94.5	7%	97.3	5%
	Newton	105.2	8%	413.3	22%

Table 5.8 Reservoir properties for simulation case study for BSB oil

Dimensions	500 ft × 10 ft × 45 ft
Number of grid cells	50 × 1 × 9
	Top / Middle / Bottom
Thickness (ft)	20.0 / 10.0 / 15.0
Porosity	0.08 / 0.10 / 0.09
Permeability (mD)	7.0 / 11.2 / 9.8
Reservoir temperature	105ºF
Initial reservoir pressure	1100 psia
Relative permeability model	Corey
	W / L_1 / G / L_2*
Residual saturation	0.40 / 0.20 / 0.05 / 0.05
Endpoint relative permeability	0.35 / 0.50 / 0.65 / 0.65
Exponent	3.0 / 3.0 / 3.0 / 3.0
Initial saturation	0.4 / 0.6 / 0.0 / 0.0

* W: Aqueous phase, L_1: Oleic phase, G: Gaseous phase, L_2: CO_2-rich liquid phase

Table 5.9 Breakdown of computational time for simulations for BSB oil

		10 components			
		(RSA, RF)		(CSA, MG)	
Overall simulation (sec)		1225.4	100%	1434.4	100%
Phase equilibrium (sec)		973.9	79%	1175.5	82%
Stability analysis (sec)	SS	553.2	45%	581.7	41%
	Newton	53.5	4%	86.1	6%
Flash calculations (sec)	SS	235.6	19%	240.8	17%
	Newton	131.7	11%	266.9	19%

		20 components			
		(RSA, RF)		(CSA, MG)	
Overall simulation (sec)		2849.9	100%	3967.5	100%
Phase equilibrium (sec)		2133.7	75%	3224.9	81%
Stability analysis (sec)	SS	1282.1	45%	1341.4	34%
	Newton	88.1	3%	378.3	10%
Flash calculations (sec)	SS	529.3	19%	545.3	14%
	Newton	234.1	8%	959.9	24%

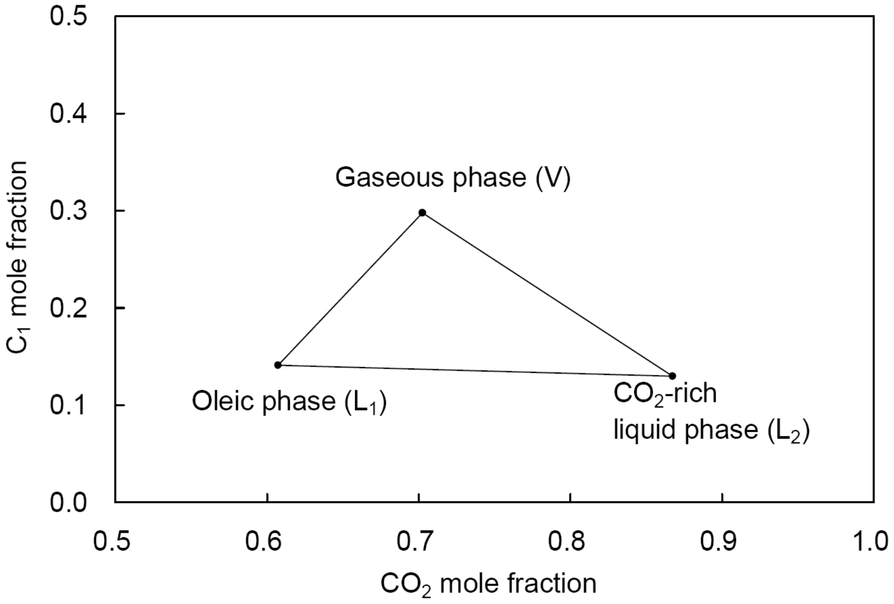

Figure 5.1 Tie-triangle for the ternary mixture given in Table 5.1 at 40°F and 1000 psia using the Peng-Robinson EOS.

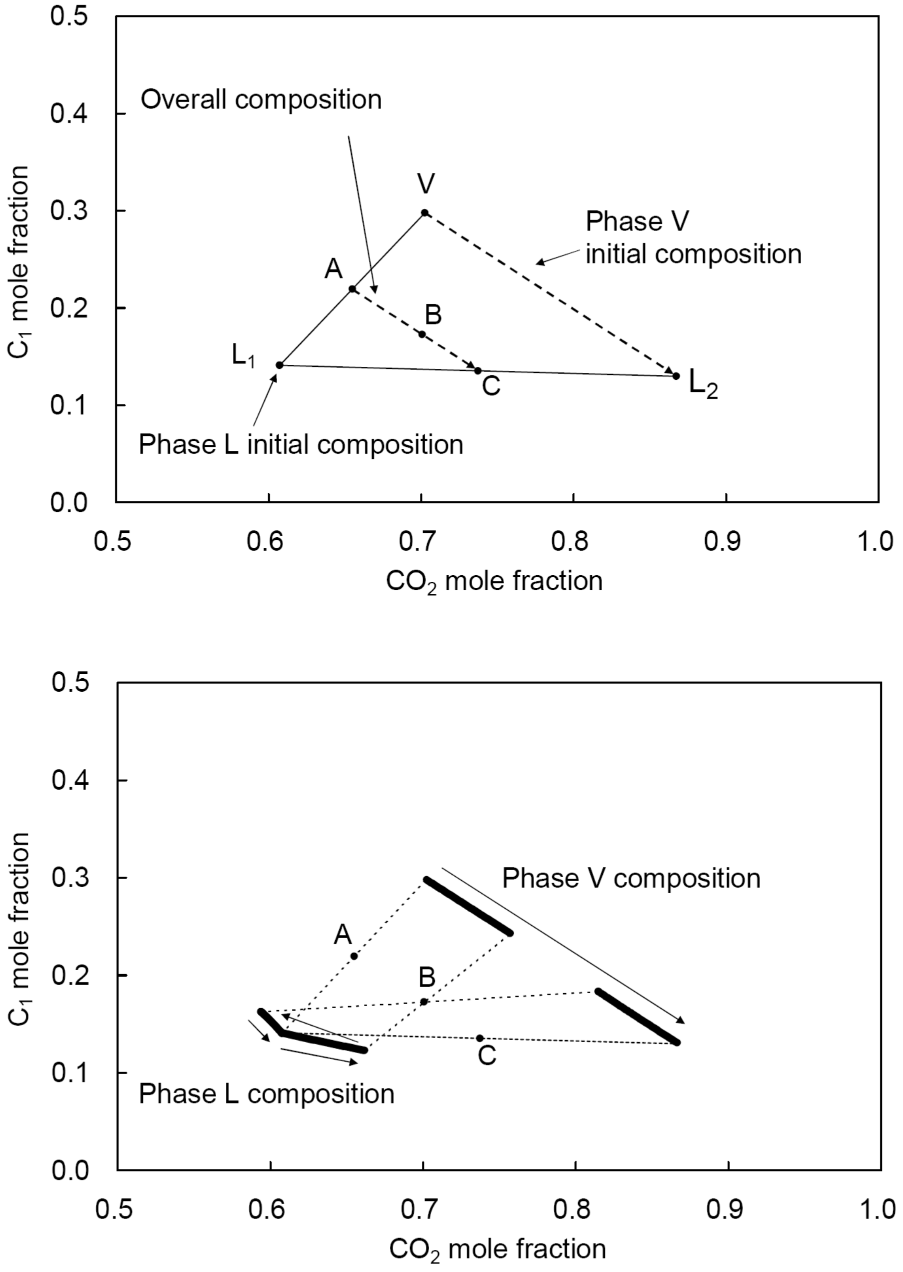

Figure 5.2 Top: Overall compositions and initial estimates for two-phase flash calculations in the three-phase region. Bottom: Resulting two-phase flash calculations in the three-phase region for those overall compositions.

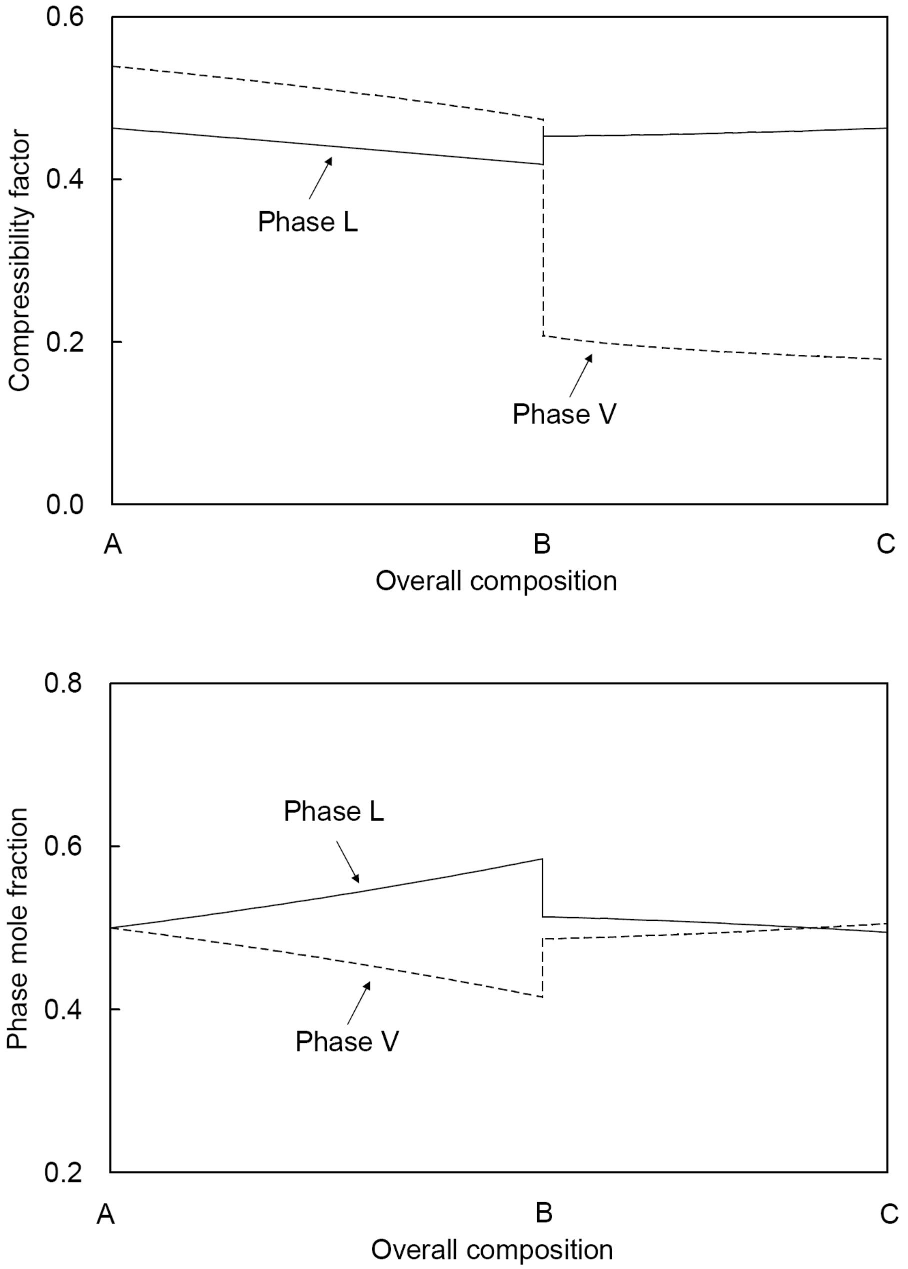

Figure 5.3 Top: Variation of compressibility factors for the two-phase solutions with changing overall composition from composition A to C as shown in Figure 5.1. Bottom: Variation of phase mole fractions for the two-phase solutions with changing overall composition.

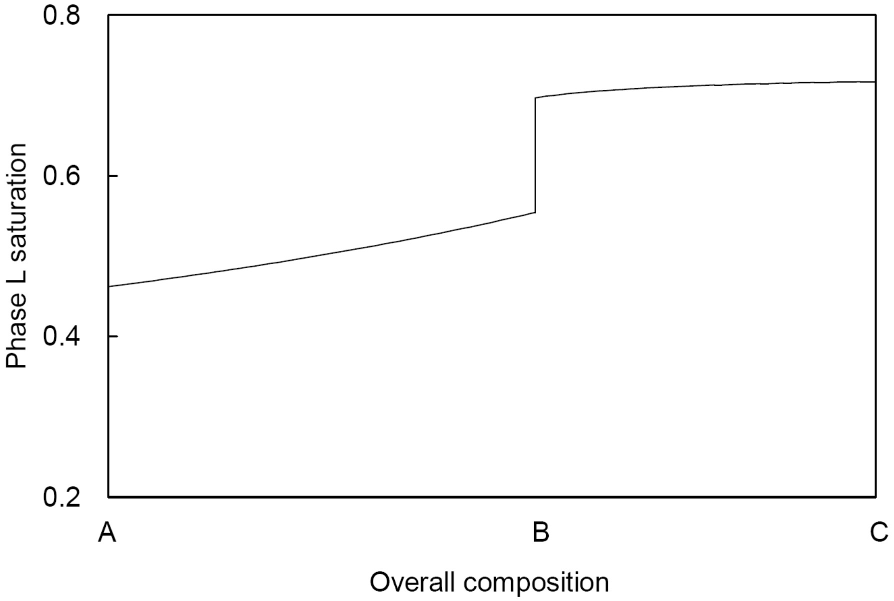

Figure 5.4 Variation of saturation for phase L with changing overall composition assuming two-phase equilibrium.

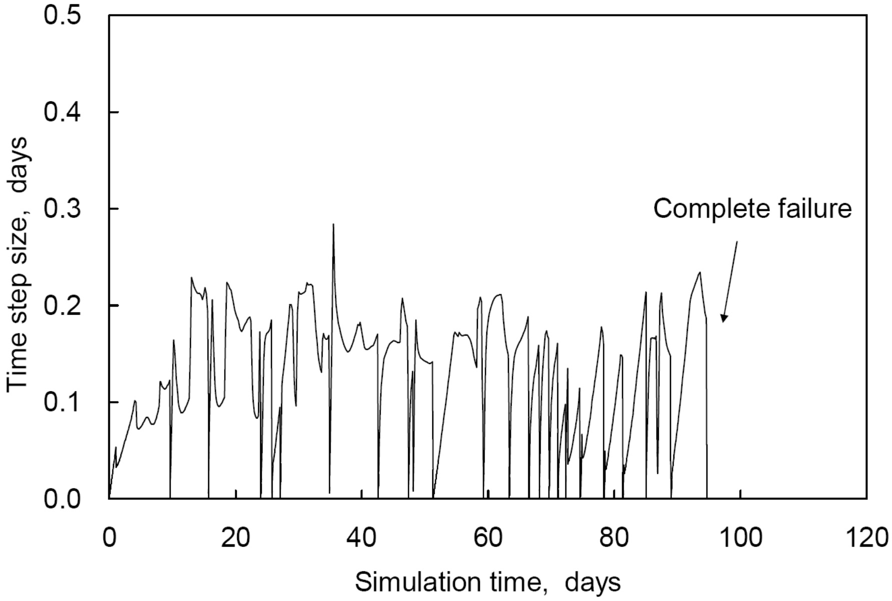

Figure 5.5 Time-step size behavior during a simulation using only two-phase flash calculations in the three-phase region.

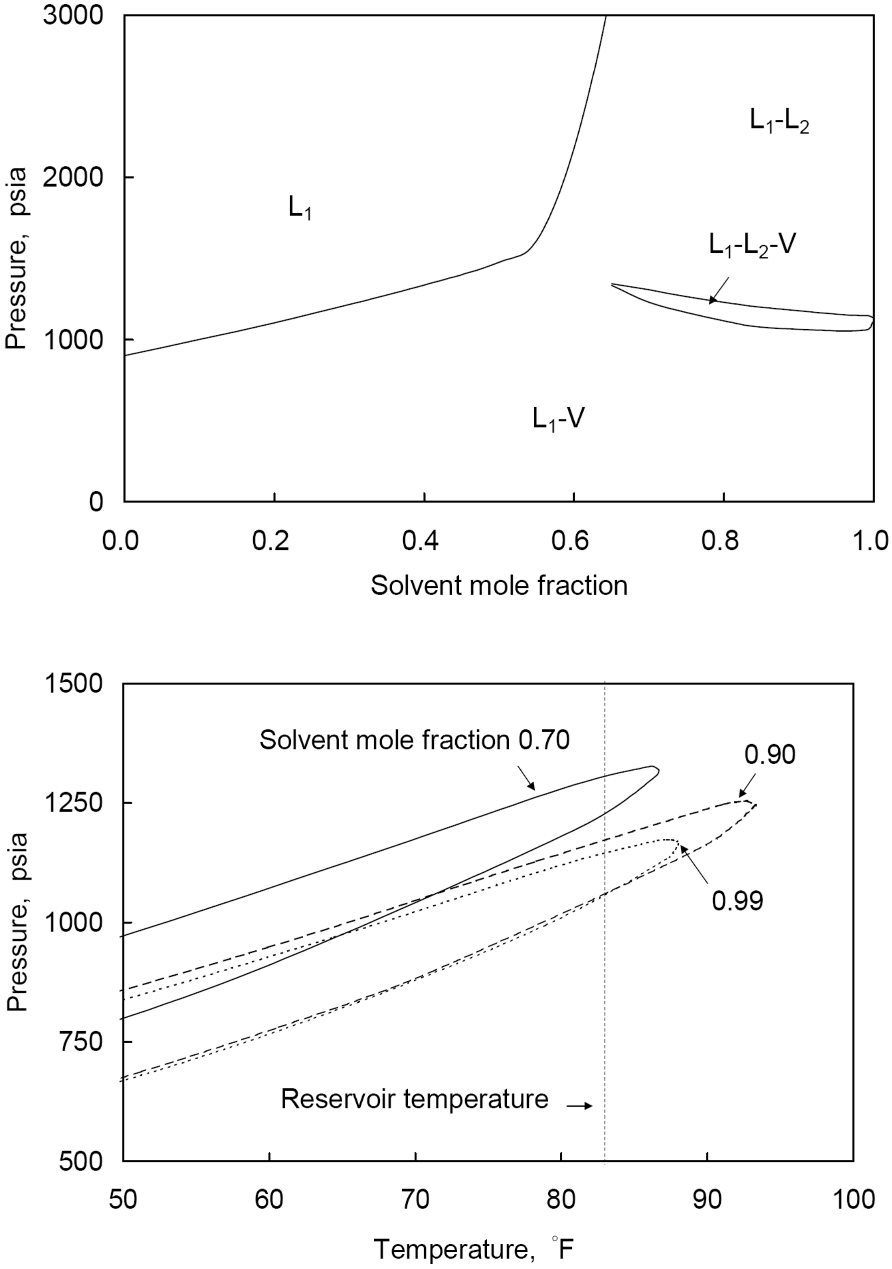

Figure 5.6 Top: *P*-*x* diagram at 83˚F for the NWE oil and injection gas (solvent) given in Table 5.2. Bottom: *P*-*T* diagrams for mixtures of the NWE oil and injection gas given in Table 5.2 for different oil-gas mixtures.

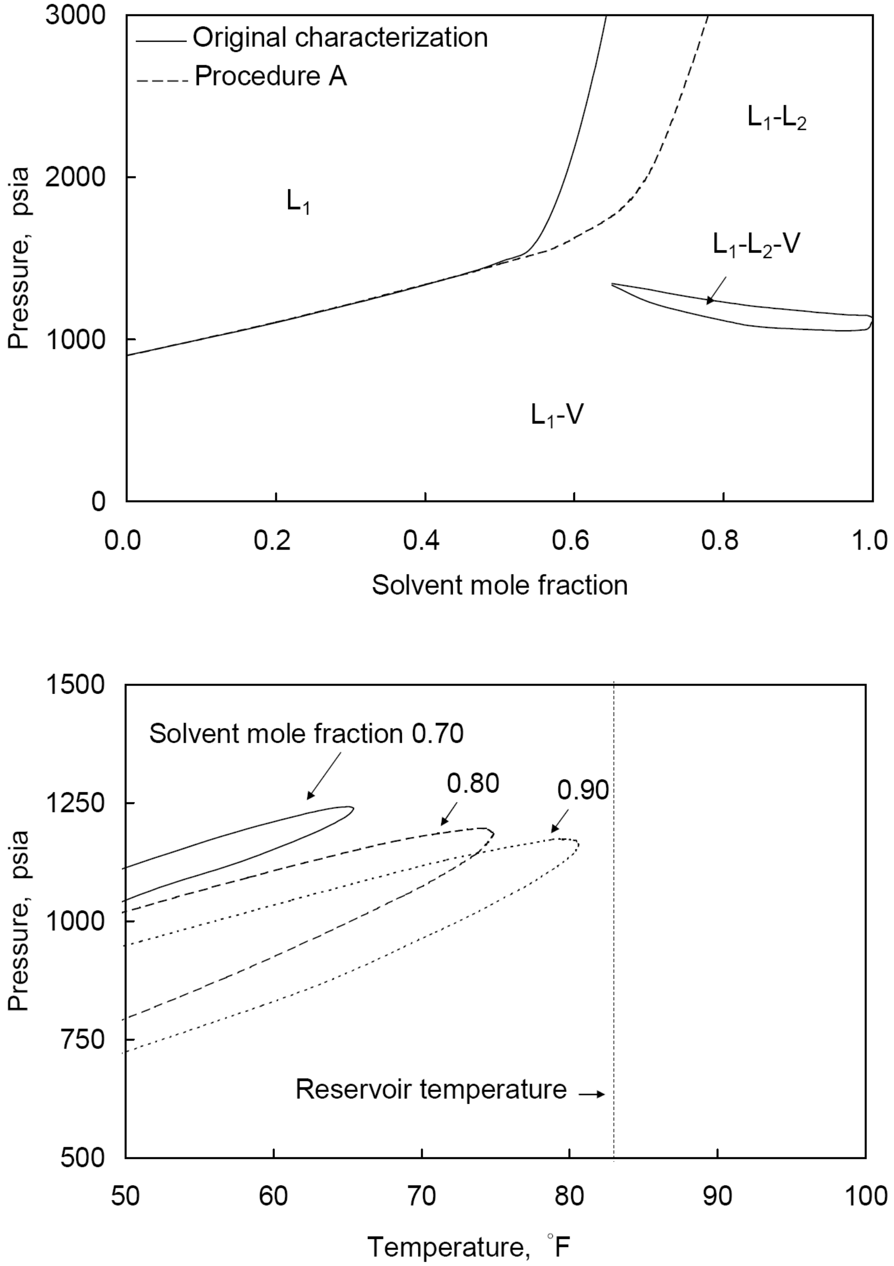

Figure 5.7 Top: Comparison of *P*-*x* diagram at 83°F from procedure A with that from the original characterization for the NWE oil and injection gas (solvent) given in Table 5.2. Bottom: *P*-*T* diagrams at different mixing ratios of the NWE oil and injection gas using procedure A.

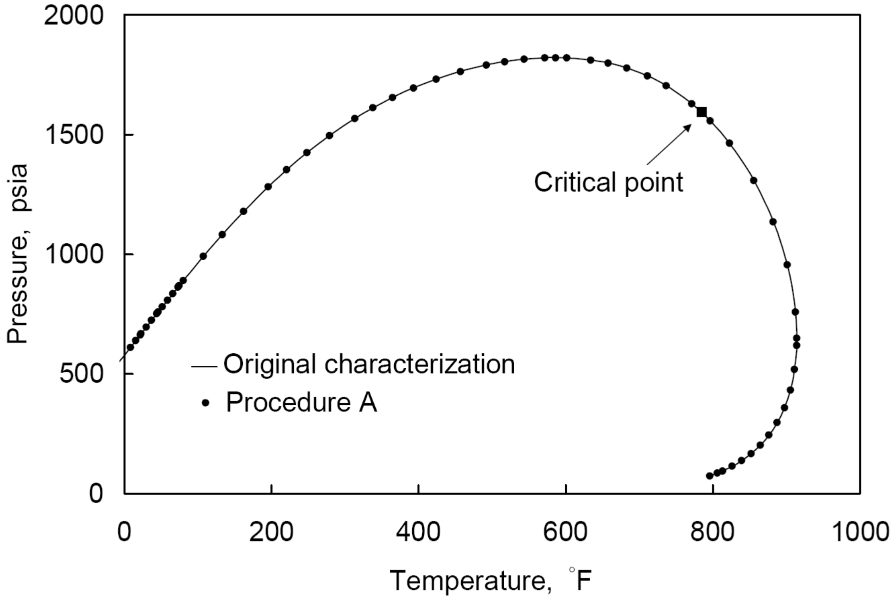

Figure 5.8 Comparison of *P-T* diagram from procedure A with that from the original characterization for the NWE oil.

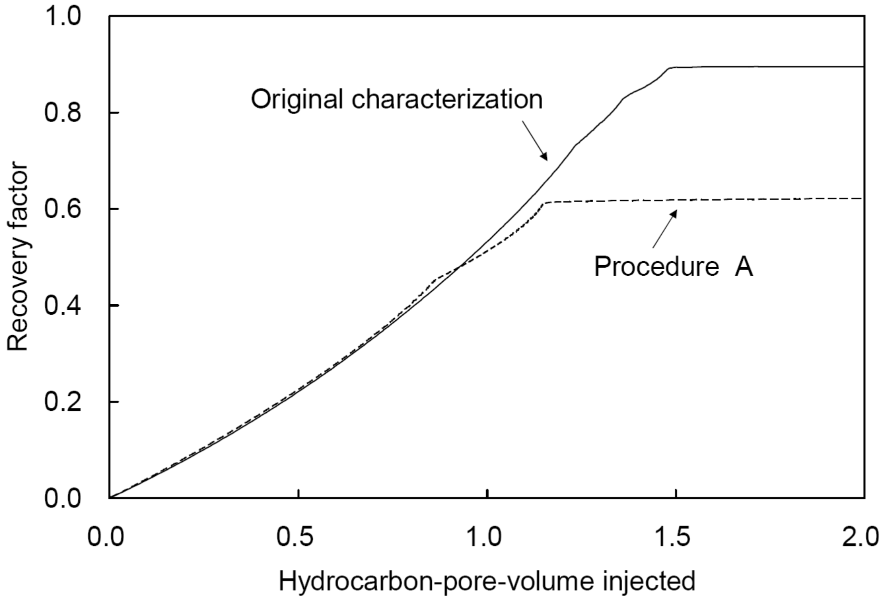

Figure 5.9 Recoveries for one-dimensional simulations with characterization procedure A and the original characterization for the NWE oil.

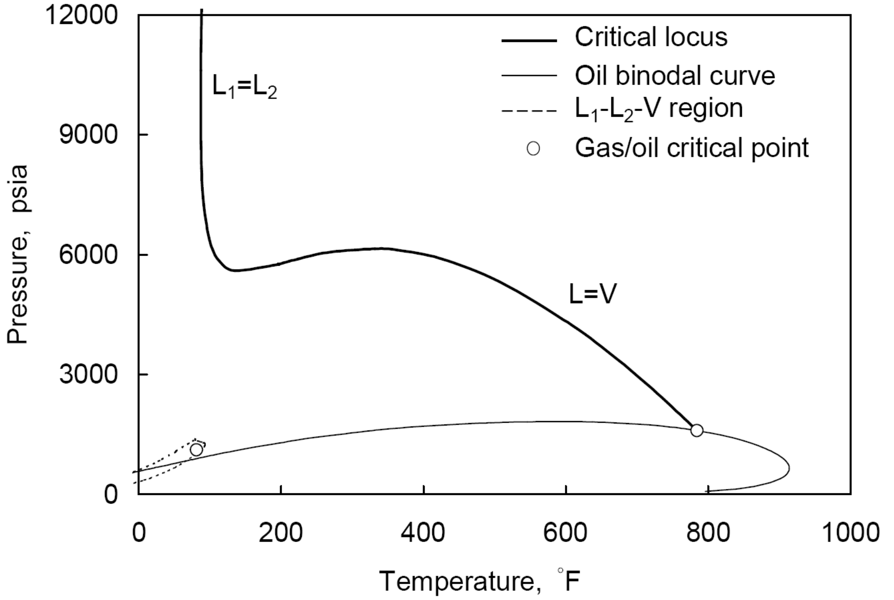

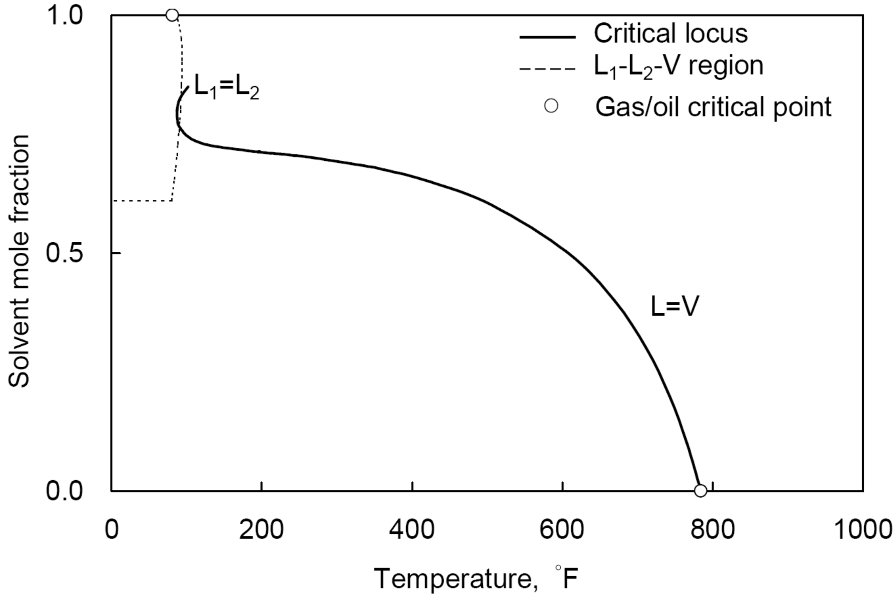

Figure 5.10 *P*-*T* and *T*-*x* projections of the *P*-*T*-*x* diagram for the pseudo-binary mixture of the NWE oil and injection gas given in Table 5.2.

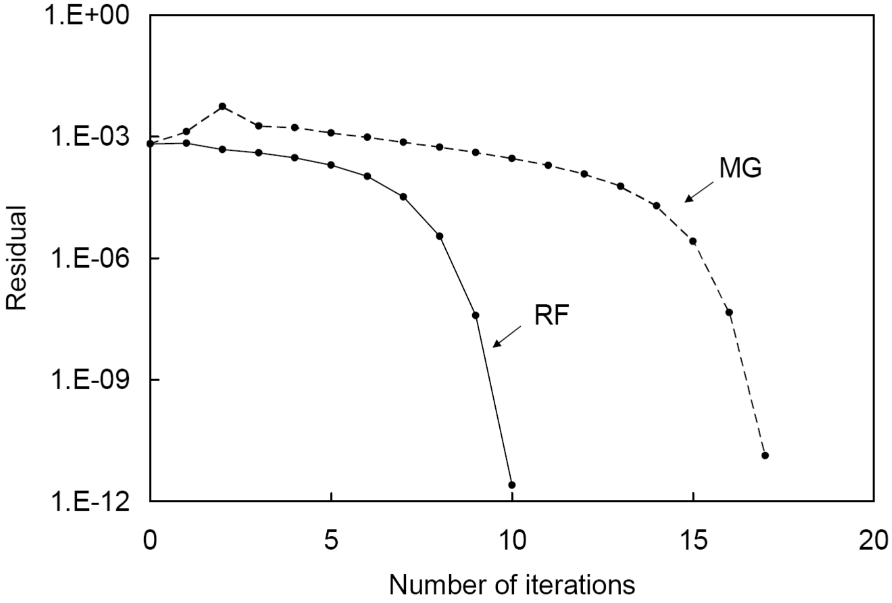

Figure 5.11 Convergence behaviors of the reduced flash (RF) and the minimization of the Gibbs free energy (MG) for an example three-phase calculation.

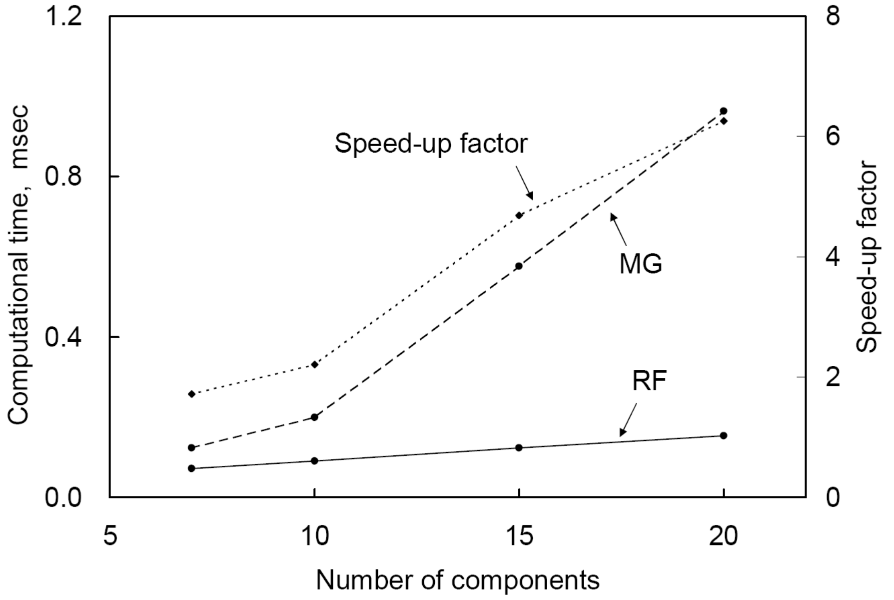

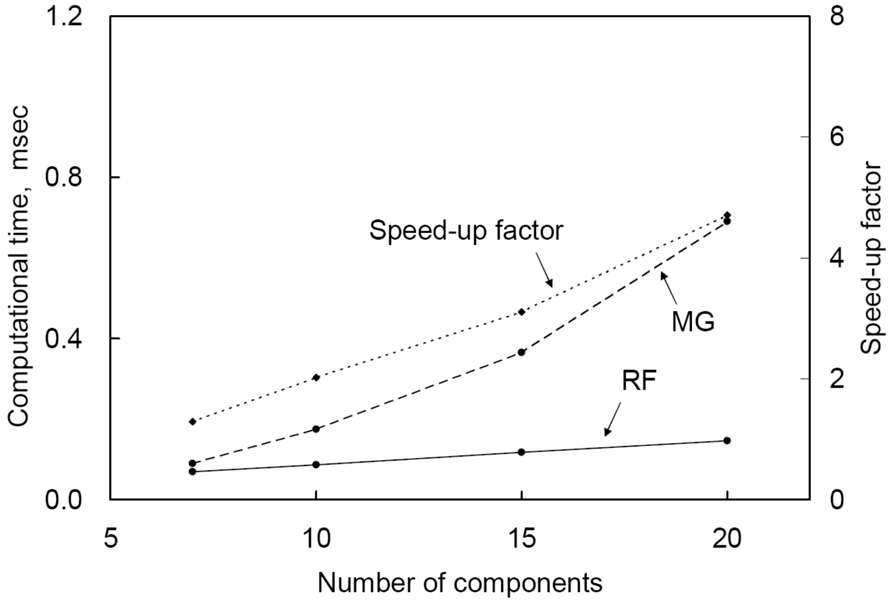

Figure 5.12 Comparisons of computational time per iteration for three-phase flash calculations using RF and MG. Top: When SS is switched to either RF or MG with a switching criterion of $\max_{ij}\{|F_{ij}|\}<10^{-3}$. Bottom: When SS is switched to either RF or MG with a switching criterion of $\max_{ij}\{|F_{ij}|\}<10^{-7}$.

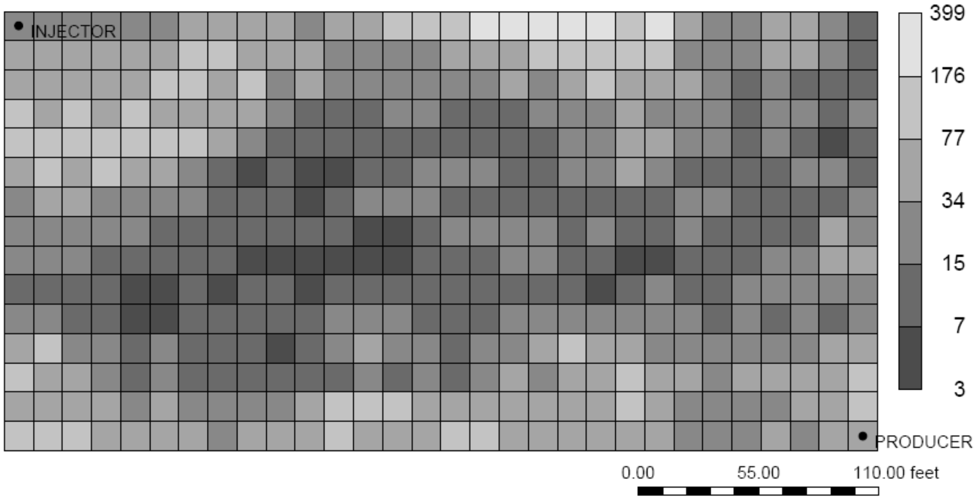

Figure 5.13 Permeability field for the simulation case study with the NWE oil in mD.

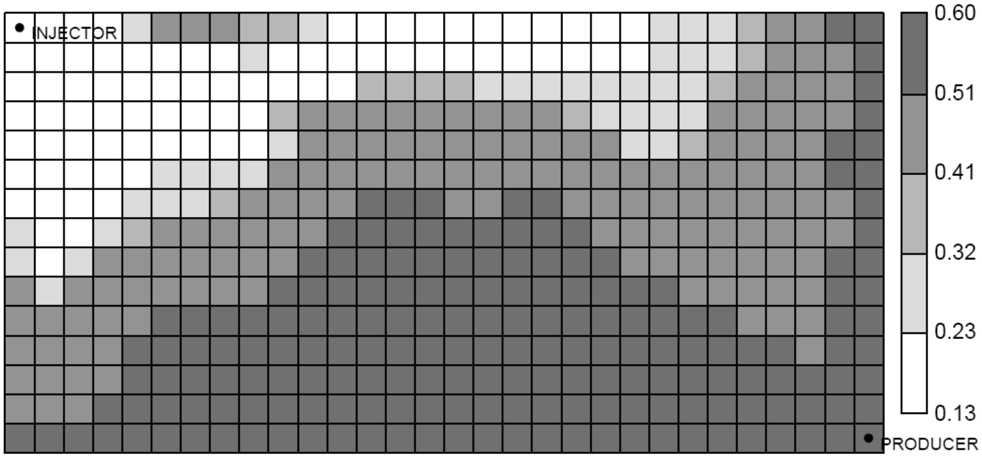

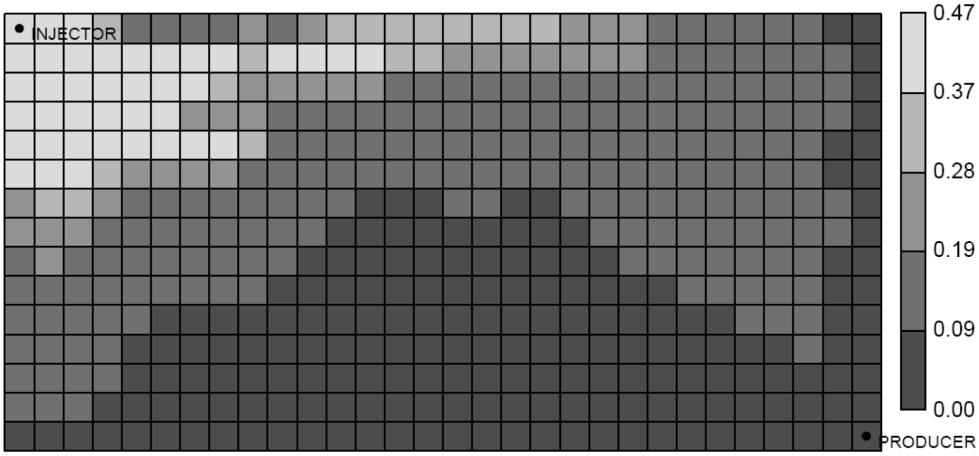

Figure 5.14 Top: Saturation distribution of the oleic phase at 0.5 HCPVI for the NWE oil displacement. Bottom: Saturation distribution of the gaseous phase at 0.5 HCPVI.

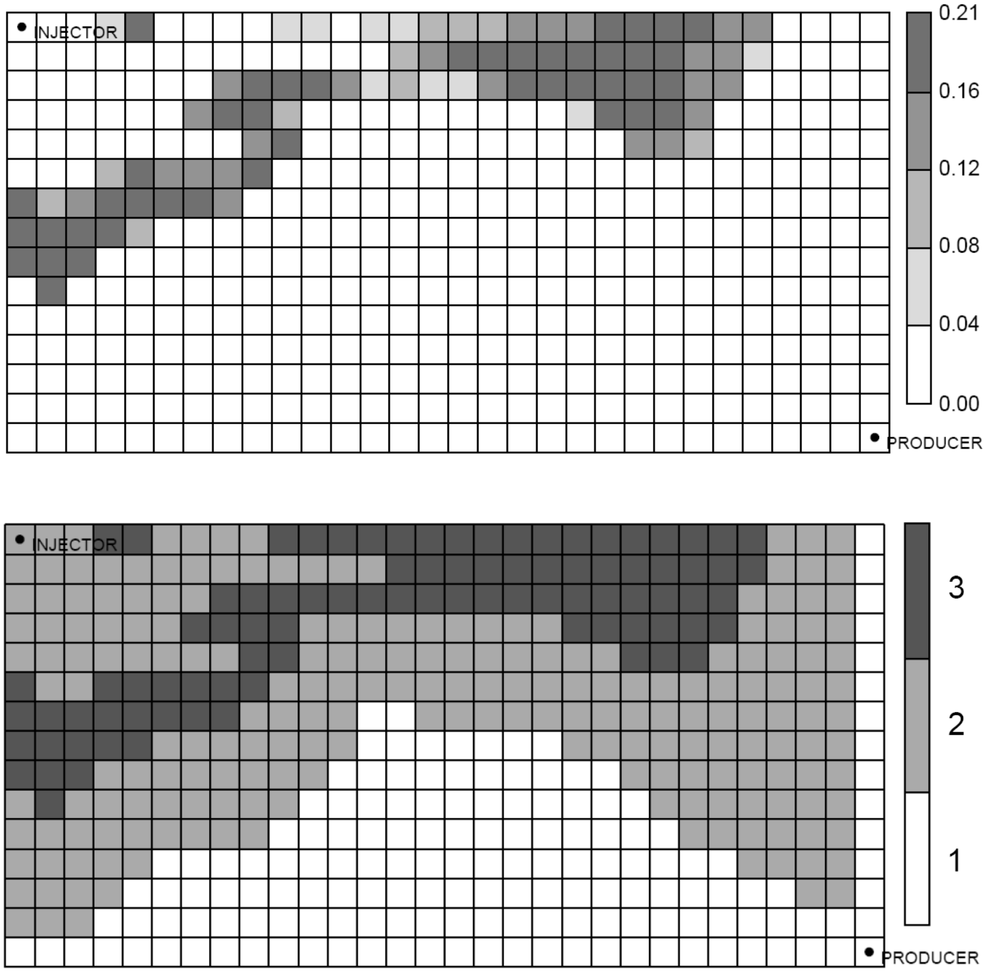

Figure 5.15 Top: Saturation distribution of the CO_2-rich liquid phase. Bottom: Distribution of the number of hydrocarbon-phases at 0.5 HCPVI.

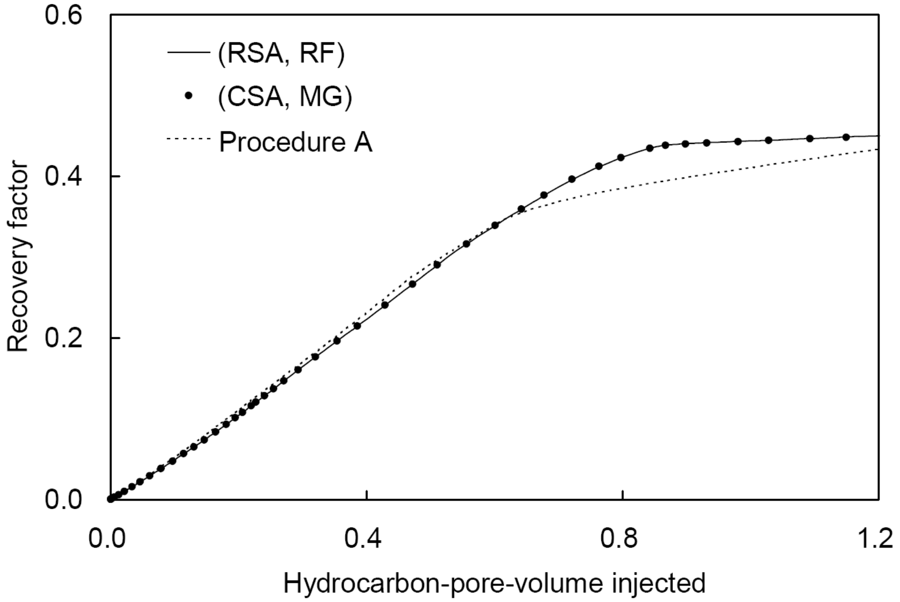

Figure 5.16 Recovery factors for cases (RSA, RF) and (CSA, MG) are almost identical with each other, but significantly different from that with procedure A.

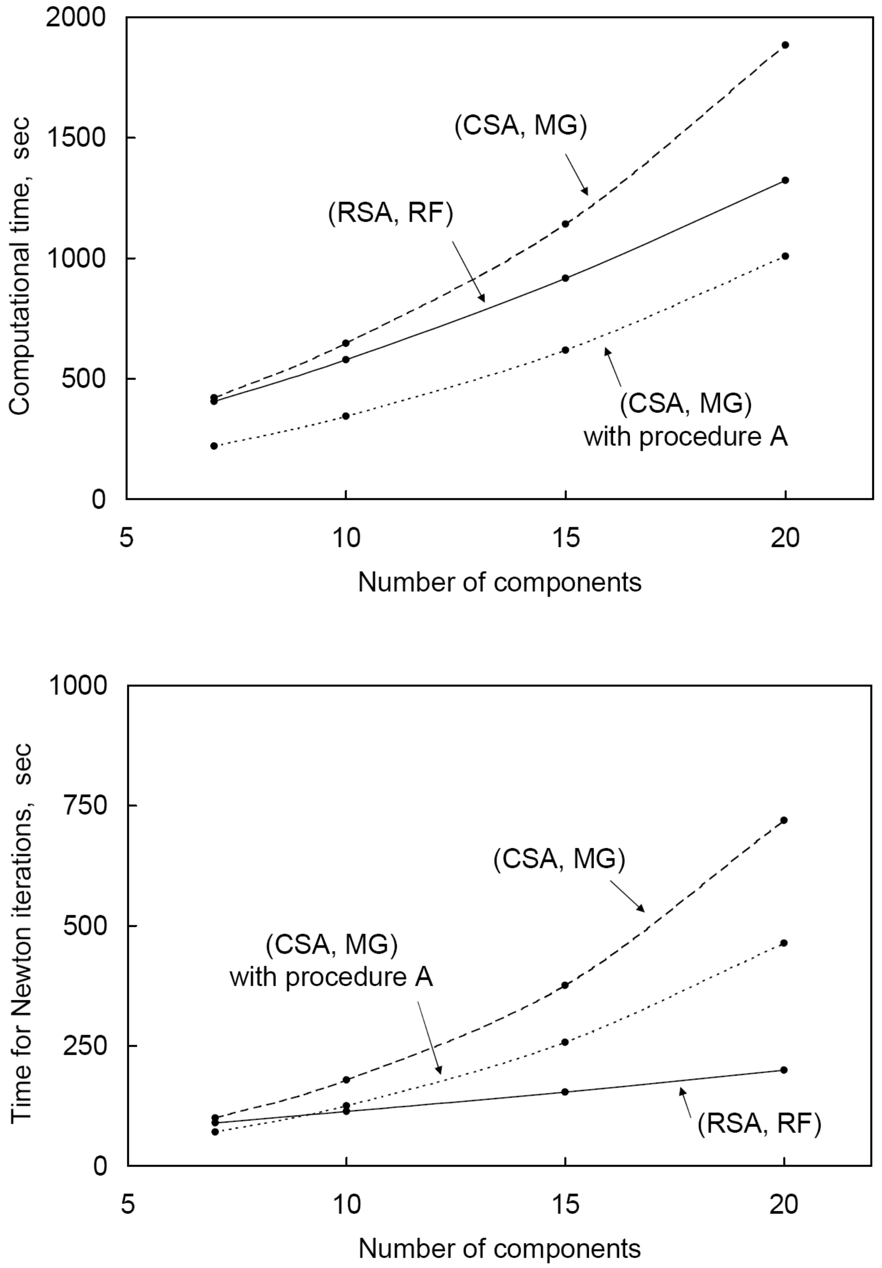

Figure 5.17 Top: Comparison of computational times with (RSA, RF), (CSA, MG), and (CSA, MG) with procedure A for the NWE oil displacement simulation. Bottom: Comparisons of computational times for phase equilibrium calculations with the second-order convergence methods for the NWE oil displacement.

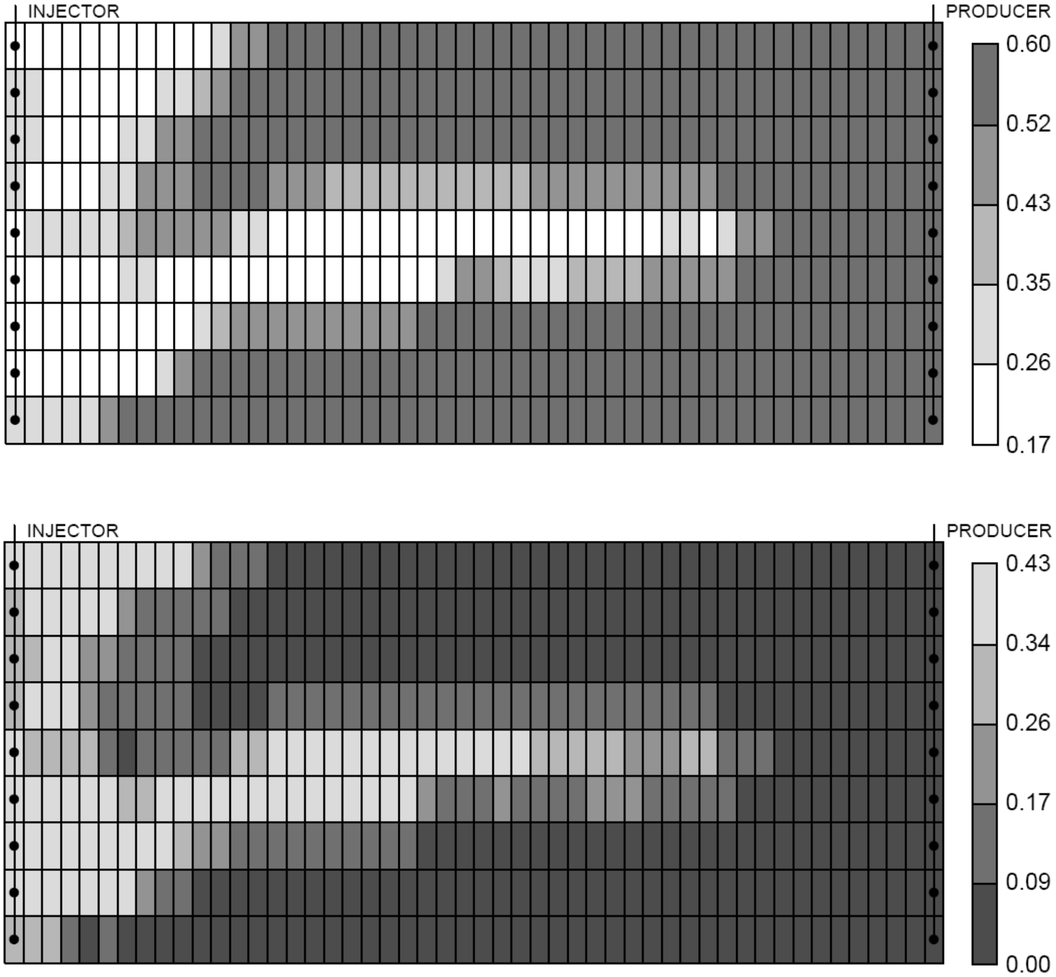

Figure 5.18 Top: Saturation distribution of the oleic phase at 0.4 HCPVI for the BSB oil displacement. Bottom: Saturation distribution of the gaseous phase at 0.4 HCPVI.

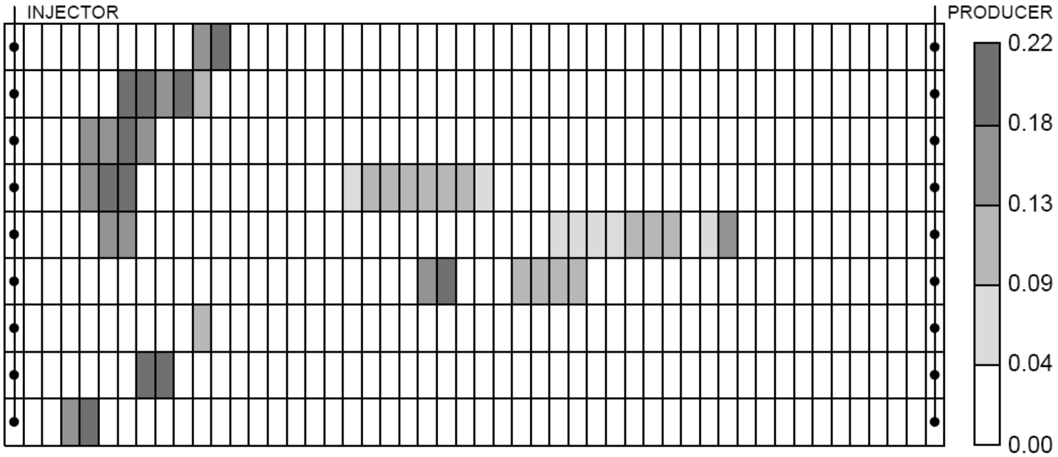

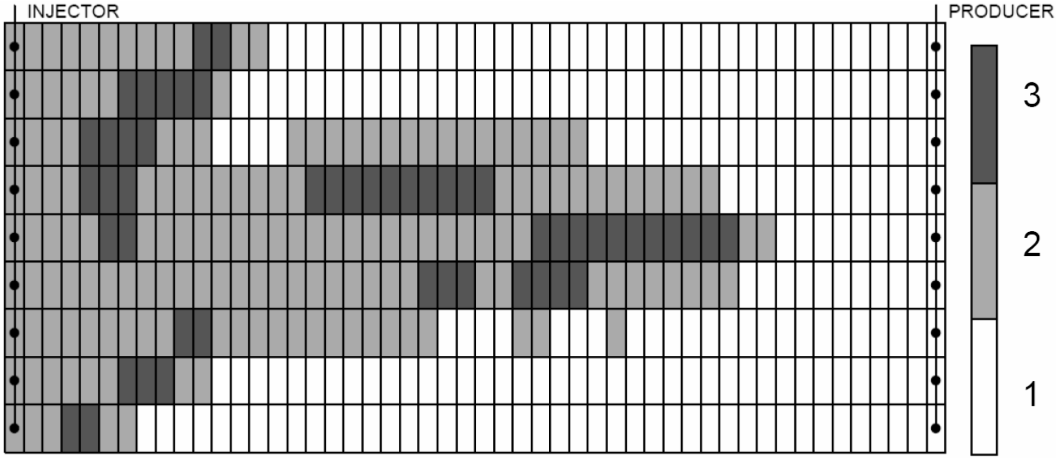

Figure 5.19 Top: Saturation distribution of the CO_2-rich liquid phase at 0.4 HCPVI.
Bottom: Distribution of the number of hydrocarbon-phases at 0.4 HCPVI.

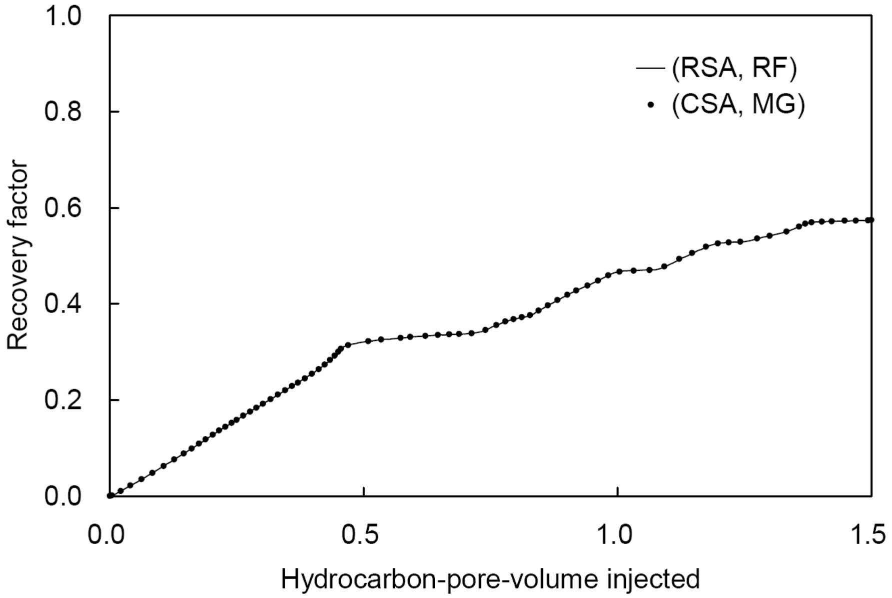

Figure 5.20 Recovery factors for the BSB oil displacement simulations using (RSA, RF) and (CSA, MG) are nearly identical with each other.

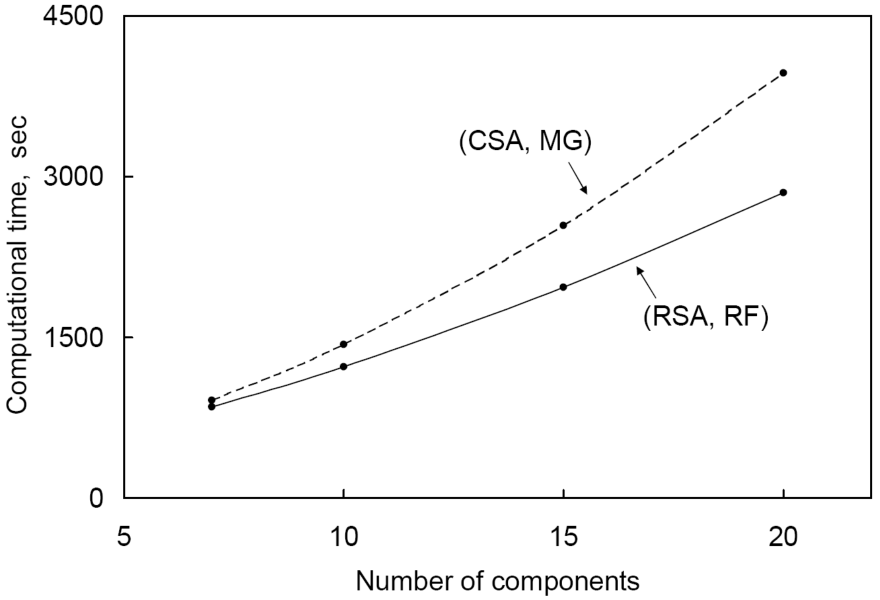

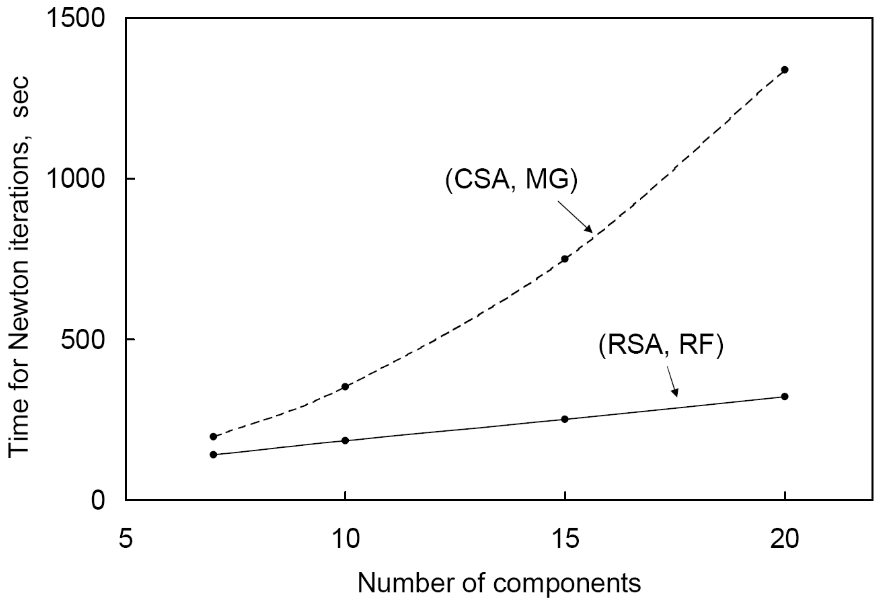

Figure 5.21 Top: Comparison of computational times with (RSA, RF) and (CSA, MG) for the BSB oil displacement simulation. Bottom: Comparisons of computational times for phase equilibrium calculations with the second-order convergence methods for the BSB oil displacement.

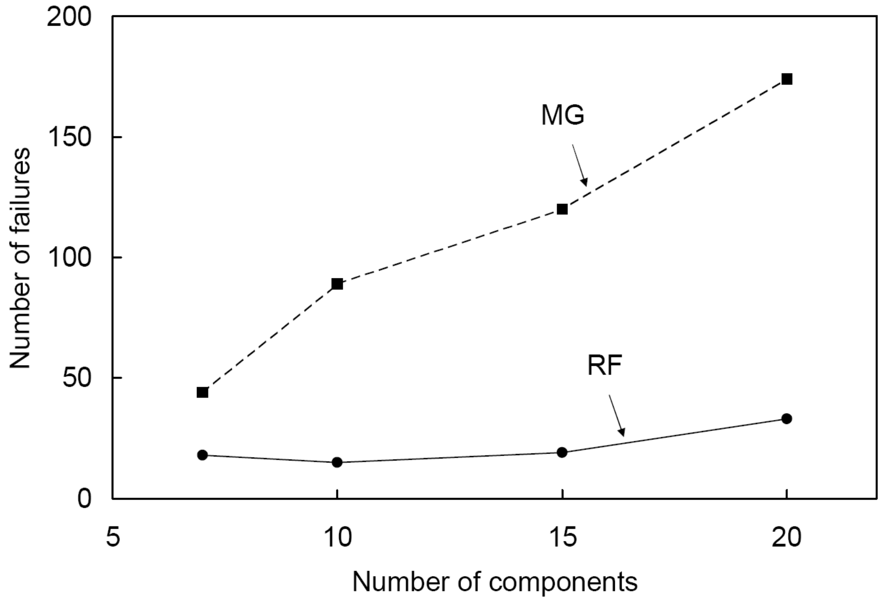

Figure 5.22 Comparison of the number of failures in three-phase flash calculations with RF and MG for different numbers of components for the BSB oil displacement.

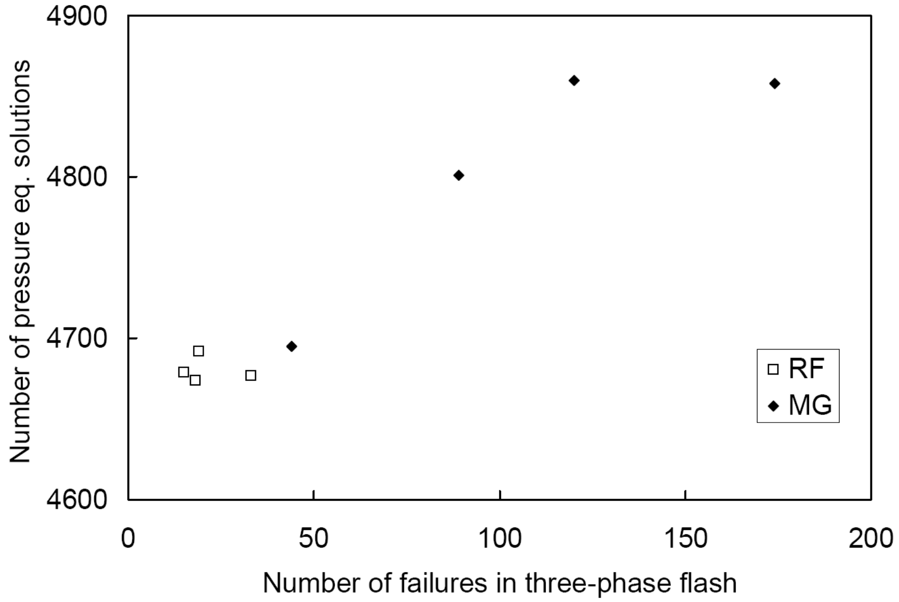

Figure 5.23 Frequency of solution of pressure equations during the simulation is positively correlated with the number of failures in three-phase flash calculations.

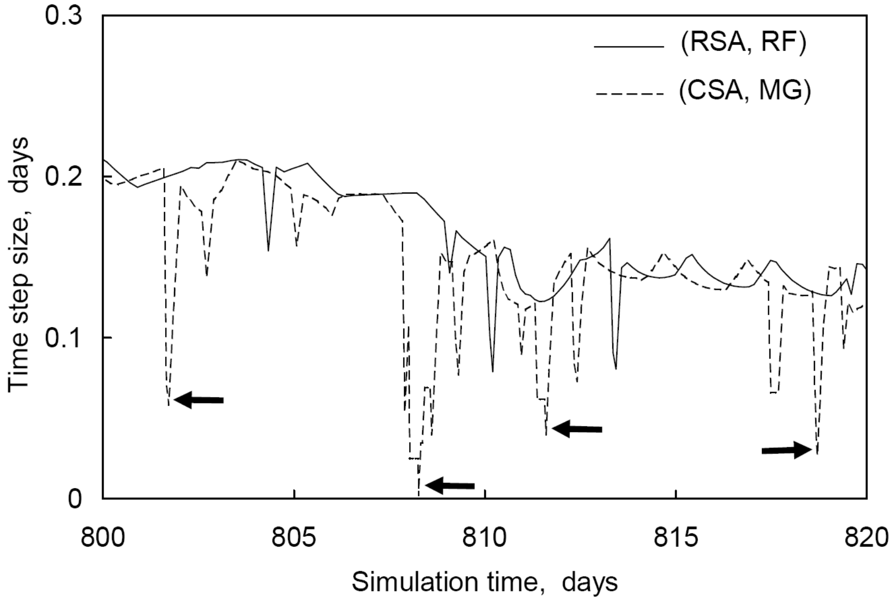

Figure 5.24 Variation of time-step sizes for simulations with (RSA, RF) and (CSA, MG). The four arrows indicate failure points of MG for three-phase flash calculations. There are no failures for RF within this time window.

6. Effect of Three Hydrocarbon-Phases on CO_2-Flood Displacement Efficiency

Mixtures of reservoir oil and CO_2 can exhibit complex phase behavior, especially at temperatures typically below 120ºF where a CO_2-rich liquid (L_2) phase can coexist with the oleic (L_1) phase, or the L_1 and gaseous (V) phases. Slim-tube measurements reported in the literature show that low-temperature oil displacements by CO_2 involving three hydrocarbon-phases can result in high displacement efficiency of more than 90%, even though the phases are not miscible. Prior research attributed the high displacement efficiency to efficient extraction of oil components by the L_2 phase. However, the efficient extraction does not fully describe the complex three-phase displacement because extraction of oil components by the L_2 phase is only a part of mass transfer among the three phases, L_1, L_2 and V. Several authors showed that high displacement efficiency can result from near-miscibility in a L_1-L_2 two-phase region flowing ahead of or behind the L_1-L_2-V three-phase region. In this chapter, however, we show that oil displacements involving L_1-L_2-V equilibrium can achieve more than 95% displacement efficiency even if a two phase region exhibits significant immiscibility.

Understanding L_1-L_2-V displacements requires knowledge of complex three-phase behavior. However, details of complex three-phase behavior during low-temperature CO_2 flooding are little known. This is firstly because such phase behavior is conventionally presented using a pressure-composition (*P*-*x*) diagram, which presents phase behavior along the mixing line between the oil and injection gas, instead of the actual composition path observed during the displacement. The second reason is because most compositional simulators are not capable of robust three-phase equilibrium calculations. The third reason is because prior research used ternary diagrams to study the effect of three-phase behavior on displacement efficiency. Three-phase behavior is invariant in a ternary diagram because a tie-triangle has zero degrees of freedom there, which is not true for real reservoir fluids.

There are two main objectives in this chapter. The first objective is to examine what controls the efficiency of displacements involving complex three-phase behavior. The second objective is to study thermodynamic predictions of three-phase behavior during low-temperature oil displacements by CO_2. We use UTCOMP (Chang *et al.* 1990), which has been updated with the robust phase equilibrium algorithms developed in Chapters 3-5. One-dimensional displacements are simulated using UTCOMP for three different oils from west Texas, for which EOS fluid models are available in the literature. We also use quaternary EOS fluid models for oil/solvent mixtures to investigate the effect of three-phase behavior on displacement efficiency with varying pressure, temperature, and oil properties.

6.1 THREE-PHASE BEHAVIOR FOR EFFICIENT OIL DISPLACEMENT

This section presents simulations of one-dimensional CO_2 floods for three different oils for which EOS fluid models are available in the literature. Because those displacements exhibit complex three-hydrocarbon-phase behavior, they are simulated using UTCOMP where the robust algorithms developed in this dissertation have been implemented. These displacements can result in more than 95% oil recovery even though there remains immiscible multiphase flow. Phase behavior during the displacements is examined to explain why high displacement efficiency is achieved.

Phase equilibrium calculations throughout this chapter are performed using the Peng-Robinson EOS (Peng and Robinson 1976a). For viscosity calculations, the correlation of Lohrenz *et al.* (1964) is used as implemented in UTCOMP by Chang *et al.* (1990).

6.1.1 Bob Slaughter Block Oil Displacement

The Bob Slaughter Block (BSB) oil is a west Texas oil with a reservoir temperature of 105°F. Khan *et al.* (1992) characterized the BSB oil using the Peng-Robinson EOS, for which the EOS parameters are given in Table 6.1. Parameters *h* and *g* are also given for use of the reduced method presented in Chapters 4 and 5. Khan *et al.* (1992) adjusted the critical temperature of methane to match the bubble point pressure of the oil. Although current practice recommends not adjusting EOS parameters for well-defined components like methane, the fluid characterization given in Table 6.1 keeps physical trends of critical temperature (T_C) and pressure (P_C), and acentric factor (ω); *e.g.*, T_C increases with carbon number.

We consider BSB oil displacements by the injection gas (CO_2 95% and C_1 5%) given in Table 6.1. Figure 6.1 shows the *P-x* diagram at the reservoir temperature of 105°F for pseudo-binary mixtures of the BSB oil with solvent. The three-phase region exists in a narrow pressure range from 1354 psia to 1433 psia on the *P-x* diagram. However, as will be shown later, the three-phase equilibrium occurs in a different, wider pressure range during the displacements because the *P-x* diagram represents phase behavior along the mixing line between the oil and injection gas, instead of along the actual composition path.

The thermodynamic MMP (see section 2.2.6.3 for the definition) for the BSB oil/solvent given in Table 6.1 is unknown because methods for a thermodynamic MMP capable of handling three-phase equilibrium have not been developed. This is also true for all oil/solvent systems studied in this chapter.

Table 6.2 summarizes reservoir properties for simulations of the one-dimensional oil displacements with no gravity. Those reservoir properties are used for all simulations in this chapter. Aqueous phase exists at the residual saturation, so it does not flow. We perform a series of one-dimensional simulations at different pressures. The injection and production wells are operated at constant bottom-hole pressures to minimize the effect of pressure on phase behavior during the simulations. The pressure difference along the reservoir is set to be 10 psia for all simulations studied in this chapter. For example, in a simulation at the displacement pressure of 1200 psia, we set the injection well bottom-hole pressure to be 1200 psia and the production well bottom-hole pressure to be 1190 psia. Thus, injection rate varies with time.

Figure 6.2 shows oil recoveries for the one-dimensional displacements at five different pressures 1150, 1200, 1250, 1300, and 1350 psia. All the displacements exhibit immiscible three-hydrocarbon-phase flow even though the pressure range for the three phases in Figure 6.1 is only from 1354 to 1433 psia. The displacement at 1300 psia results in 93% oil recovery at 2.0 hydrocarbon-pore-volumes injected (HCPVI). The increment in oil recovery becomes marginal above 1300 psia as shown in Figure 6.3. The displacement at 1350 psia recovers 94% of the original oil; only 1% improved recovery compared to 1300 psia.

Figures 6.4, 6.5, and 6.6 show phase saturation profiles at 0.5 HCPVI for the displacements at 1150, 1200, and 1300 psia, respectively. The oscillation near the injection well is an artifact caused by numerical simulation. The L_1-V two-phase regions flow ahead of and behind the L_1-L_2-V three-phase region. The gas bank at the displacement front does not efficiently displace the oil, leaving the high L_1 phase saturation behind it. As pressure increases, the three-phase region becomes narrower and the L_2 phase saturation increases in the three-phase region. The sharp reduction in the L_1 phase saturation and increase in the L_2 phase saturation at the front of the three-phase region indicate the efficient extraction of components in the oil by the L_2 phase.

The extraction becomes more significant as pressure increases, resulting in greater oil recovery.

To see the increased extraction, we calculate the molar distribution of component i in phase j at each grid cell in the three-phase region as $\beta_j x_{ij}/z_i$, where β_j is the phase mole fraction of phase j, x_{ij} is the phase component mole fraction of component i in phase j, and z_i is $\sum_j \beta_j x_{ij}$ by definition ($i = 1,\ldots,N_C$ and $j = 1,\ldots,N_P$). Figures 6.7, 6.8, and 6.9 give the molar distributions of heavy components ($C_{7\text{-}15}$, $C_{16\text{-}27}$, and C_{28+}) at 0.5 HCPVI for the displacements at pressures 1150, 1200, and 1300 psia, respectively. The L_2 phase extracts lighter components more efficiently than it does heavier components at a fixed pressure. Those figures also show that the extraction of components by the L_2 phase becomes more significant as pressure increases.

The common explanation for the high efficiency of low-temperature oil displacements by CO_2 is the efficient extraction of intermediate and heavy components in the oil by the L_2 phase (*e.g.*, Holm and Josendal 1974, 1982, Orr *et al.* 1981, 1983, Gardner *et al.* 1981, Nghiem and Li 1986, Turek *et al.* 1988, Creek and Sheffield 1993). The results shown in Figures 6.7, 6.8, and 6.9 are consistent with that explanation because as pressure increases the extraction becomes more significant and displacement efficiency becomes greater. However, the extraction efficiency is determined by equilibrium phase properties, which depend on the composition path and phase behavior at the operating conditions. That is, the efficient extraction should be a consequence of both flow behavior and the complex three-phase behavior. The common explanation cannot tell under what conditions the efficient extraction occurs. As will be shown later, efficient mass transfer among phases (not just extraction of oil components by the L_2 phase) is related to the occurrence of a particular type of critical behavior in the three-phase region.

The actual phase behavior during the displacements is more complex than the simple extraction behavior described above. Figures 6.10, 6.11, and 6.12 show the profiles of phase mass densities at 0.5 HCPVI for pressures of 1150, 1200, and 1300 psia, respectively. At the front of the three-phase region, mass densities of the L_1 and L_2 phases become close to each other. The densities become closer as pressure increases because the L_2 phase extracts oil components more efficiently and the gas components dissolve into the L_1 phase more significantly. At the tail of the three-phase region, the density of the L_2 phase becomes close to that of the V phase at 1300 psia. The similarity in density indicates that the two phases are nearly critical, considering that phase density is a function of the corresponding phase composition at a fixed temperature and pressure. The interfacial tension between the phases is small as a consequence of near-miscibility. The L_1 and L_2 phases become nearly critical at the front of the three-phase region, while the L_2 and V phases do so at the tail of the three-phase region at 1300 psia.

The degree of criticality between two phases can be measured by the distance between the two phase-compositions in composition space. At a critical point between two phases, the distance is zero. *K*-values are commonly used to see the level of miscibility between two phases (*e.g.*, Michelsen 1998, Moulds *et al.* 2005). However, use of *K*-values for that purpose can be misleading. For example, consider that the vapor phase composition is (0.001, 0.999) and the liquid phase composition is (10^{-6}, 0.999999). The two points are very close to each other in composition space with a distance of 0.0014. However, the *K*-values are calculated as (1000, 0.999), which looks far from the critical point. The distance between two equilibrium phase-compositions, which is used in this chapter, better represents the level of criticality at a fixed temperature and pressure.

Figure 6.13 shows phase composition distances at 0.5 HCPVI for the displacement at 1150 psia. In the figure, $d_{\mathrm{L1\text{-}V}}$ represents the distance between the L_1 phase composition and the V phase composition. Similarly, $d_{\mathrm{L1\text{-}L2}}$ and $d_{\mathrm{L2\text{-}V}}$ represent the distances between the L_1 and L_2 phase compositions and between the L_2 and V phase compositions, respectively. Similar plots are given in Figure 6.14 for 1200 psia and in Figure 6.15 for 1300 psia. $d_{\mathrm{L2\text{-}V}}$ exhibits the most significant sensitivity to displacement pressure. At 1150 psia, the L_2 phase is highly immiscible with the V phase in the three-phase region although $d_{\mathrm{L2\text{-}V}}$ is smaller than $d_{\mathrm{L1\text{-}L2}}$ and $d_{\mathrm{L1\text{-}V}}$ except near the front of the three-phase region. At 1200 psia, $d_{\mathrm{L2\text{-}V}}$ becomes smaller inside the three-phase region. At 1300 psia, $d_{\mathrm{L2\text{-}V}}$ asymptotically decreases at the tail of the three-phase region, indicating a near-critical state between the L_2 and V phases. However, as $d_{\mathrm{L1\text{-}L2}}$ indicates, another coexisting phase L_1 is immiscible with the L_2 and V phases at the tail of the three-phase region. $d_{\mathrm{L1\text{-}L2}}$ is smaller at the front of the three-phase region compared with other points in the three-phase region. The V phase is immiscible with the coexisting L_1 and L_2 phases at the front of the three-phase region as shown by $d_{\mathrm{L1\text{-}V}}$.

The $d_{\mathrm{L1\text{-}V}}$ plots exhibit significant immiscibility between the L_1 and V phases along the entire displaced region including two- and three-phase regions. This is true even for the displacement at 1300 psia which results in 93% oil recovery. That is, displacement efficiency is not controlled by miscibility in a two-phase region in those displacements. This is a significant difference from typical two-phase gas flooding, where displacement efficiency becomes higher when a two-phase region exhibits more miscibility. No paper has reported a displacement that results in high displacement efficiency with significant immiscibility in two-phase regions. The oil displacements simulated by Orr *et al.* (1983) and Nghiem and Li (1986) resulted in high displacement efficiency with three-hydrocarbon-phase flow. In their simulations, however, the high displacement efficiency was controlled by near-miscibility in the L_1-L_2 two-phase region flowing behind or ahead of the three-phase region.

The profiles of the phase composition distances suggest the existence of two critical endpoints (CEPs) in composition space at the operating temperature and pressure. CEPs are critical states where two of the three coexisting phases become identical (critical) (Uzunov 1993). There are two types of CEPs in the context of phase behavior of CO_2/hydrocarbon mixtures. The first CEP is where the L_1 and L_2 phases merge in the presence of the V phase (L_1=L_2-V). The other CEP is where the L_2 and V phases merge in the presence of the L_1 phase (L_1-L_2=V).

To the best of our knowledge, no research has reported an oil displacement that exhibits the phase behavior characterized by a three-phase region bounded by the two types of CEPs. Such phase behavior, however, is observed in binary phase behavior types IV and V according to the classification of van Konynenburg and Scott (1968, 1970, 1980). The three-phase region bounded by the two types of CEPs was observed in static experiments for hydrocarbon mixtures (Rowlinson and Freeman 1961, Davenport and Rowlinson 1963, Davenport *et al.* 1966, Kohn *et al.* 1966, Wagner *et al.* 1968) and CO_2/*n*-C_{13} mixtures (Enick *et al.* 1985, Galindo and Blas 2002).

For binary three-phase behavior bounded by the two CEPs, the CEP of type L_1=L_2-V occurs at the low-temperature end of the three-phase curve in *P*-*T*-*x* space. The CEP of type L_1-L_2=V occurs at the high-temperature end of the three-phase curve in *P*-*T*-*x* space. Therefore, the phase behaviors L_1=L_2-V and L_1-L_2=V are referred to as the lower critical endpoint (LCEP) and the upper critical endpoint (UCEP), respectively. Although the notation of “upper” and “lower” CEPs does not indicate any thermodynamic conditions due to the higher degrees of freedom for mixtures, in this dissertation we refer to the phase behavior L_1=L_2-V as the LCEP behavior and L_1-L_2=V as the UCEP behavior for mixtures.

In the BSB oil displacements, the high displacement efficiency is achieved when the composition path goes near the UCEP and, to a lesser extent, LCEP as indicated in Figure 6.15. This can be interpreted as described below. When the composition path goes near the LCEP at the front of the three-phase region, mass transfer between the L_2 and L_1 phases becomes significant because of near miscibility between the two phases. At the tail of the three-phase region, the L_2 phase disappears to result in the L_1-V two phases. When the composition path goes from the three-phase region to the two-phase region, the composition path must go near the UCEP for high oil recovery because the L_1 phase saturation must be minimized behind the three-phase region. That is, when disappearing at the tail of the three-phase region, the L_2 phase must be vaporized into the V phase, instead of condensed into the L_1 phase, for high oil recovery.

We assumed that the V and L_2 phases have the same relative permeability as shown in Table 6.2 in the simulations presented in this section. To see the effect of L_2 phase relative permeability on the BSB oil displacement, the BSB oil displacements at 1200 and 1300 psia are repeated assuming that the L_1 and L_2 phases have the same value, 0.50, for endpoint relative permeability. Figure 6.2 shows a marginal effect of L_2 phase relative permeability on the BSB oil displacement efficiency at 1200 psia. We also observed that the value of 0.50 for the L_2 phase endpoint relative permeability results in the same oil recovery as the original simulation case given in Table 6.2 although the comparison is not shown in Figure 6.2 for clarity.

The BSB oil displacements presented in this section exhibit complex three-phase behavior involving the two CEPs. High displacement efficiency is achieved when the composition path goes near the UCEP. No research studied such complex three-phase behavior for high efficiency of low-temperature oil displacements by CO_2. In the subsequent two subsections, we show that similar phase behavior to the BSB oil displacement can be also observed for other two reservoir oils, the North Ward Estes oil and the Monahans Clearfork oil. The JEMA oil and Oil G, for which Khan *et al.* (1992) gave EOS fluid models, exhibit the same displacement characteristics as the BSB oil although they are not shown in this dissertation.

6.1.2 North Ward Estes Oil Displacement

The North Ward Estes (NWE) is a low-temperature oil reservoir (83°F) in west Texas (Winzinger *et al.* 1991). Table 5.2 gives the characterization for the NWE oil (Khan *et al.* 1992) using the Peng-Robinson EOS. Figure 5.6 shows the *P-x* diagram at 83°F for the NWE oil and injection solvent (CO_2 95% and C_1 5%) given in Table 5.2. The L_1-L_2-V region exists between 1050 and 1350 psia at solvent mole fractions greater than 0.65. The three-phase region on the *P-x* diagram is larger than that for the BSB oil presented in section 6.1.1. Reservoir properties for the one-dimensional simulation are shown in Table 6.2.

Figure 6.16 shows the oil recoveries at three different pressures 1000, 1050, and 1110 psia. The three displacements exhibit three-hydrocarbon-phase flow. The displacement at 1110 psia results in a high recovery factor of 96%. Figures 6.17, 6.18, and 6.19 give the profiles for phase saturations at 0.5 HCPVI for 1000, 1050, and 1110 psia, respectively. Unlike the BSB oil displacements, the three-phase region is largest for the highest displacement efficiency among the three displacements.

Figures 6.20, 6.21, and 6.22 show profiles of phase composition distances ($d_{L1\text{-}V,}$ $d_{L1\text{-}L2}$, and $d_{L2\text{-}V}$) at 0.5 HCPVI for the displacement pressures 1000, 1050, and 1110 psia, respectively. As in the BSB oil displacements, $d_{L1\text{-}L2}$ is smaller at the front of the three-phase region than at other points within the three-phase region. The minimum value of

$d_{L2\text{-}V}$ on the tail side of the three-phase region becomes smaller as pressure increases. However, unlike the BSB oil displacements, $d_{L2\text{-}V}$ does not asymptotically decrease at the tail of the three-phase region for the high displacement efficiency of 96% at 1110 psia. As will be demonstrated in section 6.2.3.2, the behavior of the $d_{L2\text{-}V}$ profile depends on the reservoir temperature. The L_1-V two-phase regions flowing ahead of and behind the three-phase region are far from miscibility, indicating that the high displacement efficiency of 96% at 1110 psia cannot be attributed to miscibility developed in a two-phase region. As in the BSB oil displacements, the NWE oil displacements result in high displacement efficiency when the composition path goes near the UCEP and, to a lesser extent, the LCEP.

6.1.3 Monahans Clearfork Oil Displacement

The Monahans Clearfork (MC) oil is a low-temperature reservoir oil (90°F) from west Texas. An EOS fluid model was developed by Lim *et al.* (1992) using the Peng-Robinson EOS as shown in Table 6.3. Figure 6.23 shows the *P-x* diagram at 90°F for the pseudo-binary mixture of the MC oil and injection gas given in Table 6.3. Because the methane concentration reaches 31% in the MC oil, the bubble point pressure of the MC oil (1377 psia) is higher than those of the other oils considered in this chapter. The three-phase region exists in a pressure range from 1142 to 1406 psia at solvent concentrations between 0.66 and 0.98. We consider oil displacements at pressures lower than the bubble point pressure so that three hydrocarbon-phases can coexist during the displacements. Thus, unlike the other displacements studied in this chapter, the reservoir fluid initially forms two equilibrium phases, the L_1 and V phases. The reservoir properties for the simulations are given in Table 6.2.

Figure 6.24 shows the oil recoveries for three different pressures 1000, 1100, and 1200 psia. Because of large compressibility of the gaseous phase, the slope of the recovery curve for 1000 psia is initially small. The displacement pressure of 1200 psia results in 98% oil recovery. Figures 6.25, 6.26, and 6.27 give the profiles of phase saturations after 0.5 HCPVI at the three different pressures 1000, 1100, and 1200 psia. Because the pressures are lower than the bubble point pressure of the oil, the region that has not been displaced exhibits the L_1-V two-phase equilibrium. The L_2 phase in the three-phase region has a higher saturation as pressure increases, leaving a lower L_1 saturation.

Figures 6.28, 6.29, and 6.30 show the phase composition distances ($d_{\mathrm{L1\text{-}V}}$, $d_{\mathrm{L1\text{-}L2}}$, and $d_{\mathrm{L2\text{-}V}}$) after 0.5 HCPVI at 1000, 1100, and 1200 psia, respectively. The profile of $d_{\mathrm{L2\text{-}V}}$ is sensitive to the displacement pressure. At the displacement pressure of 1000 psia that results in 82% oil recovery, the L_2 phase is immiscible with the V phase in the three-phase region as indicated by $d_{\mathrm{L2\text{-}V}}$. At the displacement pressure of 1200 psia which yields 98% oil recovery, $d_{\mathrm{L2\text{-}V}}$ asymptotically decreases at the tail of the three-phase region, indicating that the overall composition is close to the UCEP. Figure 6.30 also shows significant immiscibility in the two-phase regions ahead of and behind the three-phase region. The plots of $d_{\mathrm{L2\text{-}V}}$ show that the overall compositions at the front of the three-phase region are near the LCEP for all three displacements. The MC oil displacement presented in this section can achieve nearly perfect oil displacement when the composition path goes near the UCEP.

6.2 INVESTIGATION OF THREE-PHASE BEHAVIOR AND ITS EFFECT ON DISPLACEMENT EFFICIENCY

The low-temperature oil displacements presented in section 6.1 result in high displacement efficiency when the composition path goes near the UCEP. The two-phase regions flowing ahead of and behind the three-phase region exhibit significant immiscibility even for nearly perfect displacements. The nearly perfect displacements are not consequences of miscibility in the two-phase regions for those displacements.

Although we found that the phase behavior associated with CEPs is the key to the efficient oil displacements, understanding the displacements requires knowledge of the complex phase behavior involving CEPs. Also, to generalize the results for a limited number of reservoir oils presented in section 6.1, we must investigate effects of phase behavior on displacement efficiency at different thermodynamic conditions, such as temperature, pressure, and oil component properties.

In this section, we systematically investigate the complex three-phase behavior at different pressures, temperatures, and oil component properties. Orr *et al.* (1981) and Gardner *et al.* (1981) concluded that ternary representation can be used to model low-temperature oil displacements by CO_2. However, a ternary system does not have sufficient degrees of freedom to develop CEPs. We use four components to represent the three-phase behavior. Four is the minimum number of components to model CEPs in composition space as predicted by the phase rule for critical points that is derived in section 6.2.1.

6.2.1 Method for Systematic Investigation

Phase behavior of a fluid consisting of N_C components can be mathematically considered as a function that spans (N_C + 1) dimensions; temperature, pressure, and (N_C − 1) component mole fractions. Because of the high dimension, the phase behavior of solvent/reservoir-oil mixtures is conventionally presented on a pseudo-binary *P-x* diagram. However, such a *P-x* diagram does not fully describe the space for analyzing gas injection processes because it represents phase behavior only along the mixing line between the two pseudo-components (*i.e.*, oil and gas).

Orr *et al.* (1981, 1983) and Gardner *et al.* (1981) used ternary diagrams to model three-phase behavior of CO_2/low-temperature-oil mixtures and studied the effect of the L_2 phase on the displacement efficiency. They did not identify CEP behavior because a tie-triangle is invariant in a ternary diagram.

The minimum number of components required to model critical points can be determined by considering the number of equations and the number of phase rule variables. We provide a simple derivation for the phase rule for critical points. We consider a critical point where n of N_P phases are identical (critical) in the presence of the other $(N_P - n)$ phases. The equations for the critical state are identical with those for $(N_P - n + 1)$ equilibrium phases except for the criticality conditions. The mathematical conditions for a critical point were developed by Prigogine and Defay (1954), and an efficient calculation method for determining critical points was developed by Heidemann and Khalil (1980) and Michelsen and Heidemann (1988). The equations for a critical state consist of $(N_P - n)$ equations for phase temperatures, $(N_P - n)$ equations for phase pressures, $N_C(N_P - n)$ equations for fugacities, $2(n - 1)$ criticality constraints, and $(N_P - n + 1)$ summation conditions (2.19). That is, there are $(N_C + 2)(N_P - n) + N_P + n - 1$ equations. The phase rule variables are $(N_P - n + 1)$ phase temperatures, $(N_P - n + 1)$ phase pressures, and $N_C(N_P - n + 1)$ phase component mole fractions. There are $(N_C + 2)(N_P - n + 1)$ variables. Subtraction of the number of equations from the number of variables yields the degree of freedom (F)

$$F = N_C - N_P + 3 - n. \tag{6.1}$$

The degree of freedom is $(N_C - 2)$ at CEPs according to equation (6.1). The minimum number of components required is four $(2 = N_C - 2)$ to be able to model three-phase behavior involving CEPs at a given temperature and pressure. Phase behavior for four components can be visualized on a series of quaternary diagrams at different temperatures and pressures. A three-phase region has one degree of freedom at a given temperature and pressure for four components. Therefore, a three-phase region is a volume in a quaternary diagram.

Figure 6.31 shows a schematic of a three-phase region for a quaternary system at a fixed temperature and pressure. The three-phase region consists of an infinite number of tie-triangles, and it is bounded by the two CEP tie-lines. A tie-triangle changes its shape and size between the two CEP tie-lines in composition space. Two tie-triangles are shown in Figure 6.31 to illustrate tie-triangles near the UCEP and LCEP. A tie-triangle becomes elongated near a CEP because two of the three phase-compositions merge at a CEP. A CEP is not a point in composition space. It is a tie-line where two of the three phases are critical in the presence of the other non-critical phase. This critical phase behavior is historically called a critical endpoint because it occurs at an endpoint of the three-phase curve on a *P*-*T* projection of the *P*-*T*-*x* diagram for binary mixtures.

We use the Peng-Robinson EOS to provide an overview of the three-phase behavior in *P*-*T*-*x* space. Use of an EOS for this purpose provides a purely theoretical investigation, and it does not lead to quantitatively correct predictions. However, the qualitative trend should be correct considering the pioneer research by van Konynenburg and Scott (1968, 1970, 1980) and related research conducted later by various authors (see section 2.2.6.1). Use of an EOS to obtain a qualitative overview of fluid phase behavior has been applied for fundamental research on supercritical fluid extraction (van Pelt 1992). This approach is also useful to study systematically the effect of oil properties on three-phase behavior and displacement efficiency, which would be unacceptably expensive and time-consuming to study experimentally. Applying this approach, we can investigate the mechanism for high efficiency of low-temperature oil displacements by CO_2 and understand the complex three-phase behavior in the following high-dimensional space: temperature, pressure, composition, and oil properties.

We make a four-component EOS fluid model based on the original BSB oil (105°F) that consists of seven components as shown in Table 6.1. Three pseudo-components $C_{2\text{-}3}$, $C_{4\text{-}6}$, and $C_{7\text{-}15}$ are grouped into one pseudo-component C_{H1}. Two pseudo-components $C_{16\text{-}27}$ and C_{28+} are grouped into C_{H2} for the four-component model. This four-component (quaternary) model for the BSB oil is referred to as the BSB-Q oil. The EOS parameters for the BSB-Q oil are given in Table 6.4. The critical temperatures and pressures for C_{H1} and C_{H2} are adjusted to match the oil density within a pressure range from 14.7 to 2500 psia, which contains the operating pressures. Similarly, the critical volumes for C_{H1} and C_{H2} are adjusted to match the oil viscosity. The BICs for C_{H1} and C_{H2} are calculated based on the mole fraction weighted average of BICs for the member components. The P-x diagram for the pseudo-binary mixture of the BSB-Q oil and injection gas given in Table 6.4 is shown in Figure 6.32. The three-phase region exists in a pressure range between 1190 and 1485 psia at solvent mole fractions from 63 to 97%. Figure 6.32 also shows a projection of the P-T-x diagram onto a P-T diagram for the pseudo-binary mixture of the BSB-Q oil and injection gas. The three-phase equilibrium occurs near the binodal curve of the injection gas. The critical locus of L=V critical points gradually changes its behavior to L_1=L_2. This continuous transition can be observed for binary systems CO_2+n-alkane from n-C_{14} through n-C_{21} (*e.g.*, Alwani and Schneider 1976, Miller and Luks 1989).

In the subsequent sections, the BSB-Q oil is considered as the base oil. First, we examine pressure and temperature effects on three-phase behavior in the BSB-Q composition space and on the efficiency of the BSB-Q oil displacements. We then make several different oils based on the BSB-Q oil, changing the properties of the heavy components C_{H1} and C_{H2}. Those oils are compared with the BSB-Q oil in terms of three-phase behavior and displacement efficiency to see the effect of oil component properties.

6.2.2 Effect of Pressure on Phase Behavior and Displacement Efficiency

In this section, we study the effect of pressure on three-phase behavior and oil displacements using the BSB-Q oil shown in Table 6.4. First, variation of the three-phase region with changing pressure is presented on a series of quaternary diagrams at the reservoir temperature of 105°F. Then, simulations of one-dimensional displacements are preformed to see the effect of pressure on the composition path taken and displacement efficiency.

6.2.2.1 Effect of Pressure on Three-Phase Behavior

The phase equilibrium algorithms developed in Chapters 3, 4, and 5 are used to find robustly the three-phase region in a quaternary diagram. Figure 6.33 shows the three-phase region at various pressures at 105°F for the BSB-Q component system (Table 6.4). The three-phase region does not exist in composition space at pressures below about 1028 psia. It appears on the C_1-free plane at a pressure slightly above 1028 psia. The three-phase region enters the quaternary diagram with the LCEP tie-line as the front edge. As pressure increases, the three-phase region becomes larger, and the UCEP tie-line appears on the C_1-free plane at a pressure between 1150 and 1200 psia. The entire three-phase region is now contained in the quaternary diagram. At even higher pressures, the three-phase region exists at lower CO_2 concentrations and becomes smaller in size. The three-phase region eventually disappears at the tricritical point that occurs at a pressure above 3080 psia at a CO_2 concentration near 0.5. We emphasize here that we are interested in a qualitative trend of the three-phase behavior, instead of specific values for pressure, temperature, and phase compositions predicted.

In principle, a tricritical point is where three phases simultaneously become identical (Widom 1973, Griffiths 1974). The tricritical point shown in Figure 6.33 forms when the tie-lines at UCEP and LCEP merge, and it is classified as an unsymmetrical tricritical point (Knobler and Scott 1984). For hydrocarbon mixtures, Wagner *et al.* (1968) observed the unsymmetrical tricritical point for a ternary mixture of $C_2/n\text{-}C_{16}/n\text{-}C_{20}$.

The series of quaternary diagrams suggest that a pseudo-binary *P*-*x* diagram commonly used to represent phase behavior for injection-gas/reservoir-oil mixtures provides only a small portion of phase behavior. Even when a three-phase region does not appear on a *P*-*x* diagram, it might exist as a large region in composition space that does not intersect the mixing line.

Equation (6.1) predicts that the tricritical point shown in Figure 6.33 has one degree of freedom in *P*-*T*-*x* space. That is, when temperature is specified to be 105°F, a tricritical point is a point in *P*-*x* space if it exists. This is confirmed in Figure 6.33.

Figure 6.34 shows a projection of the midpoints of CEP tie-lines at 105°F onto the CO_2-free plane of the quaternary diagram. The UCEP behavior occurs at higher C_{H2} concentrations than the LCEP behavior. This is consistent with experimental results on phase behavior of the homologous series of CO_2/n-alkane mixtures (Schneider 1968, Hottovy *et al.* 1981, Fall *et al.* 1985, Galindo and Blas 2002). Specifically, the LCEP or L_1=L_2-V behavior occurs in mixtures CO_2+*n*-alkane from $n\text{-}C_7$ through $n\text{-}C_{13}$. The UCEP or L_1-L_2=V behavior occurs in mixtures CO_2+*n*-alkane from $n\text{-}C_{13}$ through $n\text{-}C_{21}$. That is, for CO_2/n-alkane binary mixtures, the LCEP occurs for lighter hydrocarbons and the UCEP occurs for heavier hydrocarbons. The LCEP behavior in the quaternary diagrams in Figure 6.33 can be considered to reflect the phase behavior between CO_2 and C_{H1}, and the UCEP behavior to reflect the phase behavior between CO_2 and C_{H2}. This qualitative accuracy of a cubic EOS, the Peng-Robinson EOS, is the basis for our approach as explained in section 6.2.1.

6.2.2.2 Effect of Pressure on Displacement Efficiency

We now perform a series of simulations of one-dimensional displacements for the BSB-Q oil and injection gas given in Table 6.4. Figure 6.32a shows the *P*-*x* diagram at the reservoir temperature of 105°F for mixtures of the BSB-Q oil and injection gas. The three-phase region exists at pressures between 1190 and 1485 psia at solvent mole fractions from 63 to 97% on the *P*-*x* diagram. Figure 6.32b shows the *P*-*T* projection of the *P*-*T*-*x* diagram for the pseudo-binary mixture of the BSB-Q oil and injection gas. The three-phase region exists near the gas critical point.

The reservoir properties for the simulations are given in Table 6.2. The displacement pressures are 1150, 1200, 1250, 1300, and 1350 psia, and the reservoir temperature is fixed to be 105°F. All the displacements exhibit three-hydrocarbon-phase flow. Figure 6.35 shows the oil recoveries for the five displacements. At the displacement pressures of 1300 and 1350 psia, the displacements are almost piston-like resulting in a recovery factor of 98%. At 1200 psia, the displacement is not as efficient because the recover factor is 80%. The relatively low displacement efficiency is in contrast to Orr and Jensen (1984) and Creek and Sheffield (1993), who related the occurrence of high displacement efficiency to the appearance of the L_2 phase on the *P*-*x* diagram as part of L_1-L_2-V equilibrium phases. At 1200 psia, the three-phase region appears on the mixing line as shown in Figure 6.32, but high displacement efficiency is not achieved. This is because a *P*-*x* diagram does not represent the phase behavior on the composition path actually observed during the displacement.

For 1200 psia, Figures 6.36 and 6.37 give the profiles of the component concentrations and the phase saturations, respectively, at 0.5 HCPVI. Figure 6.38 shows the composition path, tie-lines, and tie-triangles along the composition path. The composition path shown in Figure 6.38 connects the discrete points of overall compositions simulated at all grid cells. That is, it is an approximate composition path. At the displacement front, the methane bank generates the L_1-V two-phase region traveling ahead of the three-phase region. The front of the three-phase region is where the CO_2 concentration becomes large enough to exhibit the three-hydrocarbon-phase equilibrium at 105°F (also see Figure 6.33f for the entire three-phase region). After the three-phase region disappears along the composition path, the C_{H1} concentration becomes zero. The L_1-V two-phase exists over the portion behind the three-phase region. The oscillation near the injection well along the gas tie-line is an artifact caused by numerical simulation.

For 1250 psia, Figures 6.39 and 6.40 show the profiles of the component concentrations and the phase saturations, respectively, at 0.5 HCPVI. Figure 6.41 shows the composition path and two- and three-phase regions along the composition path. The entire three-phase region is shown in Figure 6.33g. The characteristics of the profiles are similar to those for 1200 psia, but the tie-triangles at the tail and front of the three-phase region in Figure 6.41 are smaller than those at 1200 psia in Figure 6.38. Considering the size of the tie-triangles, the composition path at 1250 psia goes closer to the CEPs than that at 1200 psia, resulting in improved oil recovery.

For 1300 psia, Figures 6.42 and 6.43 show the profiles of the component concentrations and the phase saturations, respectively, at 0.5 HCPVI. The saturation profiles show a sharp reduction in the L_1 phase saturation and a sharp increase in the L_2 phase saturation at the front of the three-phase region. At the tail of the three-phase region, the L_2 phase saturation sharply decreases to zero and the V phase saturation increases as much. That is, the L_2 phase is vaporized into the V phase to disappear at the tail of the three-phase region. Figure 6.44 shows the composition path and two- and three-phase regions along the composition path (see Figure 6.33h for the entire three-phase region). The significantly elongated tie-triangle at the tail of the three-phase region indicates that the composition path goes very near the UCEP tie-line. The tie-triangle at the front of the three-phase region has a large area indicating that the composition is not as close to the LCEP tie-line as to the UCEP tie-line.

In Figure 6.44, the composition path connects discrete points of overall compositions at the grid cells. This is why the shock from the one-phase region to the two-phase region apparently does not occur along a tie-line extension. Actually, the shock must occur along a tie-line extension as proven by Larson (1979).

Figures 6.45, 6.46, and 6.47 compare profiles of phase composition distances ($d_{L1\text{-}V}$, $d_{L1\text{-}L2}$, and $d_{L2\text{-}V}$) at 0.5 HCPVI at the three different pressures 1200, 1250, and 1300 psia. The L_1 phase is highly immiscible with the V phase over the displaced region for all the displacements as indicated by $d_{L1\text{-}V}$. At the front of the three-phase region, the degree of criticality between the L_1 and L_2 phases increases because mass transfer between the phases becomes significant. The behavior of $d_{L2\text{-}V}$ significantly changes with pressure. As pressure increases, the composition path goes closer to the UCEP tie-line. The value of $d_{L2\text{-}V}$ asymptotically decreases at the tail of the three-phase region for 1300 psia, resulting in 98% oil recovery.

Our quaternary representation qualitatively agrees with the original seven-component representation in that complex three-phase behavior associated with CEPs is properly predicted. This can be confirmed by comparing the phase composition distances for the BSB oil (Figures 6.13, 6.14, and 6.15) and those for the BSB-Q oil

(Figures 6.45, 6.46, and 6.47). Ternary representation that was proposed in the literature (Orr *et al.* 1981, Gardner *et al.* 1981, Orr *et al.* 1983) cannot model CEPs because a tie-triangle is invariant in a ternary diagram. Equation (6.1) predicts this problem with ternary representation, where $F = 1$ when $N_C = 3$, $N_P = 3$, and $n = 2$. That is, CEPs have only one degree of freedom in *P-T-x* space for ternary mixtures.

Figure 6.48 shows recovery factors, and minimum values of $d_{\mathrm{L1\text{-}L2}}$ and $d_{\mathrm{L2\text{-}V}}$ for five different pressures. An increase in pressure from 1300 to 1350 psia little changes the displacement efficiency. Actually, the oil recovery is slightly lower for 1350 psia than for 1300 psia. The minimum values of $d_{\mathrm{L1\text{-}L2}}$ and $d_{\mathrm{L2\text{-}V}}$ do not have a monotonic trend with respect to the displacement pressure. The minimum value of $d_{\mathrm{L2\text{-}V}}$, however, monotonically decreases with the increasing recovery factor. At the displacement pressures 1150, 1200, 1250, and 1300 psia, the recovery factor becomes larger when the composition path goes closer to the UCEP tie-line. The increase in pressure from 1300 psia to 1350 psia results in a slightly larger minimum value of $d_{\mathrm{L2\text{-}V}}$ and, therefore, a slightly smaller recovery factor. Those results show that the proximity of the composition path to the UCEP tie-line controls the displacement efficiency although the proximity to the LCEP tie-line is also important for efficient extraction of oil components by the L_2 phase.

Figure 6.49 gives a schematic for the role of CEP behavior in the BSB-Q oil displacement at 1300 psia, which results in a recovery factor of 98% at 2.0 HCPVI. At the front of the three-phase region, oil components are efficiently extracted by the L_2 phase because of near miscibility between the L_1 and L_2 phases (*i.e.*, near LCEP behavior). At the tail of the three-phase region, the L_2 phase disappears to result in the L_1-V two-phase region behind the three-phase region. When it disappears, the L_2 phase must be vaporized into the V phase for high displacement efficiency, instead of condensed into the L_1 phase. This is because the L_1 phase saturation in the L_1-V two-phase region must be minimized for high displacement efficiency. When the composition path goes closer to the UCEP tie-line, the L_1 phase saturation in the L_1-V two-phase region becomes smaller, resulting in higher displacement efficiency.

Figure 6.50 shows component mole fractions in phases for the BSB-Q oil displacement at 1300 psia. We calculate *K*-values based on the component mole fractions shown in Figure 6.50. There are three kinds of *K*-values, $K_{i\mathrm{V/L1}}$, $K_{i\mathrm{V/L2}}$, and $K_{i\mathrm{L2/L1}}$ ($i = 1,\ldots,N_C$), which are defined as

$$K_{i\mathrm{V/L1}} = x_{i\mathrm{V}} / x_{i\mathrm{L1}}$$
$$K_{i\mathrm{V/L2}} = x_{i\mathrm{V}} / x_{i\mathrm{L2}}$$
$$K_{i\mathrm{L2/L1}} = x_{i\mathrm{L2}} / x_{i\mathrm{L1}} .$$

As mentioned in section 6.1.1, use of *K*-values is misleading to see the level of miscibility between phases. *K*-values, however, are useful to see mass transfer of components between phases.

Figure 6.51 gives the *K*-value profiles for the BSB-Q oil displacement at 1300 psia. As $K_{\mathrm{V/L1}}$ indicates, CO_2 is condensed from the V into L_1 phase in the two-phase region ahead of the three-phase region, while CO_2 is vaporized from the L_1 into V phase in the two-phase region behind the three-phase region. In the three-phase region, $K_{\mathrm{V/L2}}$ and $K_{\mathrm{L2/L1}}$ show that CO_2 is simultaneously extracted from the V and L_1 phases into the L_2 phase.

Gardner *et al.* (1981) concluded that low-temperature oil displacement by CO_2 is a vaporizing gas drive, in which oil components are extracted (or “vaporized”) into the L_2 phase. Metcalfe and Yarborough (1979) stated that low-temperature oil displacement by CO_2 is a condensing gas drive, where CO_2 is condensed into the L_1 phase. The complex mass transfer among the three phases shown in Figure 6.51 was not identified by these authors.

Figure 6.51 also demonstrates that use of K-values is misleading to see the degree of miscibility between phases. One may consider based on the $K_{V/L1}$ profiles that the shortest tie-line occurs at a dimensionless distance of 0.365, where L_1-V two phases are present right behind the three-phase region. However, the shortest tie-line actually occurs at a dimensionless distance of 0.443, which is right ahead of the three-phase region. The $K_{V/L1}$-values are (1.66, 2.66, 1.22×10^{-1}, 1.77×10^{-4}) at 0.365 and (1.18, 2.66, 5.77×10^{-2}, 3.58×10^{-5}) at 0.443. However, $d_{L1\text{-}V}$ is 0.472 at 0.365 and 0.245 at 0.443. $d_{L1\text{-}V}$ in Figure 6.47 correctly shows that the shortest tie-line is at 0.443.

LaForce (2005) studied various displacements with ternary mixtures involving three-phase flow using the method of characteristics. She concluded that miscibility cannot be developed when the composition path goes through a three-phase region. However, nearly perfect oil recovery is achieved at 1300 and 1350 psia (see Figure 6.35) with only 500 grid cells in the BSB-Q oil displacements shown above. Also, in our displacements using four components, the CEPs exist in composition space, which LaForce (2005) did not consider. That is, the question arises whether or not miscibility can be developed for a composition path that goes through a three-phase region involving the CEPs.

To address this question, we increase the numerical Peclet number (*i.e.*, decrease the level of numerical dispersion) by increasing the number of grid cells used for the displacement at 1350 psia. The Peclet number is approximately twice the number of grid cells for the simulations considered here because UTCOMP uses an IMPES-type formulation with small time step sizes and the grid cells are equally spaced for the one-dimensional simulations.

Figure 6.52 shows the oil recoveries at 2.0 HCPVI with different Peclet numbers (N_{Pe}). As in the conventional gas flooding involving L-V two-phase equilibrium, dispersion significantly affects the displacement efficiency. For example, at 1350 psia, the recovery factor is 99% when N_{Pe} is 4000 ($1/N_{Pe} = 2.5 \times 10^{-4}$), while it decreases to 76% when N_{Pe} is 10 ($1/N_{Pe} = 0.1$). A similar effect of dispersion is observed for the displacement pressures of 1200 and 1250 psia. Figure 6.53 extrapolates the oil recovery for 1350 psia to the infinite Peclet number (*i.e.*, $1/N_{Pe} \rightarrow 0.0$) to estimate the recovery factor with no numerical dispersion. The extrapolation to the infinite Peclet number results in a recovery factor below 99.5%, which should be 100% at the thermodynamic MMP (see section 2.2.6.3). This indicates that complete miscibility may not be achieved even with no numerical dispersion for the displacement considered here.

We do not consider oil displacements where a tricritical point exists in composition space. Analogy to the conventional gas flooding involving L-V two phases suggests that existence of a tricritical point is necessary to develop miscibility for a composition path that goes through a three-phase region. Equation (6.1) predicts that at least five components must be used to model a tricritical point in composition space at a fixed temperature and pressure. A composition path that goes through a tricritical point should be investigated for potential miscibility development although it is out of scope of this dissertation.

6.2.3 Effect of Temperature on Phase Behavior and Displacement Efficiency

In this section, we examine the effect of temperature on three-phase behavior and oil displacements using the BSB-Q oil shown in Table 6.4. First, variation of the three-phase region with changing temperature is presented on a series of quaternary diagrams at 1300 psia. Then, simulations of one-dimensional displacements at two different temperatures 90°F and 120°F are compared with those at 105°F presented in section 6.2.2.

6.2.3.1 Effect of Temperature on Three-Phase Behavior

Figure 6.54 shows the three-phase region at various temperatures at 1300 psia for the BSB-Q system given in Table 6.4. The three-phase region does not exist in composition space at temperatures above about 130°F. At approximately 130°F, the three-phase region appears on the C_1-free plane, and it begins to enter the quaternary diagram with the LCEP tie-line as the front edge. As temperature decreases, the UCEP tie-line appears and the entire three-phase region becomes contained in the quaternary diagram. The angle of the LCEP tie-line with respect to the CO_2-free plane significantly changes with temperature. As temperature becomes lower, the three-phase equilibrium occurs at lower CO_2 concentrations. At approximately 70°F, the UCEP disappears on the C_{H1}-free plane, resulting in a tie-triangle on that plane. However, the UCEP tie-line appears again on the C_{H1}-free plane at approximately −128°F. Then, the three-phase region moves toward the CO_2-free plane, and it eventually disappears on that plane at approximately −309°F. For the conditions studied here, there is no tricritical point found in composition space. As mentioned earlier, the specific values for temperature and phase compositions have little significance because we are interested in the qualitative trend of the phase behavior with respect to thermodynamic parameters, *e.g.*, temperature in this section.

Figure 6.55 shows the projection of the midpoints of the CEP tie-lines at varying temperature onto the CO_2-free plane at 1300 psia. The UCEP behavior is predicted at higher C_{H2} concentrations than the LCEP behavior. As mentioned in section 6.2.2.1, this is consistent with the fact that the UCEP occurs for heavier hydrocarbons and the LCEP occurs for lighter hydrocarbons for CO_2/*n*-alkane binary mixtures.

6.2.3.2 Effect of Temperature on Displacement Efficiency

In this section, we examine the effect of temperature on displacement efficiency. We simulate one-dimensional displacements of the BSB-Q oil by the injection gas given in Table 6.4 at two different reservoir temperatures 90°F and 120°F. The results are compared with those at 105°F presented in section 6.2.2.2. The reservoir properties are shown in Table 6.2.

The P-x diagram at 90°F is shown in Figure 6.56. The three-phase region exists in a pressure range from 998 to 1310 psia at solvent concentrations between 0.64 and 0.99. Figure 6.57 shows oil recoveries at 90°F at four different pressures 1000, 1050, 1100, and 1150 psia. The displacement at 90°F and 1150 psia results in a high displacement efficiency of 97% at 2.0 HCPVI. Figures 6.58 and 6.59 show the profiles of phase saturations and phase composition distances ($d_{\mathrm{L1\text{-}V}}$, $d_{\mathrm{L1\text{-}L2}}$, and $d_{\mathrm{L2\text{-}V}}$) at 0.5 HCPVI at 1050 psia. Figure 6.60 gives the composition path and the tie-triangles and tie-lines along the composition path at 1050 psia. Similarly, Figures 6.61, 6.62, and 6.63 are for 1100 psia, and Figures 6.64, 6.65, and 6.66 are for 1150 psia. As shown in Figures 6.59, 6.60, 6.62, 6.63, 6.65, and 6.66, the two-phase regions ahead of and behind the three-phase region exhibit significant immiscibility. This is true even for the displacement at 1150 psia which results in a recovery factor of 97%. $d_{\mathrm{L1\text{-}L2}}$ decreases with increasing pressure at the front of the three-phase region. As indicated by $d_{\mathrm{L2\text{-}V}}$, the L_2 phase becomes closer to the V phase at the tail of the three-phase region as pressure increases. Figure 6.67 confirms that the recovery factor increases as the composition path goes closer to the UCEP tie-line and, to a lesser extent, the LCEP tie-line for the displacements at 90°F.

The distance between the L_2 and V phase compositions ($d_{\mathrm{L2\text{-}V}}$) does not exhibit an asymptotic reduction near the tail of the three-phase region even for the high displacement efficiency at 1150 psia. This is in contrast to the displacement at 105°F and 1300 psia which results in 98% oil recovery (see Figure 6.47). This difference in three-phase behavior along the composition path results from the lower reservoir temperature. The NWE oil displacements at 83°F (see Figure 6.22), which is the lowest reservoir temperature studied in this dissertation, also do not exhibit an asymptotic reduction of $d_{\text{L2-V}}$ for high displacement efficiency.

For 120°F, the *P-x* diagram is given in Figure 6.68. The three-phase region exists in a pressure range from 1411 to 1660 psia at solvent concentrations between 0.63 and 0.91. Figure 6.69 shows oil recoveries at 120°F for four different displacement pressures 1350, 1400, 1450, and 1500 psia. All the displacements involve three-hydrocarbon-phase flow. The displacements at 1450 and 1500 psia result in 98% oil recovery (97.89% at 1450 psia and 97.80% at 1500 psia). Figures 6.70 and 6.71 show the profiles of phase saturations and phase composition distances ($d_{\text{L1-V,}}$ $d_{\text{L1-L2}}$, and $d_{\text{L2-V}}$) at 0.5 HCPVI at 1400 psia. Figure 6.72 shows the composition path and two- and three-phase regions along the composition path at 1400 psia. Similarly, Figures 6.73, 6.74, and 6.75 are for 1450 psia and Figures 6.76, 6.77, and 6.78 are for 1500 psia. The two-phase regions ahead of and behind the three-phase region consist of the L_1 and V phases, which are highly immiscible with each other. As shown by $d_{\text{L2-V}}$, the L_2 and V phase compositions asymptotically become close to each other at the tail of the three-phase region at 1450 and 1500 psia, which result in 98% oil recovery.

Figure 6.79 shows the oil recoveries and minimum values of $d_{\text{L1-L2}}$ and $d_{\text{L2-V}}$ as functions of displacement pressure. The minimum distance between the L_2 and V phase compositions ($\min\{d_{\text{L2-V}}\}$) has a negative correlation with the recovery factor (note that the recovery factor is slightly smaller for 1500 psia than for 1450 psia). The results indicate that the UCEP controls the displacement efficiency.

Figure 6.80 summarizes the oil recoveries at 2.0 HCPVI for a series of displacements at different pressures at reservoir temperatures 90, 105, and 120°F. The results show that oil recovery significantly depends on reservoir temperature. This is consistent with the observations of Holm and Josendal (1974), Yellig and Metcalfe (1980), and Orr and Jensen (1984), who related the CO_2-MMP to reservoir temperature. The displacement efficiency depends on reservoir temperature because the three-phase behavior is sensitive to temperature as shown in Figure 6.54.

However, what controls the displacement efficiency remains the same, independent of reservoir temperature. Figure 6.81 shows the recovery factors at 2.0 HCPVI with respect to the minimum value of $d_{\mathrm{L2\text{-}V}}$ along the composition paths at different displacement pressures and reservoir temperatures for the BSB-Q oil displacements. Similarly, Figure 6.82 is given for the minimum value of $d_{\mathrm{L1\text{-}L2}}$. Figure 6.81 confirms that the BSB-Q oil displacements achieve higher displacement efficiency when the composition path goes closer to the UCEP tie-line. A composition path also should go near the LCEP tie-line for high displacement efficiency so that the L_2 phase can extract oil components efficiently. Figure 6.82, however, shows that a composition path closer to the LCEP tie-line does not necessarily result in a higher recovery factor. The value of $\min\{d_{\mathrm{L2\text{-}V}}\}$ (*i.e.*, proximity to the UCEP tie-line) is more important for high displacement efficiency than the value of $\min\{d_{\mathrm{L1\text{-}L2}}\}$ (*i.e.*, proximity to the LCEP tie-line) based on the results presented.

Figure 6.83 is given to estimate the recovery factor when overall composition passes the UCEP tie-line for the BSB-Q oil displacements. The extrapolation is based on the four data points above a recovery factor of 95% in Figure 6.81. The extrapolation suggests that complete miscibility (*i.e.*, 100% oil recovery) may not be achieved even when the composition goes through the UCEP tie-line for the BSB-Q oil displacements studied here.

6.2.4 Effect of Oil Property on Phase Behavior and Displacement Efficiency

To see the effect of oil property on three-phase behavior and displacement efficiency, we change the two components C_{H1} and C_{H2} of the BSB-Q oil in a systematic way based on the fluid characterization procedure of Pedersen *et al.* (1984ab, 1985, 1992, 2004, 2007). We then study three-phase behavior and displacements for the new oils, which are different from the BSB-Q oil only in the properties of C_{H1} and C_{H2}. The results for the different oils are compared with each other to see the oil property effect.

6.2.4.1 Systematic Procedure for Different Oil Properties

EOS parameters for heavy fractions are calculated based on the carbon numbers in the fluid characterization of Pedersen *et al.* We do not have carbon numbers for the two components C_{H1} and C_{H2} for the BSB-Q oil. Therefore, we back-calculate to obtain the carbon numbers from the molecular weights using the equation of Pedersen *et al.* $MW_i = 14C_i - 4$, where MW_i and C_i are the molecular weight and carbon number of component *i*, respectively. The carbon numbers calculated for C_{H1} and C_{H2} are 7.32 and 25.59, respectively.

We generate three different oils; one lighter oil (BSB-QL) and two heavier oils (BSB-QH1 and BSB-QH2) compared with the BSB-Q oil. For the BSB-QL oil, the carbon numbers of C_{H1} and C_{H2} in the BSB-Q oil are multiplied by 0.75, resulting in the carbon numbers 5.49 and 19.20. For the BSB-QH1 oil, the multiplication factor is 1.25 to calculate the carbon numbers 9.15 and 31.98 for C_{H1} and C_{H2}. For the BSB-QH2 oil, a multiplication factor of 1.5 is used, which results in the carbon numbers 10.98 for C_{H1} and 38.38 for C_{H2}. Those carbon numbers are then used to calculate the EOS parameters, such as T_C, P_C and acentric factors, based on the procedure of Pedersen *et al.* The BICs are the same as those for the BSB-Q oil because there are no widely accepted correlations for BICs for mixtures consisting of more than two components. Viscosity calculations in UTCOMP also require the critical volumes for components. The critical volumes for C_{H1} and C_{H2} are calculated using the correlation of Riazi and Daubert (1980) together with the correlation of Katz and Firoozabadi (1978) for boiling points, which are required in the critical volume calculations. The resulting properties for the BSB-QL, BSB-QH1, and BSB-QH2 oils are summarized in Tables 6.5, 6.6, and 6.7, respectively.

We define a dimensionless parameter ξ for a measure of dissimilarity between the oil and injection gas:

$$\xi = \left[\left(\frac{a_m}{b_m}\right)_{Oil} - \left(\frac{a_m}{b_m}\right)_{Gas}\right] \Big/ \left[\left(\frac{a_m}{b_m}\right)_{Oil} + \left(\frac{a_m}{b_m}\right)_{Gas}\right]. \tag{6.2}$$

In a cubic EOS, behavior of a pure fluid is represented by the attraction parameter ("*a* parameter") and the covolume parameter ("*b* parameter"), which are calculated using T_C, P_C and the acentric factor assigned to the component. For a mixture, the *a* and *b* parameters for the components are used to calculate the parameters for the mixture, a_m and b_m, based on mixing rules with BICs (see section 2.1.5). Those parameters, a_m and b_m, represent phase behavior of the mixture. Therefore, dissimilarity between the oil and injection gas can be measured by the difference between the parameters a_m and b_m for the oil and those for the injection gas, which is calculated by equation (6.2).

van Konynenberg and Scott (1980) introduced three dimensionless parameters to characterize binary mixtures. One of them, which has a similar form to equation (6.2), was defined as

$$\zeta = \left(\frac{a_2}{b_2^2} - \frac{a_1}{b_1^2}\right) \Big/ \left(\frac{a_2}{b_2^2} + \frac{a_1}{b_1^2}\right),$$

where a_i is the attraction parameter for pure component i, and b_i is the covolume parameter for pure component i ($i = 1, 2$).

The main difference between the parameters ξ and ζ is that the parameter ξ given in equation (6.2) can be used for mixtures of more than two components by considering two pseudo-components. For analysis of gas flooding, reservoir oil and injection gas are the two pseudo-components. The parameter ξ is zero when the oil has the same properties as the injection gas, and it tends to 1.0 as the oil becomes heavier. The parameter ξ based on a_m and b_m for the oil and gas is useful as a dissimilarity measure because a_m and b_m are the parameters that directly change the EOS calculations. For example, if carbon numbers for the heavy components were used as a dissimilarity measure, EOS calculation results would depend significantly on the correlations used for T_C, P_C, and acentric factors.

In generating the new oils BSB-QL, BSB-QH1, and BSB-QH2, we changed the parameter ξ, dissimilarity between the oil and injection gas. Changing ξ would lead to different predictions of phase behavior and displacement efficiency. The parameters a_m and b_m for the injection gas are fixed because the injection gas consists of only CO_2 and C_1, for which we do not change the EOS parameters. The parameter ξ using the Peng-Robinson EOS depends on temperature for a fixed oil/gas pair because of the temperature dependence of the attraction parameter. We fixed the reservoir temperature of 105°F for oil property effects to be studied here.

The parameter ξ using the Peng-Robinson EOS at 105°F is calculated to be 0.498 for the BSB-QL/solvent system given in Table 6.5, 0.649 for the BSB-QH1/solvent system given in Table 6.6, and 0.691 for the BSB-QH/solvent given in Table 6.7. For the BSB-Q oil/solvent in Table 6.4, the parameter ξ is 0.573.

6.2.4.2 Effect of Oil Property on Three-Phase Behavior

Figure 6.84 visualizes the three-phase regions at 105°F and 1300 psia in the four different quaternary systems; BSB-QL (ξ = 0.498), BSB-Q (ξ = 0.573), BSB-QH1 (ξ = 0.649), and BSB-QH2 (ξ = 0.691). The three-phase immiscibility increases with ξ in that the length of CEP tie-line increases with ξ.

Figure 6.85a shows the *P-x* diagram at 105°F and *P-T* projection for the pseudo-binary mixture of the BSB-QL oil and injection gas (Table 6.5). Similarly, Figures 6.85b and 6.85c are for the BSB-QH1 oil (Table 6.6) and BSB-QH2 oil (Table 6.7), respectively. The *P-x* diagram and *P-T* projection for the BSB-Q oil were previously presented in Figure 6.32. On the *P-x* diagrams, the two- and three-phase immiscibility increases as ξ increases. For example, the three-phase region exists at solvent mole fractions between 0.71 and 0.93 for the BSB-QL system, while it exists at solvent mole fractions between 0.57 and 0.98 for the BSB-QH2 system. The increasing immiscibility with ξ is more obvious in the *P-T* projections. For the BSB-QL system, the critical locus goes near the critical point of the solvent to exhibit a minimum in pressure. However, as ξ increases, the critical locus systematically shifts to higher temperature, and there is no minimum pressure observed on the critical locus for the BSB-QH2 system. Also, the three-phase region becomes larger as ξ increases.

6.2.4.3 Effect of Oil Property on Displacement Efficiency

We perform simulations of one-dimensional displacements at 105°F for BSB-QL (ξ = 0.498) and BSB-QH2 (ξ = 0.691) at different pressures. The injection gas is the same for all the simulations (CO_2 95% and C_1 5% with EOS parameters shown in Table 6.4). The results are compared with those for BSB-Q (ξ = 0.573), which were presented in section 6.2.2.2.

For the BSB-QL oil, Figure 6.86 shows the oil recoveries for displacement pressures 1150, 1200, and 1250 psia. All the displacements exhibit three-hydrocarbon-phase flow. The displacement at 1250 psia results in a recovery factor of 97%. For the displacement at 1150 psia, the phase saturations and phase composition distances ($d_{\mathrm{L1\text{-}V}},$ $d_{\mathrm{L1\text{-}L2}}$, and $d_{\mathrm{L2\text{-}V}}$) at 0.5 HCPVI are given in Figures 6.87 and 6.88, respectively. Figure 6.89 shows the composition path and two- and three-phase regions along the composition path at 1150 psia. Similarly, Figures 6.90, 6.91, and 6.92 are for the displacements at 1200 psia. Figures 6.93, 6.94, and 6.95 are for the displacements at 1250 psia.

The displacement characteristics are similar to those for the case of the BSB-Q oil except that the BSB-QL oil requires lower pressure to achieve the same displacement efficiency. For the displacement at 1250 psia, the composition at the tail of the three-phase region asymptotically becomes closer to the UCEP tie-line as shown in Figures 6.94 and 6.95. The two-phase regions flowing ahead of and behind the three-phase region exhibit significant immiscibility even for 97% oil recovery at 1250 psia. Figure 6.96 shows the oil recoveries at 2.0 HCPVI and the minimum values of $d_{\mathrm{L1\text{-}L2}}$ and $d_{\mathrm{L2\text{-}V}}$ along the composition paths at different displacement pressures. The displacement becomes more efficient as the composition path goes closer to the UCEP tie-line. This relationship cannot be observed between the recovery factor and proximity to the LCEP tie-line (*i.e.*, $\min\{d_{\mathrm{L1\text{-}L2}}\}$). The results suggest that UCEP behavior controls the displacement efficiency.

For the BSB-QH2 oil, Figure 6.97 shows the oil recoveries at pressures 1300, 1350, and 1400 psia. All the displacements exhibit three-hydrocarbon-phase flow. The displacement at 1400 psia results in 97% oil recovery. Figures 6.98 and 6.99 give the profiles of phase saturations and phase composition distances ($d_{\mathrm{L1\text{-}V}},$ $d_{\mathrm{L1\text{-}L2}}$, and $d_{\mathrm{L2\text{-}V}}$) at 0.5 HCPVI for the displacement at 1300 psia. The tie-lines and tie-triangles along the composition path are shown in Figure 9.100. Similarly, Figures 6.101, 6.102, and 6.103 are for the displacement at 1350 psia. Figures 6.104, 6.105, and 6.106 are for the displacement at 1400 psia.

The BSB-QH2 oil displacement exhibits a wider three-phase region than the BSB-QL oil displacement to achieve a similar displacement efficiency. For example, Figure 6.101 shows that the three-phase region exists from 0.137 to 0.441 in dimensionless distance from the injector for the BSB-QH2 oil displacement at 1350 psia. Figure 6.90 shows that the three-phase region exists from 0.213 to 0.379 at 0.5 HCPVI in the BSB-QL oil displacement at 1200 psia. Both displacements result in the very similar recovery factor of 93%.

What controls the displacement efficiency is again the UCEP behavior for the BSB-QH2 oil displacement. Figures 6.105 and 6.106 show that the composition path at 1400 psia goes very near the UCEP tie-line at the tail of the three-phase region. For lower pressures, Figures 6.99, 6.100, 6.102, and 6.103 show that the composition at the tail of the three-phase region is not close to the UCEP tie-line. The two-phase regions ahead of and behind the three-phase region are far from the L_1-V criticality over the displaced region at all displacement pressures. Figure 6.107 shows oil recoveries at 2.0 HCPVI and minimum values of $d_{\mathrm{L1\text{-}L2}}$ and $d_{\mathrm{L2\text{-}V}}$ along the composition path. The minimum value of $d_{\mathrm{L1\text{-}L2}}$ is insensitive to the displacement pressure, while the recovery factor becomes higher when the minimum value of $d_{\mathrm{L2\text{-}V}}$ becomes smaller. Those results confirm that the UCEP behavior controls the displacement efficiency.

Figure 6.108 summarizes the relationship between the oil recoveries at 2.0 HCPVI and proximity of the composition path to the UCEP tie-line, $\min\{d_{\mathrm{L2\text{-}V}}\}$, for the displacements of BSB-QL, BSB-Q, and BSB-QH2 at 105°F. The plots confirm that those displacements become more efficient when the composition path goes closer to the

UCEP tie-line. The perfect displacement efficiency may not be achieved even when the composition path goes through the UCEP tie-line, considering the plots near 100% oil recovery. Figure 6.109 shows that displacement efficiency is less correlated with proximity of the composition path to the LCEP tie-line than with proximity to the UCEP tie-line, although LCEP behavior helps the L_2 phase extract efficiently oil components.

The composition paths at 1300 psia and 105°F for the BSB-QL oil (Figure 6.110), BSB-Q (Figure 6.44), BSB-QH2 oil (Figure 6.100) demonstrate that the oil properties significantly affect the displacements because of the different three-phase behaviors encountered. As ξ decreases at a fixed temperature and pressure, the composition path goes closer to the UCEP tie-line resulting in more efficient displacement. This is in contrast to Yellig and Metcalfe (1980), who concluded that the efficiency of low-temperature oil displacements by CO_2 is little affected by oil properties. Figure 6.111 shows that the displacement pressure which results in a recovery factor of 97% at 2.0 HCPVI (P_1 in Figure 6.111) increases with the dissimilarity between the oil and injection gas (*i.e.*, ξ defined in equation (6.2)). The oil properties affect the displacement efficiency because it can significantly change the three-phase behavior and, therefore, the composition path taken.

Figure 6.111 also shows the minimum pressures at which three phases appear on *P*-*x* diagrams (P_2 in Figure 6.111) for different values for ξ. At these pressures, the mixing line between the oil and injection gas is tangent to the three-phase region in composition space. P_2 is lower than P_1 for the four oils studied here. The difference between the two pressures, $P_1 - P_2$, becomes larger as ξ increases. The difference is 63 psi for $\xi = 0.498$ (BSB-QL) and 159 psi for $\xi = 0.691$ (BSB-QH2). Orr and Jensen (1984) and Creek and Sheffield (1993) considered the efficiency of low-temperature oil displacement by CO_2 is related to the appearance of three phases on a *P*-*x* diagram.

However, displacement efficiency is determined by interaction between flow and phase behaviors, instead of phase behavior on a *P-x* diagram. Therefore, the minimum pressure for three phases on a *P-x* diagram can be in large error for estimation of CO_2-MMP.

6.3 SUMMARY AND CONCLUSIONS

We presented the first detailed study of the complex three-phase behavior that occurs during low-temperature oil displacements by CO_2 solvent. Simulations of one-dimensional oil displacements were performed for three different oils from west Texas. We used a compositional simulator capable of robust three-phase equilibrium calculations to derive the mechanism for high displacement efficiency. The effects of three-phase behavior on displacement efficiency were systematically investigated using four-component EOS fluid models with varying pressure, temperature, and oil component properties. The quaternary representation enabled us to visualize the complex three-phase behavior associated with critical endpoints. The conclusions are as follows:

1. High efficiency of low-temperature oil displacements by CO_2 solvent occurs when the composition path goes near the upper critical endpoint (UCEP) tie-line and, to a lesser extent, the lower critical endpoint (LCEP) tie-line. LCEP behavior at the front of the three-phase region results in efficient extraction of oil components by the L_2 phase. The L_2 phase is vaporized into the V phase when it disappears at the tail of the three-phase region because of UCEP behavior. This vaporization of the L_2 phase result in low L_1 phase saturation in the swept zone; *i.e.*, high displacement efficiency. High displacement efficiency from the CEP behavior occurs even when two-phase regions exhibit significant immiscibility. Because of the CEP behavior, CO_2 is simultaneously extracted from the V and L_1 phases into the L_2 phase within the three-phase region.

2. At least four components must be used for the EOS fluid model to develop CEPs in composition space at a fixed temperature and pressure. The quaternary representation provides qualitatively correct characteristics of the low-temperature oil displacements by CO_2 solvent studied in this chapter.
3. Complete miscibility may not be developed for a composition path that goes through a three-phase region without considering the existence of a tricritical point.
4. Reservoir temperature and oil properties can significantly affect the efficiency of low-temperature oil displacements by CO_2 solvent because their effects on the three-phase behavior lead to a significantly different composition path taken. The displacement efficiency is higher at lower reservoir temperature or for a lighter oil.
5. A *P*-*x* diagram for mixtures of reservoir oil with CO_2 solvent can be in large error for estimation of a pressure at which high displacement efficiency is achieved. This is because displacement efficiency is determined by interaction between flow and phase behaviors, instead of phase behavior on a *P*-*x* diagram.
6. Five or more components must be used to study the possibility of miscibility development at a tricritical point so that the tricritical point can be predicted in composition space at a fixed temperature and pressure.

Table 6.1 Fluid properties for simulations for Bob Slaughter Block oil (from Khan *et al.* 1992)

	Oil (Mol %)	Gas (Mol %)	Molecular weight	*Tc* (°F)	*Pc* (psia)	Acentric factor	*Vc* (ft^3/lb-mol)
CO_2	3.37	95.0	44.01	87.89	1069.87	0.225	1.51
C_1	8.61	5.0	16.04	−171.67	667.20	0.008	1.59
C_{2-3}	15.03	0.0	37.20	159.90	652.56	0.131	2.90
C_{4-6}	16.71	0.0	69.50	374.13	493.07	0.240	4.91
C_{7-15}	33.04	0.0	140.96	630.68	315.44	0.618	9.00
C_{16-27}	16.11	0.0	280.99	892.16	239.90	0.957	17.1
C_{28+}	7.13	0.0	519.62	1236.79	238.12	1.268	32.5

	h	*g*	BIC*
			CO_2
CO_2	1.0	1.000	0.000
C_1	0.0	0.055	0.055
C_{2-3}	0.0	0.055	0.055
C_{4-6}	0.0	0.055	0.055
C_{7-15}	0.0	0.105	0.105
C_{16-27}	0.0	0.105	0.105
C_{28+}	1.0	0.105	0.105

* All others are 0.0.

Table 6.2 Reservoir properties for simulations of one-dimensional oil displacements

Dimensions	1000 ft × 10 ft × 10 ft
Number of grid cells	500 × 1 × 1
Porosity	0.20
Permeability	1000 mD
Relative permeability model	Corey
	W / L_1 / G / L_2*
Residual saturation	0.40 / 0.20 / 0.05 / 0.05
Endpoint relative permeability	0.35 / 0.50 / 0.65 / 0.65
Exponent	3.0 / 3.0 / 3.0 / 3.0
Initial saturation	0.4 / 0.6 / 0.0 / 0.0

* W: Aqueous phase, L_1: Oleic phase, G: Gaseous phase, L_2: CO_2-rich liquid phase

Table 6.3 Fluid properties for simulations for Monahans Clearfork oil (from Lim *et al.* 1992)

	Oil (Mol %)	Gas (Mol %)	Molecular weight	*Tc* (°F)	*Pc* (psia)	Acentric factor	*Vc* (ft^3/lb-mol)
CO_2	0.00	95.0	44.01	87.89	1069.87	0.225	1.51
C_1	30.56	5.0	16.04	−116.59	667.20	0.008	1.59
C_{2-3}	20.27	0.0	36.27	152.35	658.59	0.127	2.84
C_{4-6}	15.89	0.0	70.42	375.39	487.51	0.240	4.99
C_{7-15}	23.27	0.0	137.84	626.68	329.42	0.609	9.28
C_{16+}	10.01	0.0	317.9	985.26	258.78	1.042	17.00

	h	*g*	BIC*
			CO_2
CO_2	1.0	1.000	0.000
C_1	0.0	0.094	0.094
C_{2-3}	0.0	0.094	0.094
C_{4-6}	0.0	0.094	0.094
C_{7-15}	0.0	0.095	0.095
C_{16+}	0.0	0.095	0.095

* All others are 0.0.

Table 6.4 Fluid properties for BSB-Q oil (a quaternary model for the BSB oil)

	Oil (Mol %)	Gas (Mol %)	Molecular weight	*Tc* (°F)	*Pc* (psia)	Acentric factor	V_C (ft^3/lb-mol)	BIC
								CO_2
CO_2	3.37	95.0	44.01	87.89	1069.87	0.225	1.51	0.000
C_1	8.61	5.0	16.04	−171.67	667.20	0.008	1.59	0.055
C_{H1}	64.78	0.0	98.45	492.58	396.21	0.481	6.60	0.081
C_{H2}	23.24	0.0	354.20	971.92	251.05	1.042	20.55	0.105

	h	*g*	BIC*
			CO_2
CO_2	1.0	1.000	0.000
C_1	0.0	0.055	0.055
C_{H1}	0.0	0.081	0.081
C_{H2}	0.0	0.105	0.105

* All others are 0.0.

Table 6.5 Fluid properties for BSB-QL oil

	Molecular weight	*Tc* (°F)	*Pc* (psia)	Acentric factor	V_C (ft^3/lb-mol)
C_{H1}	72.84	415.57	520.95	0.259	4.36
C_{H2}	264.65	909.90	225.44	0.851	17.21

* Oil/gas compositions, *h*, *g*, and BICs are the same as the BSB-Q oil in Table 6.4.

Table 6.6 Fluid properties for BSB-QH1 oil

	Molecular weight	Tc (°F)	Pc (psia)	Acentric factor	V_C (ft^3/lb-mol)
C_{H1}	124.07	594.19	352.01	0.430	7.81
C_{H2}	443.75	1212.83	188.40	1.216	29.09

* Oil/gas compositions, *h*, *g*, and BICs are the same as the BSB-Q oil in Table 6.4.

Table 6.7 Fluid properties for BSB-QH2 oil

	Molecular weight	Tc (°F)	Pc (psia)	Acentric factor	V_C (ft^3/lb-mol)
C_{H1}	149.68	663.31	308.82	0.513	9.53
C_{H2}	533.30	1348.76	180.25	1.286	35.01

* Oil/gas compositions, *h*, *g*, and BICs are the same as the BSB-Q oil in Table 6.4.

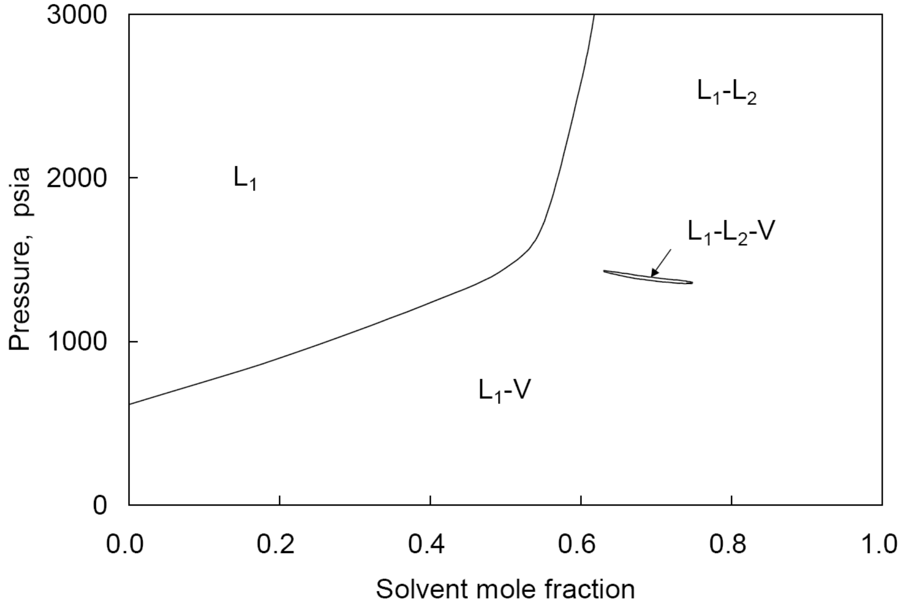

Figure 6.1 *P-x* diagram at 105˚F for the Bob Slaughter Block (BSB) oil and injection gas given in Table 6.1.

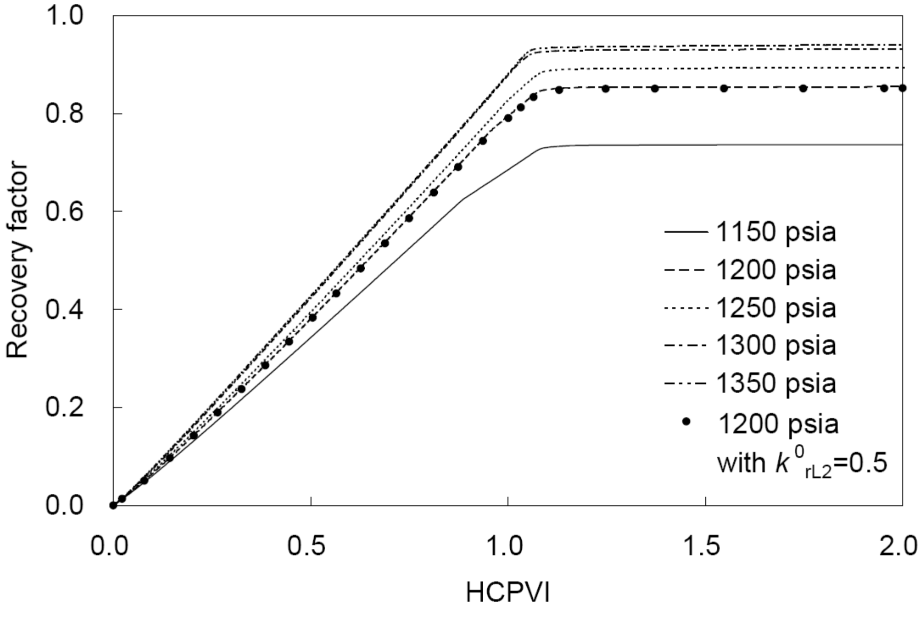

Figure 6.2 Oil recoveries for the displacements of the BSB oil (105°F) at different pressures by the injection gas shown in Table 6.1. k^0_{rL2} is the endpoint relative permeability for the L_2 phase.

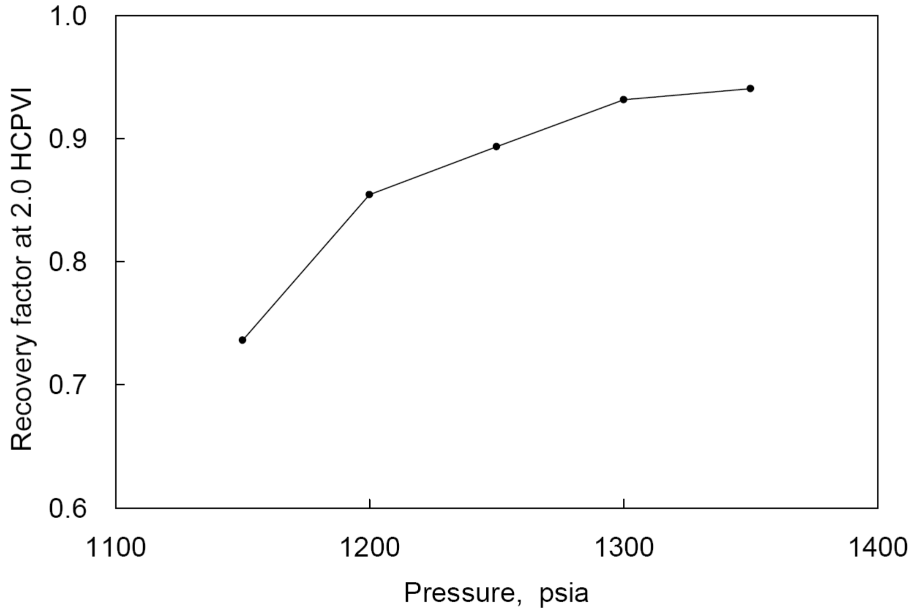

Figure 6.3 Recovery factors at 2.0 HCPVI for the displacements of the BSB oil (105°F) at different pressures by the injection gas shown in Table 6.1.

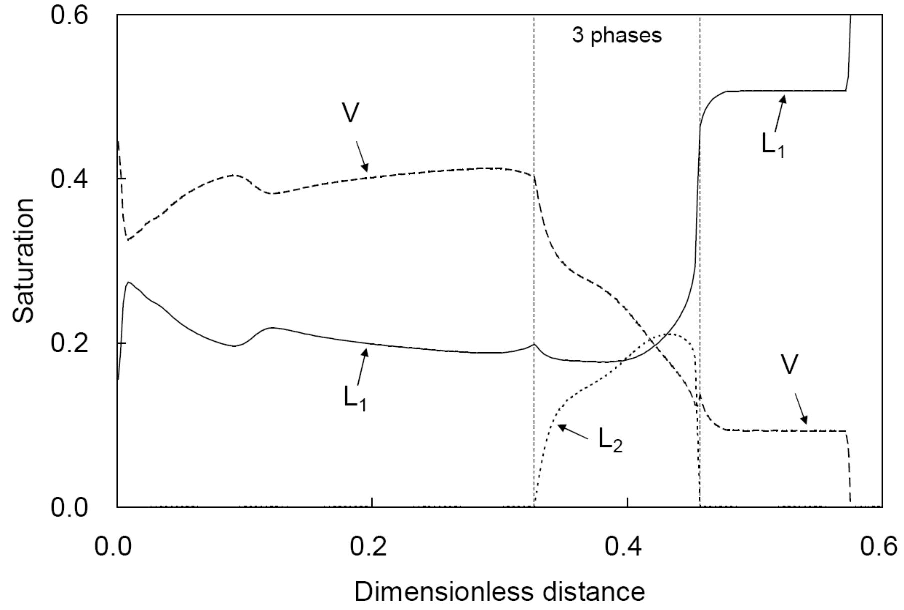

Figure 6.4 Phase saturation profiles at 0.5 HCPVI for the BSB oil displacement (105°F) at 1150 psia by the injection gas shown in Table 6.1.

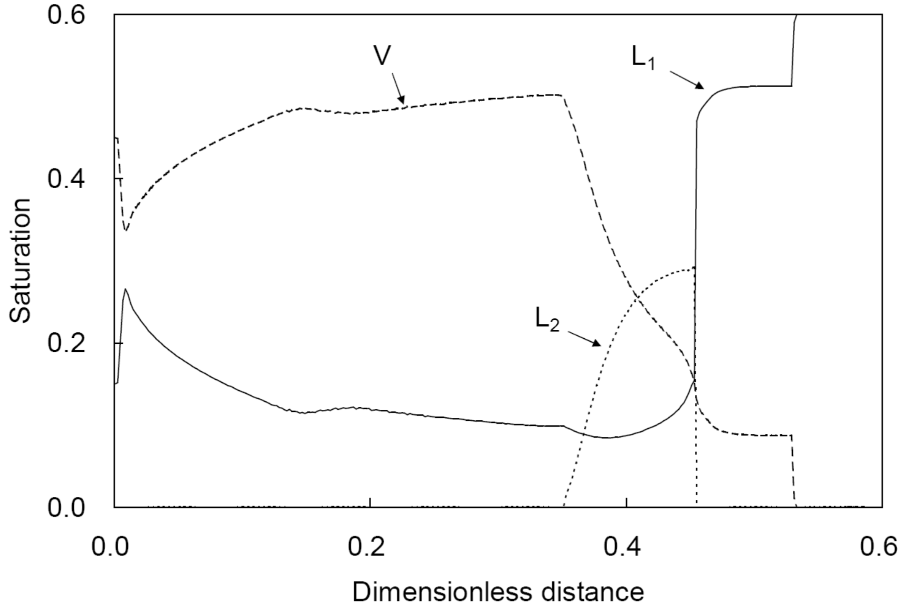

Figure 6.5 Phase saturation profiles at 0.5 HCPVI for the BSB oil displacement (105°F) at 1200 psia by the injection gas shown in Table 6.1.

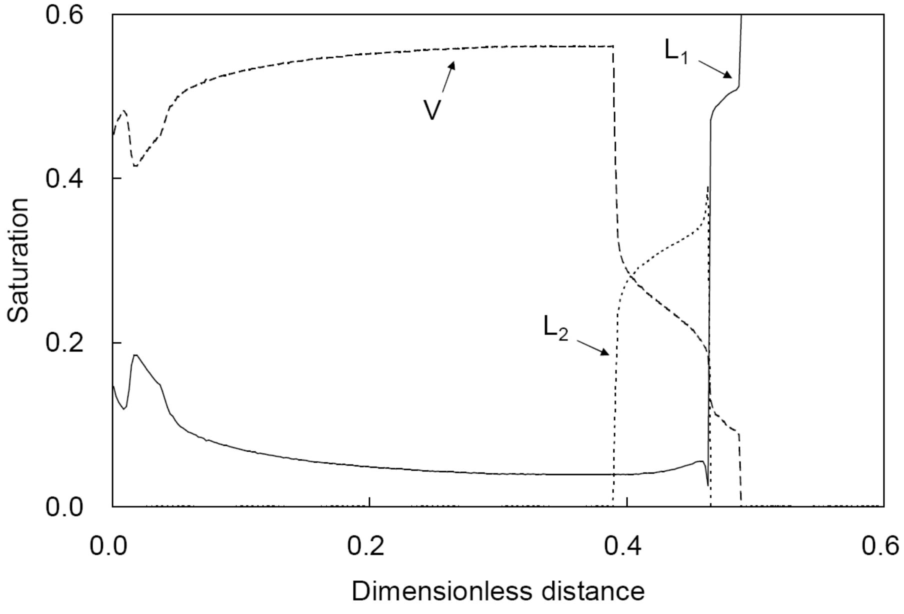

Figure 6.6 Phase saturation profiles at 0.5 HCPVI for the BSB oil displacement (105°F) at 1300 psia by the injection gas shown in Table 6.1.

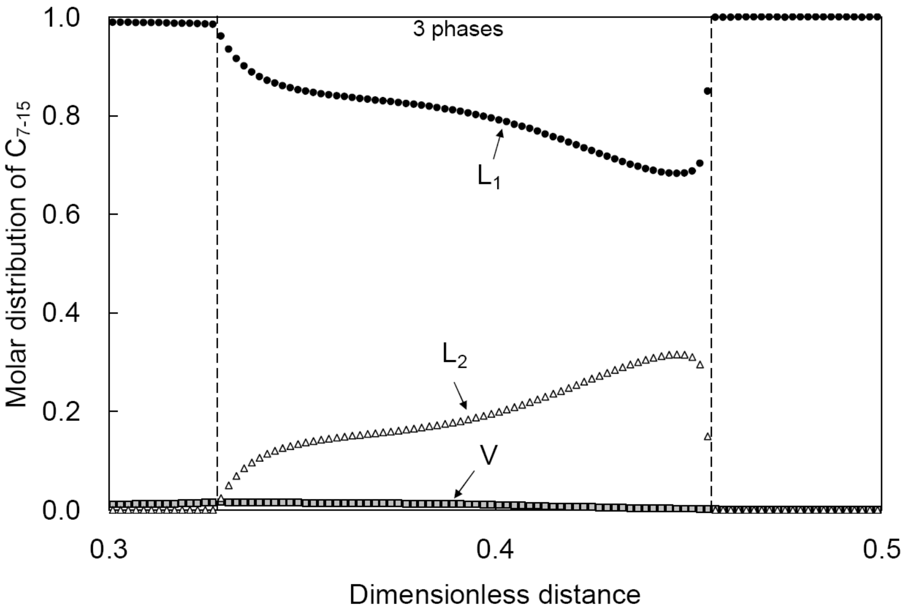

Figure 6.7a Molar distribution of C_{7-15} at 0.5 HCPVI in the BSB oil displacement (105°F) at 1150 psia by the injection gas shown in Table 6.1.

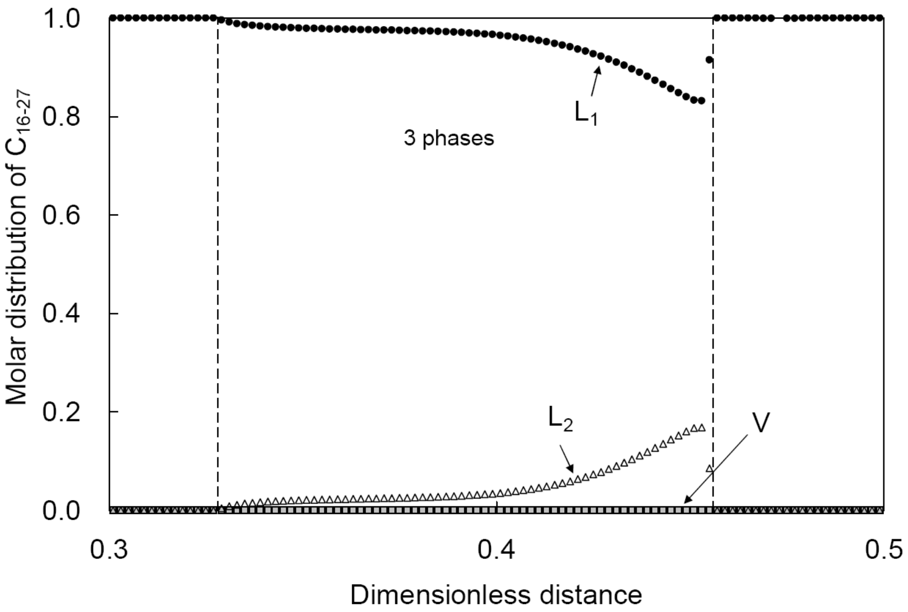

Figure 6.7b Molar distribution of C_{16-27} at 0.5 HCPVI in the BSB oil displacement (105°F) at 1150 psia by the injection gas shown in Table 6.1.

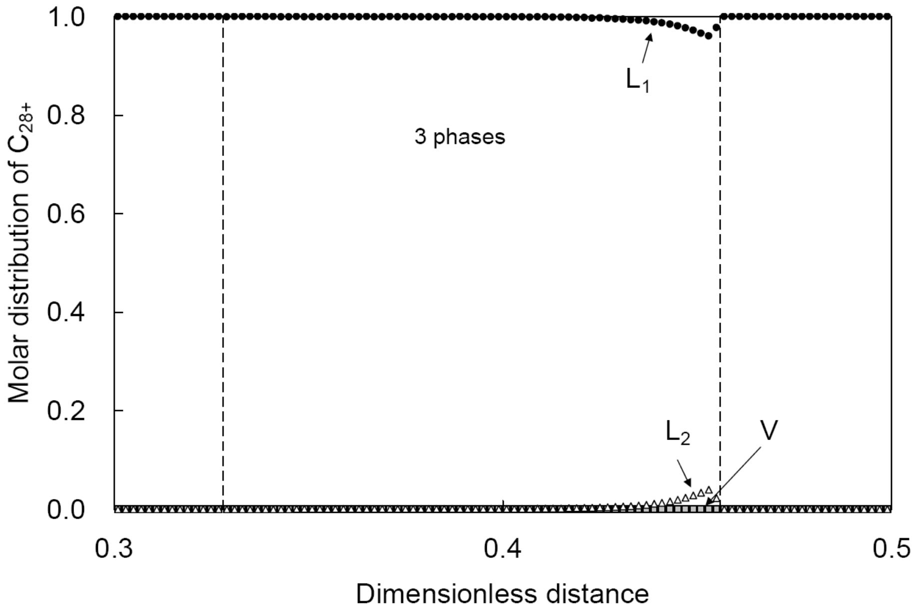

Figure 6.7c Molar distribution of C_{28+} at 0.5 HCPVI in the BSB oil displacement (105°F) at 1150 psia by the injection gas shown in Table 6.1.

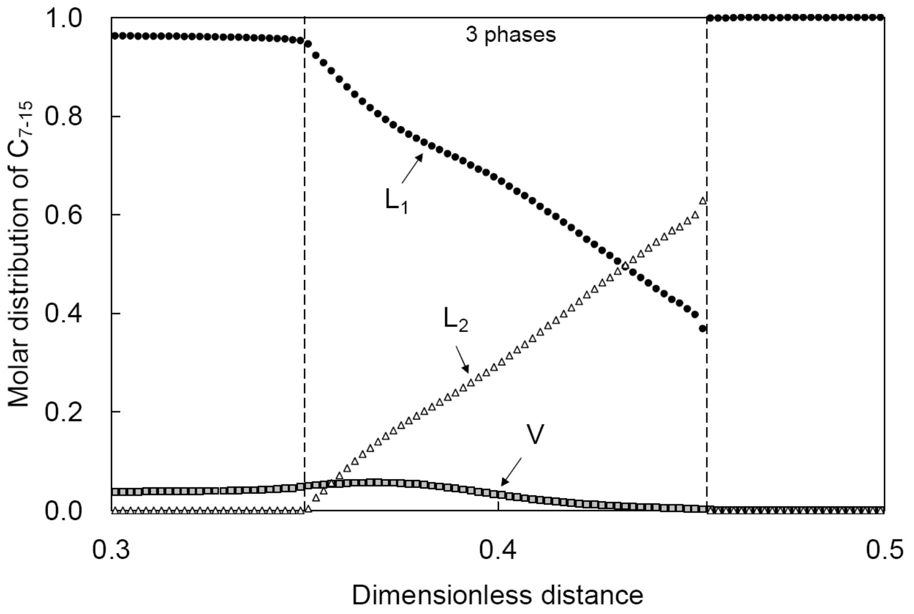

Figure 6.8a Molar distribution of C_{7-15} at 0.5 HCPVI in the BSB oil displacement (105°F) at 1200 psia by the injection gas shown in Table 6.1.

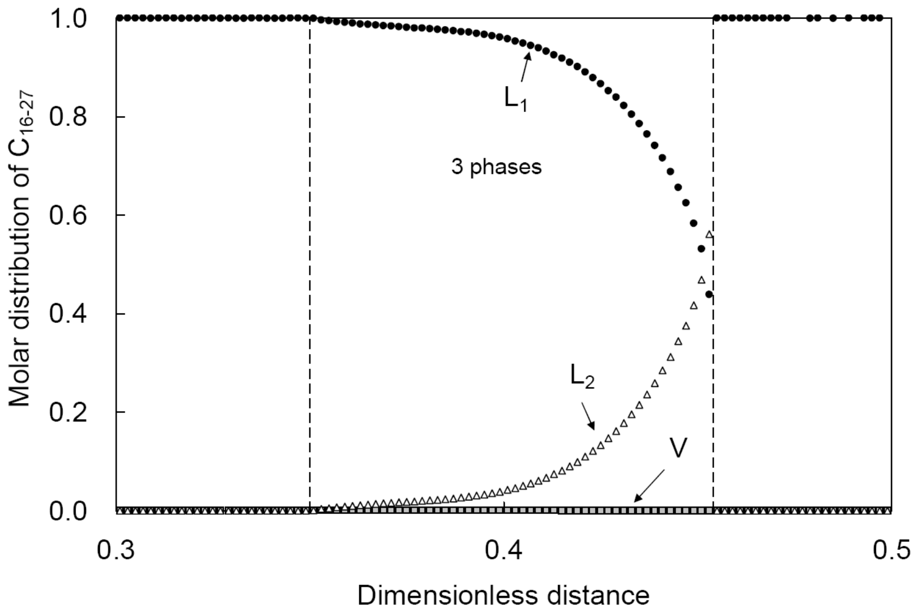

Figure 6.8b Molar distribution of C_{16-27} at 0.5 HCPVI in the BSB oil displacement (105°F) at 1200 psia by the injection gas shown in Table 6.1.

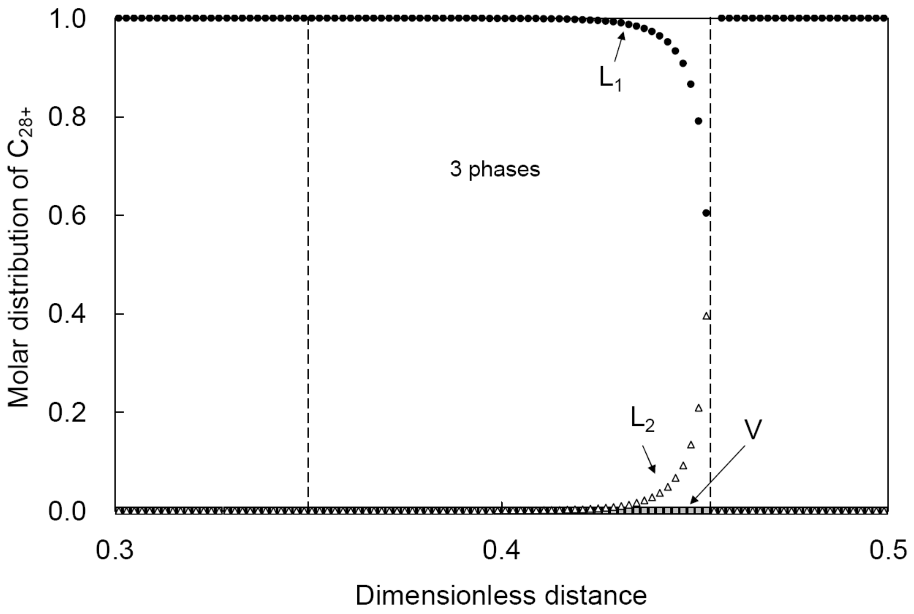

Figure 6.8c Molar distribution of C_{28+} at 0.5 HCPVI in the BSB oil displacement (105°F) at 1200 psia by the injection gas shown in Table 6.1.

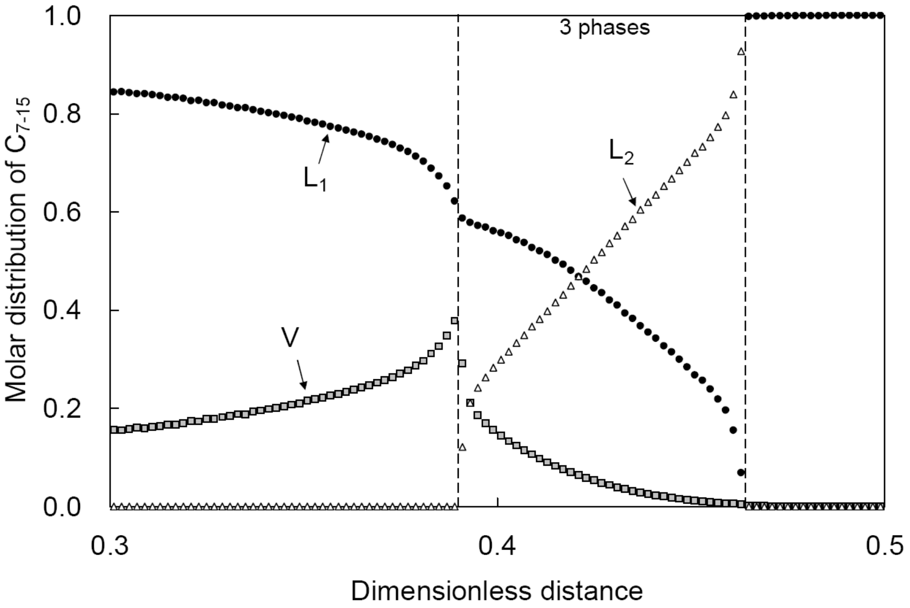

Figure 6.9a Molar distribution of C_{7-15} at 0.5 HCPVI in the BSB oil displacement (105°F) at 1300 psia by the injection gas shown in Table 6.1.

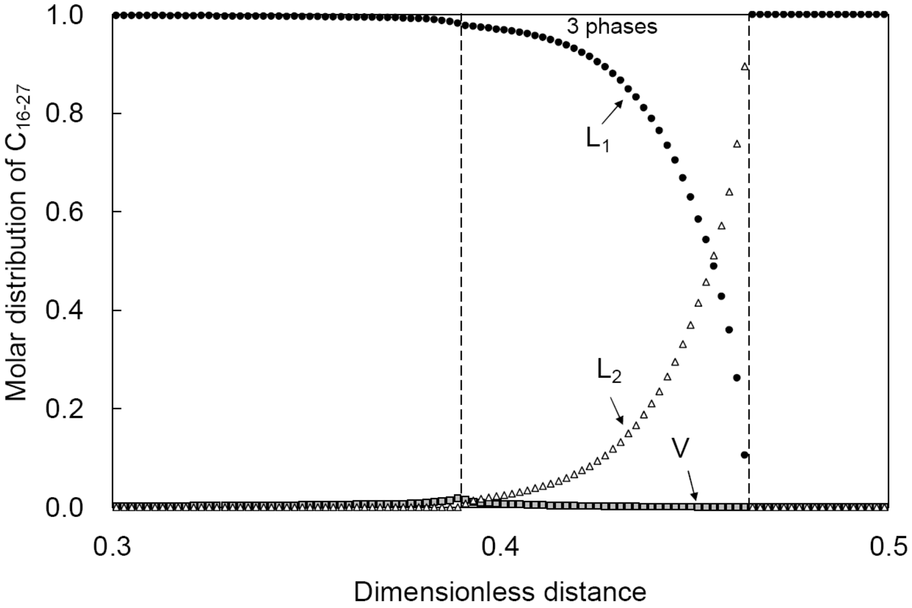

Figure 6.9b Molar distribution of C_{16-27} at 0.5 HCPVI in the BSB oil displacement (105°F) at 1300 psia by the injection gas shown in Table 6.1.

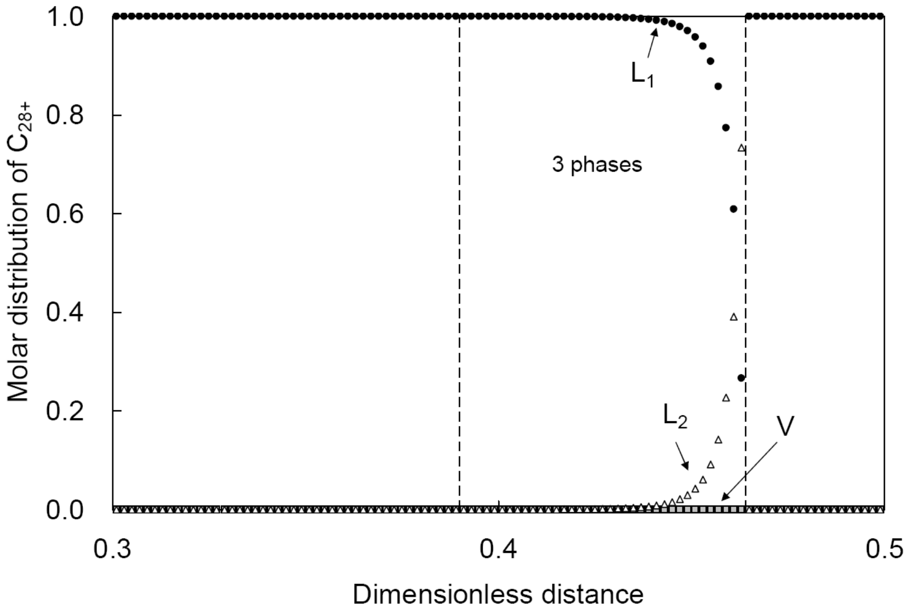

Figure 6.9c Molar distribution of C_{28+} at 0.5 HCPVI in the BSB oil displacement (105°F) at 1300 psia by the injection gas shown in Table 6.1.

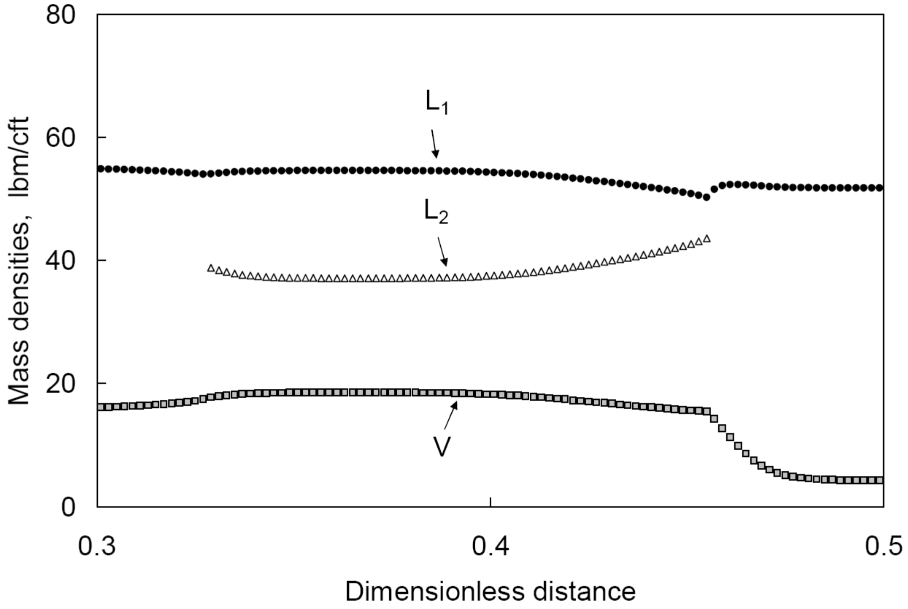

Figure 6.10 Profiles of phase mass densities at 0.5 HCPVI for the BSB oil displacement (105°F) at 1150 psia by the injection gas shown in Table 6.1.

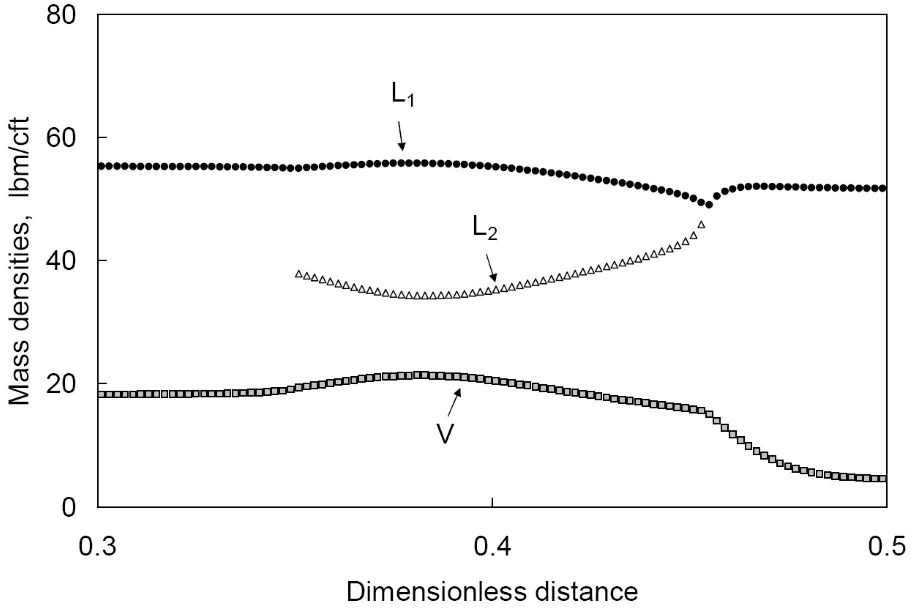

Figure 6.11 Profiles of phase mass densities at 0.5 HCPVI for the BSB oil displacement (105°F) at 1200 psia by the injection gas shown in Table 6.1.

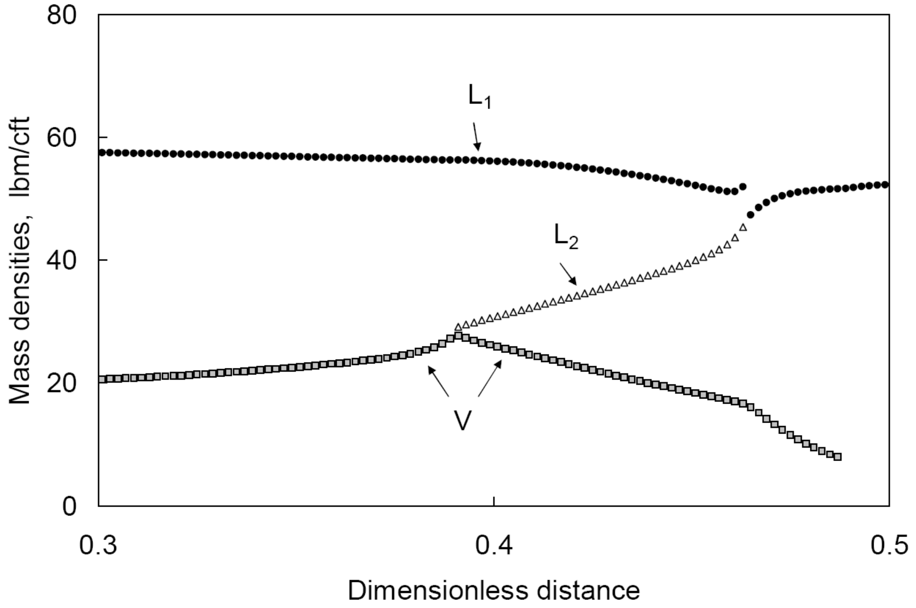

Figure 6.12 Profiles of phase mass densities at 0.5 HCPVI for the BSB oil displacement (105°F) at 1300 psia by the injection gas shown in Table 6.1.

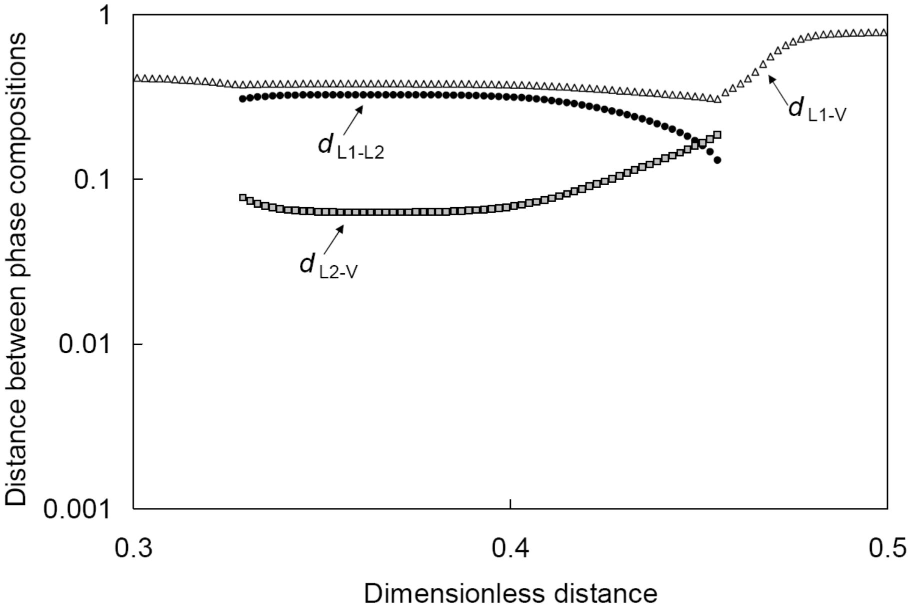

Figure 6.13 Distances between phase compositions in composition space at 0.5 HCPVI for the BSB oil displacement (105°F) at 1150 psia by the injection gas shown in Table 6.1.

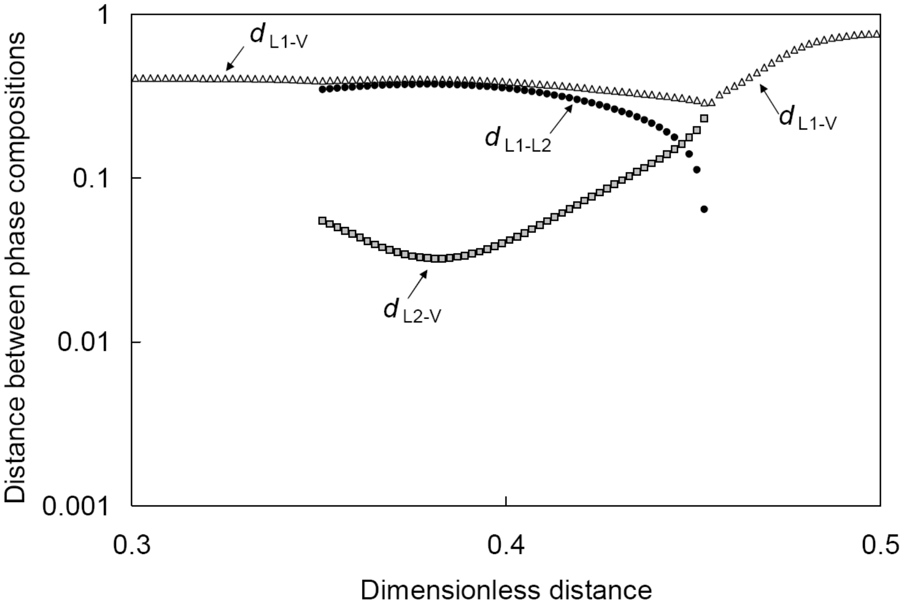

Figure 6.14 Distances between phase compositions in composition space at 0.5 HCPVI for the BSB oil displacement (105°F) at 1200 psia by the injection gas shown in Table 6.1.

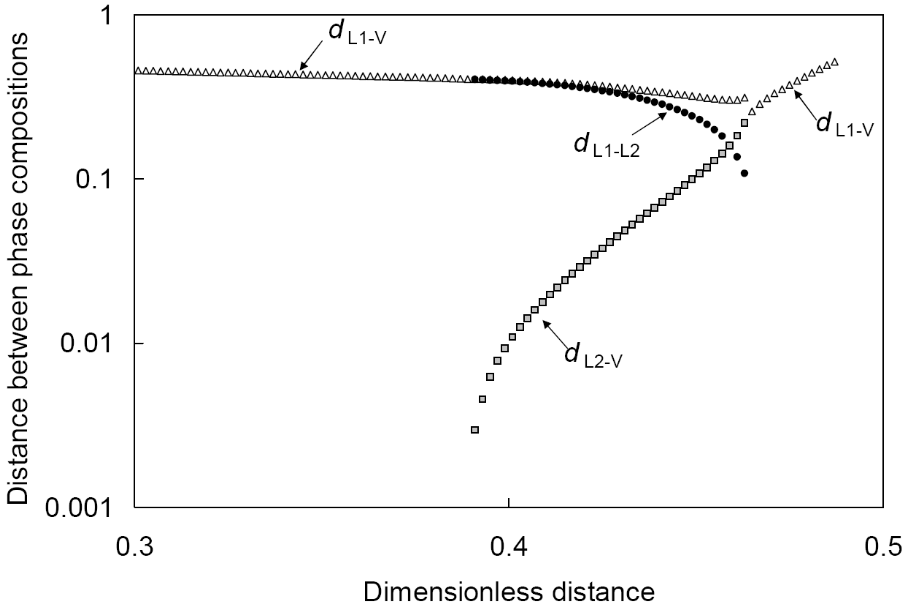

Figure 6.15 Distances between phase compositions in composition space at 0.5 HCPVI for the BSB oil displacement (105°F) at 1300 psia by the injection gas shown in Table 6.1.

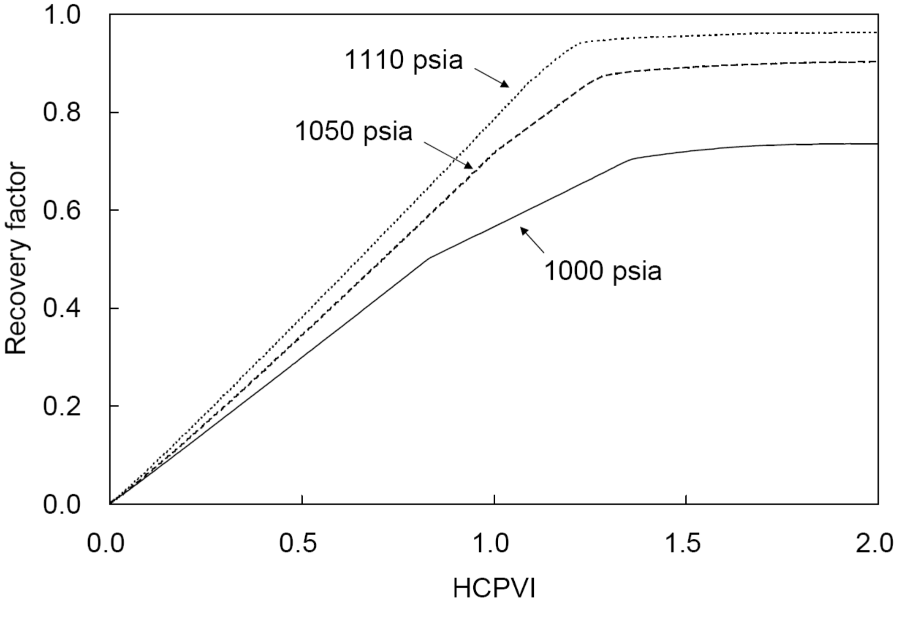

Figure 6.16 Oil recoveries for the displacements of the North Ward Estes (NWE) oil (83°F) at different pressures by the injection gas shown in Table 5.2.

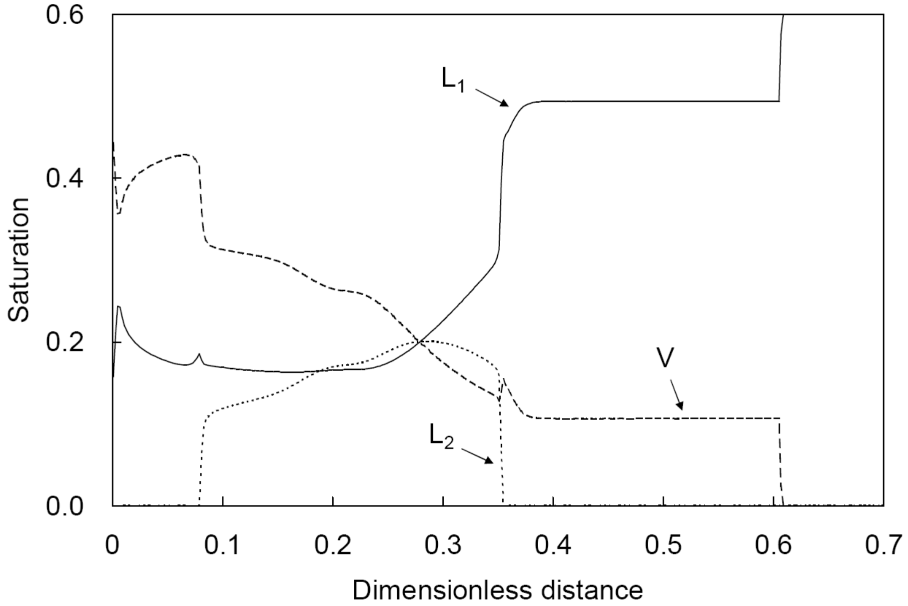

Figure 6.17 Phase saturation profiles at 0.5 HCPVI for the NWE oil displacement (83°F) at 1000 psia by the injection gas shown in Table 5.2.

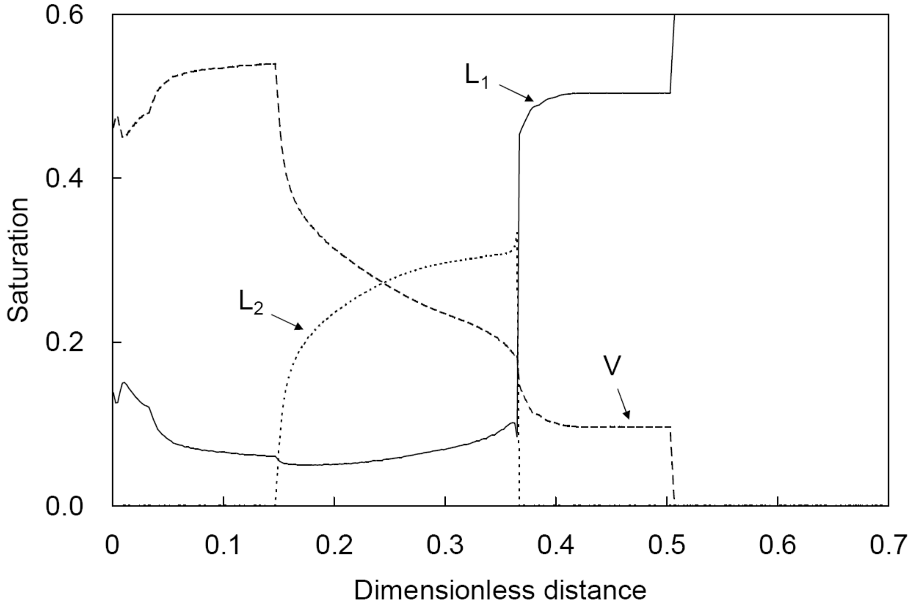

Figure 6.18 Phase saturation profiles at 0.5 HCPVI for the NWE oil displacement (83°F) at 1050 psia by the injection gas shown in Table 5.2.

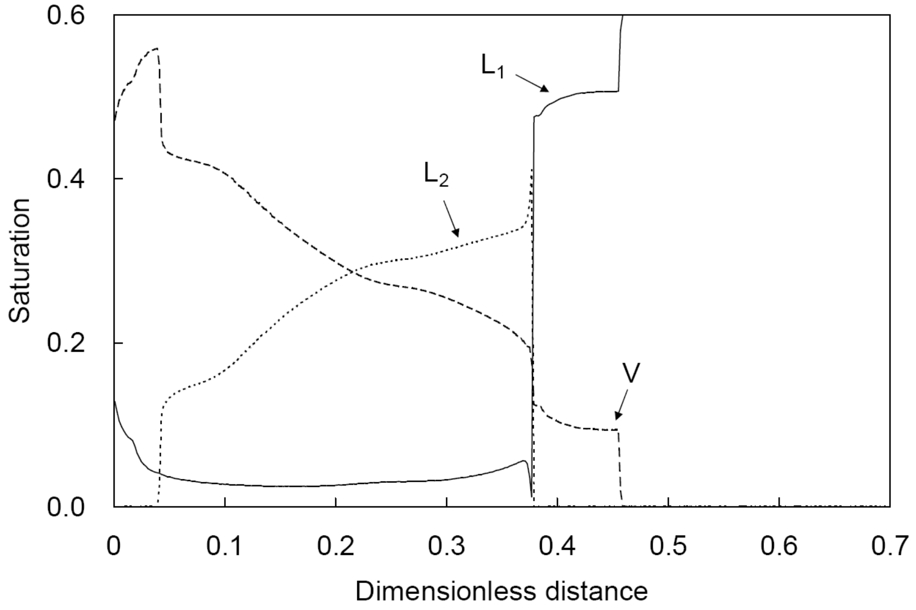

Figure 6.19 Phase saturation profiles at 0.5 HCPVI for the NWE oil displacement (83°F) at 1100 psia by the injection gas shown in Table 5.2.

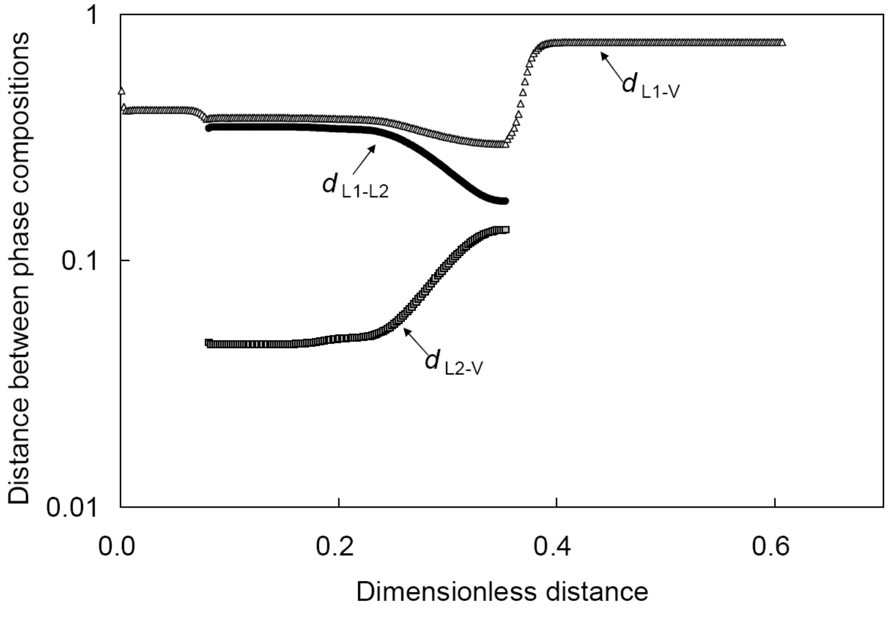

Figure 6.20 Distances between phase compositions in composition space at 0.5 HCPVI for the NWE oil displacement (83°F) at 1000 psia by the injection gas shown in Table 5.2.

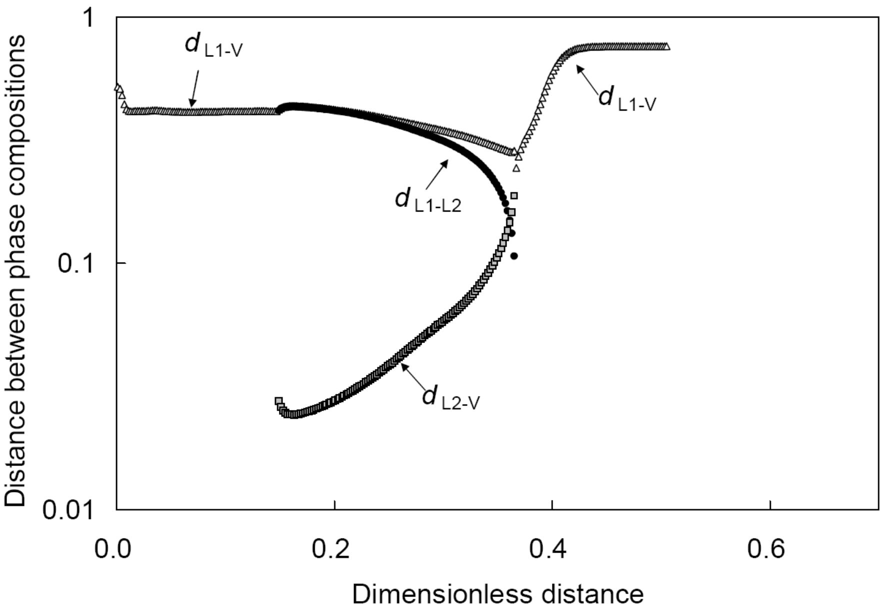

Figure 6.21 Distances between phase compositions in composition space at 0.5 HCPVI for the NWE oil displacement (83°F) at 1050 psia by the injection gas shown in Table 5.2.

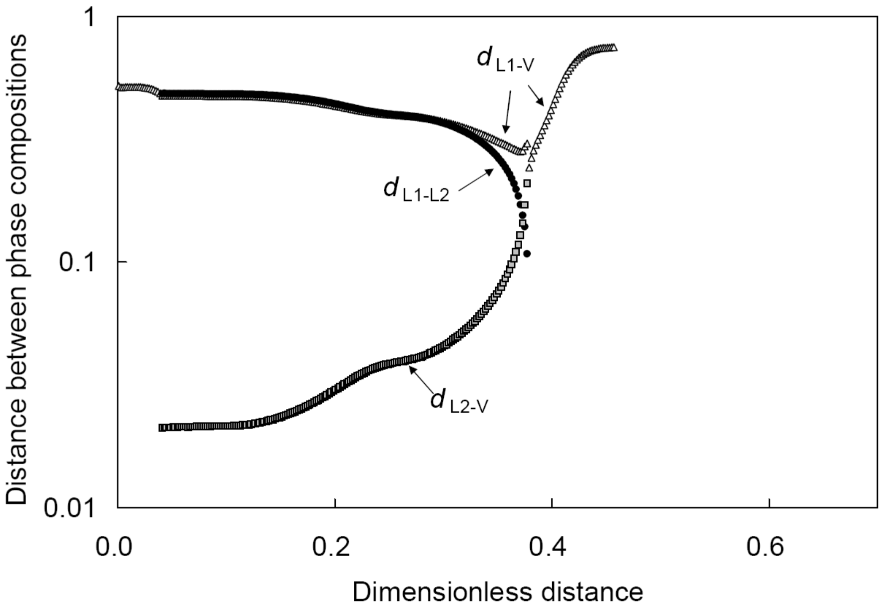

Figure 6.22 Distances between phase compositions in composition space at 0.5 HCPVI for the NWE oil displacement (83°F) at 1100 psia by the injection gas shown in Table 5.2.

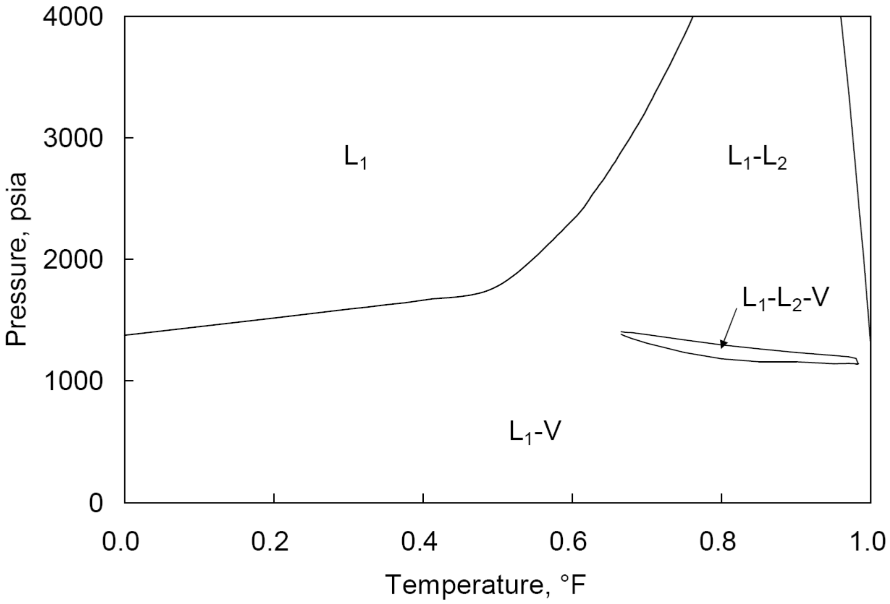

Figure 6.23 *P-x* diagram at 90˚F for the Monahans Clearfork (MC) oil and injection gas given in Table 6.3.

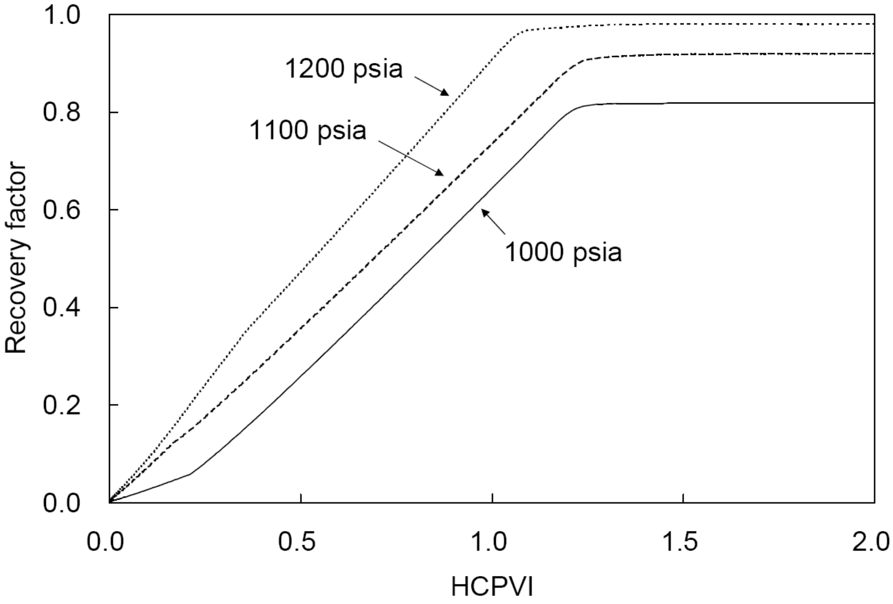

Figure 6.24 Oil recoveries for the displacements of the MC oil (90˚F) at different pressures by the injection gas shown in Table 6.3.

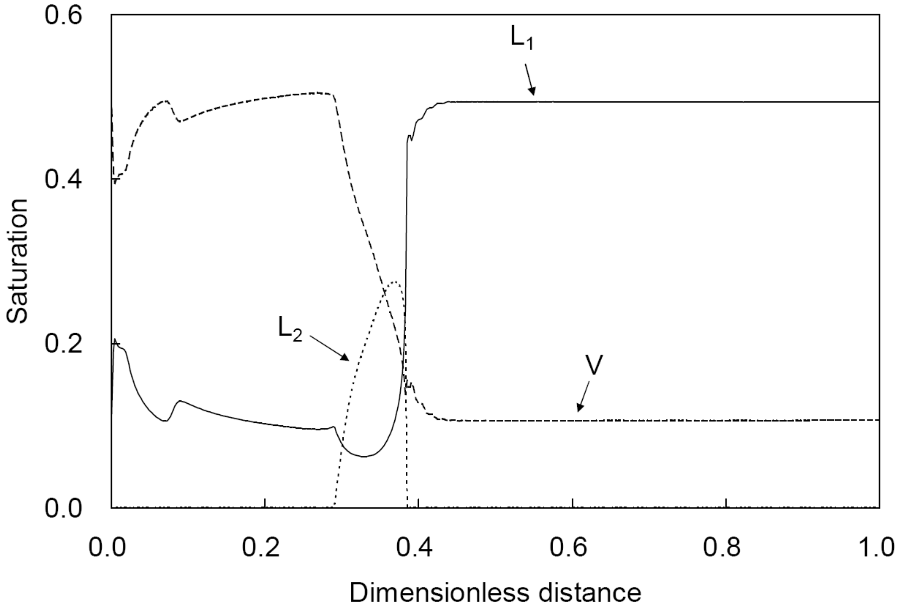

Figure 6.25 Phase saturation profiles at 0.5 HCPVI for the MC oil displacement (90˚F) at 1000 psia by the injection gas shown in Table 6.3.

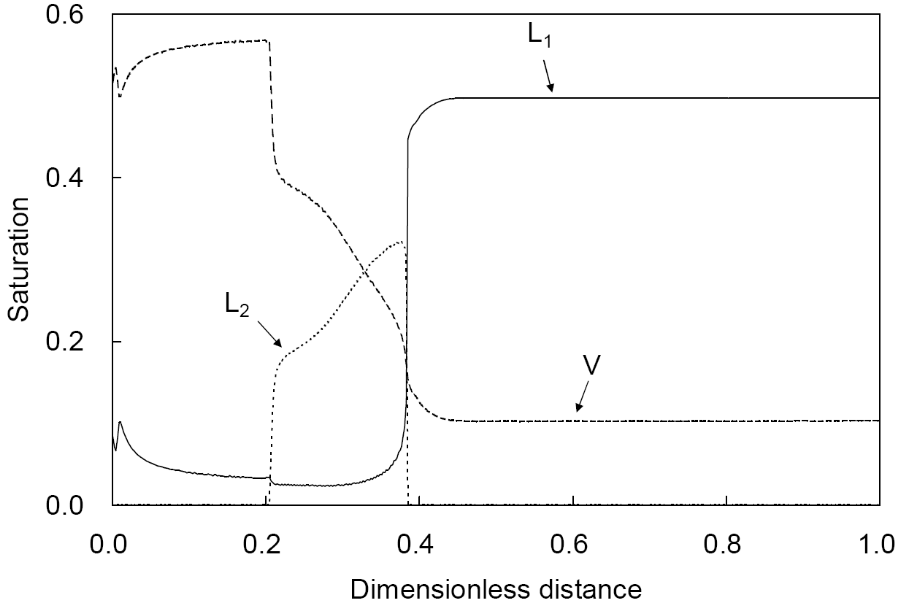

Figure 6.26 Phase saturation profiles at 0.5 HCPVI for the MC oil displacement (90˚F) at 1100 psia by the injection gas shown in Table 6.3.

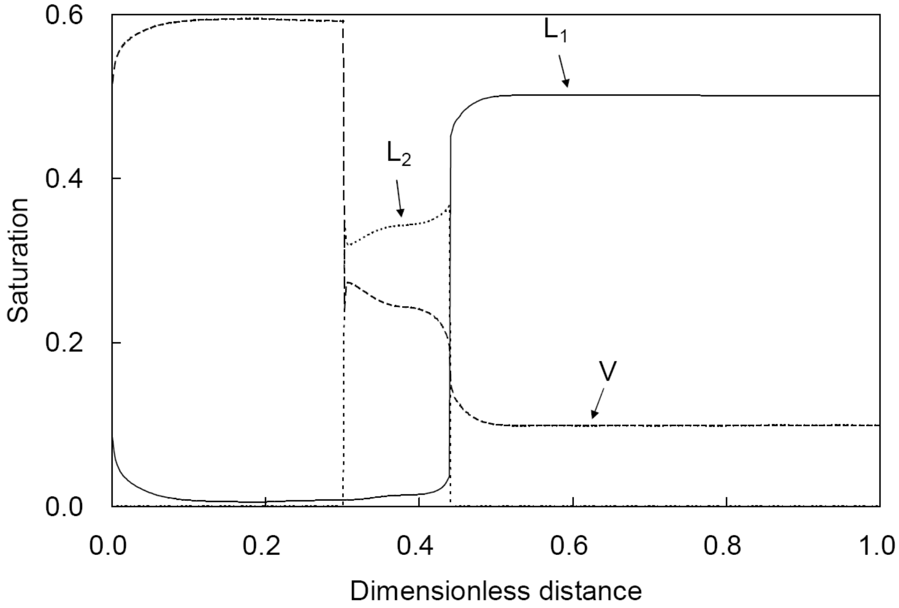

Figure 6.27 Phase saturation profiles at 0.5 HCPVI for the MC oil displacement (90˚F) at 1200 psia by the injection gas shown in Table 6.3.

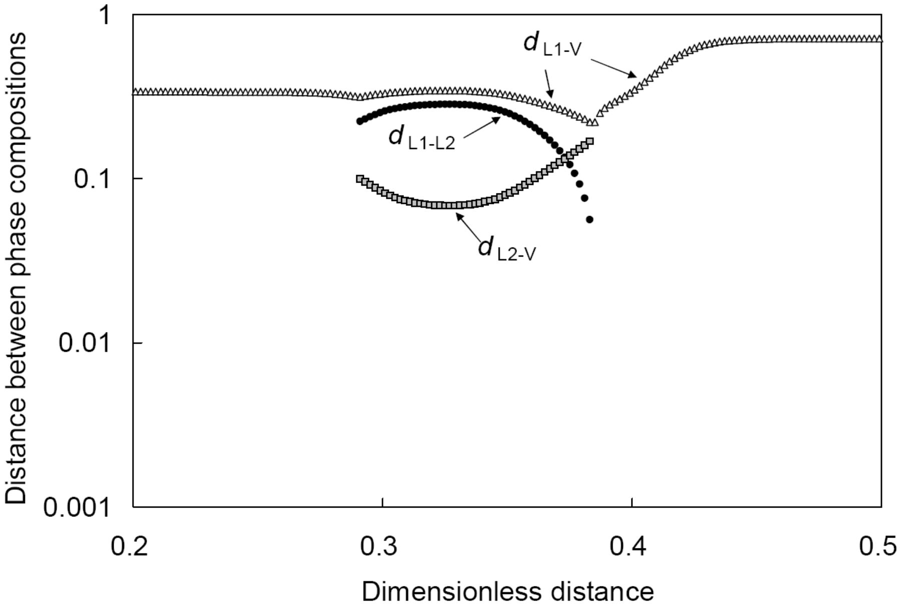

Figure 6.28 Distances between phase compositions in composition space at 0.5 HCPVI for the MC oil displacement (90˚F) at 1000 psia by the injection gas shown in Table 6.3.

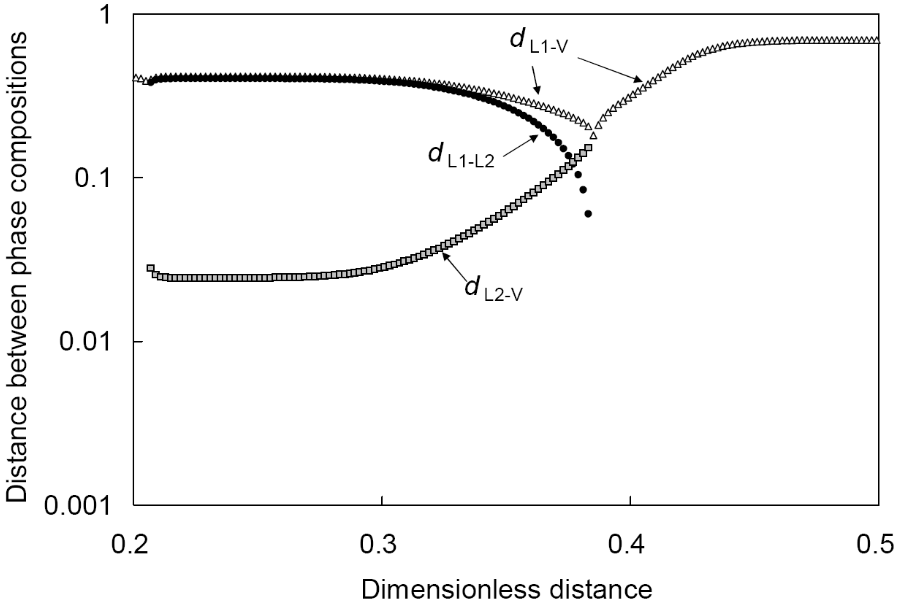

Figure 6.29 Distances between phase compositions in composition space at 0.5 HCPVI for the MC oil displacement (90˚F) at 1100 psia by the injection gas shown in Table 6.3.

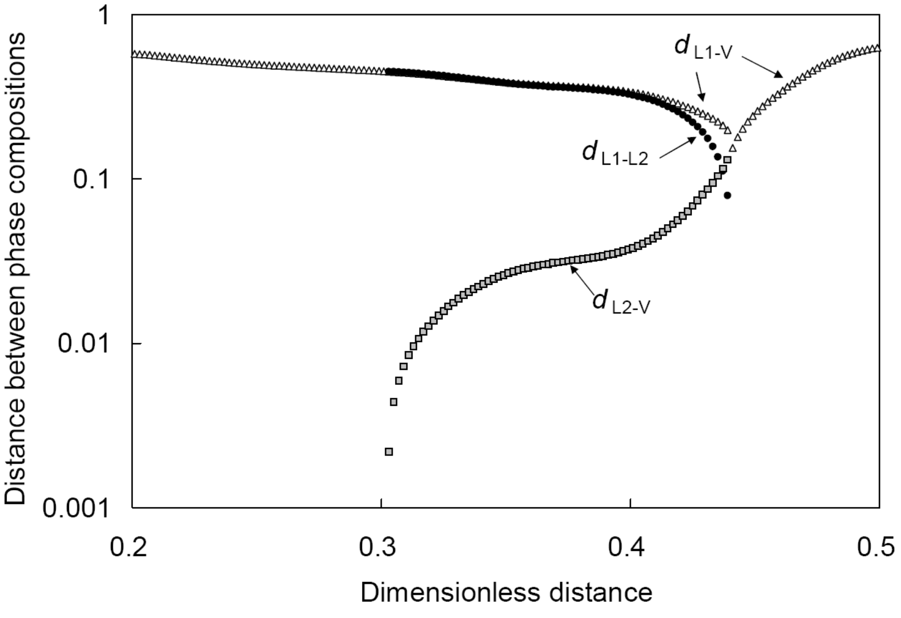

Figure 6.30 Distances between phase compositions in composition space at 0.5 HCPVI for the MC oil displacement (90˚F) at 1200 psia by the injection gas shown in Table 6.3.

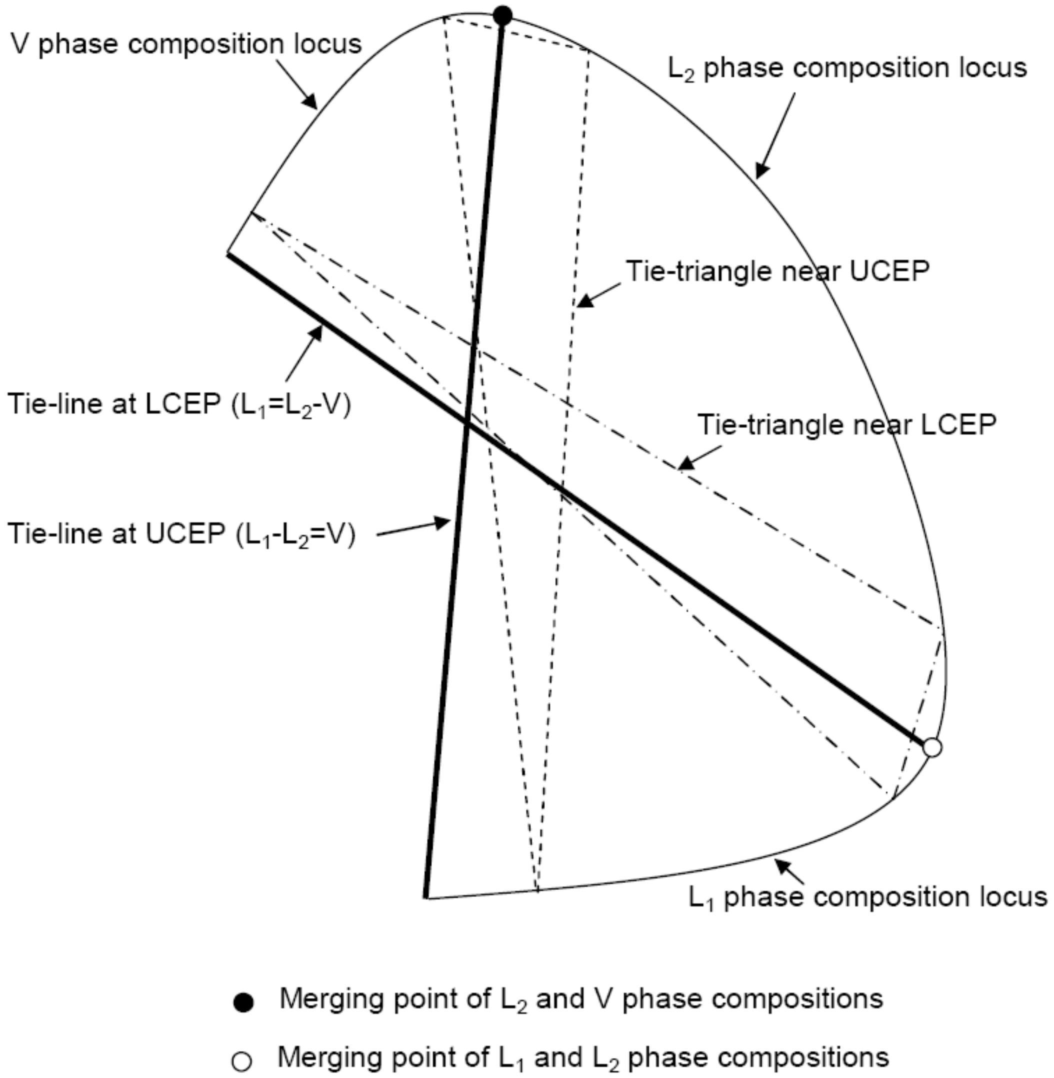

Figure 6.31 Schematic of a three-phase region bounded by critical endpoint (CEP) tie-lines for a quaternary system at a fixed temperature and pressure.

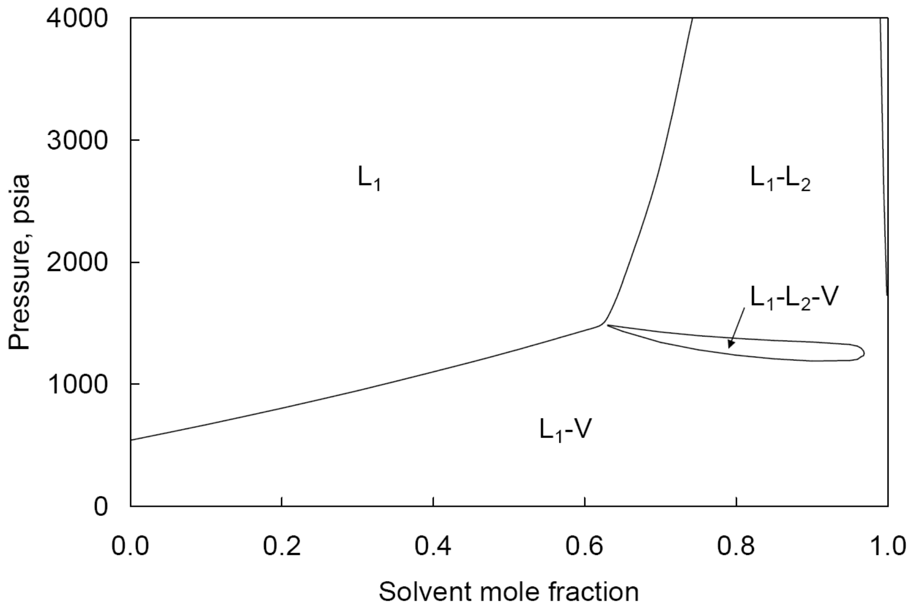

Figure 6.32a *P*-*x* diagram at 105˚F for the BSB-Q (a quaternary model for the BSB oil) oil and injection gas given in Table 6.4.

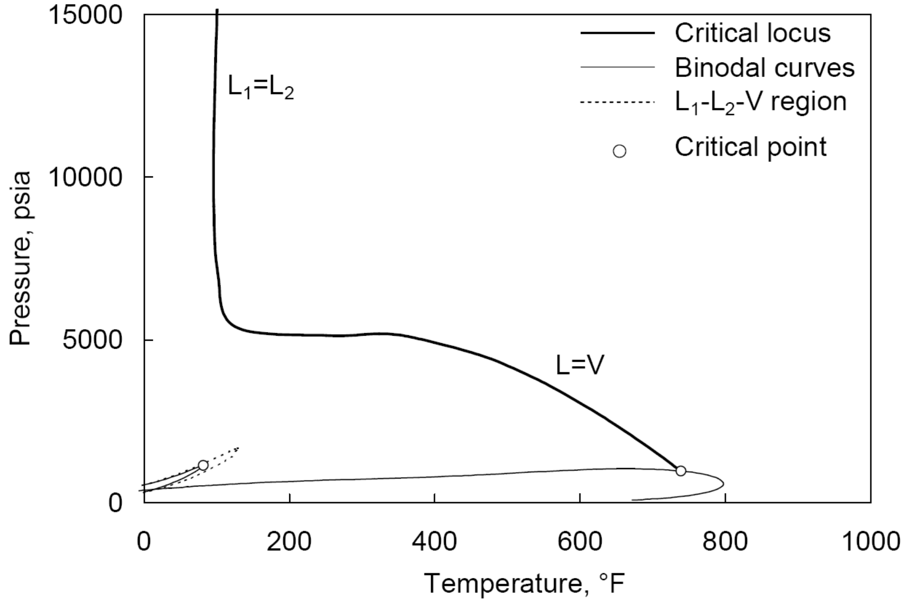

Figure 6.32b *P*-*T* projection of the *P*-*T*-*x* diagram for the pseudo-binary mixture of the BSB-Q oil and injection gas given in Table 6.4.

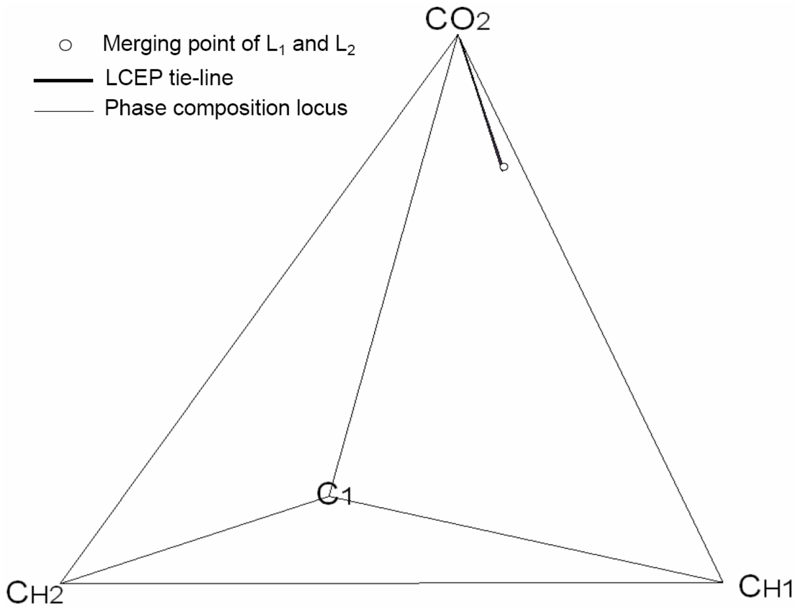

Figure 6.33a Three-phase region in BSB-Q composition space at 105°F and a pressure slightly above 1028 psia. The BSB-Q system is given in Table 6.4.

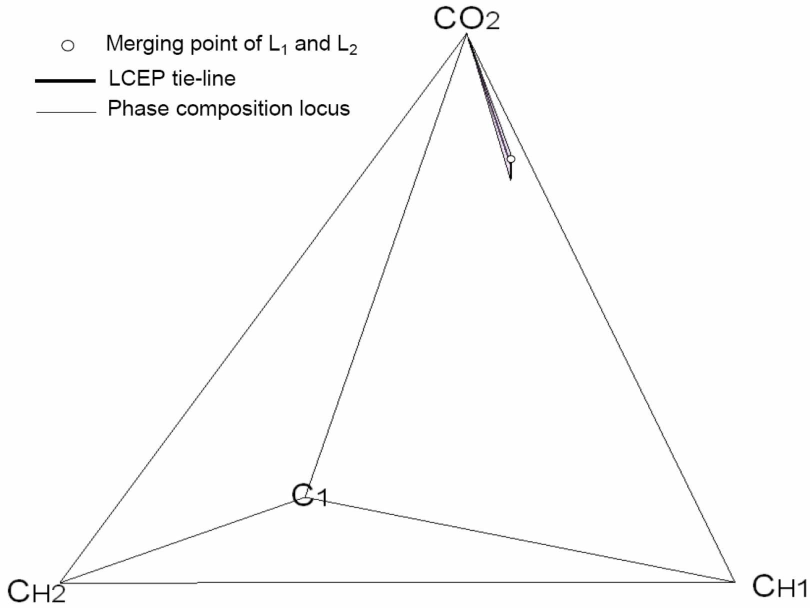

Figure 6.33b Three-phase region in BSB-Q composition space at 105°F and 1030 psia. The BSB-Q system is given in Table 6.4.

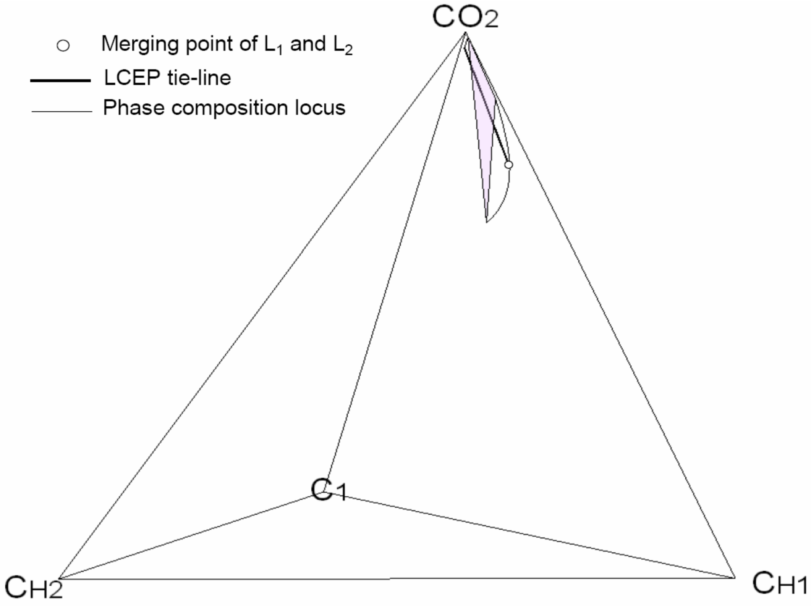

Figure 6.33c Three-phase region in BSB-Q composition space at 105°F and 1065 psia. The shaded tie-triangle is on the C_1-free plane.

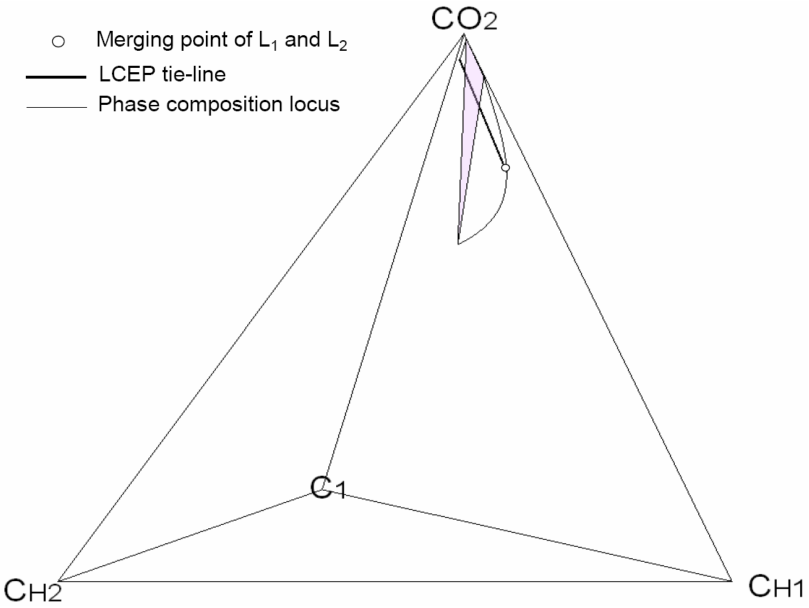

Figure 6.33d Three-phase region in BSB-Q composition space at 105°F and 1100 psia. The shaded tie-triangle is on the C_1-free plane.

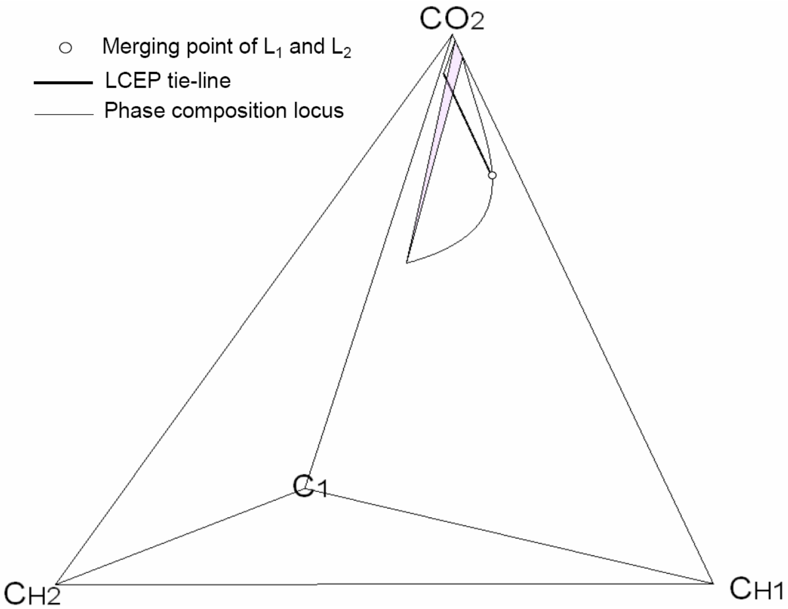

Figure 6.33e Three-phase region in BSB-Q composition space at 105°F and 1150 psia. The shaded tie-triangle is on the C_1-free plane.

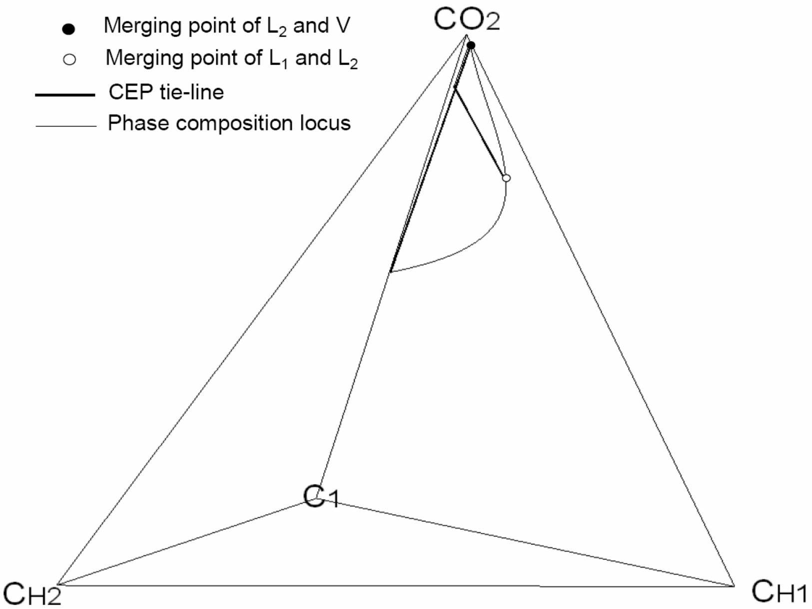

Figure 6.33f Three-phase region in BSB-Q composition space at 105°F and 1200 psia.

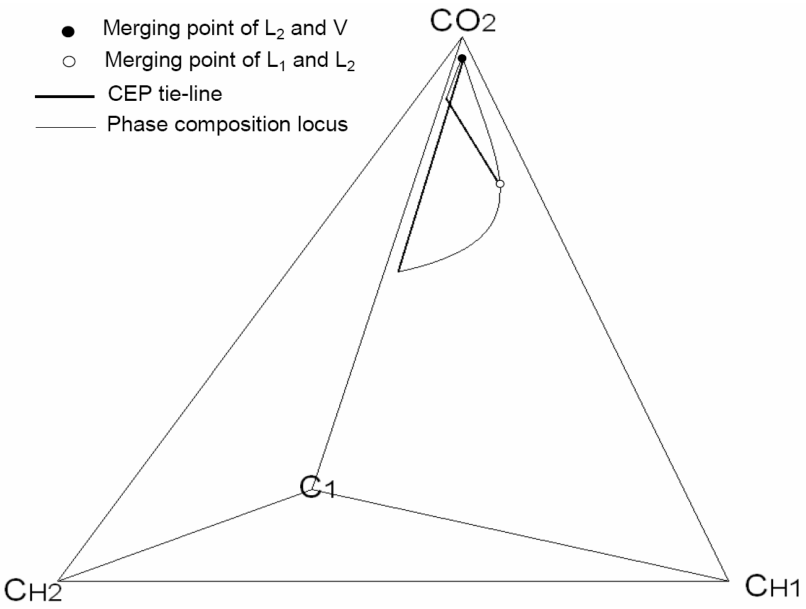

Figure 6.33g Three-phase region in BSB-Q composition space at 105°F and 1250 psia.

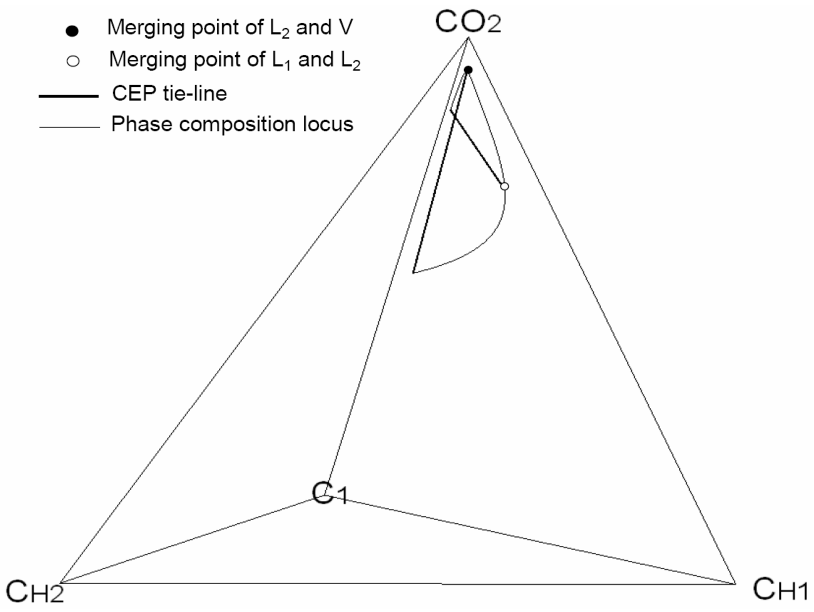

Figure 6.33h Three-phase region in BSB-Q composition space at 105°F and 1300 psia.

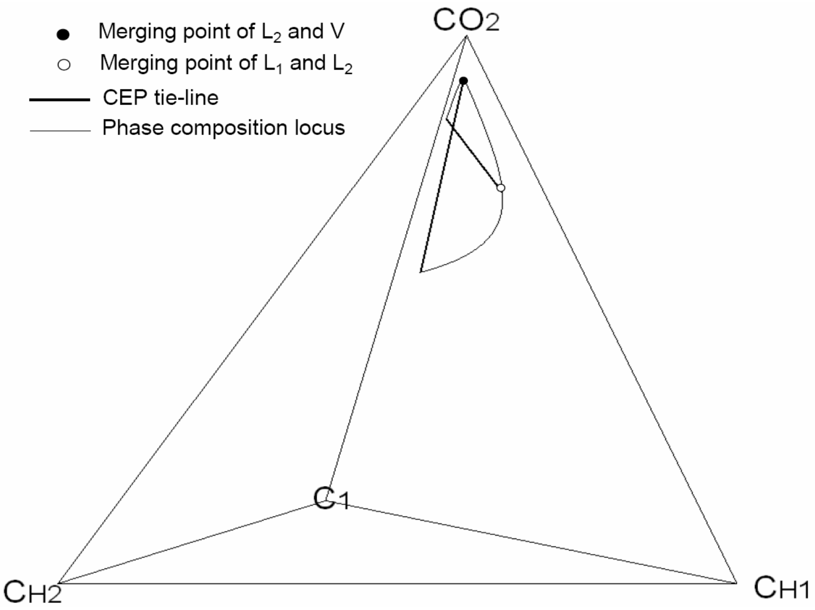

Figure 6.33i Three-phase region in BSB-Q composition space at 105°F and 1350 psia.

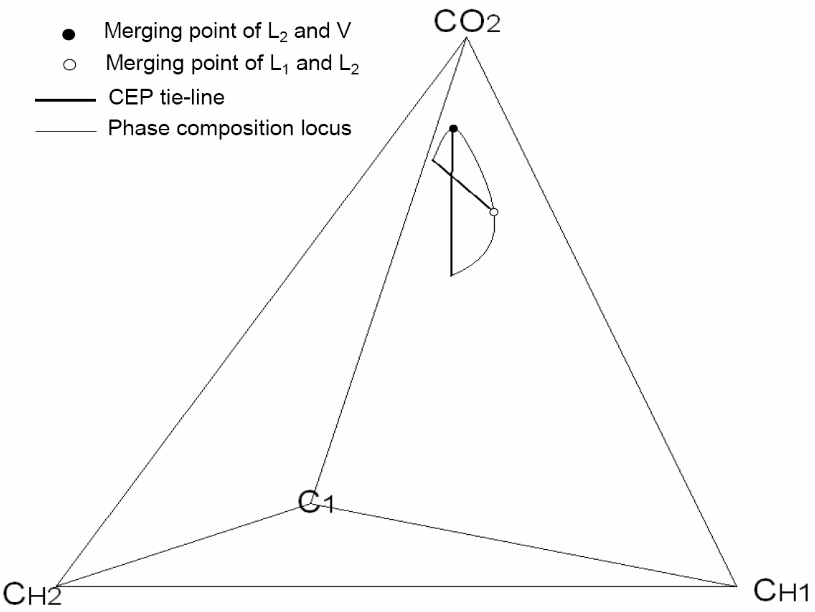

Figure 6.33j Three-phase region in BSB-Q composition space at 105°F and 1600 psia.

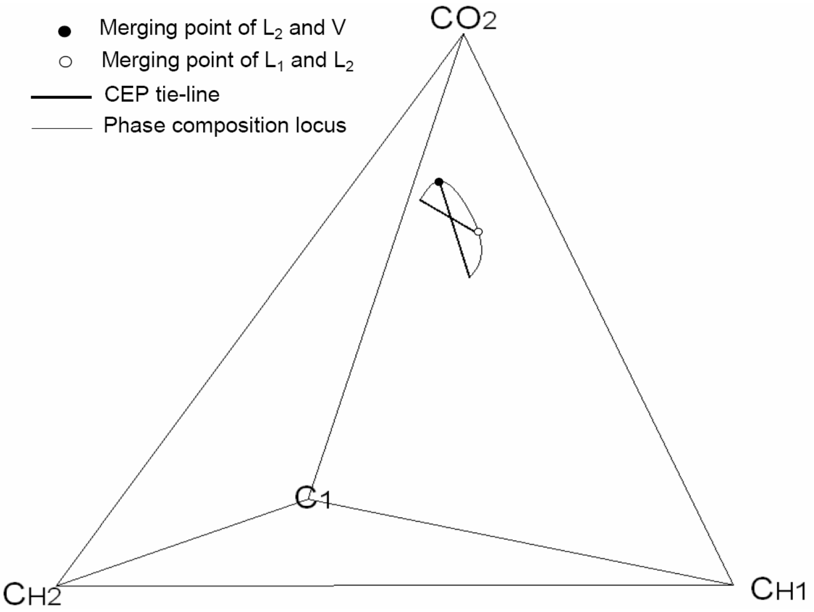

Figure 6.33k Three-phase region in BSB-Q composition space at 105°F and 2000 psia.

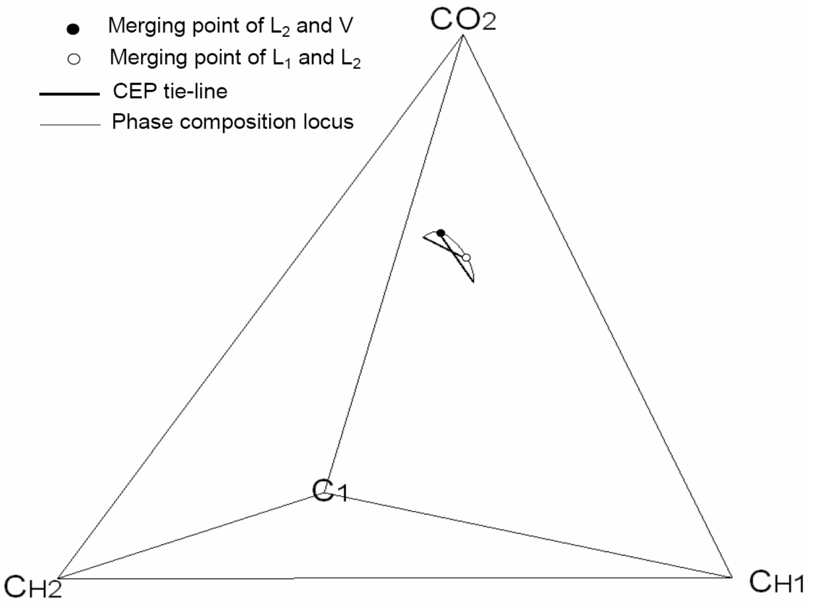

Figure 6.33l Three-phase region in BSB-Q composition space at 105°F and 2500 psia.

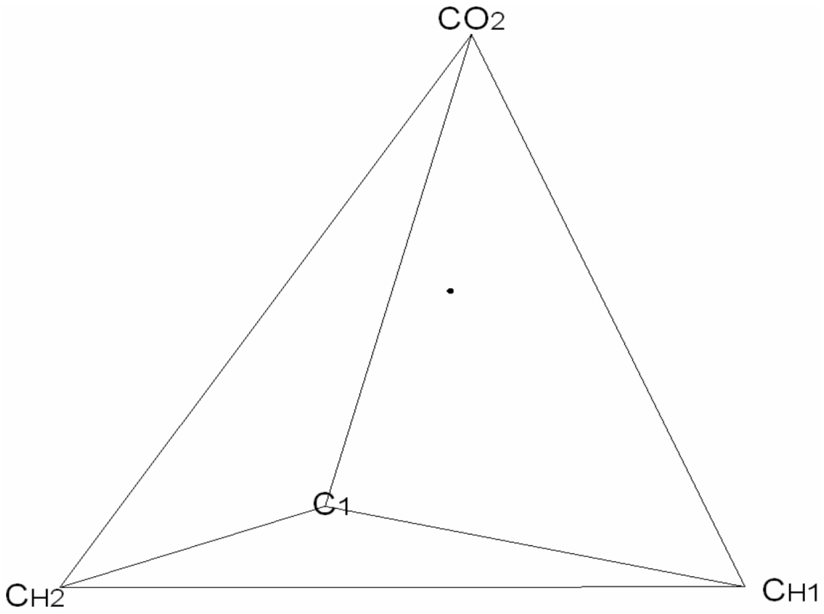

Figure 6.33m Tricritical point in BSB-Q composition space at 105°F and a pressure slightly above 3080 psia.

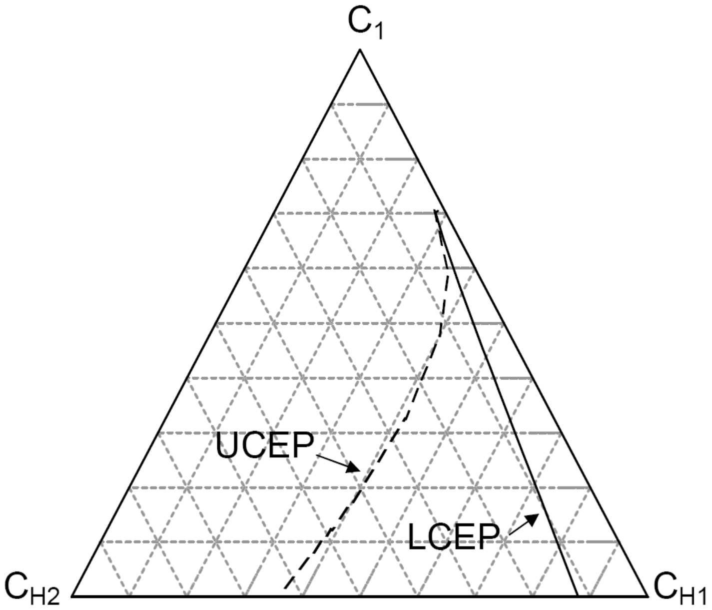

Figure 6.34 Projection of the midpoints of CEP tie-lines at 105°F onto the CO_2-free plane of the BSB-Q quaternary diagram.

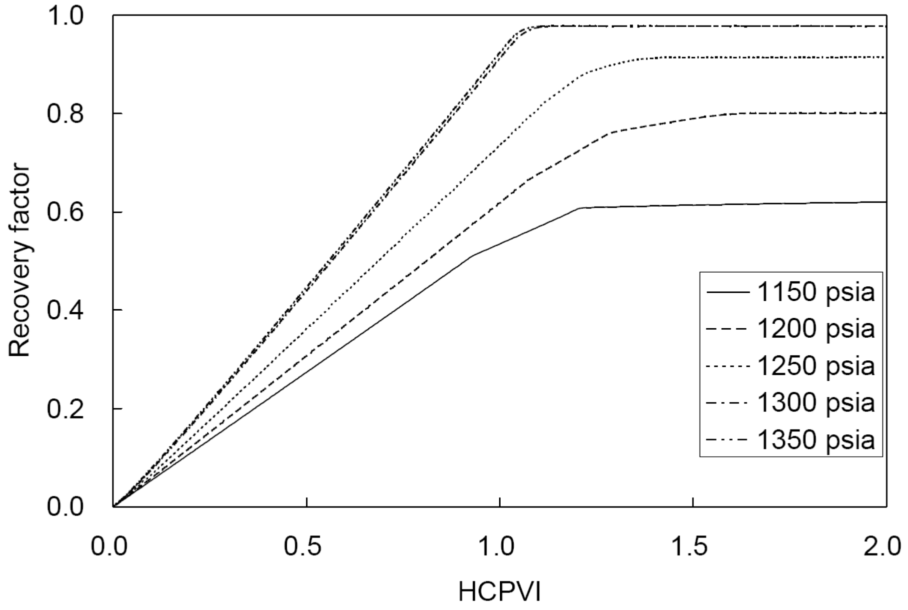

Figure 6.35 Oil recoveries for the BSB-Q oil displacements at 105°F at different pressures by the injection gas shown in Table 6.4.

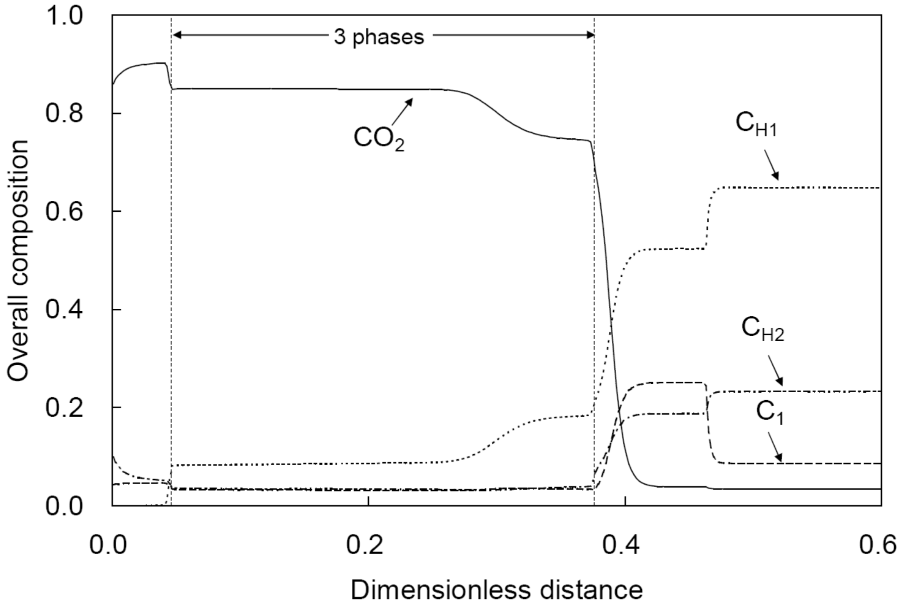

Figure 6.36 Component concentration profiles at 0.5 HCPVI for the BSB-Q oil displacement at 105°F and 1200 psia by the injection gas shown in Table 6.4.

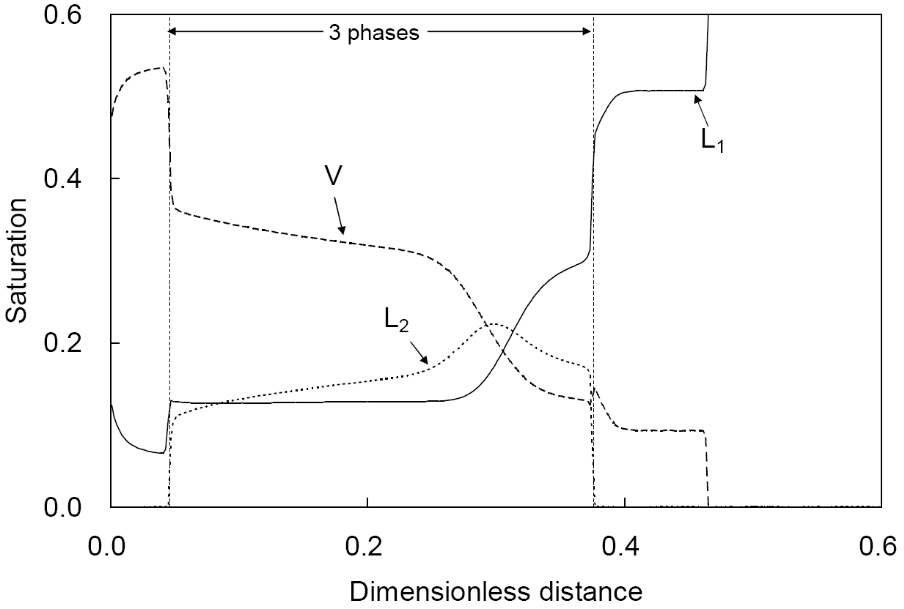

Figure 6.37 Saturation profiles at 0.5 HCPVI for the BSB-Q oil displacement at 105°F and 1200 psia by the injection gas shown in Table 6.4.

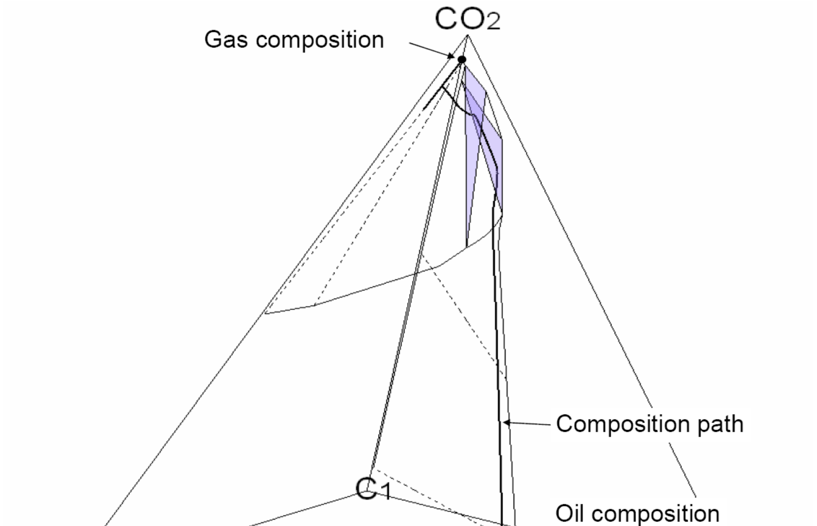

Figure 6.38 Simulated composition path and two- and three-phase regions along the path for the BSB-Q oil displacement at 105°F and 1200 psia by the injection gas shown in Table 6.4.

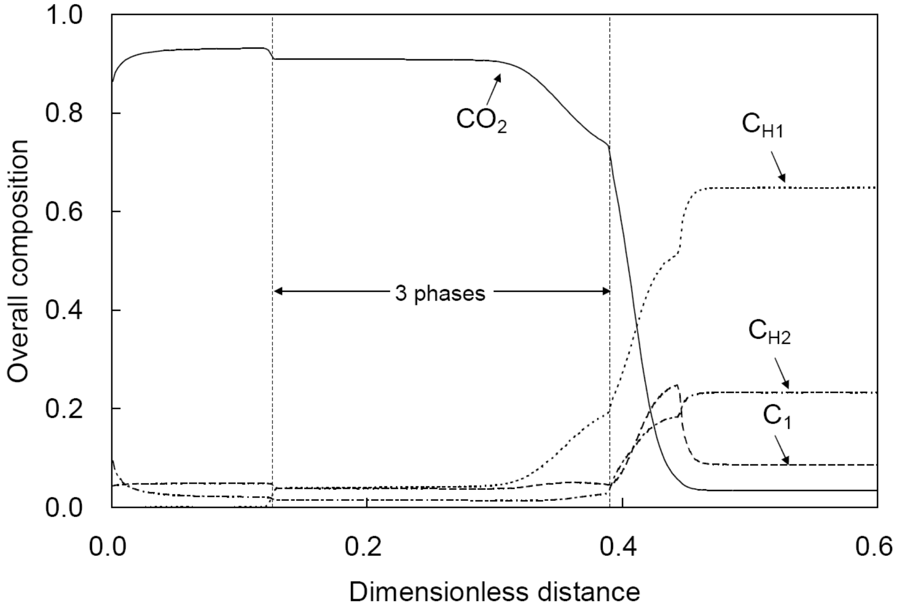

Figure 6.39 Component concentration profiles at 0.5 HCPVI for the BSB-Q oil displacement at 105°F and 1250 psia by the injection gas shown in Table 6.4.

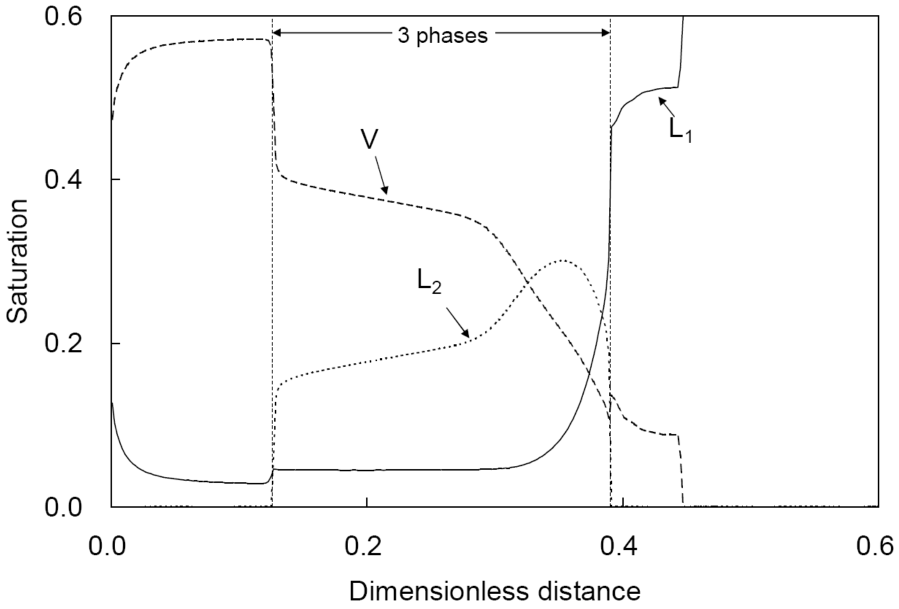

Figure 6.40 Saturation profiles at 0.5 HCPVI for the BSB-Q oil displacement at 105°F and 1250 psia by the injection gas shown in Table 6.4.

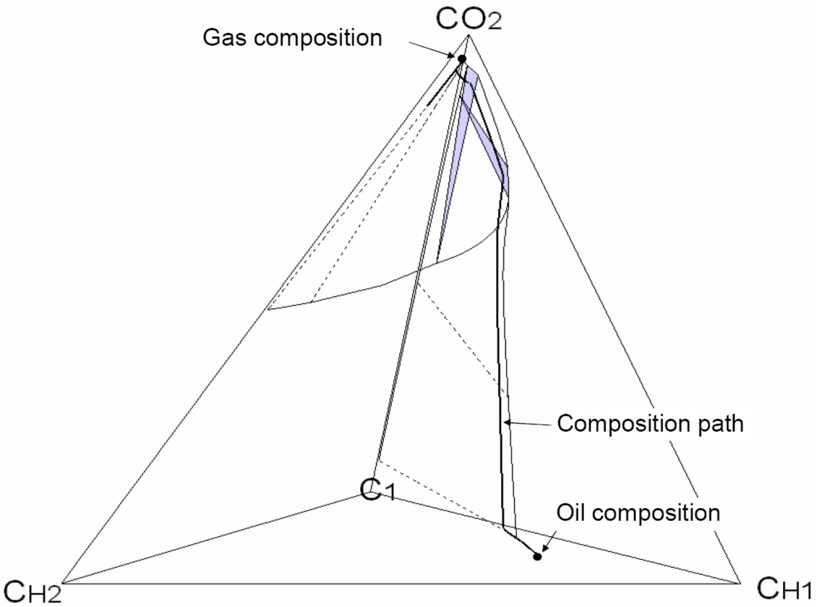

Figure 6.41 Simulated composition path and two- and three-phase regions along the path for the BSB-Q oil displacement at 105°F and 1250 psia by the injection gas shown in Table 6.4.

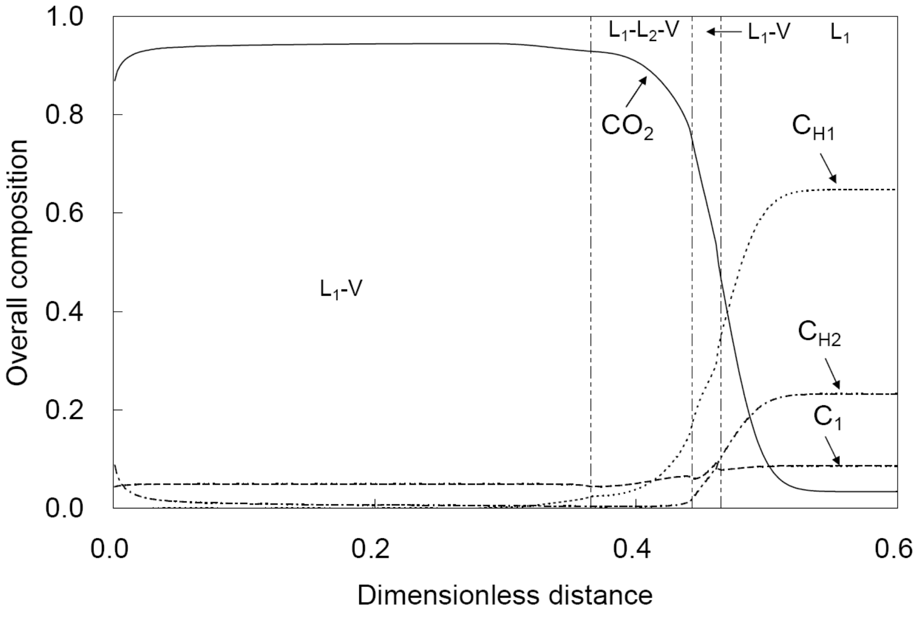

Figure 6.42 Component concentration profiles at 0.5 HCPVI for the BSB-Q oil displacement at 105°F and 1300 psia by the injection gas shown in Table 6.4.

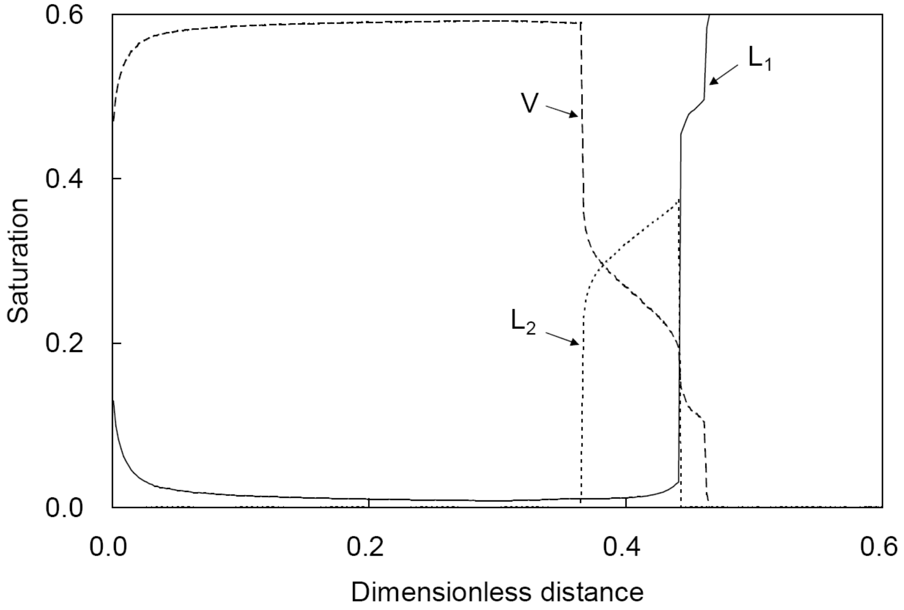

Figure 6.43 Saturation profiles at 0.5 HCPVI for the BSB-Q oil displacement at 105°F and 1300 psia by the injection gas shown in Table 6.4.

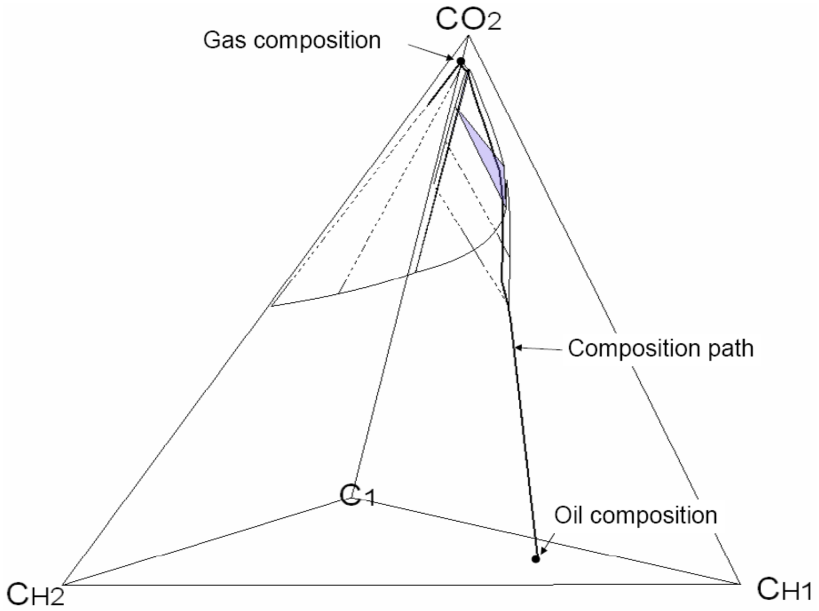

Figure 6.44 Simulated composition path and two- and three-phase regions along the path for the BSB-Q oil displacement at 105°F and 1300 psia by the injection gas shown in Table 6.4.

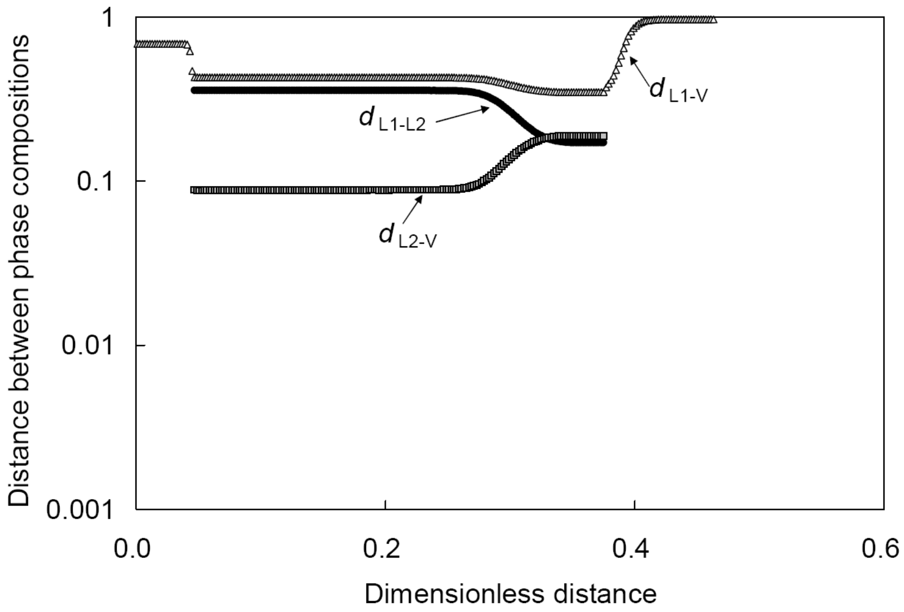

Figure 6.45 Distances between phase compositions in composition space at 0.5 HCPVI for the BSB-Q oil displacement at 105°F and 1200 psia by the injection gas shown in Table 6.4.

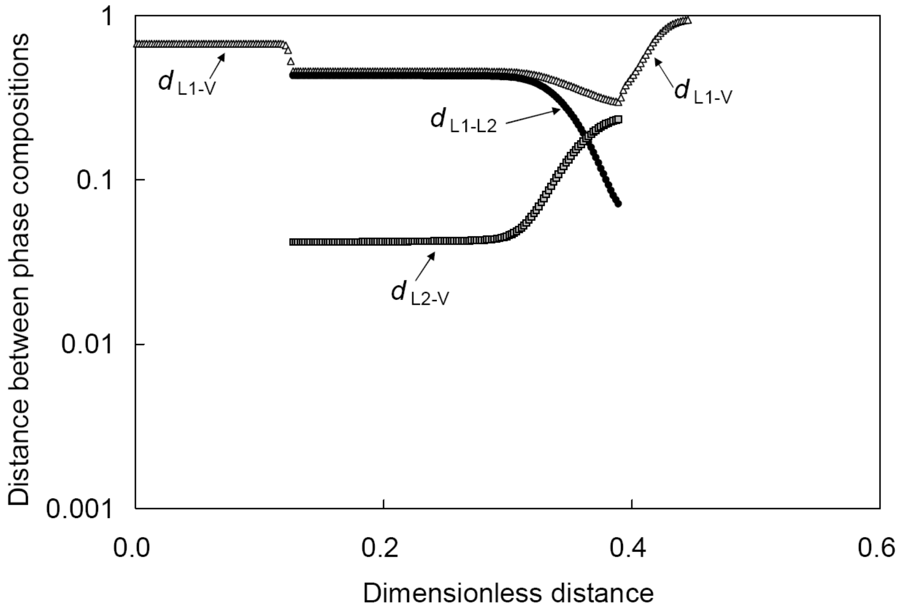

Figure 6.46 Distances between phase compositions in composition space at 0.5 HCPVI for the BSB-Q oil displacement at 105°F and 1250 psia by the injection gas shown in Table 6.4.

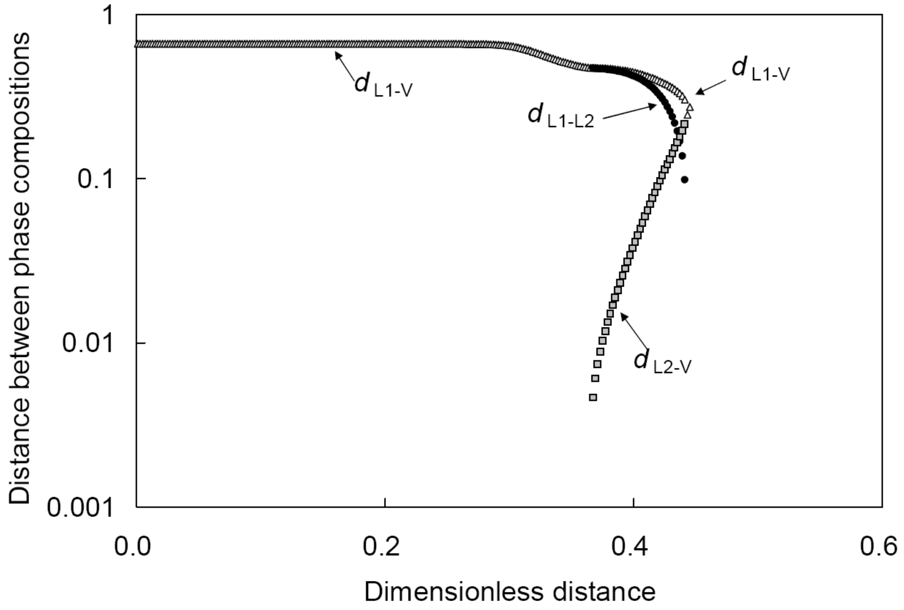

Figure 6.47 Distances between phase compositions in composition space at 0.5 HCPVI for the BSB-Q oil displacement at 105°F and 1300 psia by the injection gas shown in Table 6.4.

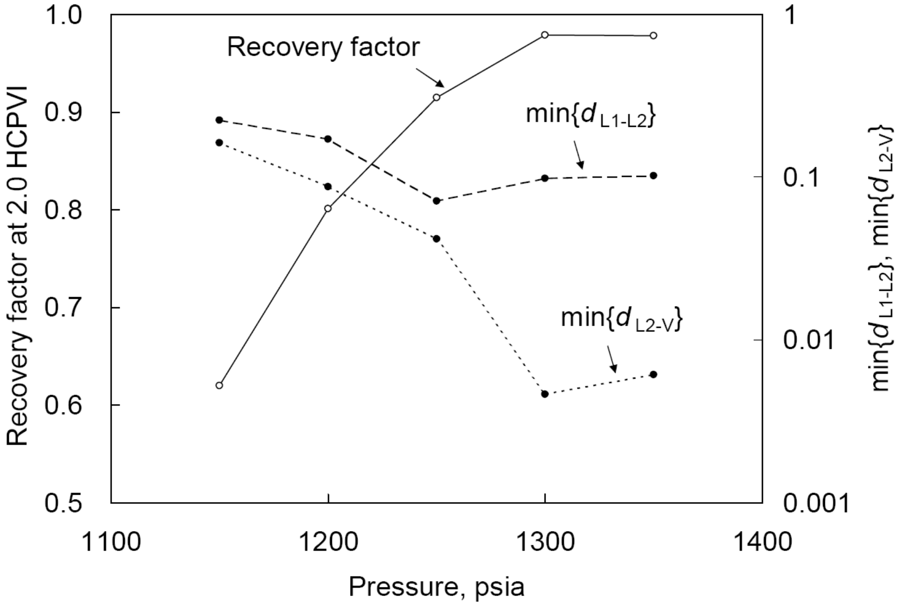

Figure 6.48 Oil recoveries at 2.0 HCPVI and minimum values of d_{L1-L2} and d_{L2-V} along the composition path for the BSB-Q oil displacements at 105°F by the injection gas shown in Table 6.4.

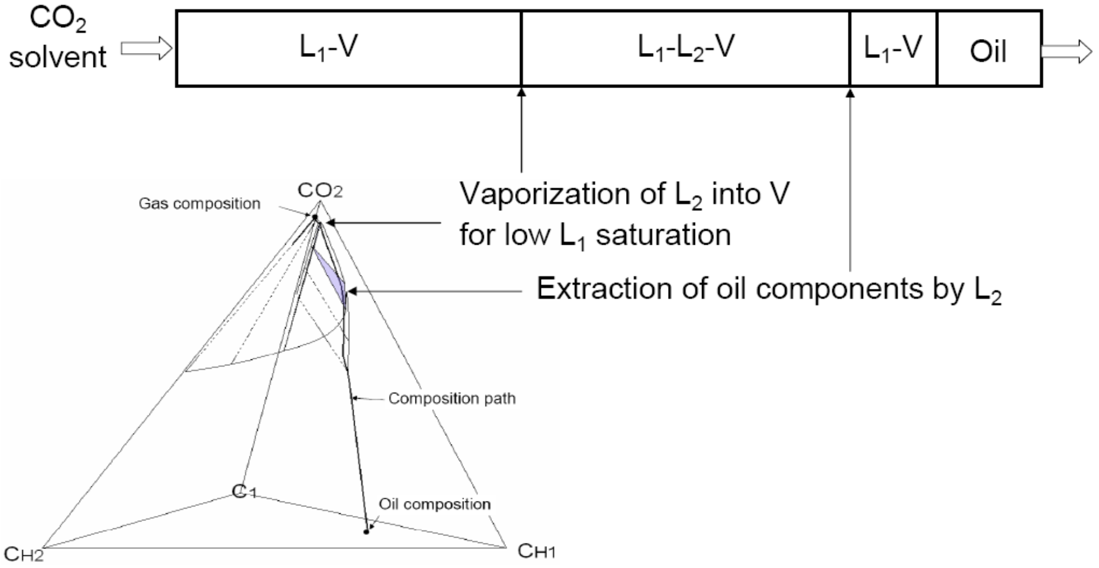

Figure 6.49 Schematic for the role of critical endpoint behavior in the BSB-Q oil displacement at 105°F and 1300 psia by the injection gas shown in Table 6.4.

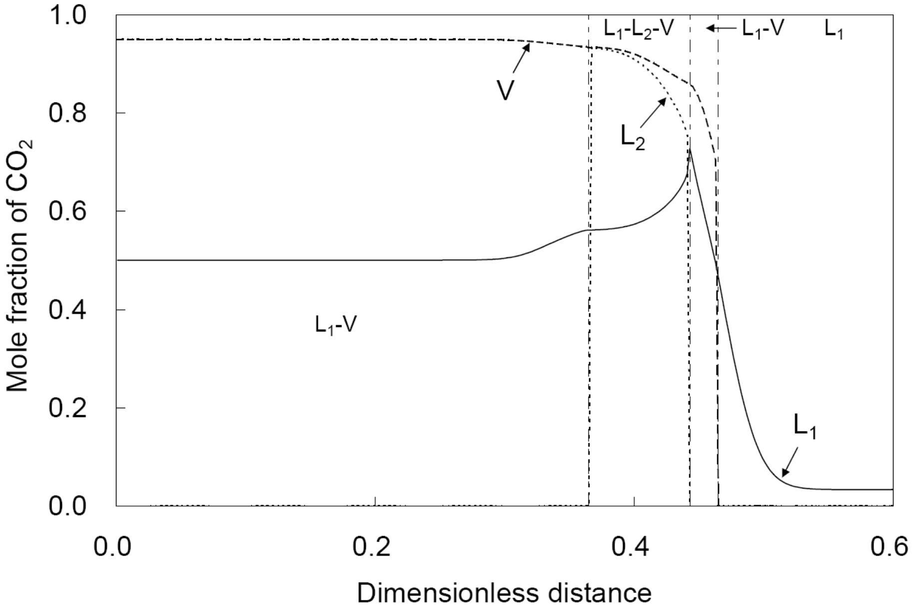

Figure 6.50a CO_2 mole fractions in phases at 0.5 HCPVI for the BSB-Q oil displacement at 105°F and 1300 psia by the injection gas shown in Table 6.4.

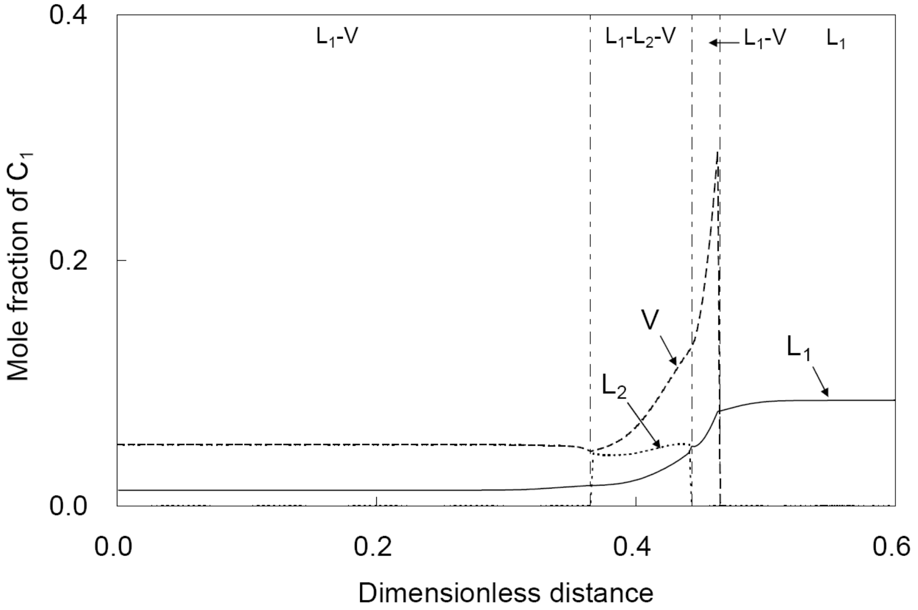

Figure 6.50b C_1 mole fractions in phases at 0.5 HCPVI for the BSB-Q oil displacement at 105°F and 1300 psia by the injection gas shown in Table 6.4.

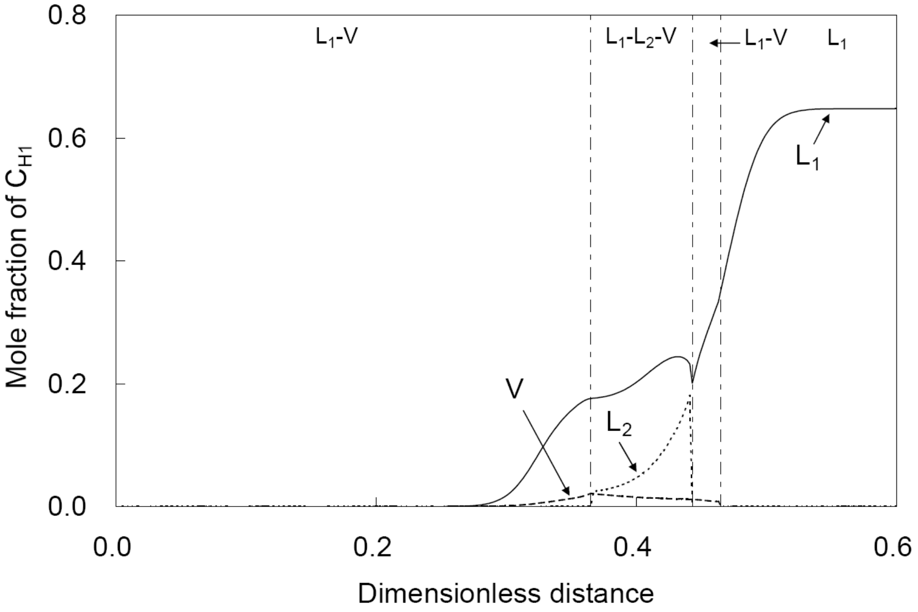

Figure 6.50c C_{H1} mole fractions in phases at 0.5 HCPVI for the BSB-Q oil displacement at 105°F and 1300 psia by the injection gas shown in Table 6.4.

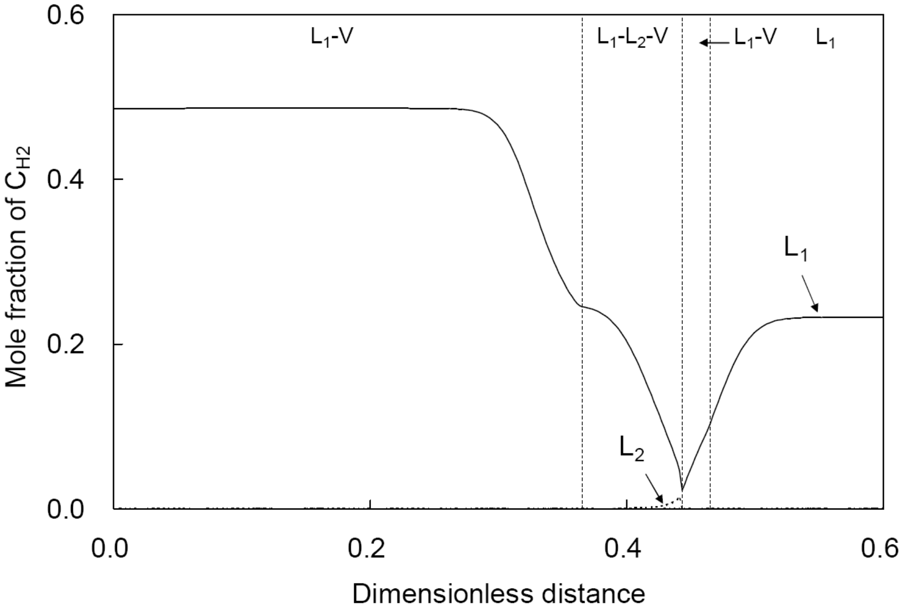

Figure 6.50d C_{H2} mole fractions in phases at 0.5 HCPVI for the BSB-Q oil displacement at 105°F and 1300 psia by the injection gas shown in Table 6.4.

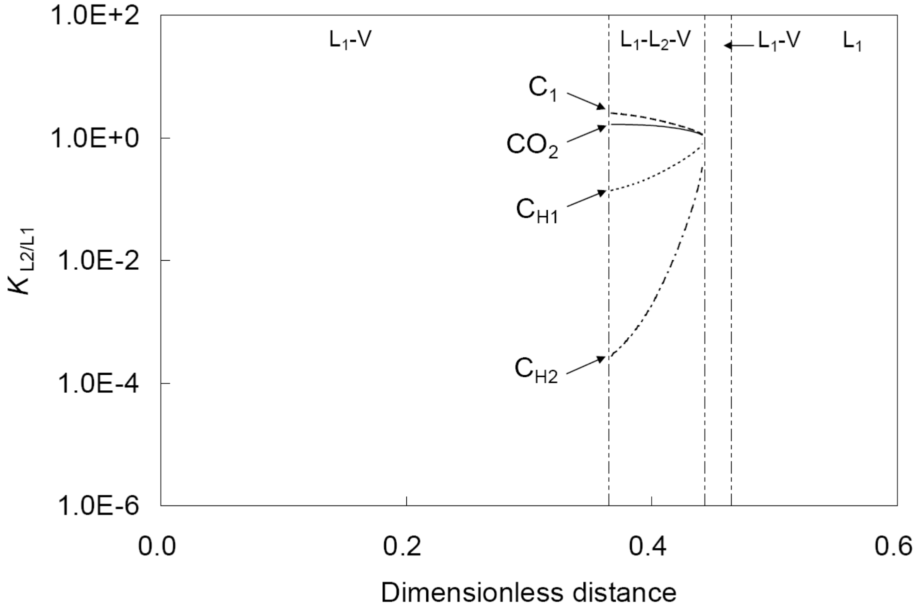

Figure 6.51a $K_{L2/L1}$ profiles at 0.5 HCPVI for the BSB-Q oil displacement at 105°F and 1300 psia by the injection gas shown in Table 6.4. $K_{iL2/L1} = x_{iL2} / x_{iL1}$.

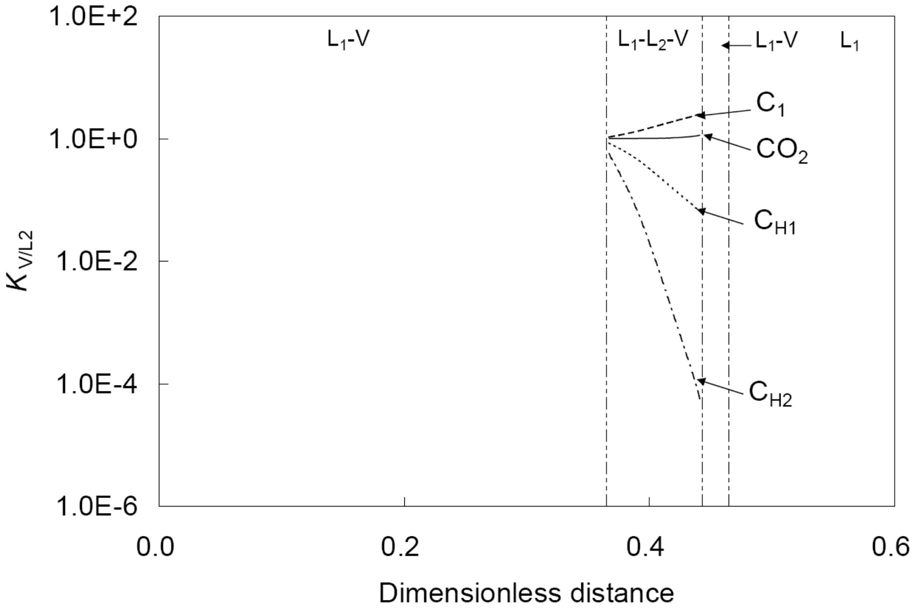

Figure 6.51b $K_{V/L2}$ profiles at 0.5 HCPVI for the BSB-Q oil displacement at 105°F and 1300 psia by the injection gas shown in Table 6.4. $K_{iV/L2} = x_{iV} / x_{iL2}$.

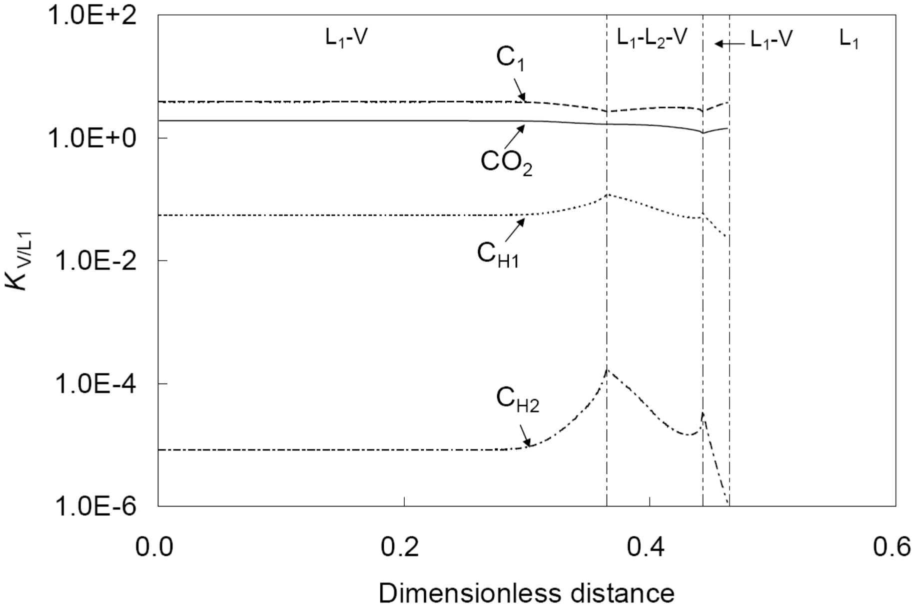

Figure 6.51c $K_{V/L1}$ profiles at 0.5 HCPVI for the BSB-Q oil displacement at 105°F and 1300 psia by the injection gas shown in Table 6.4. $K_{iV/L1} = x_{iV} / x_{iL1}$.

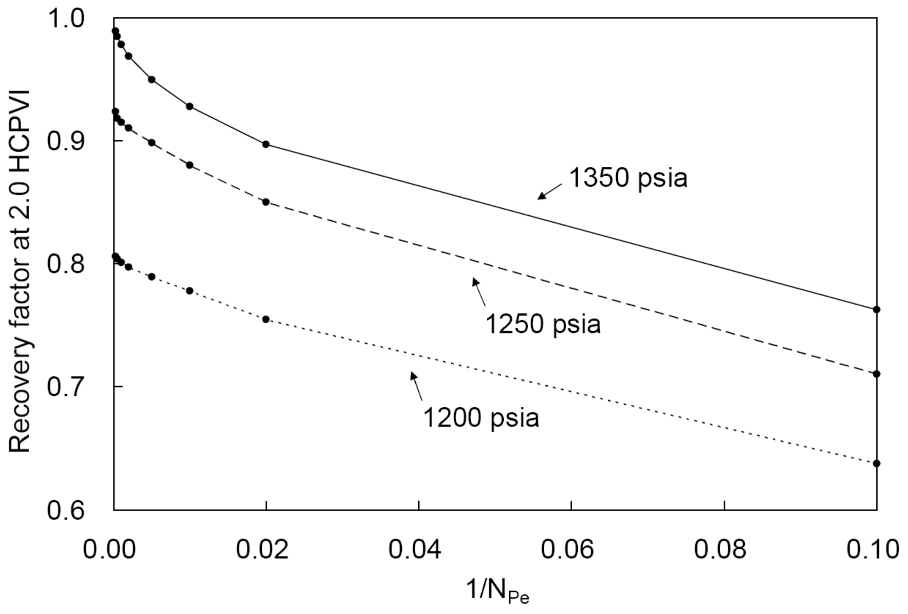

Figure 6.52 Oil recoveries at 2.0 HCPVI with different Peclet numbers and pressures for the BSB-Q oil displacements at 105°F by the injection gas shown in Table 6.4.

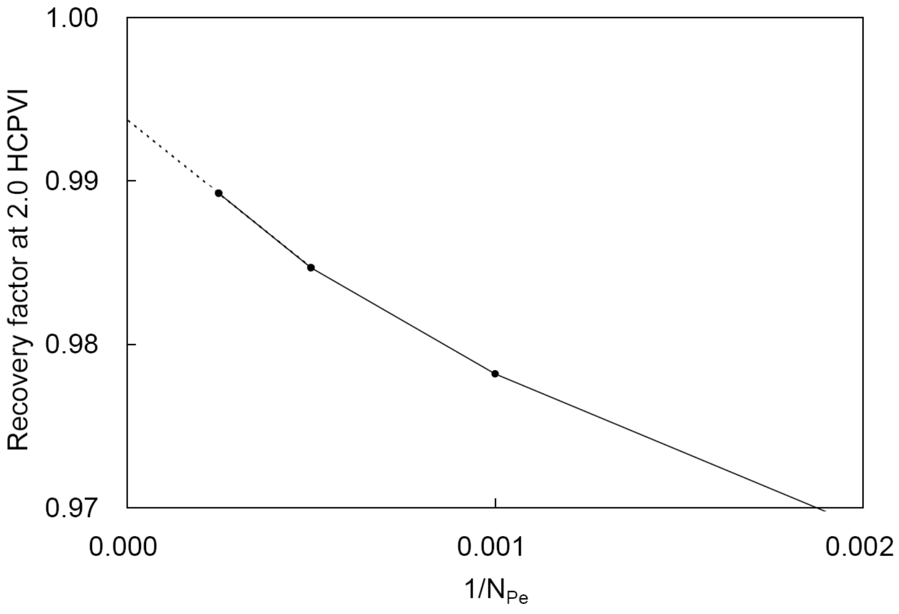

Figure 6.53 Oil recoveries at 2.0 HCPVI with different Peclet numbers for the BSB-Q oil displacements at 105°F and 1350 psia. The dashed line is an extrapolation to estimate the recovery factor with no dispersion.

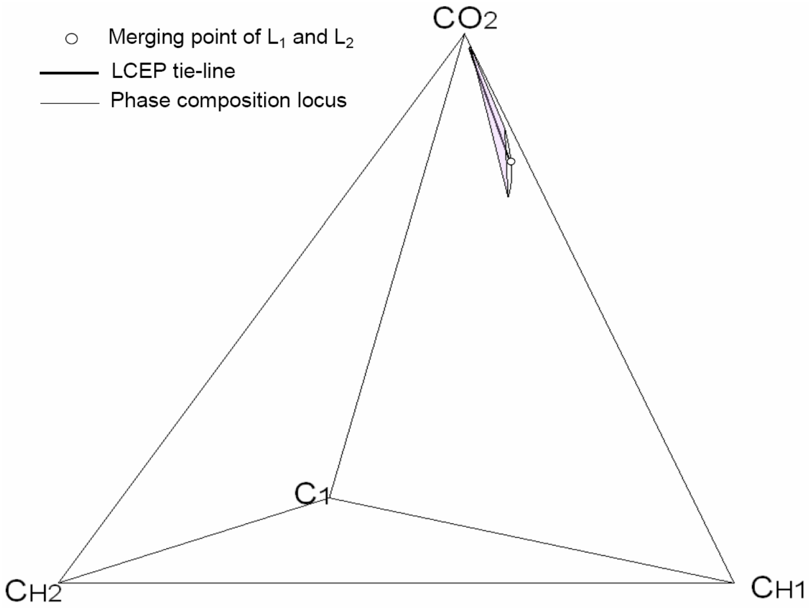

Figure 6.54a Three-phase region in BSB-Q composition space at 130°F and 1300 psia. The BSB-Q system is given in Table 6.4.

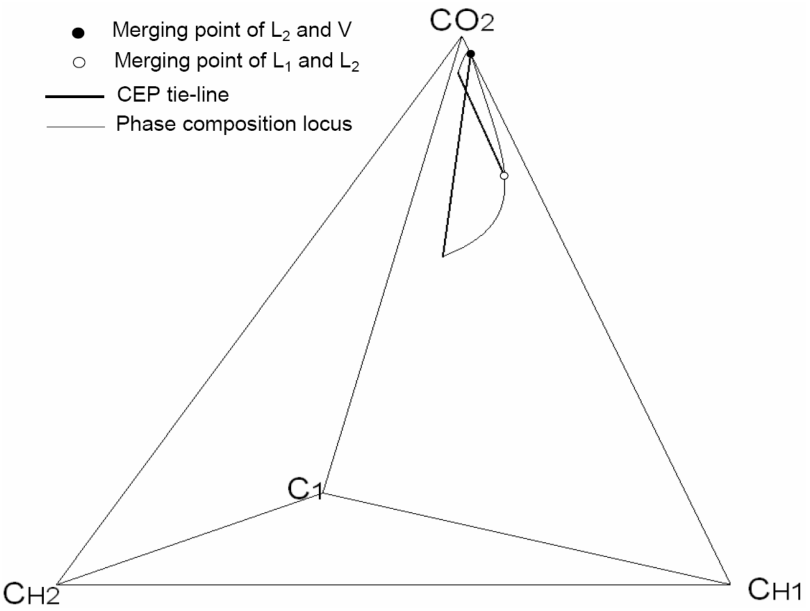

Figure 6.54b Three-phase region in BSB-Q composition space at 120°F and 1300 psia.

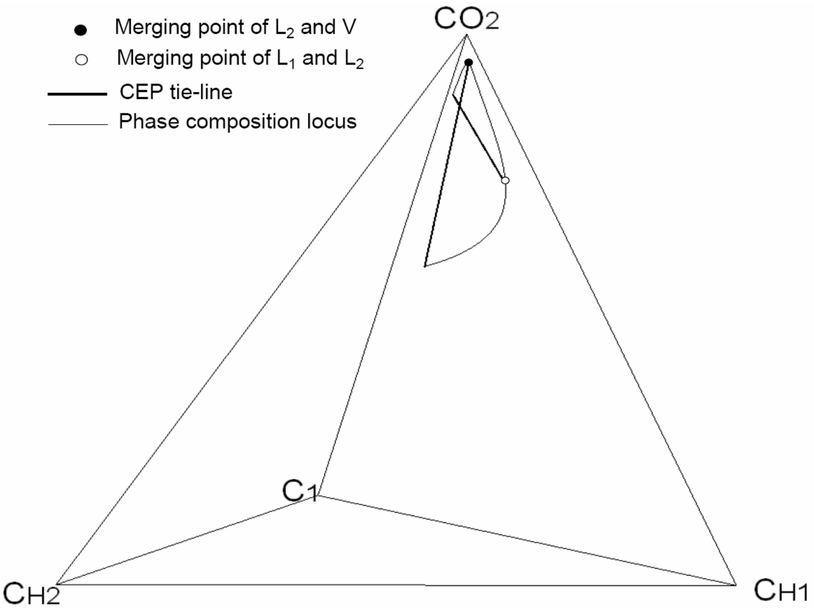

Figure 6.54c Three-phase region in BSB-Q composition space at 110°F and 1300 psia.

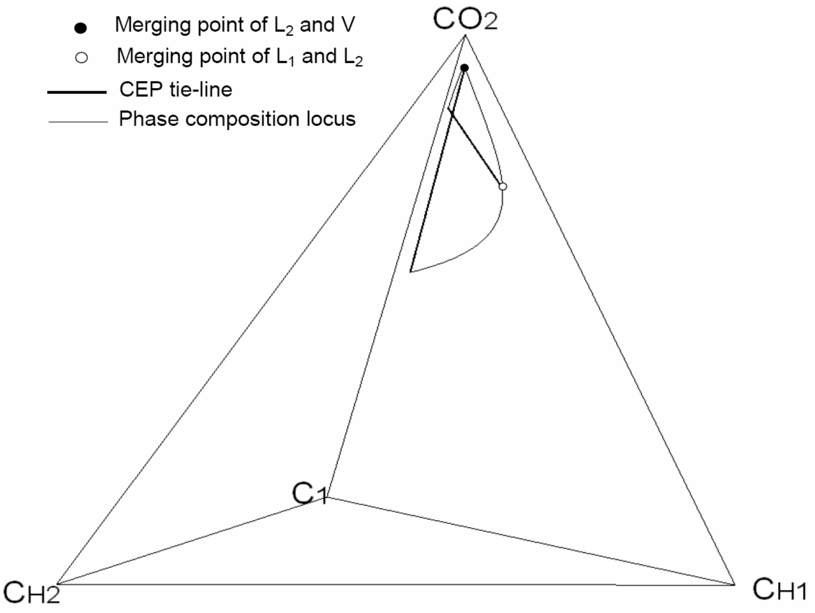

Figure 6.54d Three-phase region in BSB-Q composition space at 105°F and 1300 psia.

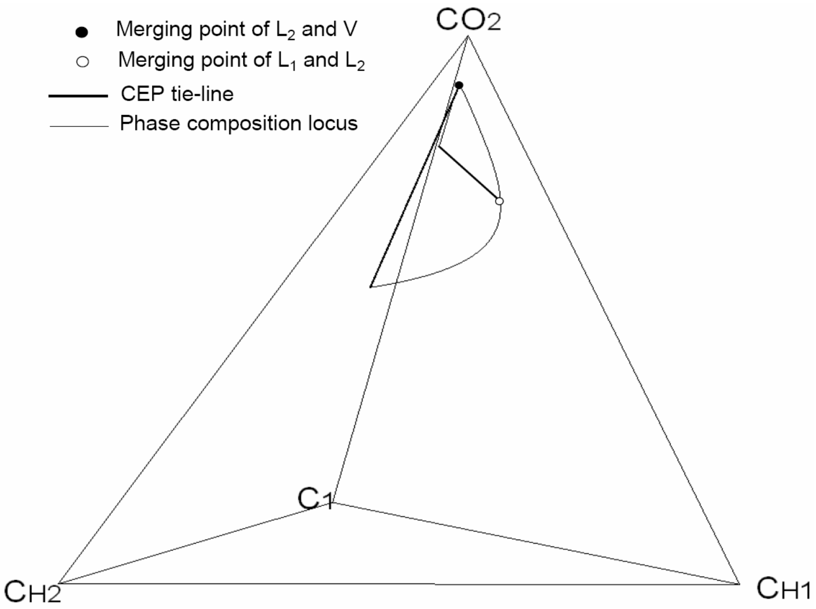

Figure 6.54e   Three-phase region in BSB-Q composition space at 90°F and 1300 psia.

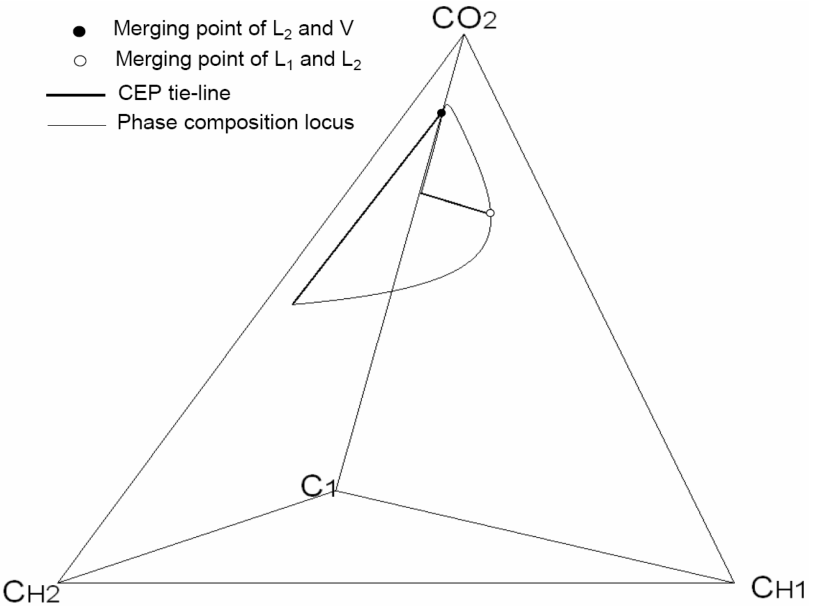

Figure 6.54f   Three-phase region in BSB-Q composition space at 70°F and 1300 psia.

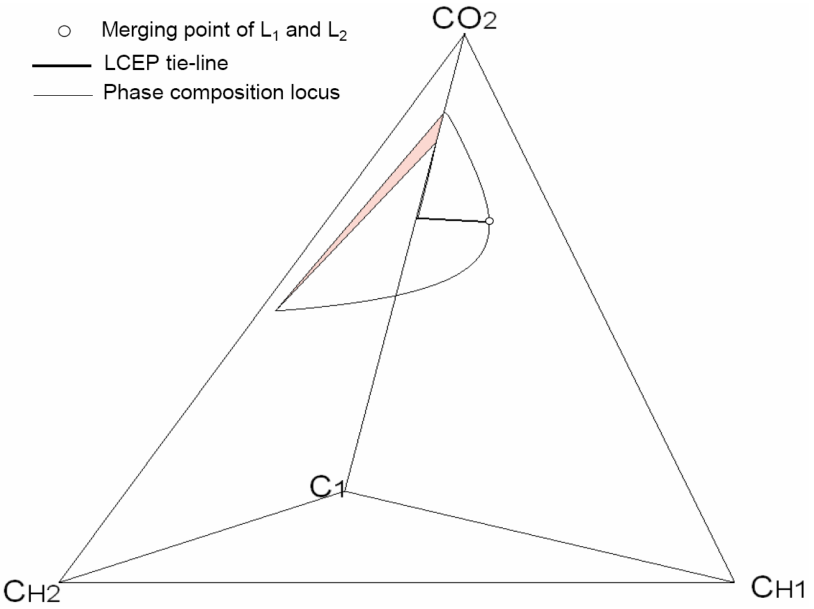

Figure 6.54g Three-phase region in BSB-Q composition space at 60°F and 1300 psia. The shaded tie-triangle is on the C_{H1}-free plane.

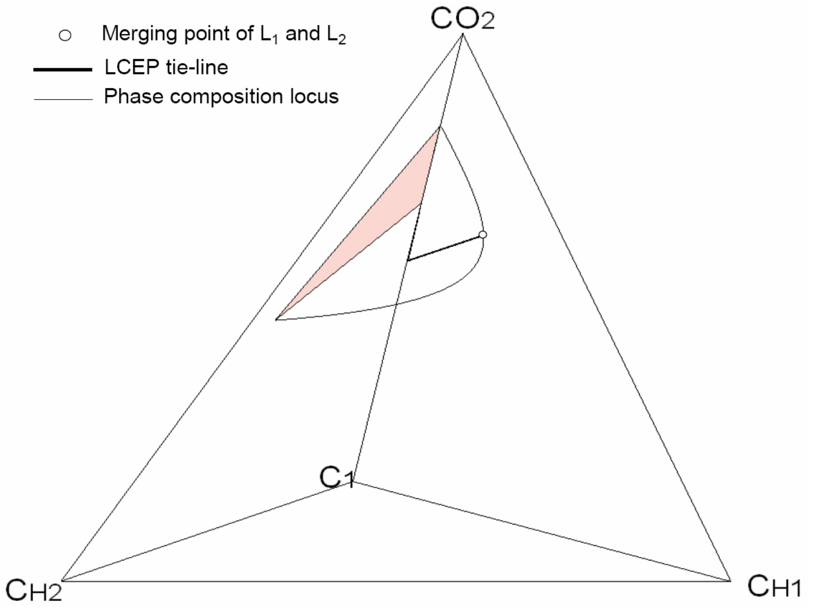

Figure 6.54h Three-phase region in BSB-Q composition space at 40°F and 1300 psia. The shaded tie-triangle is on the C_{H1}-free plane.

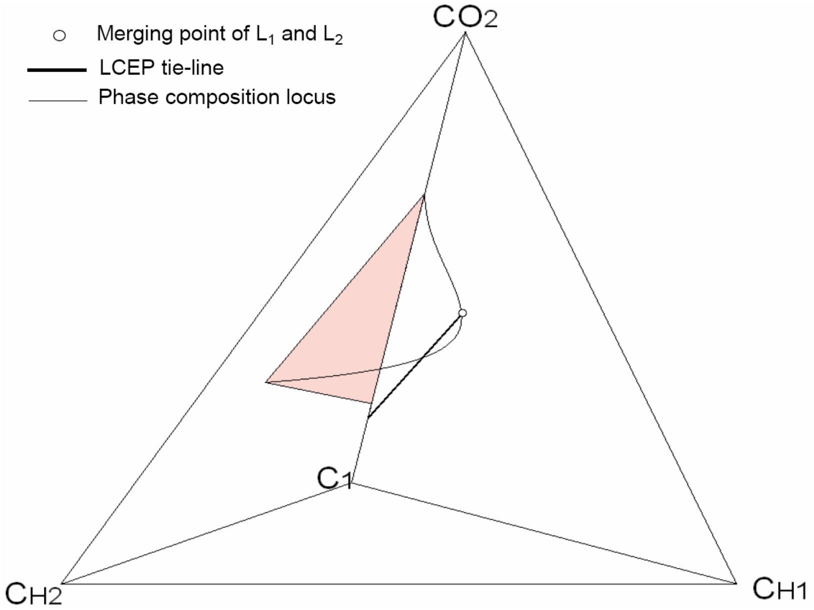

Figure 6.54i Three-phase region in BSB-Q composition space at −60°F and 1300 psia. The shaded tie-triangle is on the C_{H1}-free plane.

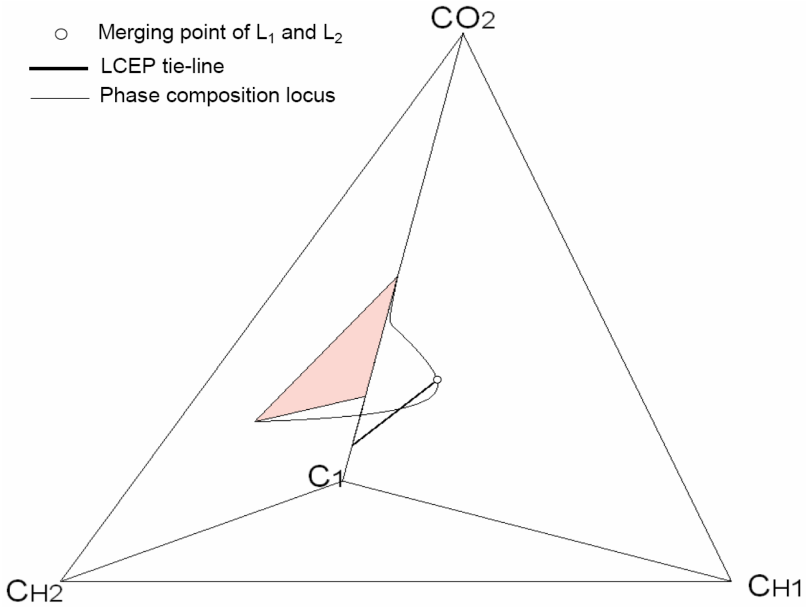

Figure 6.54j Three-phase region in BSB-Q composition space at −120°F and 1300 psia. The shaded tie-triangle is on the C_{H1}-free plane.

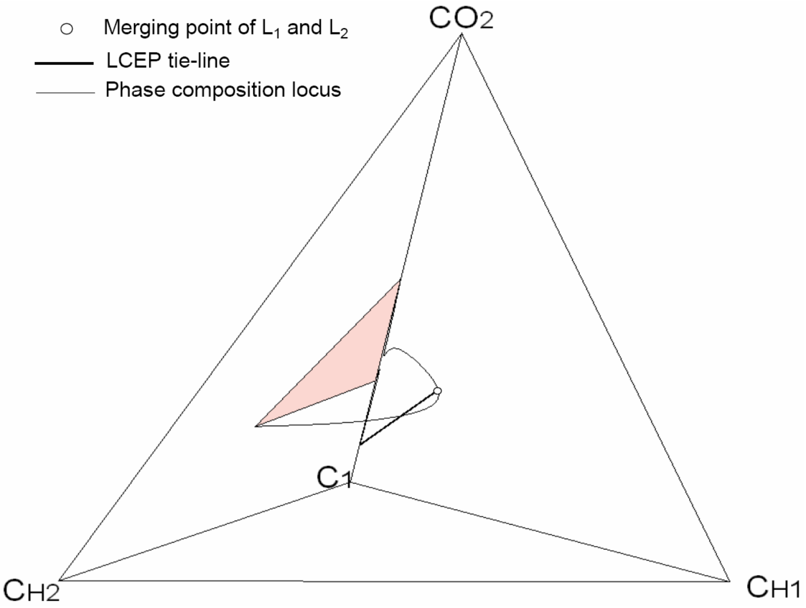

Figure 6.54k Three-phase region in BSB-Q composition space at −128°F and 1300 psia. The shaded tie-triangle is on the C_{H1}-free plane.

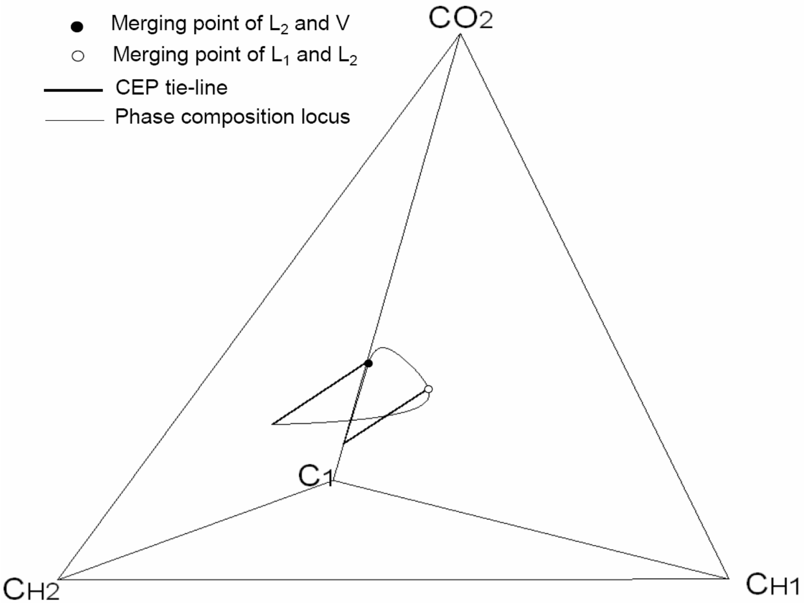

Figure 6.54l Three-phase region in BSB-Q composition space at a temperature slightly below −128°F and 1300 psia.

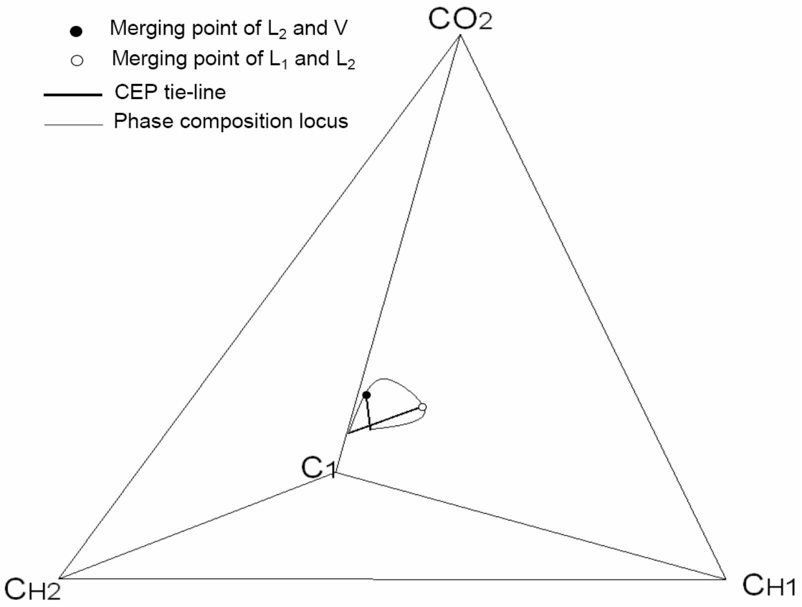

Figure 6.54m Three-phase region in BSB-Q composition space at −150°F and 1300 psia.

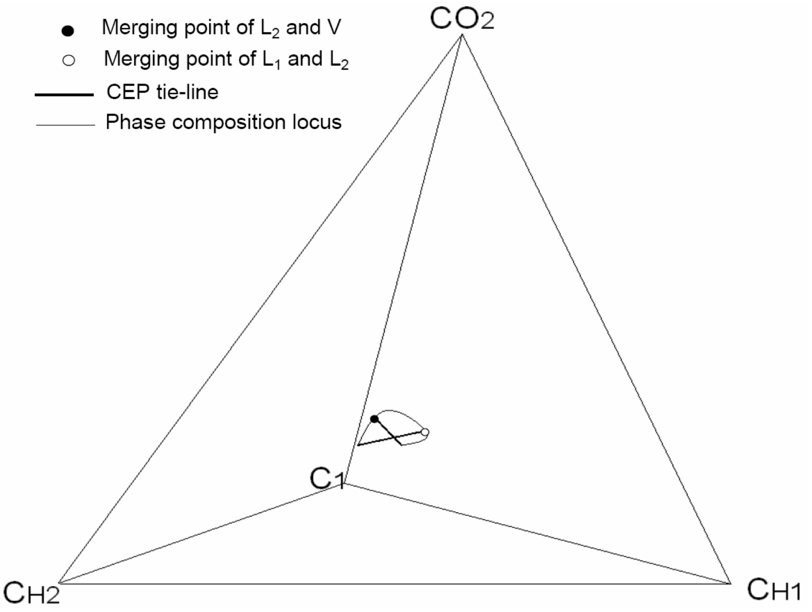

Figure 6.54n Three-phase region in BSB-Q composition space at −170°F and 1300 psia.

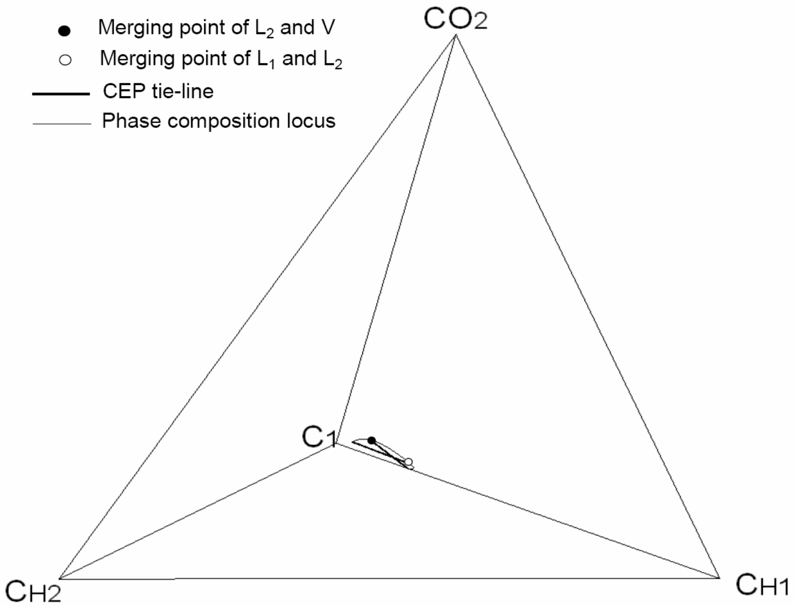

Figure 6.54o Three-phase region in BSB-Q composition space at −260°F and 1300 psia.

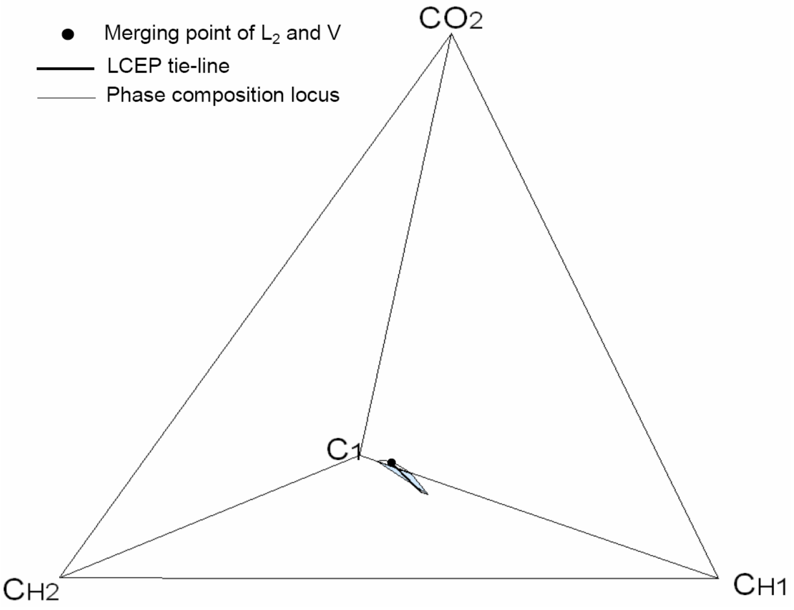

Figure 6.54p Three-phase region in BSB-Q composition space at −290°F and 1300 psia. The shaded tie-triangle is on the CO_2-free plane.

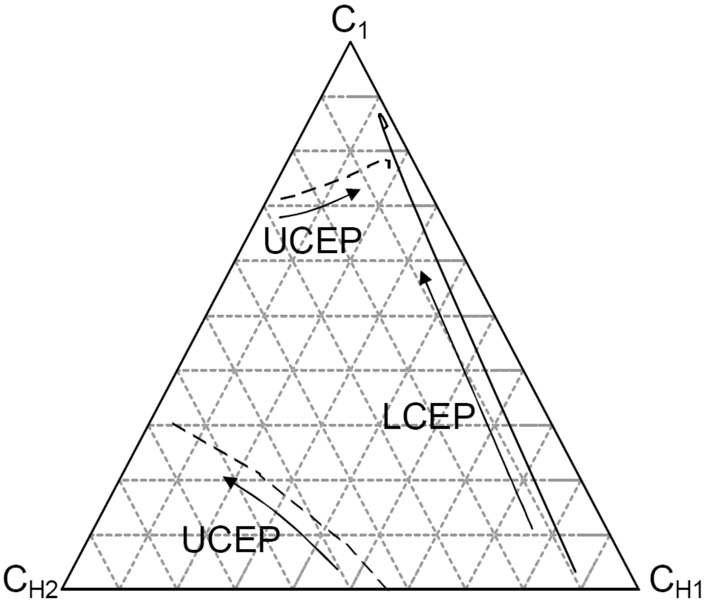

Figure 6.55 Projection of the midpoints of CEP tie-lines onto the CO_2-free plane of the BSB-Q quaternary diagram at 1300 psia. The arrows indicate decreasing temperature.

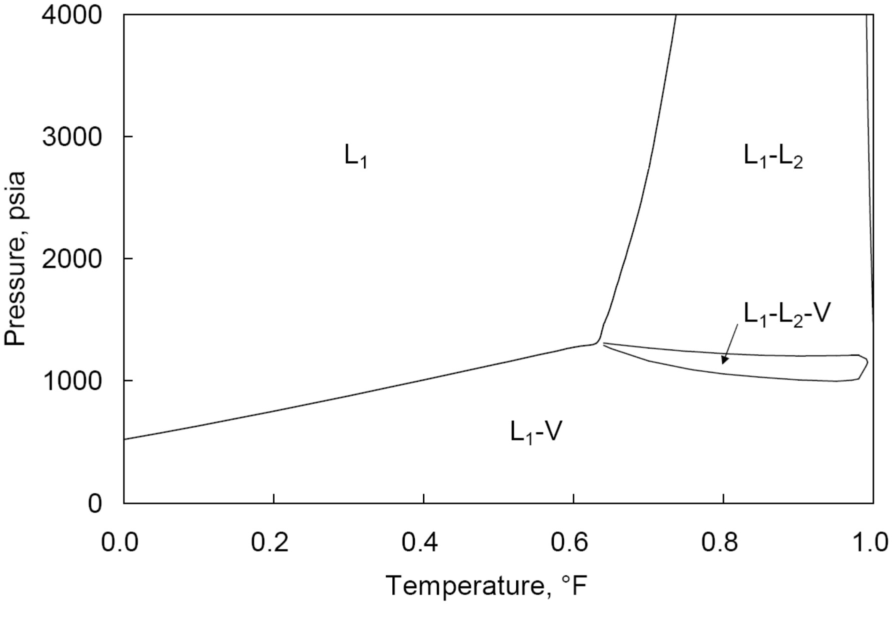

Figure 6.56 *P*-*x* diagram at 90˚F for the BSB-Q oil and injection gas given in Table 6.4.

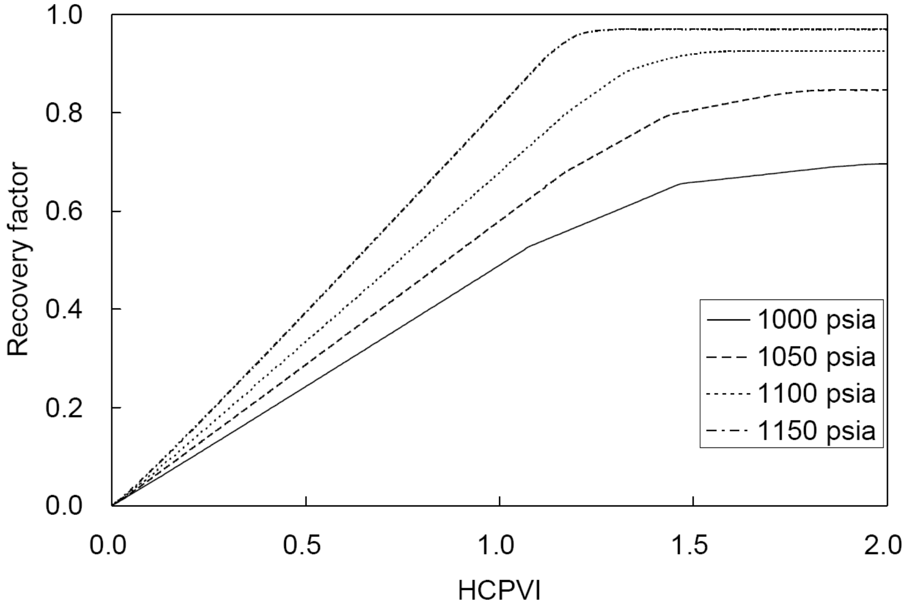

Figure 6.57 Oil recoveries for the displacements of the BSB-Q oil at 90°F at different pressures by the injection gas shown in Table 6.4.

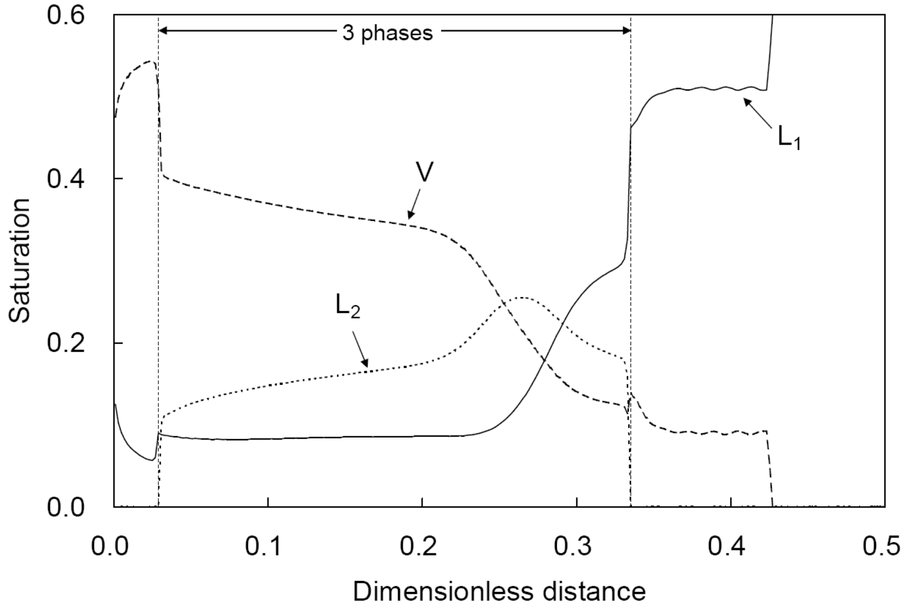

Figure 6.58 Saturation profiles at 0.5 HCPVI for the BSB-Q oil displacement at 90°F and 1050 psia by the injection gas shown in Table 6.4.

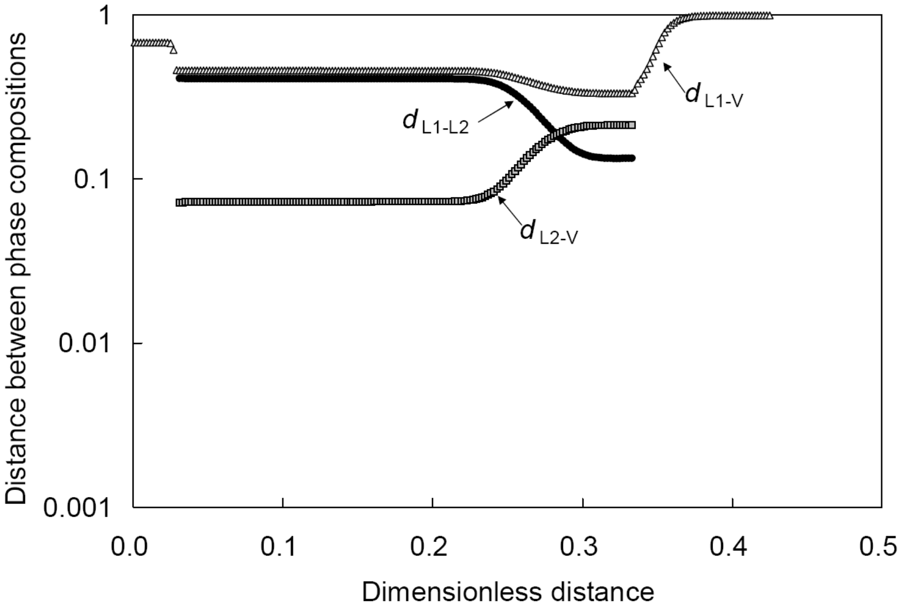

Figure 6.59 Distances between phase compositions in composition space at 0.5 HCPVI for the BSB-Q oil displacement at 90°F and 1050 psia by the injection gas shown in Table 6.4.

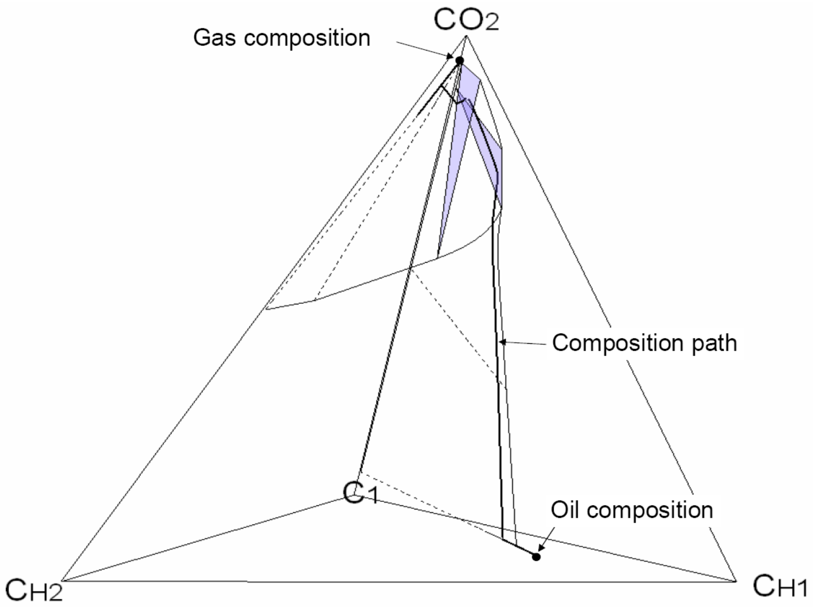

Figure 6.60 Simulated composition path and two- and three-phase regions along the path for the BSB-Q oil displacement at 90°F and 1050 psia by the injection gas shown in Table 6.4.

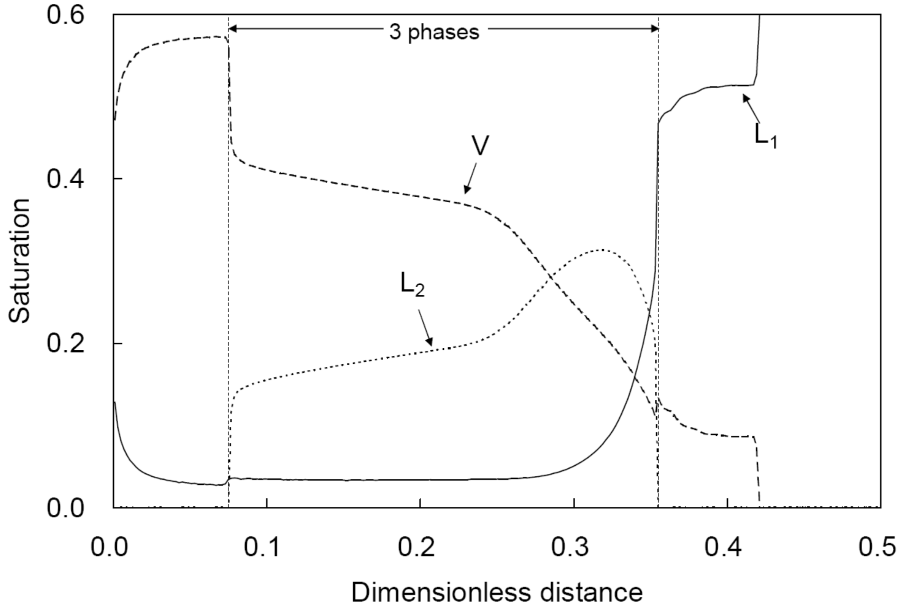

Figure 6.61 Saturation profiles at 0.5 HCPVI for the BSB-Q oil displacement at 90°F and 1100 psia by the injection gas shown in Table 6.4.

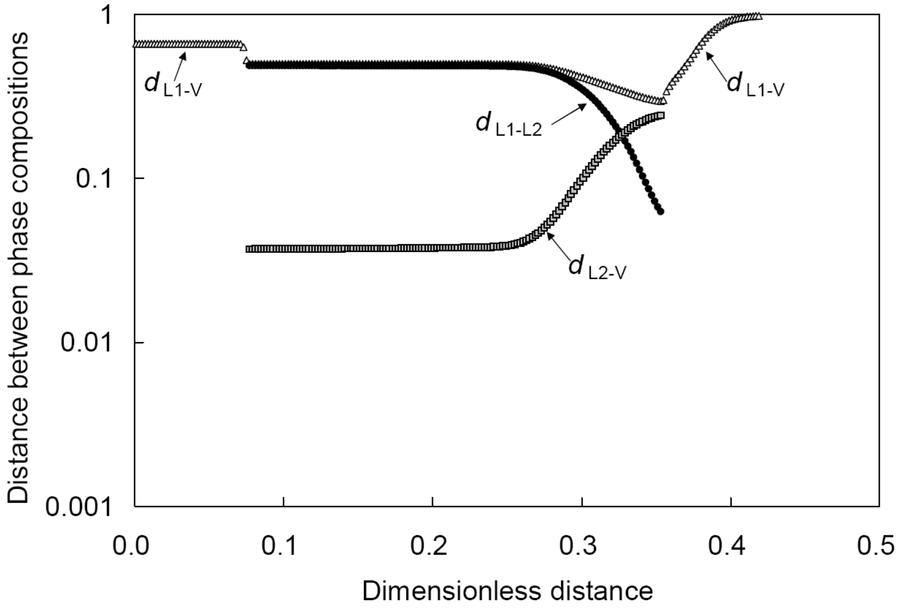

Figure 6.62 Distances between phase compositions in composition space at 0.5 HCPVI for the BSB-Q oil displacement at 90°F and 1100 psia by the injection gas shown in Table 6.4.

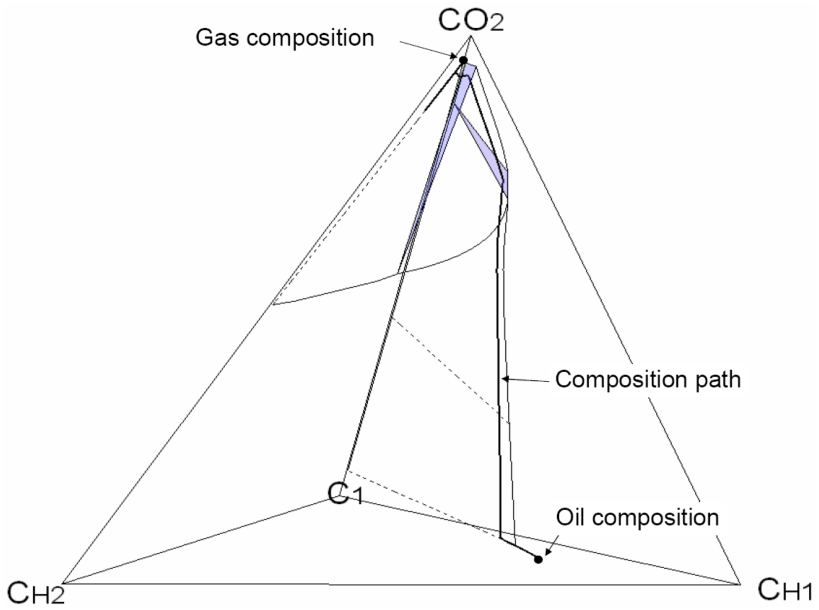

Figure 6.63 Simulated composition path and two- and three-phase regions along the path for the BSB-Q oil displacement at 90°F and 1100 psia by the injection gas shown in Table 6.4.

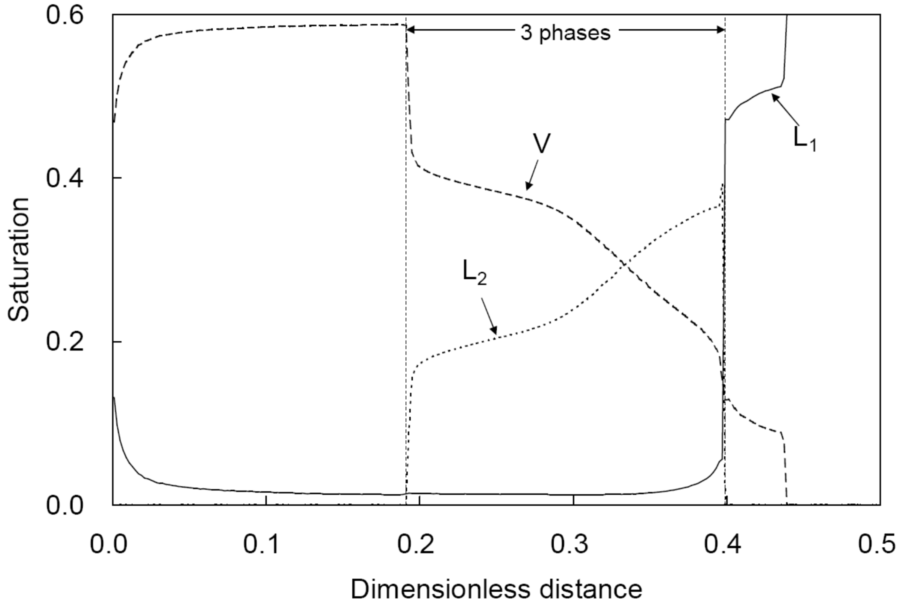

Figure 6.64 Saturation profiles at 0.5 HCPVI for the BSB-Q oil displacement at 90°F and 1150 psia by the injection gas shown in Table 6.4.

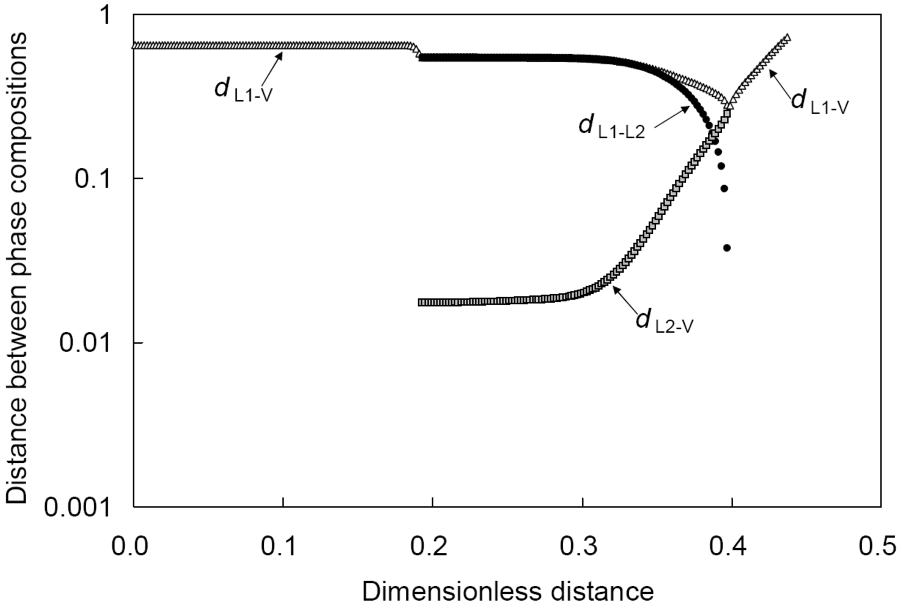

Figure 6.65 Distances between phase compositions in composition space at 0.5 HCPVI for the BSB-Q oil displacement at 90°F and 1150 psia by the injection gas shown in Table 6.4.

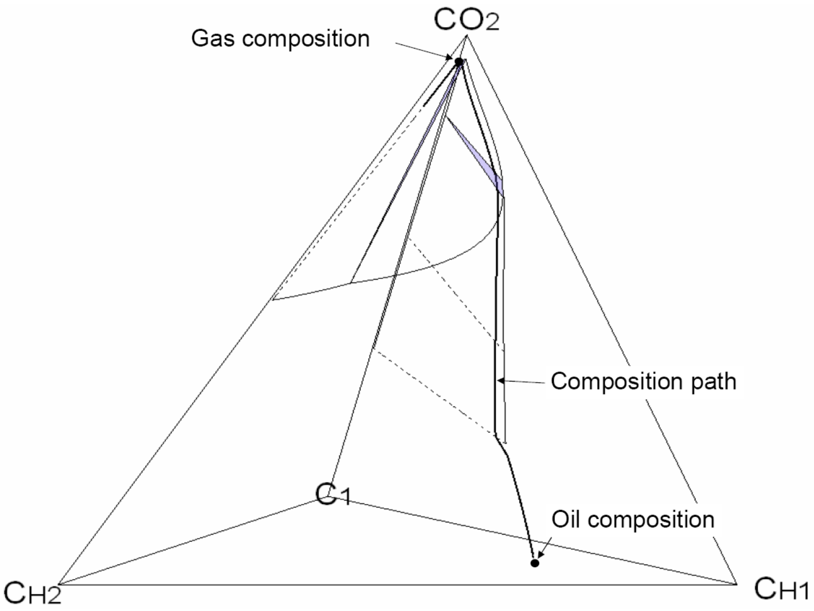

Figure 6.66 Simulated composition path and two- and three-phase regions along the path for the BSB-Q oil displacement at 90°F and 1150 psia by the injection gas shown in Table 6.4.

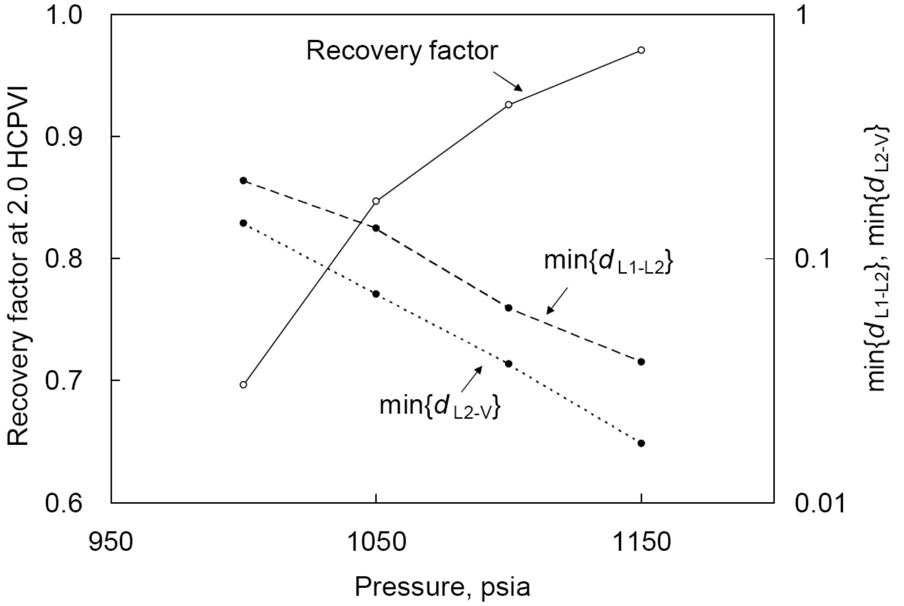

Figure 6.67 Oil recoveries at 2.0 HCPVI and minimum values of d_{L1-L2} and d_{L2-V} along the composition path for the BSB-Q oil displacements at 90°F by the injection gas shown in Table 6.4.

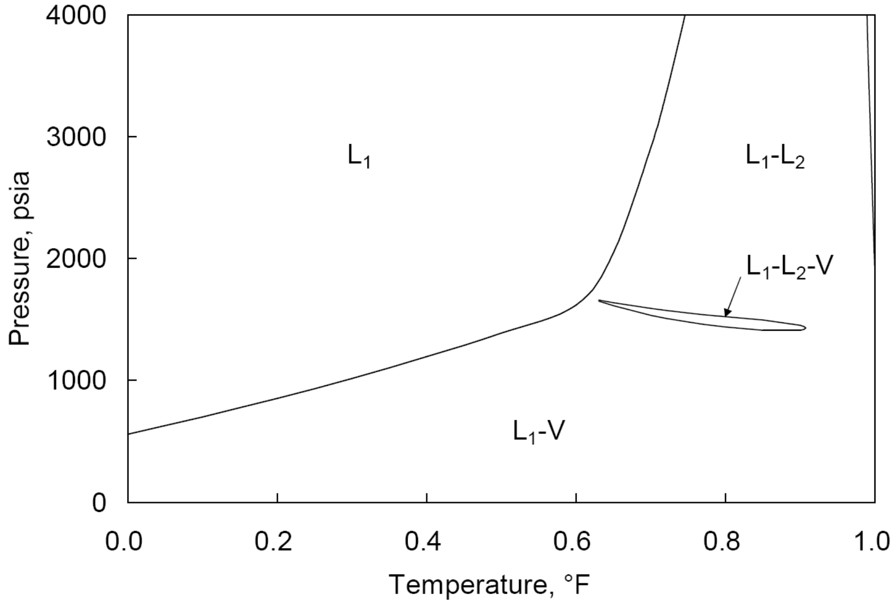

Figure 6.68 *P*-*x* diagram at 120˚F for the BSB-Q oil and injection gas given in Table 6.4.

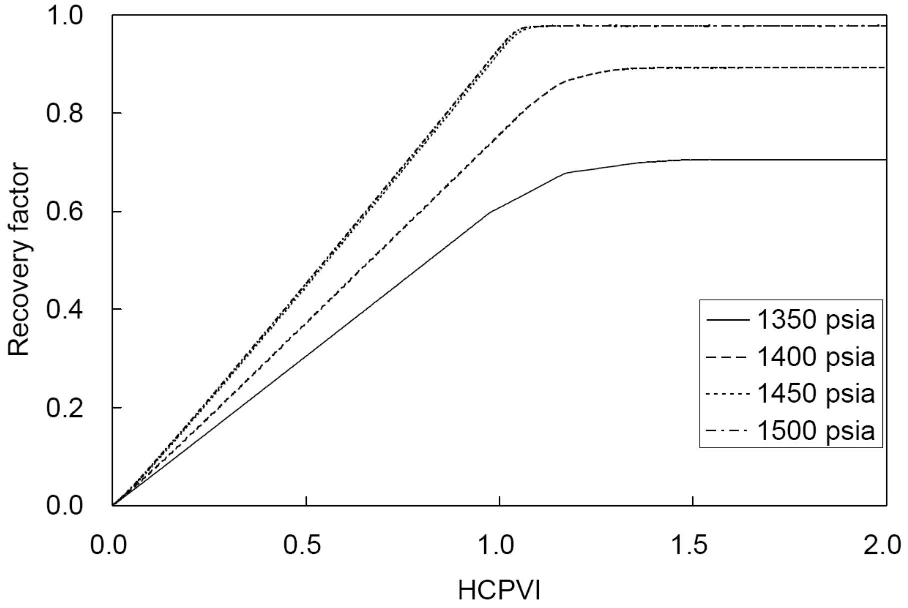

Figure 6.69 Oil recoveries for the displacements of the BSB-Q oil at 120˚F at different pressures by the injection gas shown in Table 6.4.

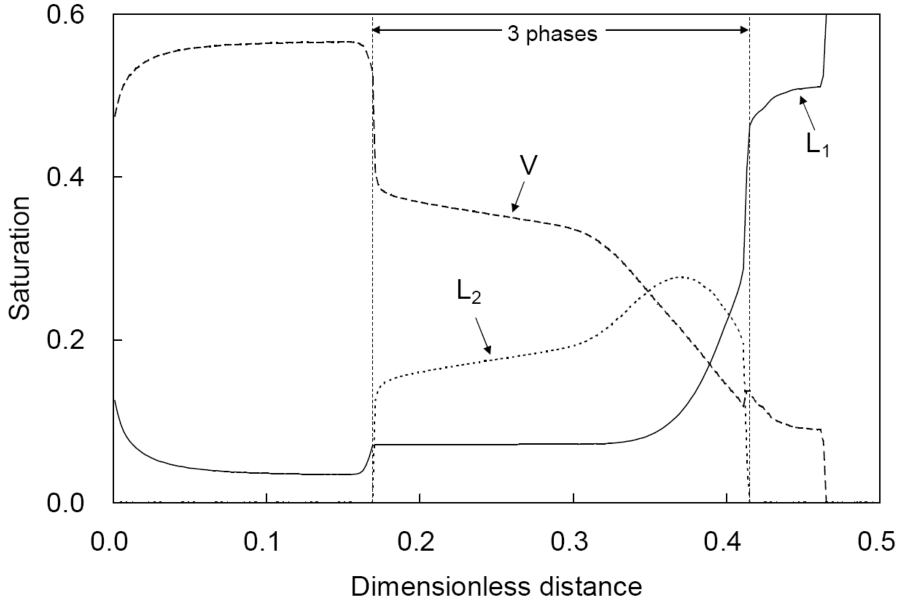

Figure 6.70 Saturation profiles at 0.5 HCPVI for the BSB-Q oil displacement at 120°F and 1400 psia by the injection gas shown in Table 6.4.

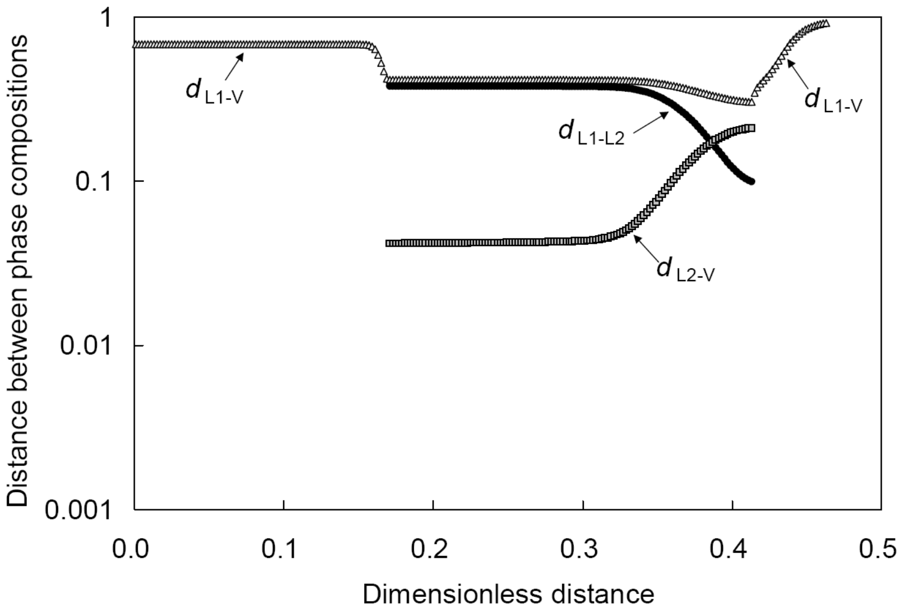

Figure 6.71 Distances between phase compositions in composition space at 0.5 HCPVI for the BSB-Q oil displacement at 120°F and 1400 psia by the injection gas shown in Table 6.4.

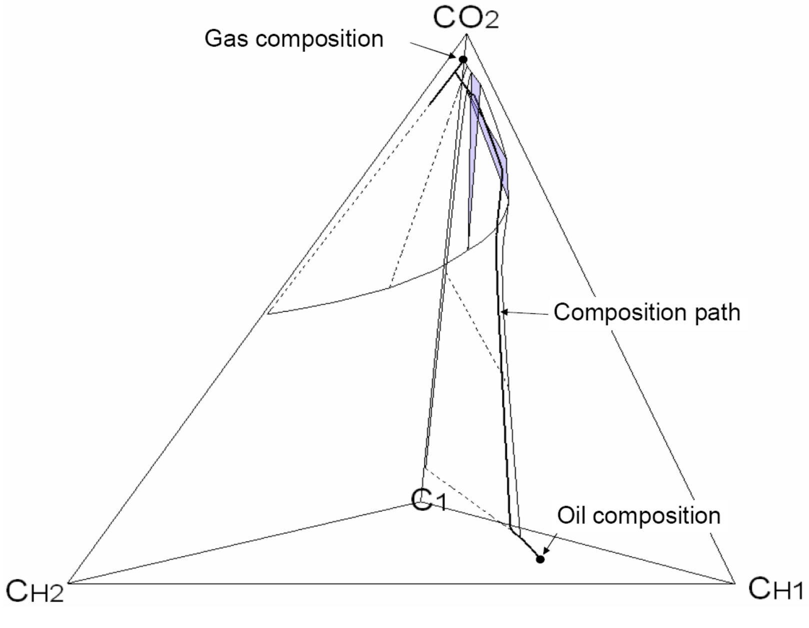

Figure 6.72 Simulated composition path and two- and three-phase regions along the path for the BSB-Q oil displacement at 120°F and 1400 psia by the injection gas shown in Table 6.4.

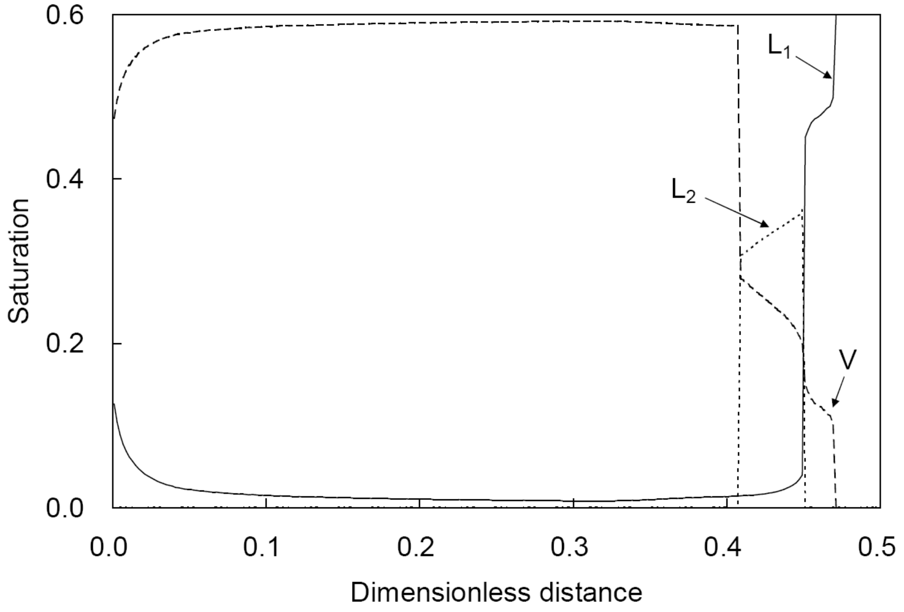

Figure 6.73 Saturation profiles at 0.5 HCPVI for the BSB-Q oil displacement at 120°F and 1450 psia by the injection gas shown in Table 6.4.

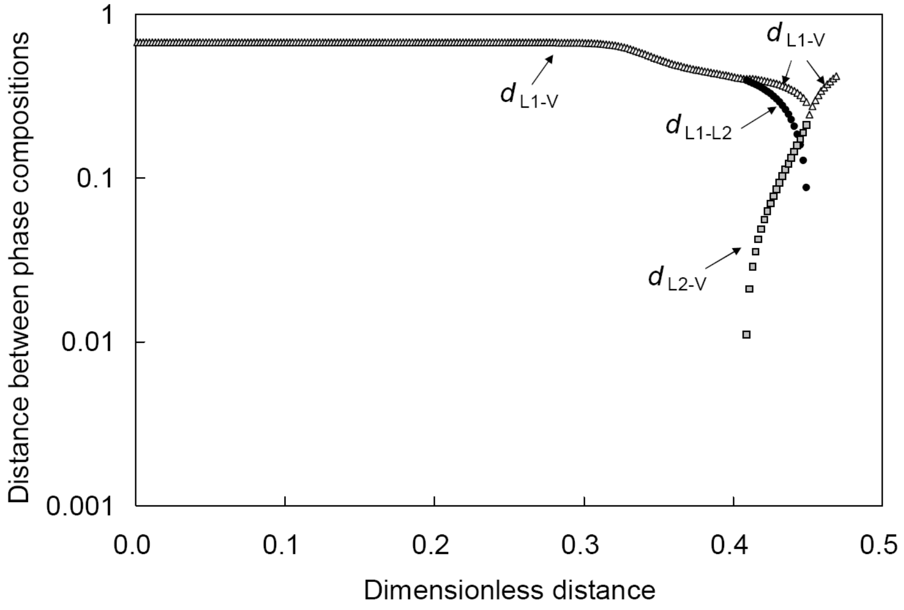

Figure 6.74 Distances between phase compositions in composition space at 0.5 HCPVI for the BSB-Q oil displacement at 120°F and 1450 psia by the injection gas shown in Table 6.4.

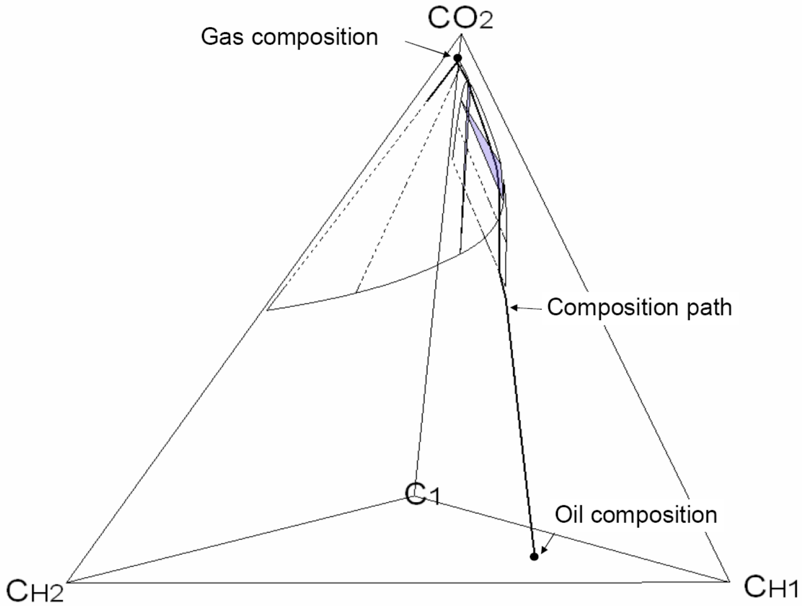

Figure 6.75 Simulated composition path and two- and three-phase regions along the path for the BSB-Q oil displacement at 120°F and 1450 psia by the injection gas shown in Table 6.4.

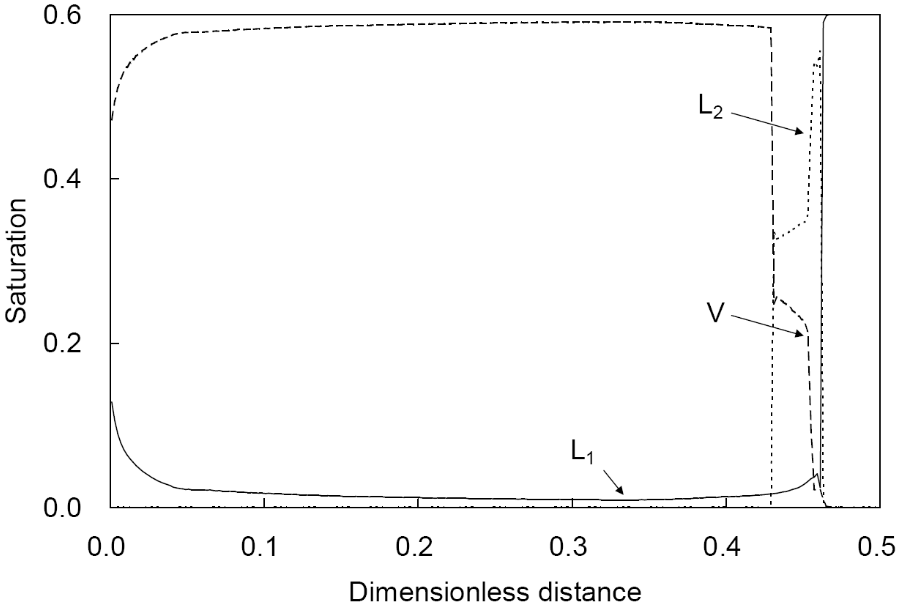

Figure 6.76 Saturation profiles at 0.5 HCPVI for the BSB-Q oil displacement at 120°F and 1500 psia by the injection gas shown in Table 6.4.

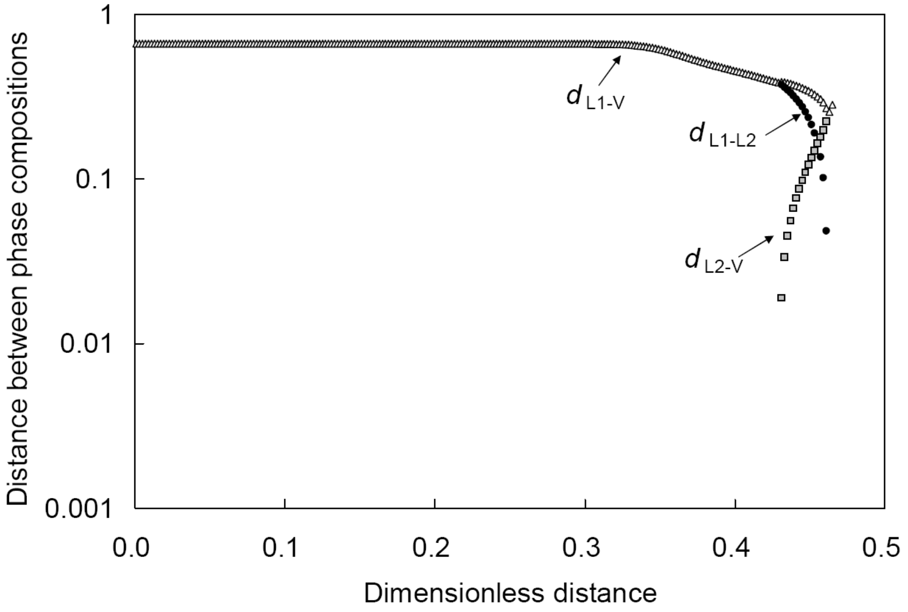

Figure 6.77 Distances between phase compositions in composition space at 0.5 HCPVI for the BSB-Q oil displacement at 120°F and 1500 psia by the injection gas shown in Table 6.4.

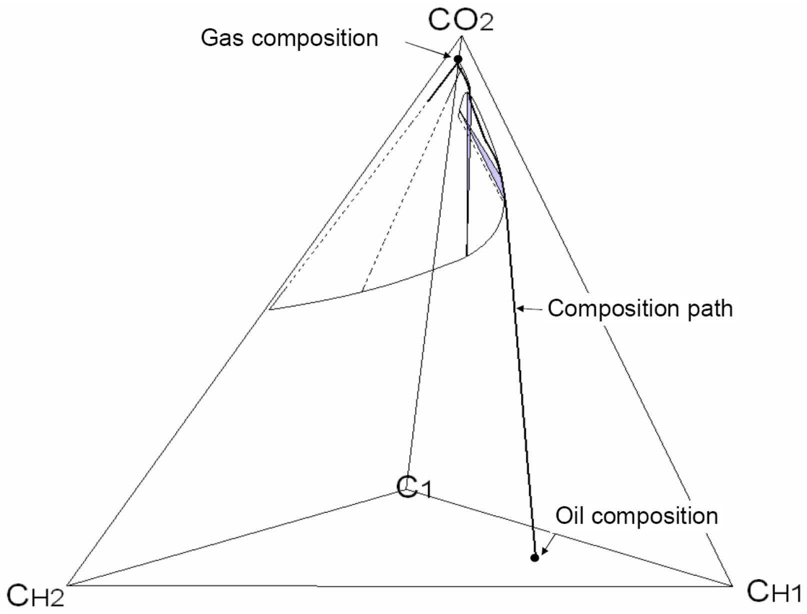

Figure 6.78 Simulated composition path and two- and three-phase regions along the path for the BSB-Q oil displacement at 120°F and 1500 psia by the injection gas shown in Table 6.4.

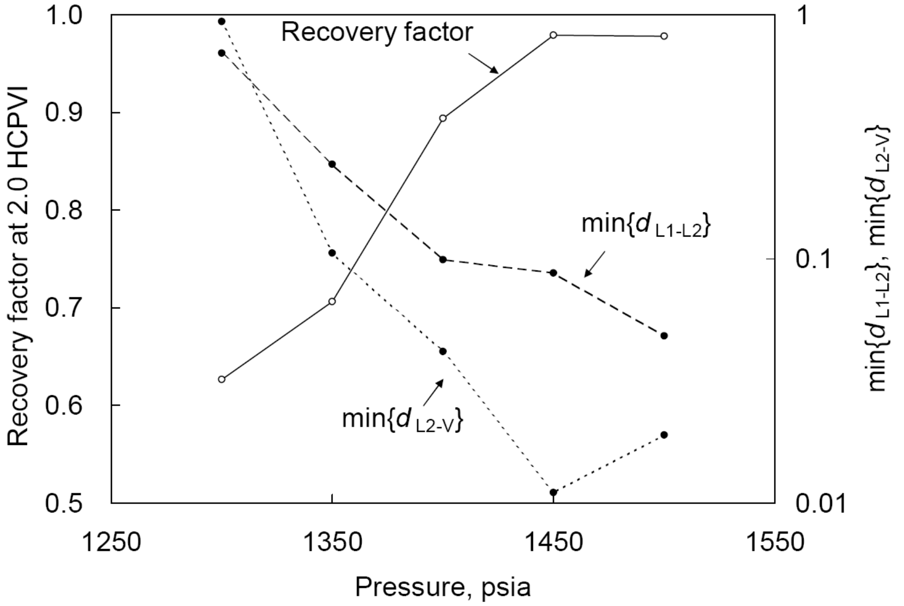

Figure 6.79 Oil recoveries at 2.0 HCPVI and minimum values of $d_{L1\text{-}L2}$ and $d_{L2\text{-}V}$ along the composition path for the BSB-Q oil displacements at 120°F by the injection gas shown in Table 6.4.

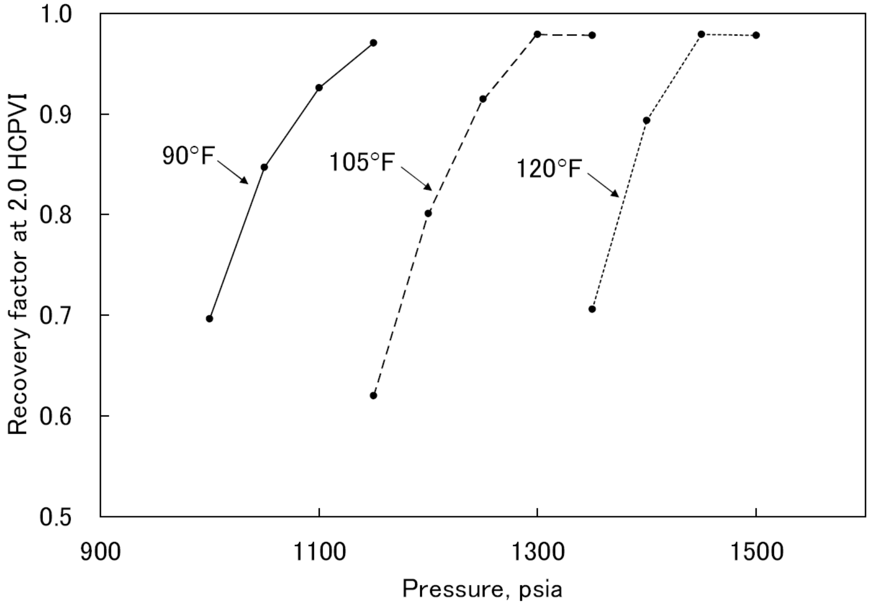

Figure 6.80 Oil recoveries at 2.0 HCPVI at different pressures and temperatures for the BSB-Q oil displacement. The fluid properties are given in Table 6.4.

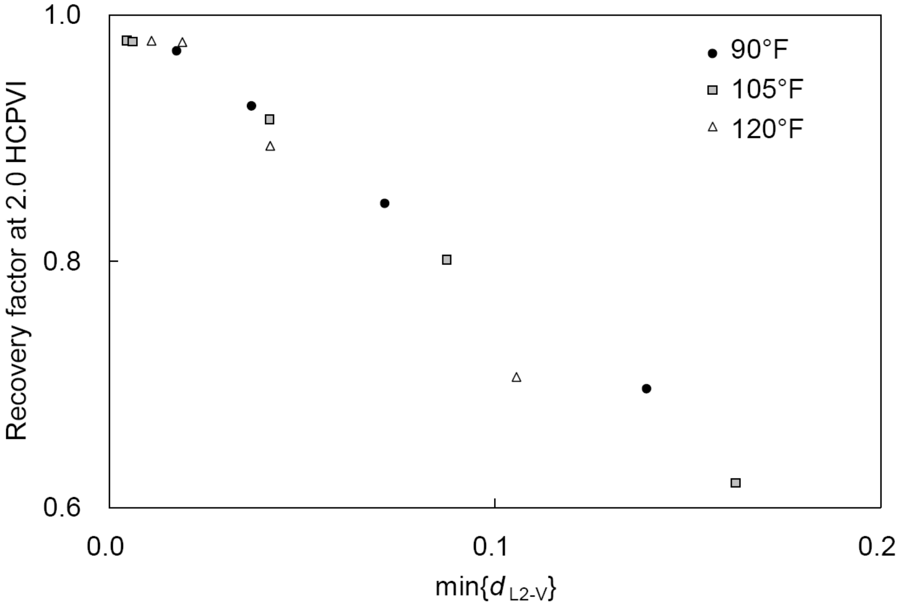

Figure 6.81 Oil recoveries at 2.0 HCPVI with respect to the minimum value of d_{L2-V} along the composition path for the BSB-Q oil displacements at different pressures and temperatures. The fluid properties are given in Table 6.4.

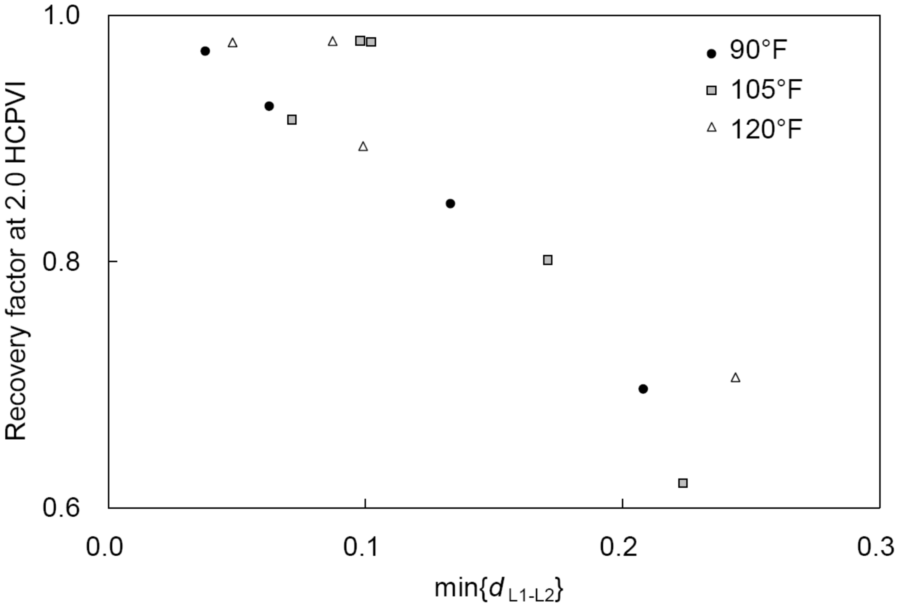

Figure 6.82 Oil recoveries at 2.0 HCPVI with respect to the minimum value of d_{L1-L2} along the composition path for the BSB-Q oil displacements at different pressures and temperatures. The fluid properties are given in Table 6.4.

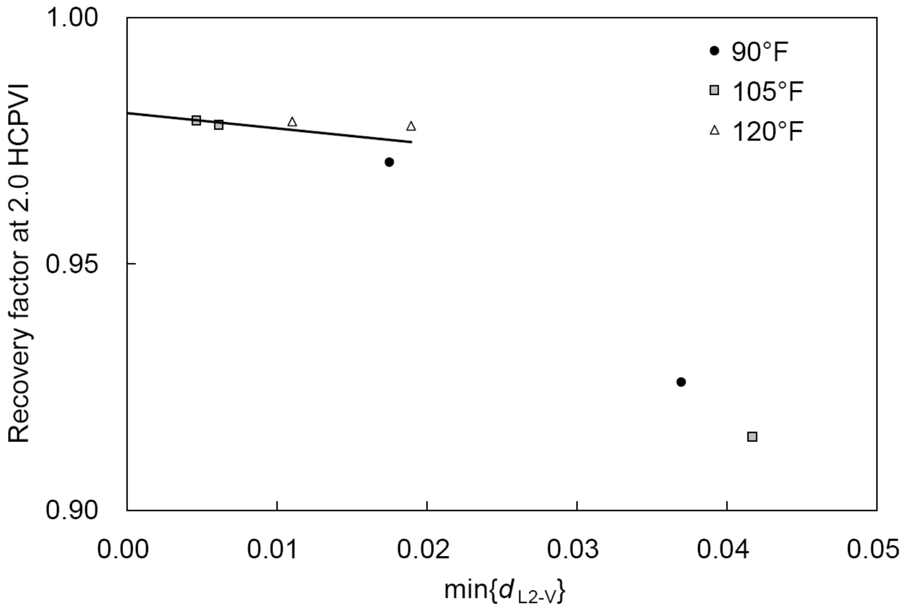

Figure 6.83 Extrapolation to estimate the oil recovery when composition path goes through the UCEP (*i.e.*, min{$d_{L2\text{-}V}$}=0) for the BSB-Q oil displacement by the injection gas shown in Table 6.4.

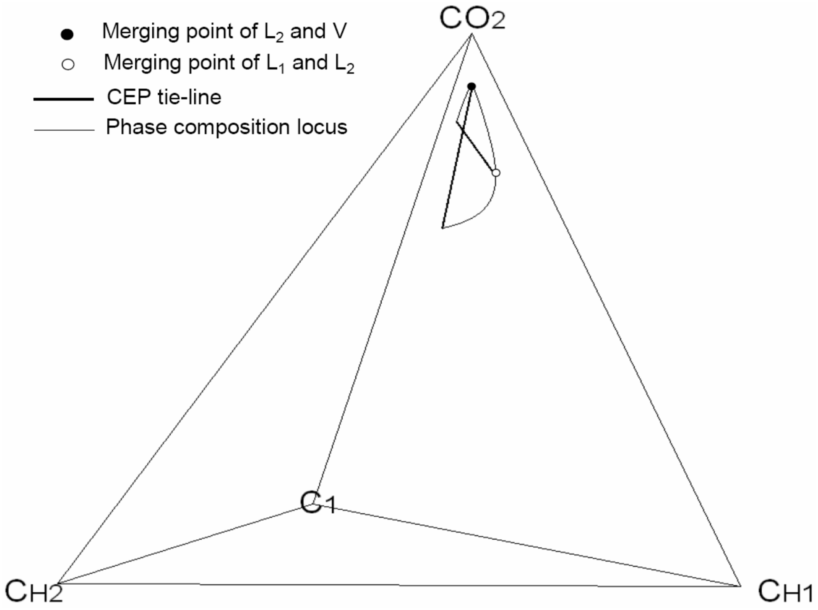

Figure 6.84a Three-phase region in BSB-QL composition space at 105°F and 1300 psia. The component properties are given in Table 6.5.

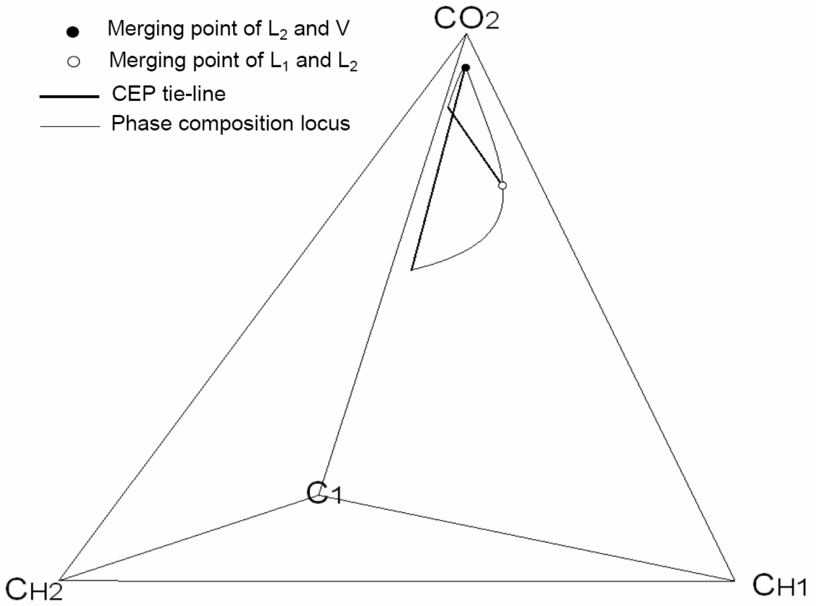

Figure 6.84b Three-phase region in BSB-Q composition space at 105°F and 1300 psia. The component properties are given in Table 6.4.

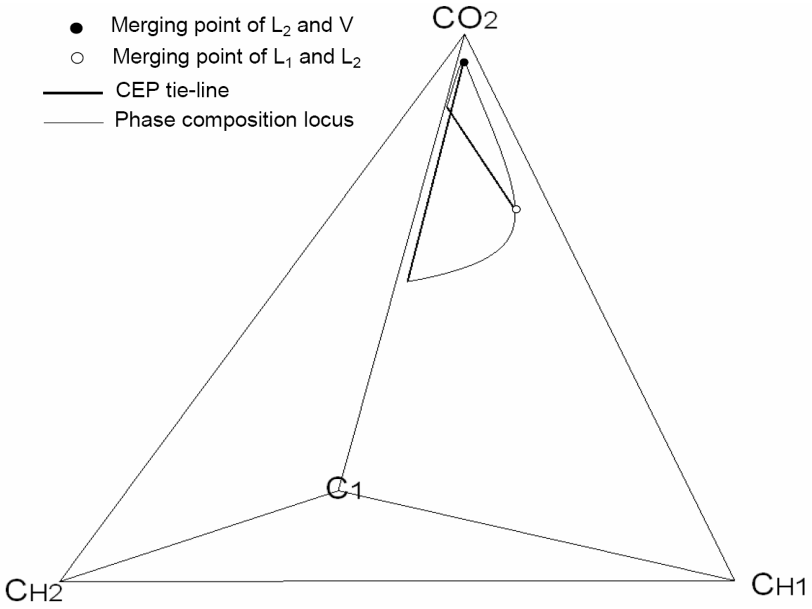

Figure 6.84c Three-phase region in BSB-QH1 composition space at 105°F and 1300 psia. The component properties are given in Table 6.6.

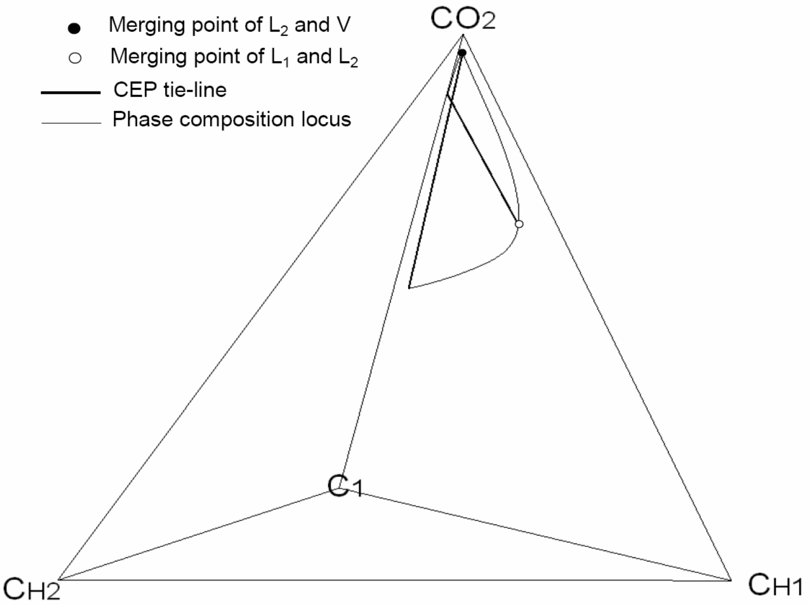

Figure 6.84d Three-phase region in BSB-QH2 composition space at 105°F and 1300 psia. The component properties are given in Table 6.7.

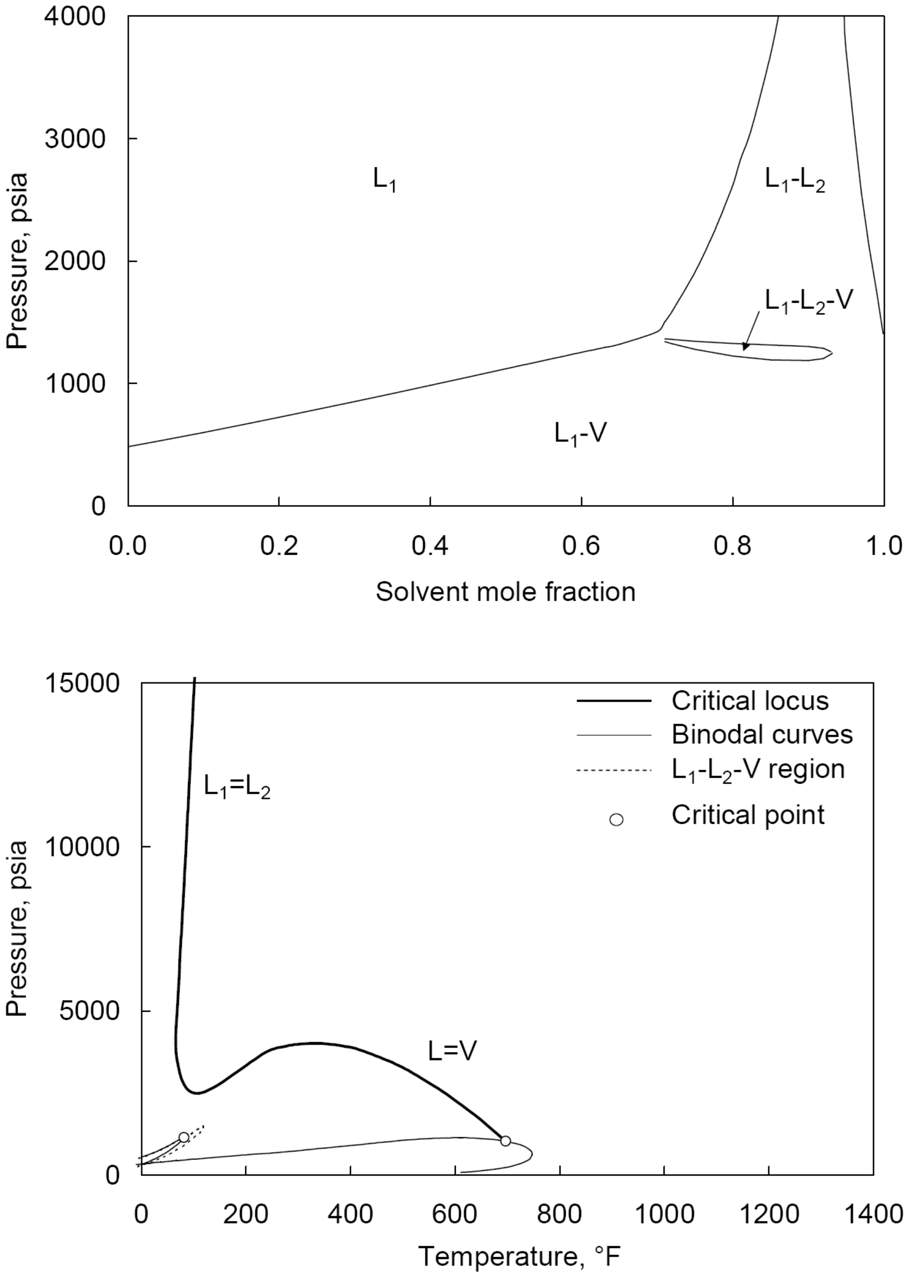

Figure 6.85a Top: *P*-*x* diagram at 105˚F for the BSB-QL oil and injection gas given in Table 6.5. Bottom: *P*-*T* projection of the *P*-*T*-*x* diagram for the pseudo-binary mixture of the BSB-QL oil and injection gas.

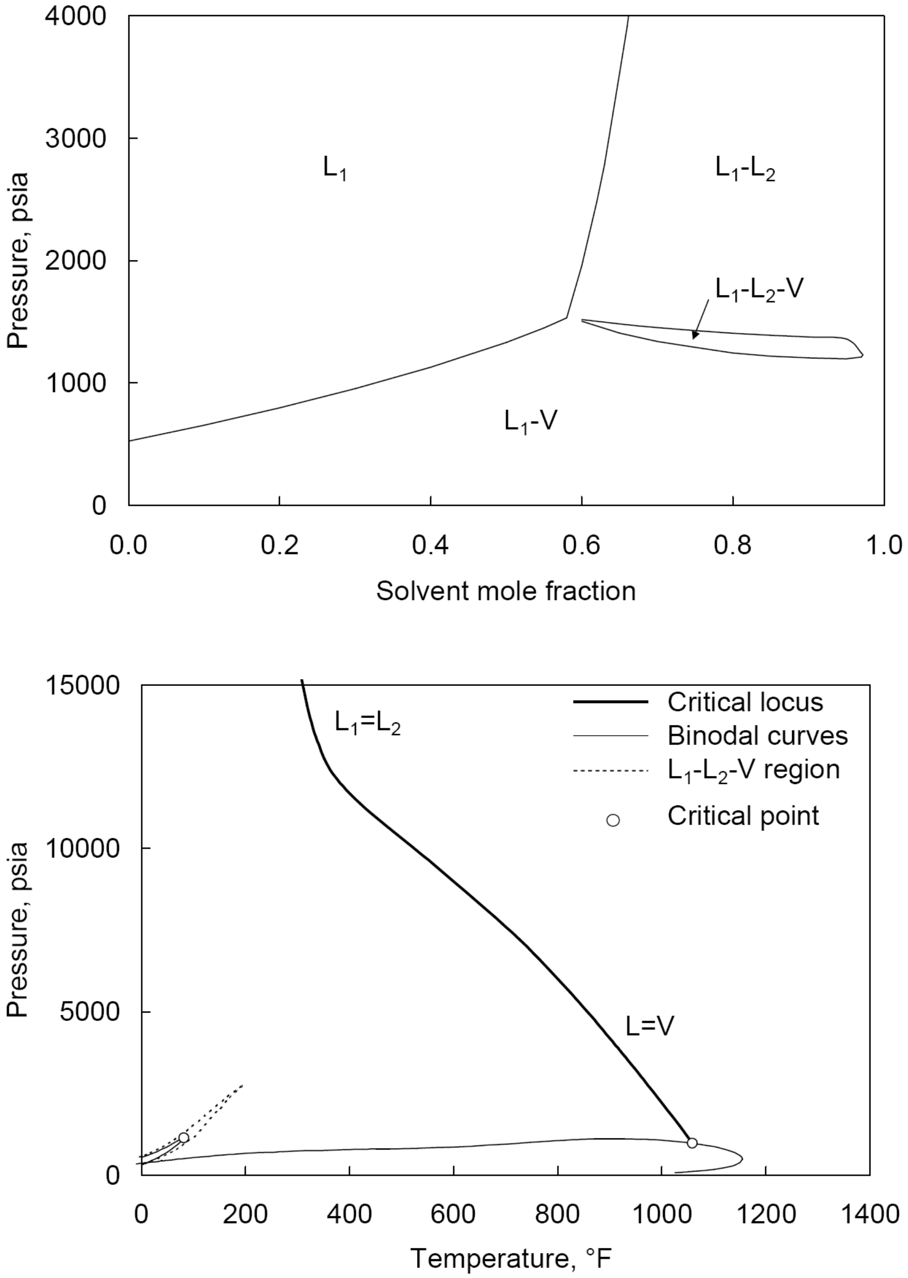

Figure 6.85b Top: *P*-*x* diagram at 105˚F for the BSB-QH1 oil and injection gas given in Table 6.6. Bottom: *P*-*T* projection of the *P*-*T*-*x* diagram for the pseudo-binary mixture of the BSB-QH1 oil and injection gas.

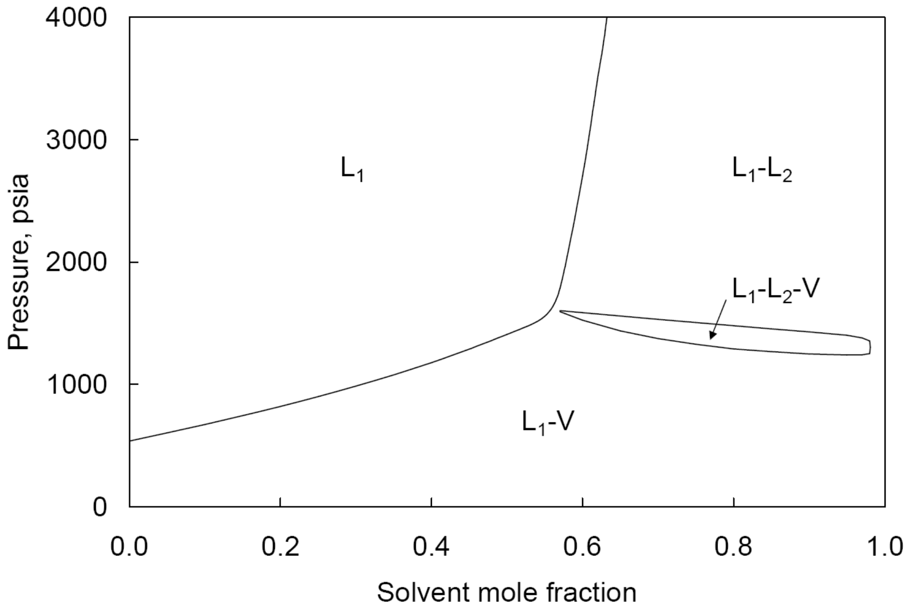

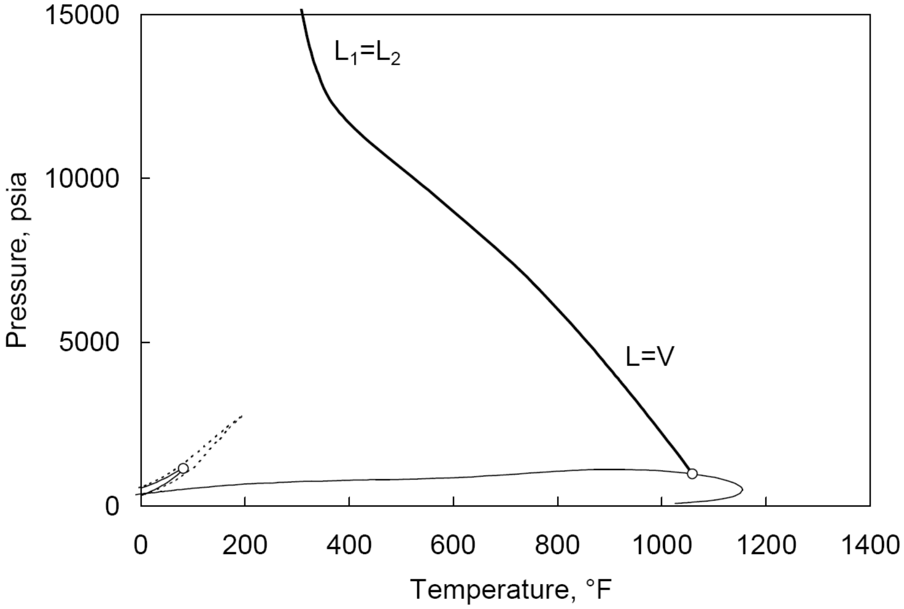

Figure 6.85c Top: *P*-*x* diagram at 105˚F for the BSB-QH2 oil and injection gas given in Table 6.7. Bottom: *P*-*T* projection of the *P*-*T*-*x* diagram for the pseudo-binary mixture of the BSB-QH2 oil and injection gas.

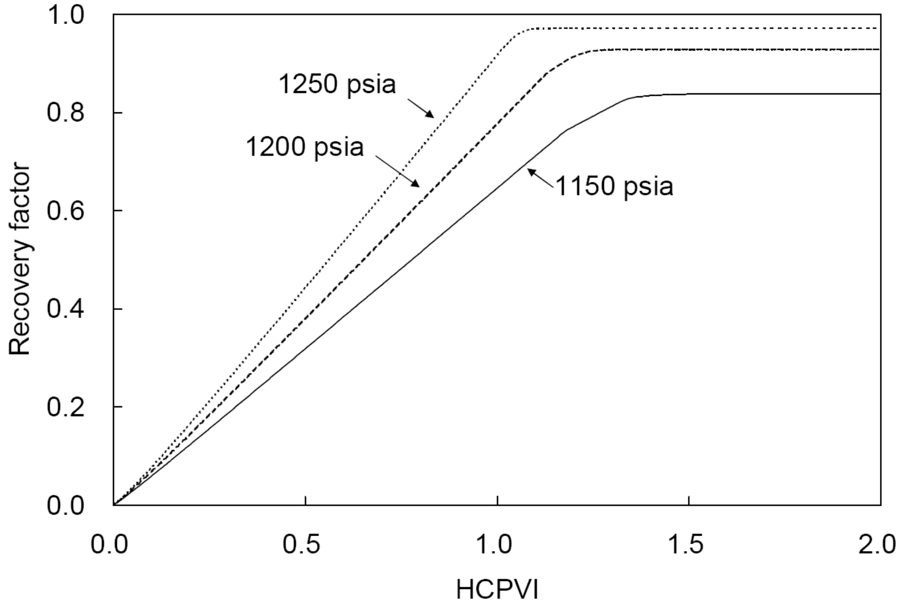

Figure 6.86 Oil recoveries for the displacements of the BSB-QL oil at different pressures at 105˚F. The fluid properties are given in Table 6.5.

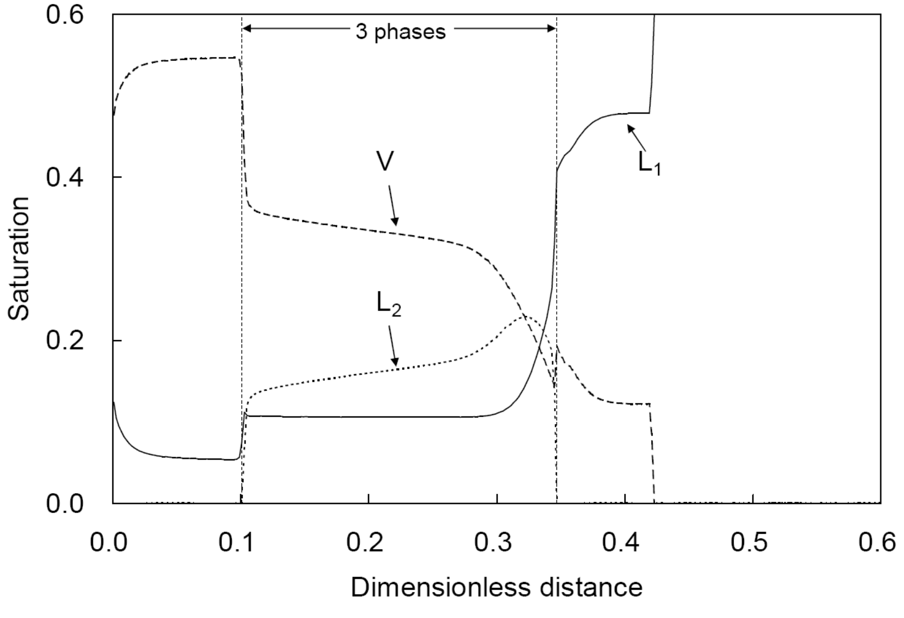

Figure 6.87 Saturation profiles at 0.5 HCPVI for the BSB-QL oil displacement at 105°F and 1150 psia. The fluid properties are given in Table 6.5.

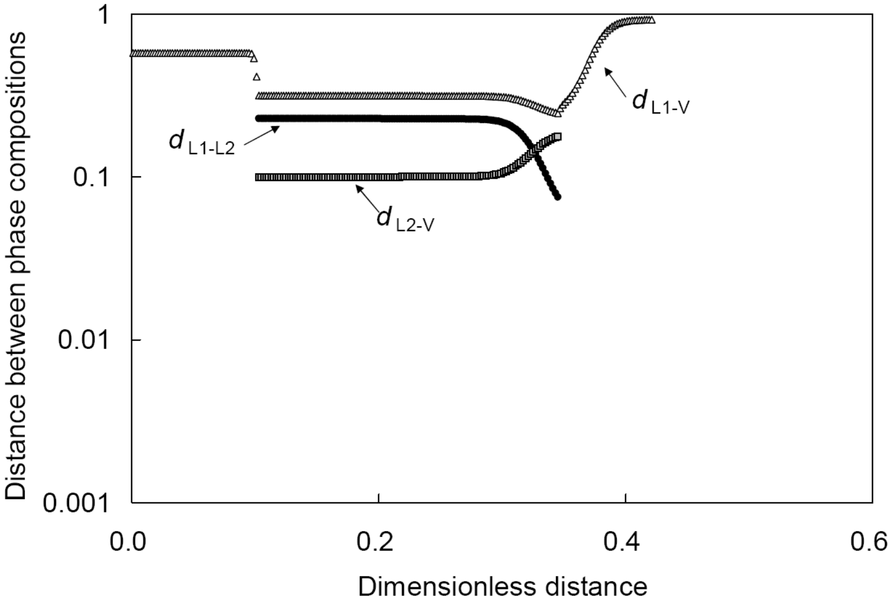

Figure 6.88 Distances between phase compositions in composition space at 0.5 HCPVI for the BSB-QL oil displacement at 105°F and 1150 psia. The fluid properties are given in Table 6.5.

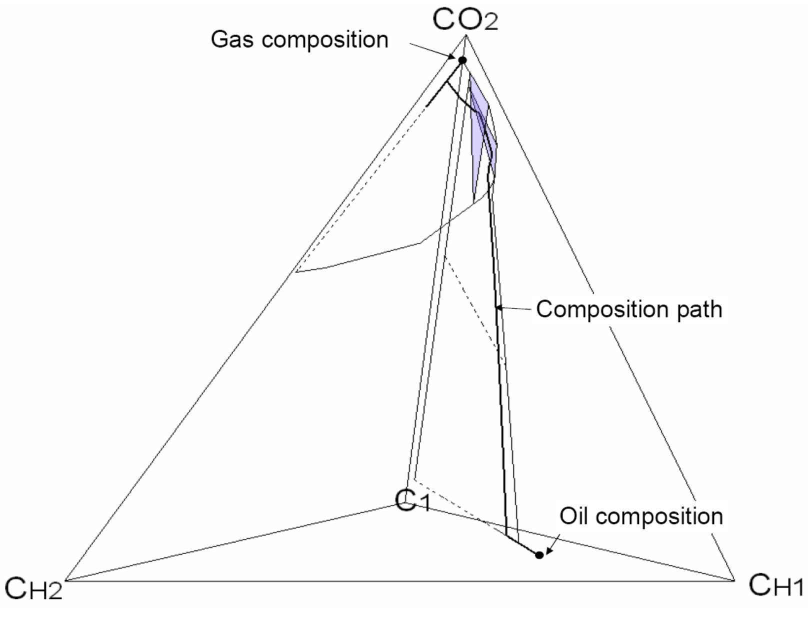

Figure 6.89 Simulated composition path and two- and three-phase regions along the path for the BSB-QL oil displacement at 105°F and 1150 psia. The fluid properties are given in Table 6.5.

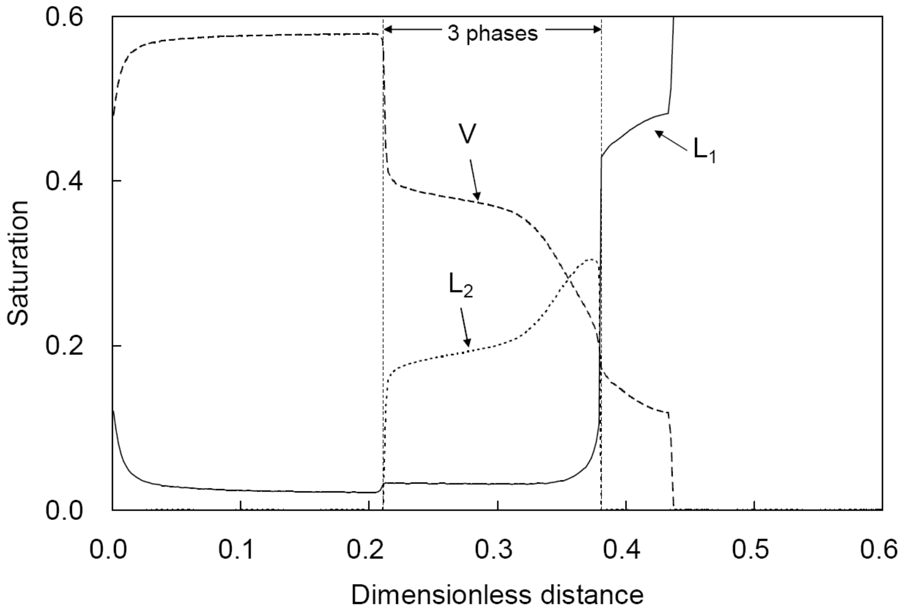

Figure 6.90 Saturation profiles at 0.5 HCPVI for the BSB-QL oil displacement at 105°F and 1200 psia. The fluid properties are given in Table 6.5.

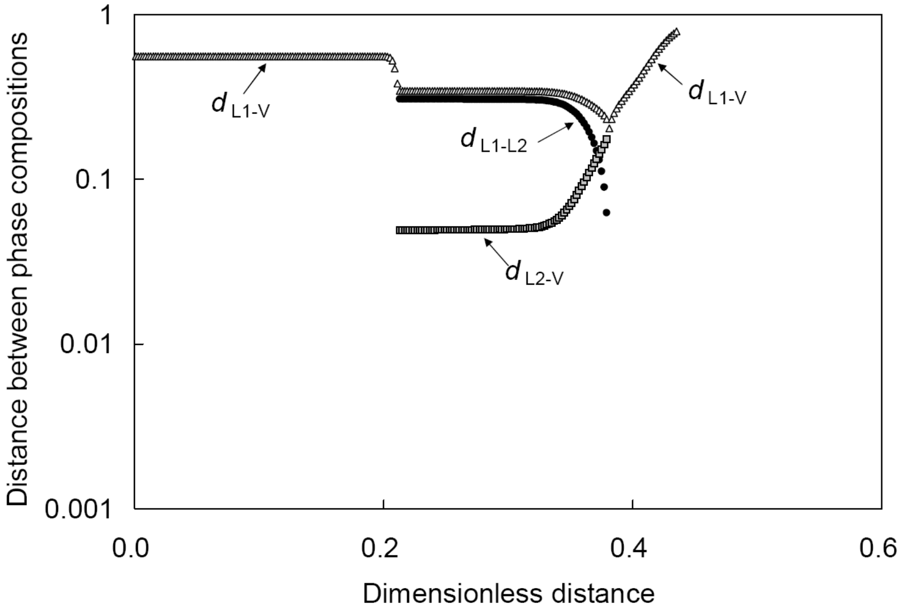

Figure 6.91 Distances between phase compositions in composition space at 0.5 HCPVI for the BSB-QL oil displacement at 105°F and 1200 psia. The fluid properties are given in Table 6.5.

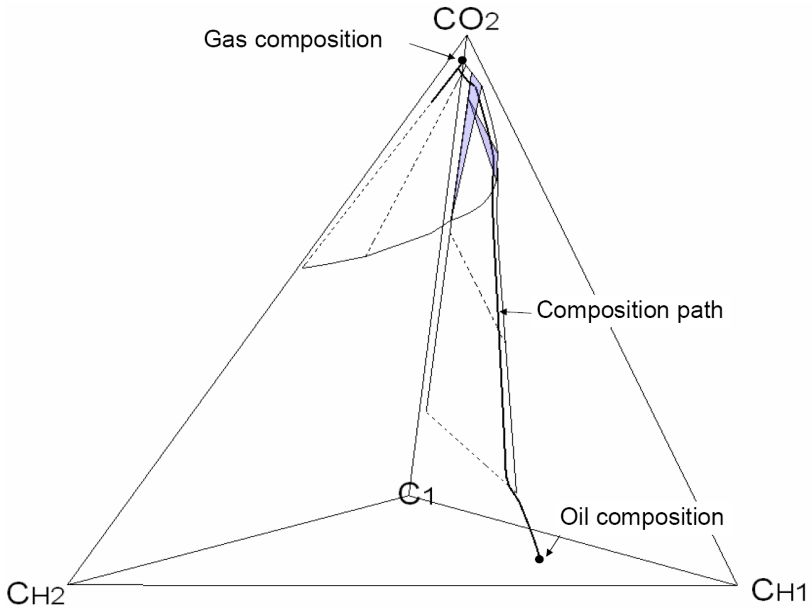

Figure 6.92 Simulated composition path and two- and three-phase regions along the path for the BSB-QL oil displacement at 105°F and 1200 psia. The fluid properties are given in Table 6.5.

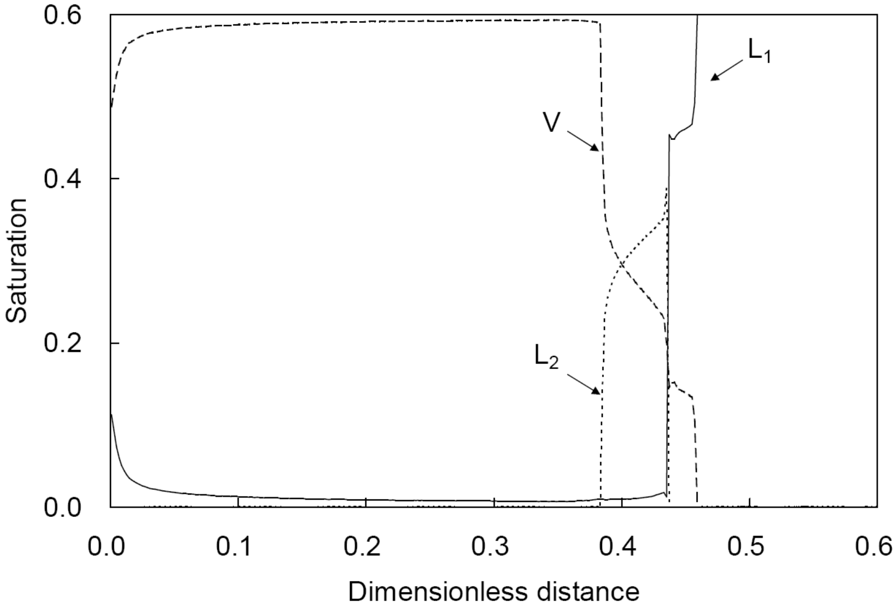

Figure 6.93 Saturation profiles at 0.5 HCPVI for the BSB-QL oil displacement at 105°F and 1250 psia. The fluid properties are given in Table 6.5.

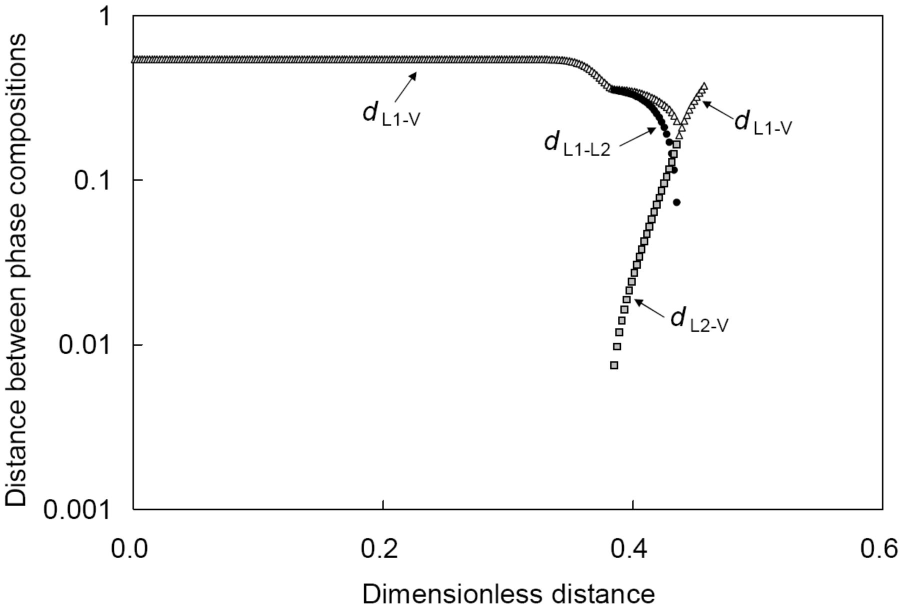

Figure 6.94 Distances between phase compositions in composition space at 0.5 HCPVI for the BSB-QL oil displacement at 105°F and 1250 psia. The fluid properties are given in Table 6.5.

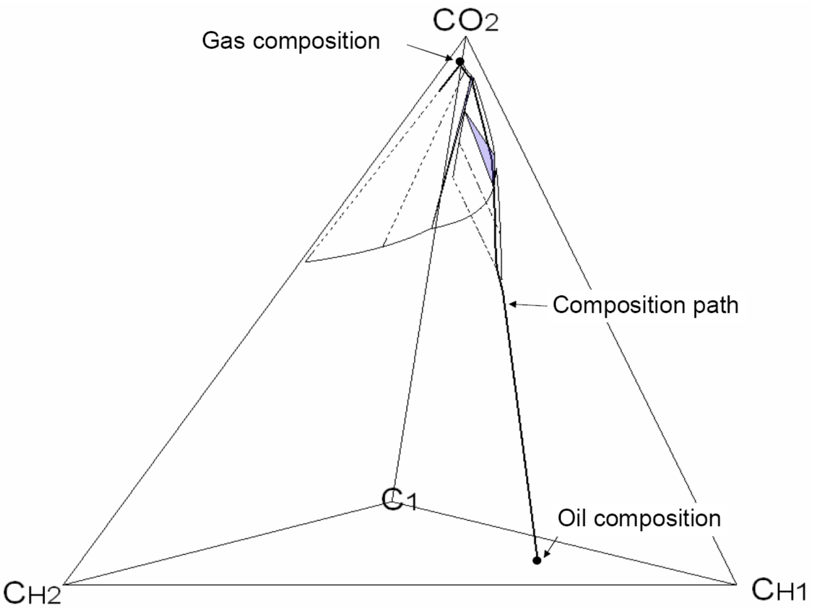

Figure 6.95 Simulated composition path and two- and three-phase regions along the path for the BSB-QL oil displacement at 105°F and 1250 psia. The fluid properties are given in Table 6.5.

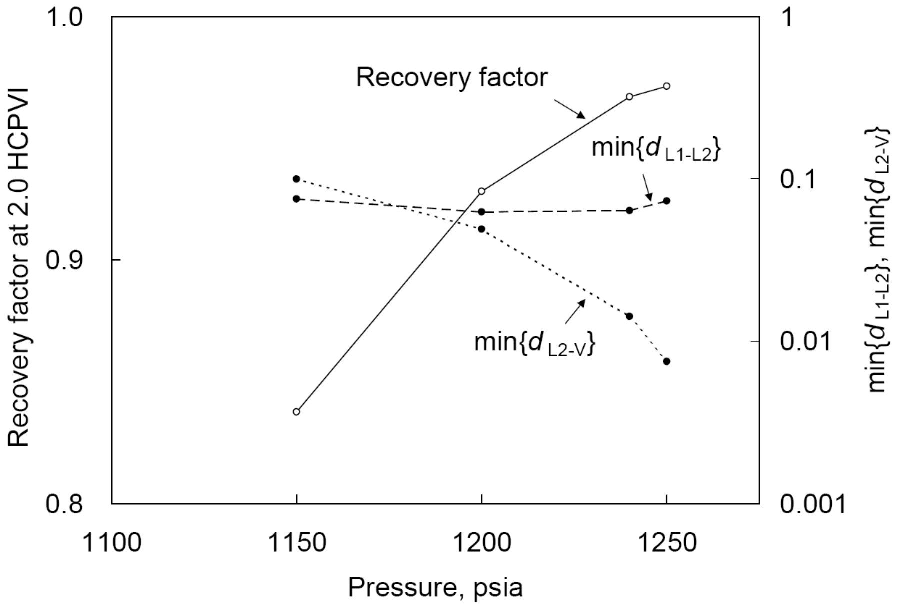

Figure 6.96 Oil recoveries at 2.0 HCPVI and minimum values of $d_{L1\text{-}L2}$ and $d_{L2\text{-}V}$ along the composition path for the BSB-QL oil displacements at 105°F. The fluid properties are given in Table 6.5.

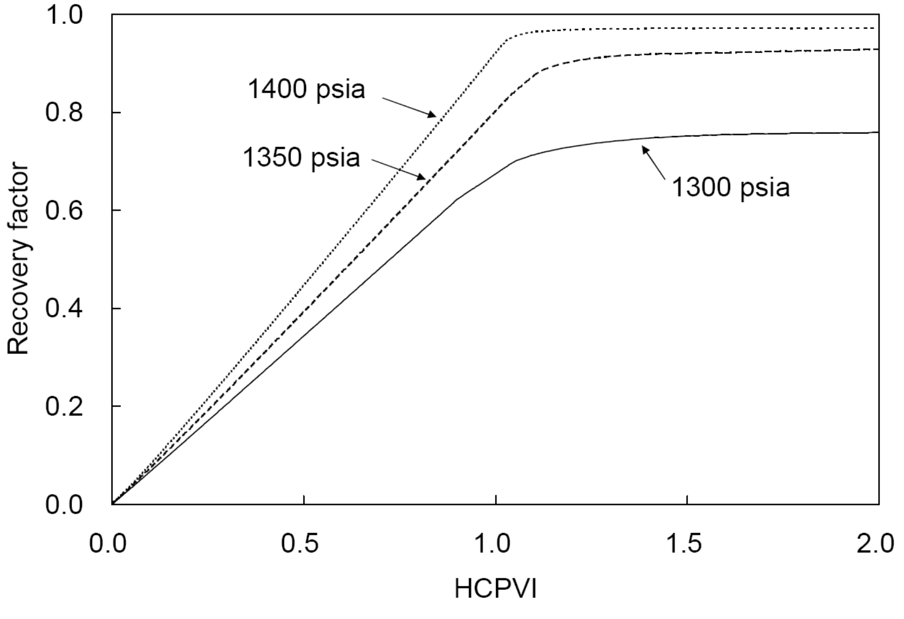

Figure 6.97 Oil recoveries for the displacements of the BSB-QH2 oil at different pressures. The fluid properties are given in Table 6.7.

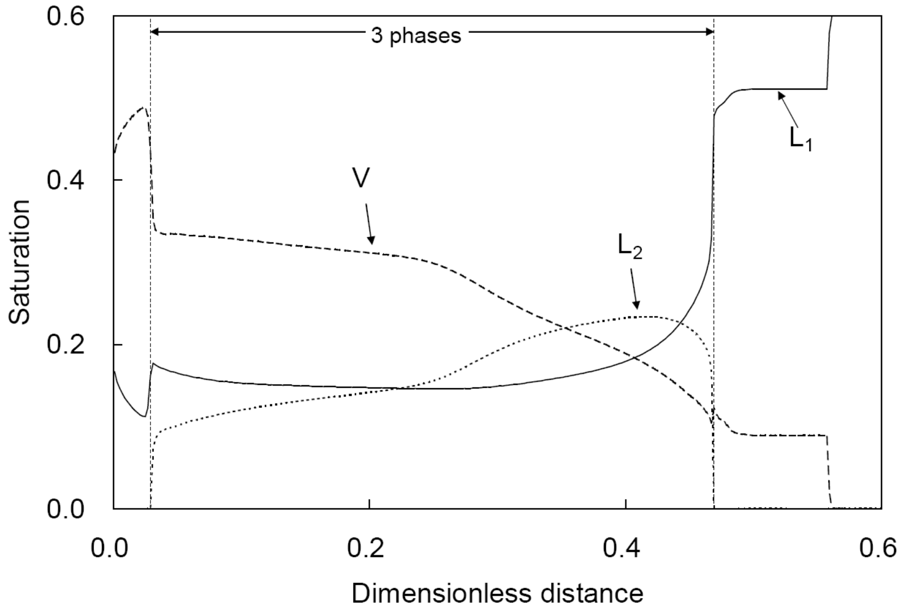

Figure 6.98 Saturation profiles at 0.5 HCPVI for the BSB-QH2 oil displacement at 105°F and 1300 psia. The fluid properties are given in Table 6.7.

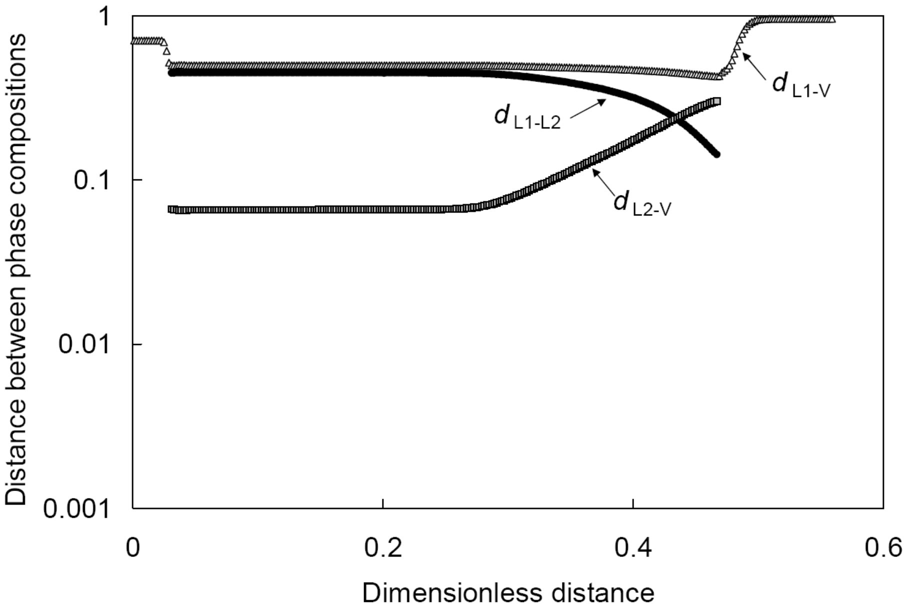

Figure 6.99 Distances between phase compositions in composition space at 0.5 HCPVI for the BSB-QH2 oil displacement at 105°F and 1300 psia. The fluid properties are given in Table 6.7.

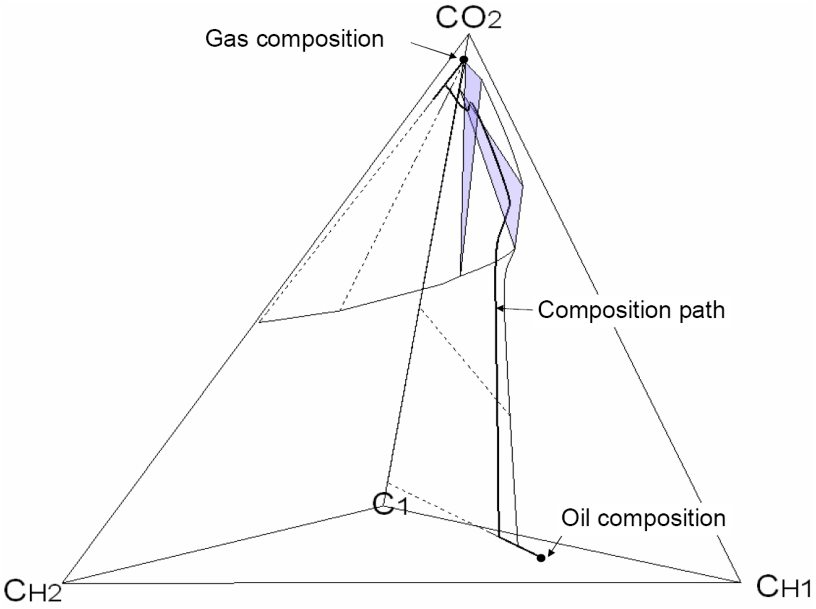

Figure 6.100 Simulated composition path and two- and three-phase regions along the path for the BSB-QH2 oil displacement at 105°F and 1300 psia. The fluid properties are given in Table 6.7.

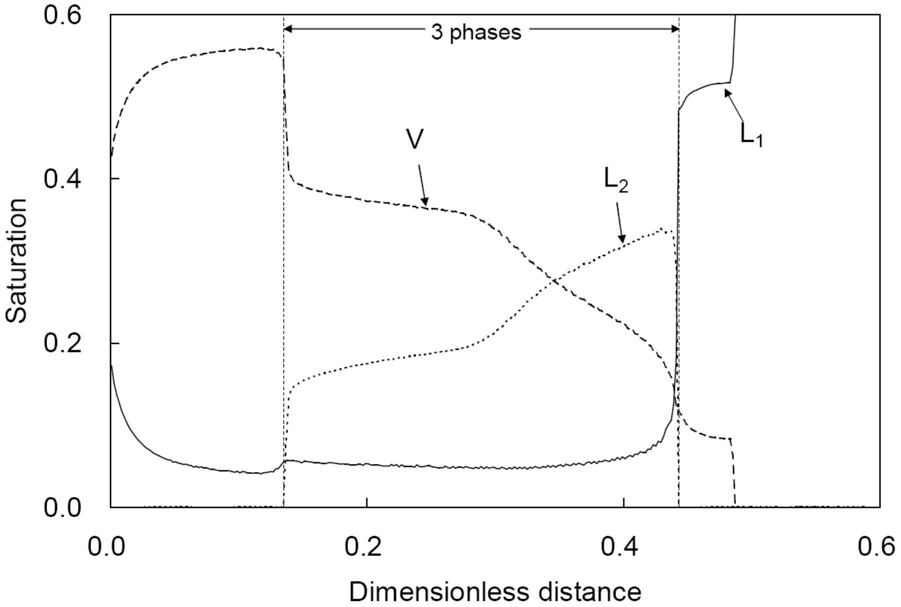

Figure 6.101 Saturation profiles at 0.5 HCPVI for the BSB-QH2 oil displacement at 105°F and 1350 psia. The fluid properties are given in Table 6.7.

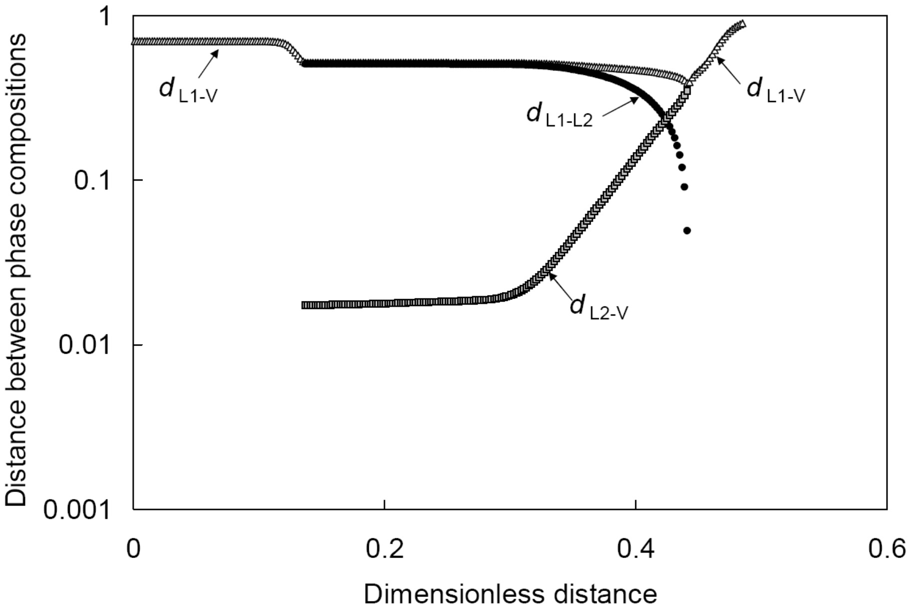

Figure 6.102 Distances between phase compositions in composition space at 0.5 HCPVI for the BSB-QH2 oil displacement at 105°F and 1350 psia. The fluid properties are given in Table 6.7.

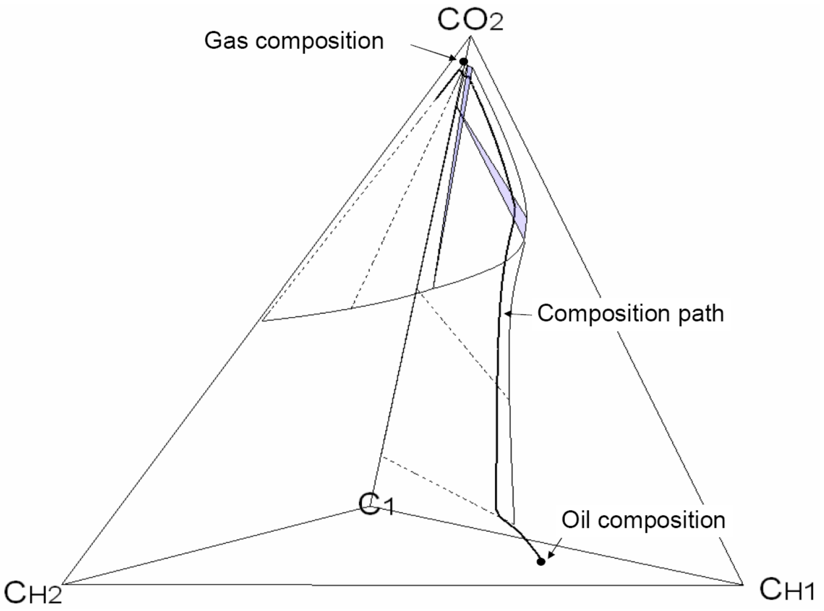

Figure 6.103 Simulated composition path and two- and three-phase regions along the path for the BSB-QH2 oil displacement at 105°F and 1350 psia. The fluid properties are given in Table 6.7.

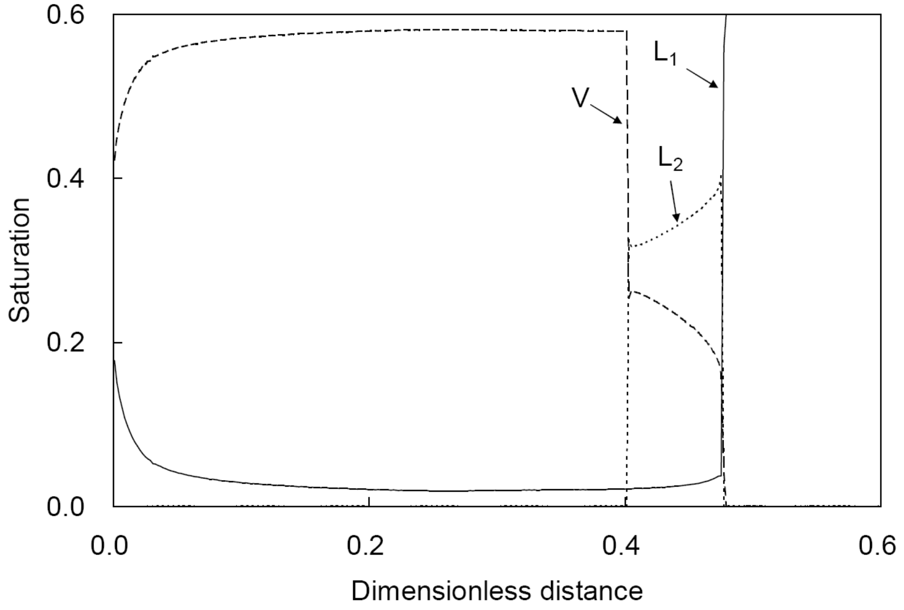

Figure 6.104 Saturation profiles at 0.5 HCPVI for the BSB-QH2 oil displacement at 105°F and 1400 psia. The fluid properties are given in Table 6.7.

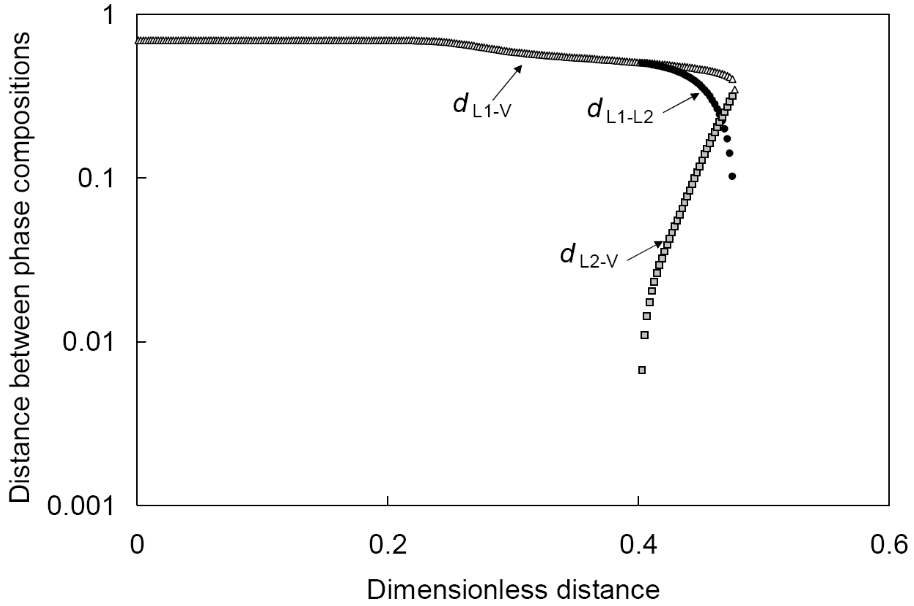

Figure 6.105 Distances between phase compositions in composition space at 0.5 HCPVI for the BSB-QH2 oil displacement at 105°F and 1400 psia. The fluid properties are given in Table 6.7.

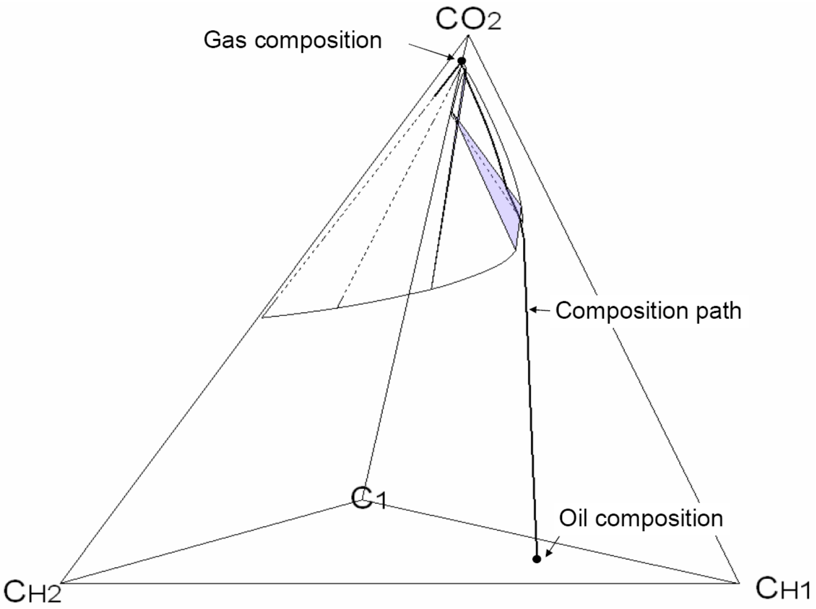

Figure 6.106 Simulated composition path and two- and three-phase regions along the path for the BSB-QH2 oil displacement at 105°F and 1400 psia. The fluid properties are given in Table 6.7.

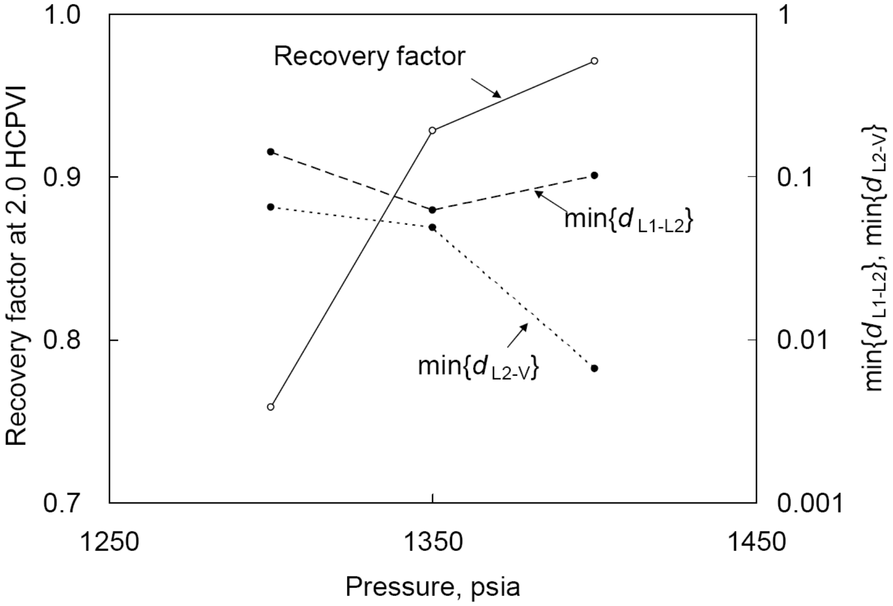

Figure 6.107 Oil recoveries at 2.0 HCPVI and minimum values of $d_{L1\text{-}L2}$ and $d_{L2\text{-}V}$ along the composition path for the BSB-QH2 oil displacements at 105°F. The fluid properties are given in Table 6.7.

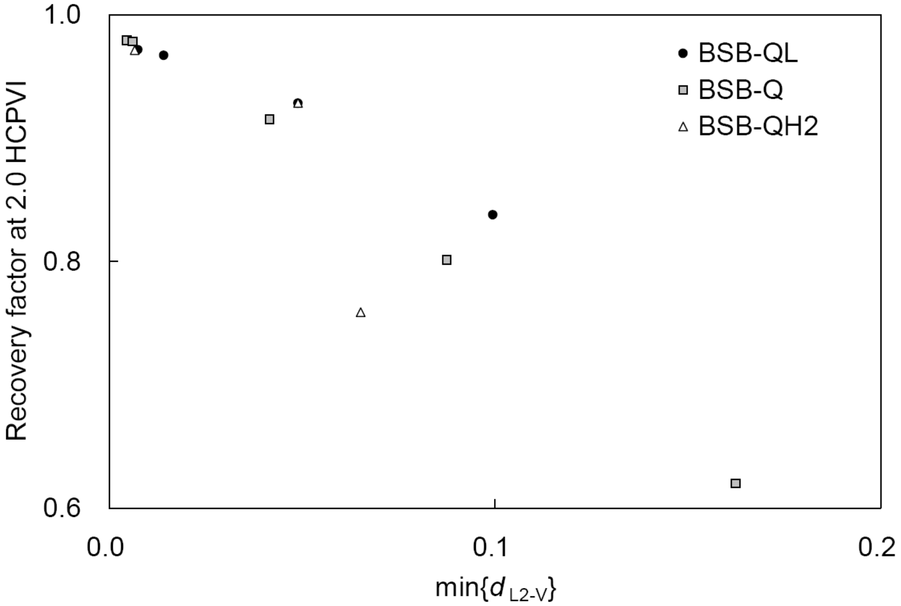

Figure 6.108 Oil recoveries at 2.0 HCPVI with respect to the minimum value of $d_{L2\text{-}V}$ along the composition path for the BSB-QL, BSB-Q, and BSB-QH2 displacements at 105°F.

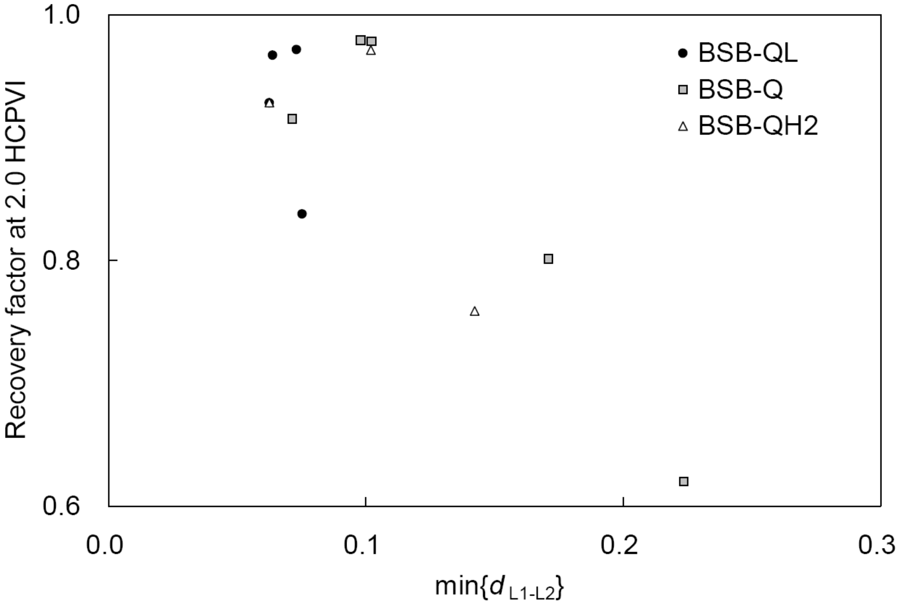

Figure 6.109 Oil recoveries at 2.0 HCPVI with respect to the minimum value of $d_{L1\text{-}L2}$ along the composition path for the BSB-QL, BSB-Q, and BSB-QH2 displacements at 105°F.

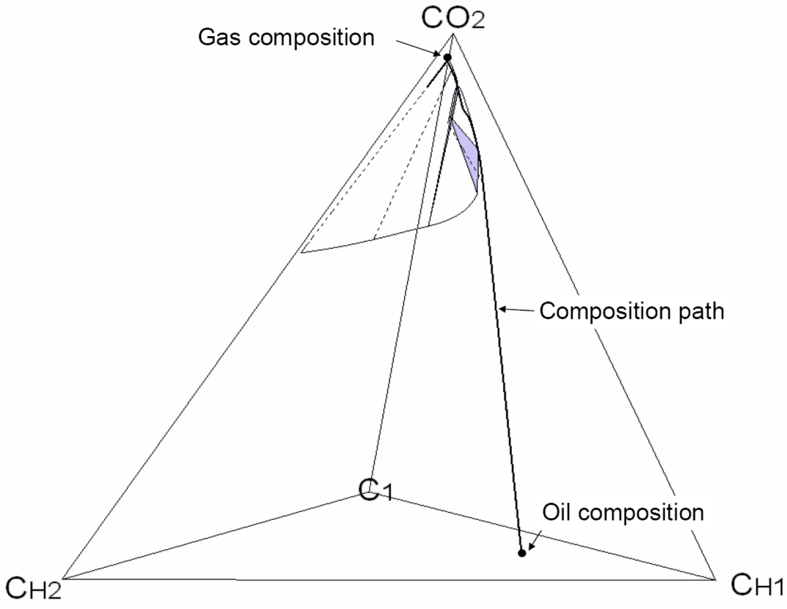

Figure 6.110 Simulated composition path and two- and three-phase regions along the path for the BSB-QL oil displacement at 105°F and 1300 psia. The fluid properties are given in Table 6.5.

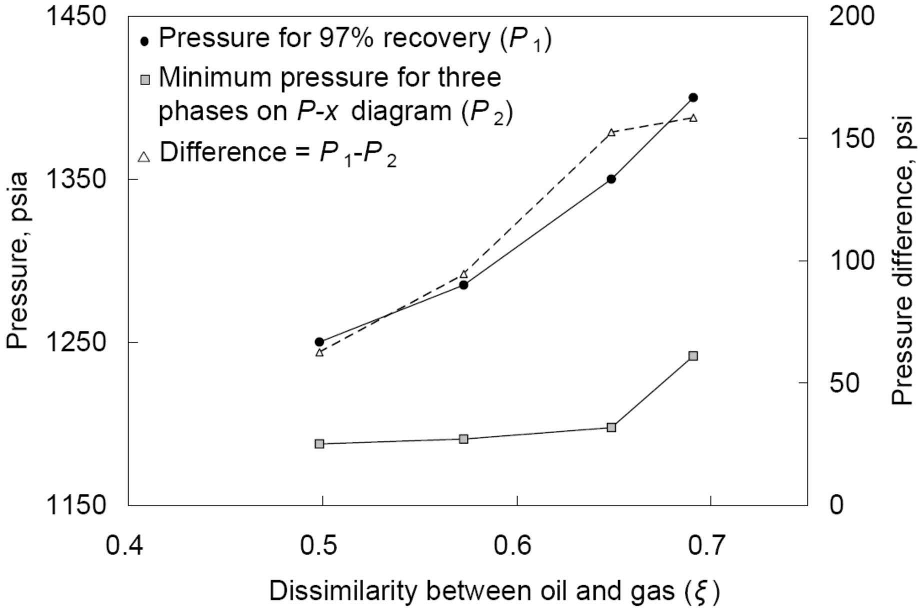

Figure 6.111 Displacement pressures for a recovery factor of 97% at 2.0 HCPVI (P_1) and the minimum pressures for three phases on P-x diagrams (P_2) for four different oil/injection-gas pairs; BSB-QL ($\xi = 0.498$), BSB-Q ($\xi = 0.573$), BSB-QH1 ($\xi = 0.649$), and BSB-QH2($\xi = 0.691$). Pressure difference on the right y-axis is defined as ($P_1 - P_2$). Parameter ξ is defined in equation (6.2).

7. Summary, Conclusions, and Recommendations for Future Research

We developed robust and efficient algorithms for phase equilibrium calculations for two and three phases. Those algorithms were implemented in a compositional reservoir simulator to show how they significantly improve efficiency and robustness. The importance of properly using three-phase equilibrium calculations in compositional reservoir simulation was demonstrated. We also showed that the mechanism for high efficiency of low-temperature oil displacements by CO_2 involves critical endpoints.

In the subsequent sections, we first summarize and conclude this research. Recommendations for future research are then described.

7.1 SUMMARY AND CONCLUSIONS

A robust algorithm for constant-K flash calculations is critical to obtain convergence in multiphase compositional simulation, and had not been satisfactorily developed unlike the traditional two-phase flash. In Chapter 3, we formulated the constant-K flash calculation with N_P phases as a minimization of a non-monotonic convex function with N_C linear constraints. We developed a robust and practical algorithm that is guaranteed to converge to the correct solution independent of the number of phases for both positive and negative flash calculations. The conclusions on constant-K flash calculations are

1. Our algorithm is guaranteed to converge because the minimization function is convex and because the small feasible region developed in this research does not contain zones near poles where the Hessian matrix is ill-conditioned.
2. Procedures for multiphase constant-K flash calculations developed prior to this research were shown not to converge for some situations or to converge slowly because of large feasible regions that are bounded by poles.

3. Our algorithm can improve the reliability and efficiency of multiphase compositional simulation as part of rigorous EOS flash calculations. Convergence within our *K*-flash calculation is not dependent on the initial guess from a prior flash calculation as we ensure that the initial guess is in the feasible region.
4. Fewer iterations are required for convergence using our algorithm because the feasible region is significantly smaller than that proposed in prior research. We demonstrated that even for five equilibrium phases our algorithm requires only six iterations at most in one-million flash calculations with different *K*-values that were randomly generated.

In Chapters 4 and 5, we developed efficient and robust algorithms for stability analysis and two- and three-phase flash calculations using a reduced method. The algorithms were implemented in UTCOMP, a multiphase compositional reservoir simulator, to demonstrate the efficiency and robustness in simulations using different fluids, number of components, and reservoir models. The conclusions on the research for phase equilibrium calculations using a cubic EOS are

1. The simple algorithm developed in this research for the reduced method improves convergence behavior near the critical region, compared to the conventional algorithms used in this research. Our reduced method is more efficient and robust when more components are used in the simulation.
2. Use of our reduced method can significantly decrease the computational time of reservoir simulation without loss of accuracy. Our reduced method gave 40% speed-up of gas flooding simulations using 20 components with a two-dimensional reservoir model, compared to the standard algorithms used in this research.
3. Because of the significant speed-up, use of our reduced method allows for more components to be used in the simulation. Using more components in reservoir

simulation can improve accuracy of the fluid characterization and reservoir–surface integrated modeling.

4. Based on the simulation case studies using UTCOMP, the robust flash calculations with our reduced method decreases the computational time for reservoir simulation not only because of reduced computational time involved in flash calculations and stability analysis but also because of improved time-step sizes.

To avoid three-phase flash calculations in reservoir simulation, two-phase equilibrium approximations for complex three-phase behavior were proposed in the literature. In Chapter 5, we investigated the importance of using three-phase flash calculations in compositional simulation. We conclude that the two-phase equilibrium approximations proposed in the literature can lead to a complete failure of simulation or erroneous simulation results when three phases are present. Simulations with the two-phase equilibrium approximations can fail because two-phase flash calculations in a three-phase region can result in discontinuous changes in phase properties over the time steps.

In Chapter 6, we showed that oil displacements by CO_2 involving L_1-L_2-V equilibrium can achieve more than 95% displacement efficiency even if the two-phase regions exhibit significant immiscibility. The mechanism for high displacement efficiency was explained for the first time. The effects of three-phase behavior on displacement efficiency were then systematically investigated using quaternary EOS fluid models with varying pressure, temperature, and oil component properties. The quaternary representation enabled us to visualize the complex three-phase behavior associated with critical endpoints. The conclusions on low-temperature oil displacements by CO_2 solvent are

1. High efficiency of low-temperature oil displacements by CO_2 solvent occurs when the composition path goes near the upper critical endpoint (UCEP) tie-line and, to a lesser extent, the lower critical endpoint (LCEP) tie-line. LCEP behavior at the front of the three-phase region results in efficient extraction of oil components by the L_2 phase. The L_2 phase is vaporized into the V phase when it disappears at the tail of the three-phase region because of UCEP behavior. This vaporization of the L_2 phase result in low L_1 phase saturation in the swept zone; *i.e.*, high displacement efficiency. High displacement efficiency resulting from the critical endpoint (CEP) behavior occurs even when two-phase regions exhibit significant immiscibility. Because of the CEP behavior, CO_2 is simultaneously extracted from the V and L_1 phases into the L_2 phase within the three-phase region.
2. At least four components must be used for the EOS fluid model to develop CEPs in composition space at a fixed temperature and pressure. The quaternary representation provides qualitatively correct characteristics of the low-temperature oil displacements by CO_2 solvent studied in this research.
3. Complete miscibility may not be developed for a composition path that goes through a three-phase region without considering the existence of a tricritical point.
4. Reservoir temperature and oil properties can significantly affect the efficiency of low-temperature oil displacements by CO_2 solvent because their effects on the three-phase behavior lead to a significantly different composition path taken. The displacement efficiency is higher at lower reservoir temperature or for a lighter oil.
5. A *P-x* diagram for mixtures of reservoir oil with CO_2 solvent can be in large error for estimation of a pressure at which high displacement efficiency is achieved. This is because displacement efficiency is determined by interaction between flow and phase behaviors, instead of phase behavior on a *P-x* diagram.

6. Five or more components must be used to study the possibility of miscibility development at a tricritical point so that the tricritical point can be predicted in composition space at a fixed temperature and pressure.

7.2 RECOMMENDATIONS FOR FUTURE RESEARCH

The increasing interest and complexity of enhanced oil recovery for heavy oil and shallow oil reservoirs will lead to the need to model a larger number of equilibrium phases in compositional reservoir simulation. Stability analysis for multiple phases needs to be improved because multiple local minima of the TPD function frequently occur for multiple phases. Current methods cannot guarantee location of the global minimum of the TPD function.

A potential solution would be achieved by developing new mathematical conditions for phase stability, by using different equations and/or independent variables, or by improving the robustness of existing algorithms. Use of a reduced method can eliminate some of local minima on the TPD function (Firoozabadi and Pan 2002), indicating that use of a reduced method potentially improves the robustness of multiphase stability analysis. The tie-simplex tabulation (Voskov and Tchelepi 2008) would also be a possibility because, if complete tie-simplex information is available in *P*-*T*-*x* space of interest, there should be no failure in identification of the number of equilibrium phases during the simulation. The tie-simplex tabulation could also be applied using a reduced method.

Flash calculations for more than three phases should be developed. The Gibbs free energy would exhibit a larger number of local minima as the number of phases increases. Convergence to a false solution can be an issue especially in compositional simulation with a fully implicit formulation because good initial estimates are not available due to the long time-step sizes. For more than three phases, minimization of the Gibbs free energy in reduced space might be beneficial because the Gibbs free energy would have fewer local minima in reduced space than in conventional space. The tie-simplex tabulation (Voskov and Tchelepi 2008) can also be used for such complex phase behavior predictions for reservoir simulation.

In simulation of multicontact miscible gas flooding, a large number of flash calculations can be performed in near-critical regions. A nearly singular Hessian or Jacobian matrix is an issue in those calculations. A method to modify ill-conditioned systems (*e.g.*, Trangenstein 1987) can be applied although our reduced method improved this problem compared to standard algorithms.

A robust algorithm for phase identification in compositional reservoir simulation should be developed for more than two hydrocarbon-phases. The current algorithm within UTCOMP requires a unique threshold density to distinguish the gaseous phase from the solvent-rich liquid phase during a simulation. However, the gaseous phase at a grid cell can be denser than the solvent-rich phase at a different grid cell. That is, the unique threshold density can fail to label correctly the phases. The mislabeling would incorrectly assign phase relative permeabilities to loose the reliability of simulation results. Density inversion can also happen between two liquid phases in simulation of rich gas or CO_2 flooding.

Development of miscibility has not been found for a composition path that goes through a three-phase region. This might be because a tricritical point was not considered in composition space in previous research. A composition path that goes through a tricritical point should be investigated for miscibility development for three-phase flow. The phase rule for critical points (equation (6.1)) predicts that at least five components must be used to model a tricritical point in composition space at a fixed temperature and pressure. The method of characteristics can be used for the study on miscibility development for three-phase flow. Development of a mixing-cell method for three phases would also improve our understanding of miscibility development for three-phase flow.

Appendix A. Flow Chart of Multiphase Equilibrium Calculations in UTCOMP (from Chang 1990)

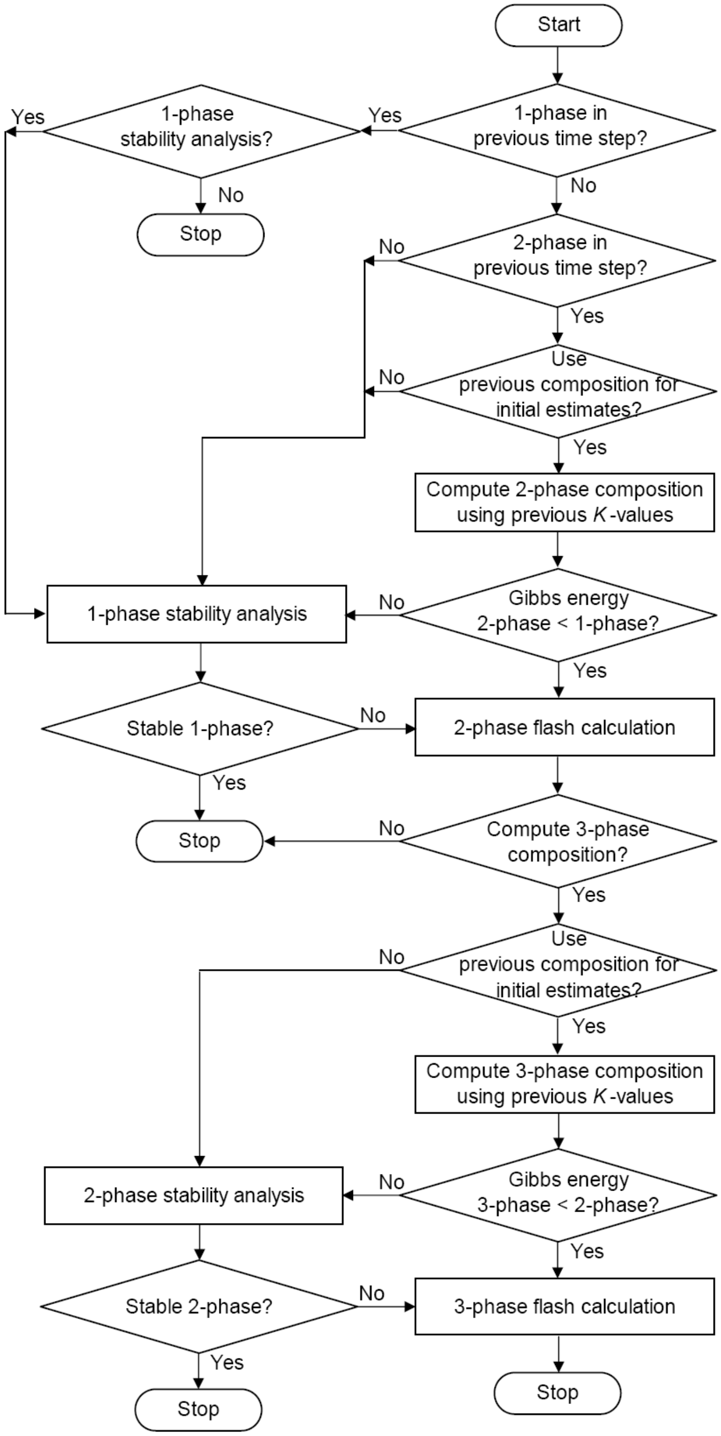

Appendix B. Derivatives for the Reduced Method

B.1 DERIVATIVES FOR STABILITY ANALYSIS USING THE REDUCED METHOD

The non-linear equations to be solved for the reduced stability analysis are

$$S_j^R\left(\underline{\theta}\right) = \sum\nolimits_{i=1}^{N_C}\left(\theta_j - \eta_{ji}\right)D_i \big/ \varphi_i\left(\underline{\theta}\right) = 0, \text{ where } j = 1,\ldots,5 \text{ and } D_i = z_i\varphi_i\left(\underline{z}\right).$$

The reduced parameters are defined as

$$\theta_k = \sum\nolimits_{i=1}^{N_C}\eta_{ki}x_i,$$

where $\eta_i = \left(B_i,\ \sqrt{A_i},\ \sqrt{A_i}h_i g_i,\ \sqrt{A_i}h_i^2 g_i,\ \sqrt{A_i}g_i\right)$ and $k = 1,\ldots,5$. A_i and B_i are the EOS parameters in dimensionless form (see section 2.1.5).

The partial derivatives of S_j^R with respect to θ_k (j, k = 1,…,5) are

$$\frac{\partial S_j^R}{\partial\theta_k} = \sum\nolimits_{i=1}^{N_C} D_i\left[\frac{\delta_{jk}}{\varphi_i} - \frac{\left(\theta_j - \eta_{ji}\right)}{\left(\varphi_i\right)^2}\frac{\partial\varphi_i}{\partial\theta_k}\right]$$

$$= \sum\nolimits_{i=1}^{N_C}\frac{D_i}{\varphi_i}\left[\delta_{jk} - \left(\theta_j - \eta_{ji}\right)\frac{\partial\ln\varphi_i}{\partial\theta_k}\right], \text{ where } \delta_{jk} \text{ is the Kronecker delta.}$$

The fugacity coefficient of component *i* using the Peng-Robinson EOS is

$$\ln\varphi_i = \frac{B_i}{B_m}\left(Z-1\right) - \ln\left(Z - B_m\right) - \frac{A_m}{\left(\beta-\alpha\right)B_m}\left(\frac{2\sum\nolimits_{j=1}^{N_C}x_j A_{ij}}{A_m} - \frac{B_i}{B_m}\right)\ln\left(\frac{Z+\beta B_m}{Z+\alpha B_m}\right),$$

where $\alpha = 1 - 2^{0.5}$ and $\beta = 1 + 2^{0.5}$. The derivatives of $\ln\varphi_i$ (i = 1,…,N_C) with respect to θ_1 are

$$\frac{\partial \ln \varphi_i}{\partial \theta_1} = \left(\frac{B_i}{B_m} - \frac{1}{Z - B_m} \right) \frac{\partial Z}{\partial \theta_1} - \frac{B_i}{B_m^2} \left(Z - 1 \right) + \frac{1}{Z - B_m}$$

$$+ \frac{1}{\left(\beta - \alpha \right) B_m} \left(\frac{B_i}{B_m} A_m - 2 \sum\nolimits_{j=1}^{N_C} A_{ij} x_j \right) \left(\frac{\dfrac{\partial Z}{\partial \theta_1} + \beta}{Z + \beta B_m} - \frac{\dfrac{\partial Z}{\partial \theta_1} + \alpha}{Z + \alpha B_m} \right)$$

$$+ \frac{2}{\left(\beta - \alpha \right) B_m^2} \left(\sum\nolimits_{j=1}^{N_C} A_{ij} x_j - \frac{B_i}{B_m} A_m \right) \ln \left(\frac{Z + \beta B_m}{Z + \alpha B_m} \right).$$

The derivatives of lnφ_i ($i = 1,\ldots,N_C$) with respect to θ_k ($k = 2,\ldots,5$) are

$$\frac{\partial \ln \varphi_i}{\partial \theta_k} = \left(\frac{B_i}{B_m} - \frac{1}{Z - B_m} \right) \frac{\partial Z}{\partial \theta_k}$$

$$+ \frac{\partial Z}{\partial \theta_k} \frac{1}{\left(\beta - \alpha \right) B_m} \left(\frac{1}{Z + \beta B_m} - \frac{1}{Z + \alpha B_m} \right) \left(\frac{B_i}{B_m} A_m - 2 \sum\nolimits_{j=1}^{N_C} A_{ij} x_j \right)$$

$$+ \frac{1}{\left(\beta - \alpha \right) B_m} \ln \left(\frac{Z + \beta B_m}{Z + \alpha B_m} \right) \left[\frac{B_i}{B_m} \frac{\partial A_m}{\partial \theta_k} - 2 \frac{\partial \left(\sum\nolimits_{j=1}^{N_C} A_{ij} x_j \right)}{\partial \theta_k} \right].$$

The derivatives of the compressibility factor with respect to the independent variables are easily derived as

$$\frac{\partial Z}{\partial \theta_k} = \frac{-Z^2 + 2\left(3B_m + 1 \right) Z + \left(A_m - 2B_m - 3B_m^2 \right)}{3Z^2 + 2\left(B_m - 1 \right) Z + \left(A_m - 3B_m^2 - 2B_m \right)} \text{ for } k = 1$$

$$\frac{\partial Z}{\partial \theta_k} = \frac{-Z + B_m}{3Z^2 + 2\left(B_m - 1 \right) Z + \left(A_m - 3B_m^2 - 2B_m \right)} \left(\frac{\partial A_m}{\partial \theta_k} \right) \text{ for } k = 2, \ldots, 5.$$

As shown in section 4.1.1,

$$A_m = \theta_2^2 - 2\theta_4 \theta_5 + 2\theta_3^2 \text{ and}$$

$$\sum\nolimits_{j=1}^{N_C} x_j A_{ij} = \sqrt{A_i}\,\theta_2 - \sqrt{A_i}\,h_i^2 g_i \theta_5 - \sqrt{A_i}\,g_i \theta_4 + 2\sqrt{A_i}\,h_i g_i \theta_3.$$

Therefore,

$$\frac{\partial A_m}{\partial \theta_k} = \left(0,\ 2\theta_2,\ 4\theta_3,\ -2\theta_5,\ -2\theta_4 \right)$$

$$\frac{\partial\left(\sum_{j=1}^{N_C} A_{ij} x_j\right)}{\partial \theta_k} = \left(0,\ \sqrt{A_i},\ 2\sqrt{A_i} h_i g_i,\ -\sqrt{A_i} g_i,\ -\sqrt{A_i} h_i^2 g_i\right),$$

where $i = 1,\ldots,N_C$ and $k = 1,\ldots,5$.

B.2 DERIVATIVES FOR THREE-PHASE FLASH CALCULATIONS USING THE REDUCED METHOD

The independent variables for three-phase flash calculations using the reduced method are $\psi = (\theta_{11},\ldots, \theta_{51}, \beta_1, \theta_{12},\ldots, \theta_{52}, \beta_2)$, where θ_{kj} is the k^{th} reduced parameter for phase j, and β_j is the mole fraction of phase j. The number of independent variables is 12 because there are six independent variables for each of two independent phases. The non-linear equations to be solved for three-phase flash calculations using the reduced method are

$$F_j^R = \psi_j - \sum_{i=1}^{N_C} \eta_{ji} x_{i1} = 0 \quad \text{for } j = 1,\ldots,5$$
$$F_j^R = \sum_{i=1}^{N_C} \left(x_{i3} - x_{i1}\right) = 0 \quad \text{for } j = 6$$
$$F_j^R = \psi_j - \sum_{i=1}^{N_C} \eta_{(j-6)i} x_{i2} = 0 \quad \text{for } j = 7,\ldots,11$$
$$F_j^R = \sum_{i=1}^{N_C} \left(x_{i3} - x_{i2}\right) = 0 \quad \text{for } j = 12.$$

In the above equations, phase 3 is arbitrarily selected as the reference phase.

The derivatives of F_j^R ($j = 1,\ldots,12$) with respect to ψ_k ($k = 1,\ldots,12$) are

$$\frac{\partial F_j^R}{\partial \psi_k} = \delta_{jk} - \sum_{i=1}^{N_C} \eta_{ji} \frac{\partial x_{i1}}{\partial \psi_k} \quad \text{for } j = 1,\ldots,5$$
$$\frac{\partial F_j^R}{\partial \psi_k} = \sum_{i=1}^{N_C} \left(\frac{\partial x_{i3}}{\partial \psi_k} - \frac{\partial x_{i1}}{\partial \psi_k} \right) \quad \text{for } j = 6$$
$$\frac{\partial F_j^R}{\partial \psi_k} = \delta_{jk} - \sum_{i=1}^{N_C} \eta_{(j-6)i} \frac{\partial x_{i2}}{\partial \psi_k} \quad \text{for } j = 7,\ldots,11$$
$$\frac{\partial F_j^R}{\partial \psi_k} = \sum_{i=1}^{N_C} \left(\frac{\partial x_{i3}}{\partial \psi_k} - \frac{\partial x_{i2}}{\partial \psi_k} \right) \quad \text{for } j = 12,$$

where δ_{jk} is the Kronecker delta for indices j and k.

As presented in section 2.2.1.2, phase component mole fractions are expressed as

$x_{iN_P} = z_i / t_i$ and $x_{ij} = K_{ij} x_{iN_P}$,

where $t_i = 1 - \left[\sum_{j=1}^{N_P - 1} \left(1 - K_{ij}\right) \beta_j \right]$ for $i = 1, ..., N_C$ and $j = 1, ..., \left(N_P - 1\right)$. For three phases, $N_P = 3$ is used in the above equations, and $\beta_1 = \psi_6$ and $\beta_2 = \psi_{12}$. Then,

$$\frac{\partial x_{i3}}{\partial \psi_k} = -\frac{z_i}{t_i^2} \left[\left(K_{i1} - 1\right) \delta_{6k} + \left(K_{i2} - 1\right) \delta_{12k} + \psi_6 \frac{\partial K_{i1}}{\partial \psi_k} + \psi_{12} \frac{\partial K_{i2}}{\partial \psi_k} \right]$$

$$\frac{\partial x_{i1}}{\partial \psi_k} = \frac{z_i}{t_i^2} \left\{ -K_{i1} \left(K_{i1} - 1\right) \delta_{6k} - K_{i1} \left(K_{i2} - 1\right) \delta_{12k} \right.$$
$$\left. + \left[\left(K_{i2} - 1\right) \psi_{12} - \psi_6 + 1 \right] \frac{\partial K_{i1}}{\partial \psi_k} - K_{i1} \psi_{12} \frac{\partial K_{i2}}{\partial \psi_k} \right\}$$

$$\frac{\partial x_{i2}}{\partial \psi_k} = \frac{z_i}{t_i^2} \left\{ -K_{i2} \left(K_{i1} - 1\right) \delta_{6k} - K_{i2} \left(K_{i2} - 1\right) \delta_{12k} \right.$$
$$\left. - K_{i2} \psi_6 \frac{\partial K_{i1}}{\partial \psi_k} + \left[\left(K_{i1} - 1\right) \psi_6 - \psi_{12} + 1 \right] \frac{\partial K_{i2}}{\partial \psi_k} \right\}.$$

K-values are calculated as $K_{ij} = \varphi_{i3}/\varphi_{ij}$, where $i = 1,\ldots,N_C$ and $j = 1, 2$. The derivatives of *K*-values with respect to the independent variables are

$$\frac{\partial K_{i1}}{\partial \psi_k} = K_{i1} \left(\frac{\partial \ln \varphi_{i3}}{\partial \psi_k} - \frac{\partial \ln \varphi_{i1}}{\partial \psi_k} \right) \text{ and } \frac{\partial K_{i2}}{\partial \psi_k} = K_{i2} \left(\frac{\partial \ln \varphi_{i3}}{\partial \psi_k} - \frac{\partial \ln \varphi_{i2}}{\partial \psi_k} \right),$$

where $i = 1,\ldots,N_C$ and $k = 1,\ldots,12$. $\partial \ln\varphi_{i1}/\partial\psi_k$ and $\partial \ln\varphi_{i2}/\partial\psi_k$ are zero for $k = 6$ and 12 because $\varphi_{i1} = \varphi_{i1}(\psi_1, \psi_2, \psi_3, \psi_4, \psi_5)$ and $\varphi_{i2} = \varphi_{i2}(\psi_7, \psi_8, \psi_9, \psi_{10}, \psi_{11})$. The derivatives of $\ln\varphi_i$ ($i = 1,\ldots,N_C$) with respect to θ_k ($k = 1,\ldots,5$) presented in section B.1 can be directly used for non-zero terms in $\partial \ln\varphi_{i1}/\partial\psi_k$ and $\partial \ln\varphi_{i2}/\partial\psi_k$. The derivatives of $\ln\varphi_{i3}$ with respect to ψ_k are

$$\frac{\partial \ln \varphi_{i3}}{\partial \varphi_k} = -\frac{\psi_6}{1-\psi_6-\psi_{12}} \frac{\partial \ln \varphi_{i3}}{\partial \theta_{k3}} \quad \text{for } k = 1,\ldots,5$$

$$\frac{\partial \ln \varphi_{i3}}{\partial \varphi_k} = \frac{1}{\left(1-\psi_6-\psi_{12}\right)^2} \sum_{j=1}^{5} \left[\theta_j^z - \left(1-\psi_{12}\right)\psi_j - \psi_{12}\psi_{(j+6)}\right] \frac{\partial \ln \varphi_{i3}}{\partial \theta_{j3}} \quad \text{for } k = 6$$

$$\frac{\partial \ln \varphi_{i3}}{\partial \varphi_k} = -\frac{\psi_{12}}{1-\psi_6-\psi_{12}} \frac{\partial \ln \varphi_{i3}}{\partial \theta_{(k-6)3}} \quad \text{for } k = 7,\ldots,11$$

$$\frac{\partial \ln \varphi_{i3}}{\partial \varphi_k} = \frac{1}{\left(1-\psi_6-\psi_{12}\right)^2} \sum_{j=1}^{5} \left[\theta_j^z - \psi_6\psi_j - \left(1-\psi_6\right)\psi_{(j+6)}\right] \frac{\partial \ln \varphi_{i3}}{\partial \theta_{j3}} \quad \text{for } k = 12,$$

where $\theta_j^z = \sum_i \eta_{ji} z_i$, $i = 1,\ldots,N_C$, and $j = 1,\ldots,5$. Because $\varphi_{i3} = \varphi_{i3}(\theta_{13}, \theta_{23}, \theta_{33}, \theta_{43}, \theta_{53})$, the derivatives of $\ln\varphi_i$ ($i = 1,\ldots,N_C$) with respect to θ_k ($k = 1,\ldots,5$) presented in section B.1 can be directly used for $\partial\ln\varphi_{i3}/\partial\theta_{j3}$.

Glossary

Roman symbols

a	Attraction parameter for a cubic equation of state
A	Dimensionless attraction parameter for a cubic equation of state
b	Covolume parameter for a cubic equation of state
B	Dimensionless covolume parameter for a cubic equation of state
d	Vector representing a search direction
$d_{\mathrm{L1\text{-}V}}$	Phase composition distance between the L_1 and V phases
$d_{\mathrm{L2\text{-}V}}$	Phase composition distance between the L_2 and V phases
$d_{\mathrm{L1\text{-}L2}}$	Phase composition distance between the L_1 and L_2 phases
D	Tangent plane distance function defined in equation (2.24) or diagonal matrix
f_{ij}	Fugacity of component *i* in phase *j*
F	Function or fugacity equation defined in equations (4.3)
g_i	Parameter for component *i* for the reduced method
G	Gibbs free energy
$\underline{G}$	Molar Gibbs free energy
$\overline{G}_{ij}$	Partial molar Gibbs free energy of component *i* in phase *j*
h_i	Parameter for component *i* for the reduced method
H	Hessian matrix
J	Jacobian matrix
k_{ij}	Binary interaction coefficient between components *i* and *j*
K_{ij}	*K*-value of component *i* in phase *j*
L	Liquid phase or liquid phase mole fraction
L_1	Oleic phase
L_2	Solvent-rich liquid phase
n_{ij}	Number of moles of component *i* in phase *j*
N_C	Number of components
N_P	Number of phases

P	Pressure
P_R	Reduced pressure
q	Heat
R	Gas constant
S	Entropy or stationarity equation defined in equations (4.8) or saturation
t_i	Function defined in equations (2.46)
T	Temperature or a tangent plane function
T_C	Critical temperature
T_R	Reduced temperature
U	Internal energy or matrix defined in equation (2.52)
V	Volume, or vapor phase mole fraction, or gaseous phase
$\overline{V}_i$	Partial molar volume of component *i*
w	Work
w_{ij}	Variables defined in equations (2.40)
x_{ij}	Mole fraction of component *i* in phase *j*
X_i	Independent variable for component *i* used for stability analysis
y_i	Mole fraction of component *i* in a vapor phase
z_i	Mole fraction of component *i* in a mixture
Z_j	Compressibility factor of phase *j*

Greek letters

α	Step size for minimization algorithms or temperature dependent term of a cubic equation of state
β	Mole fraction of phase *j*
δ	Kronecker delta
η	Matrix defined in equations (4.2)
θ_i	*i*th reduced parameter
θ_{ij}	*i*th reduced parameter in phase *j*
ξ	Dimensionless parameter defined in equation (6.2)
φ_{ij}	Fugacity coefficient of component *i* in phase *j*

ψ_i	i^{th} independent variable for the reduced method
ω	Acentric factor

Superscripts

E	Excess term
I	Ideal term
IG	Ideal gas
IGM	Ideal gas mixture
k	Index for iteration steps
R	Reduced method
T	Transpose
0	Reference state
-1	Inverse

Subscripts

C	Critical property
m	Mixture
R	Reduced quantity
u	Upper bound
max	Maximum

Abbreviations

BIC	Binary interaction coefficient
BSB	Bob Slaughter Block oil
CEP	Critical endpoint
CSA	Conventional algorithm for stability analysis
EOS	Equation of state
HCPVI	Hydrocarbon-pore-volume injected
LCEP	Lower critical endpoint
MC	Monahans Clearfork oil

MG	Minimization algorithm for the Gibbs free energy
MMP	Minimum miscibility pressure
MS	Minimization algorithm with constraint set *S* defined in section 3.2
NWE	North Ward Estes oil
PVI	Pore-volume injected
RF	Reduced method for flash calculations
RL	Root-finding algorithm with constraint set *L* defined in section 3.2
RR	Rachford-Rice equations
RSA	Reduced method for stability analysis
SCF	Standard cubic feet
SS	Successive substitution algorithm
TPD	Tangent plane distance function
UCEP	Upper critical endpoint
UTCOMP	IMPEC multiphase compositional reservoir simulator developed at the University of Texas at Austin

References

Abbott, M.M. 1979. Cubic Equations of State: An Interpretive Review. In *Equations of State in Engineering and Research*, ed. Chao, K.C. and Robinson Jr., R.L., Chap. 3, 47-70. Advances in Chemistry Series, American Chemical Society, Washington, D.C.

Abhvani, A.S. and Beaumont, D.N. 1987. Development of an Efficient Algorithm for the Calculation of Two-Phase Flash Equilibria. *SPE Reservoir Engineering* 2(4): 695-702.

Alwani, Z. and Schneider, G.M. 1976. Fluid Mixtures at High Pressure. Phase Separation and Critical Phenomena in Binary Mixtures of a Polar Component With Supercritical Carbon Dioxide, Ethane, and Ethene up to 1000 Bar. *Berichte der Bunsengesellschaft fuer Physikalische Chemie* 80(12): 1310-1315.

Ammar, M.N. and Renon, H. 1987. The Isothermal Flash Problem: New Methods for Phase Split Calculations. *AIChE Journal* 33(6): 926-939.

Asselineau, L., Bogdanic, G., and Vidal, J. 1979. A Versatile Algorithm for Calculating Vapour-Liquid Equilibria. *Fluid Phase Equilibria* 3(4):273-290.

Baker, L.E., Pierce, A.C., and Luks, K.D. 1982. Gibbs Energy Analysis of Phase Equilibria. *SPE Journal* 22(5): 731-742.

Bertsekas, D.P. 1999. *Nonlinear Programming*, second edition. Athena Scientific, Belmont, MA.

Bluma, M. and Deiters, U.K. 1999. A Classification of Phase Diagrams of Ternary Fluid Systems. *Physical Chemistry Chemical Physics* 1(18): 4307-4313.

Boston, J.F. and Britt, H.I. 1978. A Radically Different Formulation and Solution of the Single-Stage Flash Problem. *Computers and Chemical Engineering* 2(2-3): 109-122.

Bryoden, C.G. 1970a. The Convergence of a Class of Double-Rank Minimization Algorithms: 1. General Considerations. *IMA Journal of Applied Mathematics* 6(1): 76-90.

Bryoden, C.G. 1970b. The Convergence of a Class of Double-Rank Minimization Algorithms: 2. The New Algorithm. *IMA Journal of Applied Mathematics* 6(3): 222-231.

Bünz, A.P., Dohrn, R., and Prausnitz, J.M. 1991. Three-Phase Flash Calculations for Multicomponent Systems. *Computers & Chemical Engineering* 15(1): 47-51.

Chaback, J.J. and Turek, E.A. 1986. Phase Behavior of Mixtures of San Andres Formation Oils With Acid Gases. Application of a Modified Redlich-Kwong Equation of State. In *Equations of State Theories and Applications*, ed. Chao, K.C. and Robinson Jr., R.L., Chap. 20, 406-433. ACS Symposium Series, American Chemical Society, Washington, D.C.

Chang, Y.-B. 1990. *Development and Application of an Equation of State Compositional Simulator*. PhD dissertation, the University of Texas at Austin, Austin, Texas.

Chang, Y.-B., Pope, G.A., and Sepehrnoori, K. 1990. A Higher-Order Finite-Difference Compositional Simulator. *Journal of Petroleum Science and Engineering* 5(1): 35-50.

Chien, M.C. 1983. A New Equilibrium Coefficient Correlation Method for Compositional Simulators. Paper presented at the SPE Reservoir Simulation Symposium, San Francisco, California, 15-18 November.

Coutinho, J.A.P., Jørgensen, M., and Stenby, E.H. 1995. Predictions of Three-Phase Regions in CO_2-Oil Mixtures. *Journal of Petroleum Science and Engineering* 12(3): 201-208.

Creek, J.L. and Sheffield, J.M. 1993. Phase Behavior, Fluid Properties, and Displacement Characteristics of Permian Basin Reservoir Fluid/CO_2 Systems. *SPE Reservoir Engineering* 8(1): 34-42.

Davenport, A.J. and Rowlinson, J.S. 1963. The Solubility of Hydrocarbons in Liquid Methane. *Transactions of the Faraday Society* 59: 78-84.

Davenport, A.J., Rowlinson, J.S., and Saville, G. 1966. Solutions of Three Hydrocarbons in Liquid Methane. *Transactions of the Faraday Society* 62: 322-327.

Deam, J.R. and Maddox, R.N. 1969. How to Figure Three-Phase Flash. *Hydrocarbon Processing* 48: 163-164.

Deiters, U.K. and Pegg, I.L. 1989. Systematic Investigation of the Phase Behavior in Binary Fluid Mixtures. I. Calculations Based on the Redlich-Kwong Equation of State. *The Journal of Chemical Physics* 90(11): 6632-6641.

Deiters, U. and Schneider, G.M. 1976. Fluid Mixtures at High Pressures. Computer Calculations of the Phase Equilibria and the Critical Phenomena in Fluid Binary Mixtures From the Redlich-Kwong Equation of State. *Berichte der Bunsengesellschaft fuer Physikalische Chemie* 80(12): 1316-1321.

Dennis, Jr., J.E. and Schnabel, R.B. 1996. *Numerical Methods for Unconstrained Optimization and Nonlinear Equations.* SIAM, Philadelphia, PA.

DeRuiter, R.A., Nash, L.J., and Singletary, M.S. 1994. Solubility and Displacement Behavior of a Viscous Crude With CO_2 and Hydrocarbon Gases. *SPE Reservoir Engineering* 9(2): 101-106.

Dindoruk, B. 1992. *Analytical Theory of Multiphase, Multicomponent Displacement in Porous Media.* PhD dissertation, Stanford University, Palo Alto, California.

Dupré, A. 1869. *Théorie Mécanique de la Chaleur.* Gauthier-Villars, Paris.

Enick, R., Holder, G.D., and Morsi, B.I. 1985. Critical and Three Phase Behavior in the Carbon Dioxide/Tridecane System. *Fluid Phase Equilibria* 22(2): 209-224.

Eubank, P.T. 2006. Equations and Procedures for VLLE Calculations. *Fluid Phase Equilibria* 241: 81-85.

Eubank, P.T., Elhassan, A.E., Barrufet, M.A., and Whiting, W.B. 1992. Area Method for Prediction of Fluid-Phase Equilibria. *Industrial and Engineering Chemistry Research* 31(3): 942-949.

Evelein, K.A., Moore, R.G., and Heidemann, R.A. 1976. Correlation of the Phase Behavior in the Systems Hydrogen Sulfide-Water and Carbon Dioxide-Water. *Industrial & Engineering Chemistry Process Design and Development* 15(3): 423-428.

Fall, D.J., Fall, J.L, and Luks, K.D. 1985. Liquid-Liquid-Vapor Immiscibility Limits in Carbon Dioxide + *n*-Paraffin Mixtures. *Journal of Chemical and Engineering Data* 30(1): 82-88.

Firoozabadi, A. and Pan, H. 2002. Fast and Robust Algorithm for Compositional Modeling: Part I-Stability Analysis Testing. *SPE Journal* 7(1): 79-89.

Fletcher, R. 1970. A New Approach to Variable Metric Algorithms. *The Computer Journal* 13(3): 317-322.

Fong, W.S., Sheffield, J.M., Ehrlich, R., and Emanuel, A.S. 1992. Phase Behavior Modeling Techniques for Low-Temperature CO_2 Applied to McElroy and North Ward Estes Projects. Paper presented at the SPE/DOE Enhanced Oil Recovery Symposium, Tulsa, Oklahoma, 22-24 April.

Fussell, L.T. 1979. Technique for Calculating Multiphase Equilibria. *SPE Journal* 19(4): 203-210.

Fussell, D.D. and Yanosik, J.L. 1978. An Iterative Sequence for Phase-Equilibria Calculations Incorporating the Redlich-Kwong Equation of State. *SPE Journal* 18(3): 173-182.

Fussell, L.T. and Fussell, D.D. 1979. An Iterative Technique for Compositional Reservoir Models. *SPE Journal* 19(4): 211-220.

Galindo, A. and Blas, F.J. 2002. Theoretical Examination of the Global Fluid Phase Behavior and Critical Phenomena in Carbon Dioxide + *n*-Alkane Binary Mixtures. *The Journal of Physical Chemistry B* 106(17): 4343-4564.

Gardner, J.W., Orr Jr., F.M., and Patel, P.D. 1981. The Effect of Phase Behavior on CO_2-Flood Displacement Efficiency. *Journal of Petroleum Technology* 33(11): 2067-2081.

Gasmi, C.F., Voskov, D.V., and Tchelepi, H.A. 2009. A New Method for Thermodynamic Equilibrium Computation of Systems With an Arbitrary Number of Phases. Paper presented at the SPE Reservoir Simulation Symposium, The Woodlands, Texas, 2-4 February.

Gautam, R. and Seider, W.D. 1979. Computation of Phase and Chemical Equilibrium. *AIChE Journal* 25(6): 991-1007.

Gauter, K. 1999. *Fluid Multiphase Behavior in Ternary Systems of Near-Critical* CO_2. PhD dissertation, the Technical University of Berlin, Berlin, Germany.

Gauter, K., Heidemann, R.A., and Peters, C.J. 1999. Modeling of Fluid Multiphase Equilibria in Ternary Systems of Carbon Dioxide as the Near-Critical Solvent and Two Low-Volatile Solutes. *Fluid Phase Equilibria* 158-160: 133-141.

Gibbs, J.W. 1873a. Graphical Methods in the Thermodynamics of Fluids. *Transactions of the Connecticut Academy*, II: 309-342.

Gibbs, J.W. 1873b. A Method of Geometrical Representation of the Thermodynamic Properties of Substances by Means of Surfaces. *Transactions of the Connecticut Academy*, II: 382-404.

Gill, P.E. and Murray, W. 1974. Newton-Type Methods for Unconstrained and Linearly Constrained Optimization. *Mathematical Programming* 7(3): 311-350.

Gill, P.E., Murray, W., and Wright, M.H. 1986. *Practical Optimization.* Elsevier.

Goldfarb, D. 1970. A Family of Variable-Metric Methods Derived by Variational Means. *Mathematics of Computation* 24(109): 23-26.

Goldfarb, D. 1976. Factorized Variable Metric Methods for Unconstrained Optimization. *Mathematics of Computation* 30(136): 796-811

Gregorowicz, J. and de Loos, Th.W. 1996. Modeling of the Three Phase LLV Region for Ternary Hydrocarbon Mixtures With the Soave-Redlich-Kwong Equation of State. *Fluid Phase Equilibria* 118(1): 121-132.

Gregorowicz, J. and de Loos, Th.W. 2001. Prediction of Liquid-Liquid-Vapor Equilibria in Asymmetric Hydrocarbon Mixtures. *Industrial and Engineering Chemistry Research* 40(1): 444-451.

Griffiths, R.B. 1974. Thermodynamic Model for Tricritical Points in Ternary and Quaternary Fluid Mixtures. *The Journal of Chemical Physics* 60(1): 195-206.

Grigg R.B. and Siagian, U.W.R. 1998. Understanding and Exploiting Four-Phase Flow in Low-Temperature CO_2 Floods. Paper presented at SPE Permian Basin Oil and Gas Recovery Conference, Midland, Texas, 23-26 March.

Guler, B., Wang, P., Delshad, M., Pope, G.A., and Sepehrnoori, K. 2001. Three- and Four-Phase Flow Compositional Simulations of CO_2/NGL EOR. Paper presented at the SPE Annual Technical Conference and Exhibition, New Orleans, Louisiana, 30 September-3 October.

Gupta, A.K., Bishnoi, P.R., and Kalogerakis, N. 1991. A Method for the Simultaneous Phase Equilibria and Stability Calculations for Multiphase Reacting and Non-Reacting Systems. *Fluid Phase Equilibria* 63(1-2): 65-89.

Haugen, K.B., Sun, L., and Firoozabadi, A. 2007. Three-Phase Equilibrium Calculations for Compositional Simulation. Paper presented at the SPE Reservoir Simulation Symposium, Houston, Texas, 26-28 February.

Heidemann, R.A. 1983. Computation of High Pressure Phase Equilibria. *Fluid Phase Equilibria* 14: 55-78.

Heidemann, R.A. and Khalil, A.M. 1980. The Calculation of Critical Points. *AIChE Journal* 26(5): 769-779.

Heidemann, R.A. and Michelsen, M.L. 1995. Instability of Successive Substitution. *Industrial and Engineering Chemistry Research* 34(3): 958-966.

Hendriks, E.M. 1988. Reduction Theorem for Phase Equilibrium Problems. *Industrial and Engineering Chemistry Research* 27(9): 1728-1732.

Hendriks, E.M. and van Bergen, A.R.D. 1992. Application of a Reduction Method to Phase Equilibria Calculations. *Fluid Phase Equilibria* 74: 17-34.

Henry, R.L. and Metcalfe, R.S. 1983. Multiple-Phase Generation During Carbon Dioxide Flooding. *SPE Journal* 23(4): 595-601.

Hill, T.L. 1986. *An Introduction to Statistical Thermodynamics.* Dover Publications, Inc., New York.

Holm, L.W. and Josendal, V.A. 1974. Mechanisms of Oil Displacement by Carbon Dioxide. *Journal of Petroleum Technology* 26(12): 1427-1438.

Holm, L.W. and Josendal, V.A. 1980. Discussion of Determination and Prediction of CO_2 Minimum Miscibility Pressures. Paper associated with Yellig, W.F. and Metcalfe, R.S. 1980. *Journal of Petroleum Technology* 32(1):160-168.

Holm, L.W. and Josendal, V.A. 1982. Effect of Oil Composition on Miscible-Type Displacement by Carbon Dioxide. *SPE Journal* 22(1): 87-98.

Honami, Y., Arihara, N., and Yazawa, N. 2000. Accuracy and Efficiency Evaluation of EOS Computation Methods for Compositional Simulation. Paper presented at the SPE Asia Pacific Conference on Integrated Modeling for Asset Management, Yokohama, Japan, 25-26 April.

Hoteit, H. and Firoozabadi, A. 2006. Simple Phase Stability-Testing Algorithm in the Reduction Method. *AIChE Journal* 52(8): 2909-2920.

Hottovy, J.D., Luks, K.D., and Kohn, J.P. 1981. Three-Phase Liquid-Liquid-Vapor Equilibria Behavior of Certain Binary CO_2-*n*-Paraffin Systems. *Journal of Chemical and Engineering Data* 26(3): 256-258.

Huang, E.T.S. and Tracht, J.H. 1974. The Displacement of Residual Oil by Carbon Dioxide. Paper presented at the SPE Improved Oil Recovery Symposium, Tulsa, Oklahoma, 22-24 April.

Huie, N.C. 1972. *The Heterogeneous Phase Equilibria of Carbon Dioxide-Normal Paraffin Systems.* PhD dissertation, the University of Notre Dame, Notre Dame, Indiana.

Hutchinson Jr., C.A. and Braun, P.H. 1961. Phase Relations of Miscible Displacement in Oil Recovery. *AIChE Journal* 7(1): 64-72.

Jensen, B.H. and Fredenslund, A. 1987. A Simplified Flash Procedure for Multicomponent Mixtures Containing Hydrocarbons and One Non-Hydrocarbon Using Two-Parameter Cubic Equations of State. *Industrial and Engineering Chemistry Research* 26(10): 2129-2134.

Johns, R.T. 1992. *Analytical Theory of Multicomponent Gas Drives With Two-Phase Mass Transfer.* PhD dissertation, Stanford University, Palo Alto, California.

Joshi, D.K. and Prausnitz, J.M. 1984. Supercritical Fluid Extraction With Mixed Solvents. *AIChE Journal* 30(3): 522-525.

Katz, D.L. and Firoozabadi, A. 1978. Predicting Phase Behavior of Condensate/Crude-Oil Systems Using Methane Interaction Coefficients. *Journal of Petroleum Technology* 30(11): 1649-1655.

Kaul, P.K. 1992. *A New and Efficient Approach for Two Phase Equilibrium Prediction Using Cubic Equations of State*. MS thesis, Mississippi State University, Mississippi State, Mississippi.

Kaul, P.K. 1999. *An Analysis of Phase Behavior and Displacement Characteristics of Multicomponent Mixtures*. PhD dissertation, Stanford University, Palo Alto, California.

Kaul, P. and Thrasher, R.L. 1996. A Parameter-Based Approach for Two-Phase-Equilibrium Prediction With Cubic Equations of State. *SPE Reservoir Engineering* 11(4): 273-279.

Khan, S.A. 1992. *An Expert System to Aid in Compositional Simulation of Miscible Gas Flooding*. PhD dissertation, the University of Texas at Austin, Austin, Texas.

Khan, S.A., Pope, G.A., and Sepehrnoori, K. 1992. Fluid Characterization of Three-Phase CO_2/Oil Mixtures. Paper presented at the SPE/DOE Enhanced Oil Recovery Symposium, Tulsa, Oklahoma, 22-24 April.

Knobler, C.M. and Scott, R.L. 1984. Multicritical Points in Fluid Mixtures: Experimental Studies. In *Phase Transitions and Critical Phenomena vol. 9*, ed. Domb, C. and Lebowitz, J.L., Chap. 2, 163-231. Academic Press, London.

Kohn, J.P., Kim, Y.J., and Pan, Y.C. 1966. Partial Miscibility Phenomena in Binary Hydrocarbon Systems Involving Ethane. *Journal of Chemical and Engineering Data* 11(3):333-335.

LaForce, T.C. 2005. *Mathematics of Partially Miscible Three-Phase Flow*. PhD dissertation, the University of Texas at Austin, Austin, Texas.

Larson, R.G. 1979. The Influence of Phase Behavior on Surfactant Flooding. *SPE Journal* 19(6): 411-422.

Larson, L.L., Silva, M.K., Taylor, M.A., and Orr Jr., F.M. 1989. Temperature Dependence of L_1/L_2/V Behavior in CO_2/Hydrocarbon Systems. *SPE Reservoir Engineering* 4(1): 105-114.

Lee, K.-H. 1986. *The Generalized van der Waals Partition Function: Theory and Applications*. PhD dissertation, the University of Delaware, Newark, Delaware.

Leibovici, C.F., Barker, J.W., Waché, D. 2000. Method for Delumping the Results of Compositional Reservoir Simulation. *SPE Journal* 5(2): 227-235.

Leibovici, C.F. and Neoschil, J. 1992. A New Look at the Rachford-Rice Equation. *Fluid Phase Equilibria* 74: 303-308.

Leibovici, C.F. and Neoschil, J. 1995. A Solution of Rachford-Rice Equations for Multiphase Systems. *Fluid Phase Equilibria* 112: 217-221.

Leibovici, C.F. and Nichita, D.V. 2008. A New Look at Multiphase Rachford-Rice Equations for Negative Flashes. *Fluid Phase Equilibria* 267: 127-132.

Li, Y. and Johns, R.T. 2006. Rapid Flash Calculations for Compositional Simulation. *SPE Reservoir Evaluation and Engineering* 9(4): 521-529.

Li, Y. and Johns, R.T. 2007. A Rapid and Robust Method to Replace Rachford-Rice in Flash Calculations. Paper presented at the SPE Reservoir Simulation Symposium, Houston, Texas, 26-28 February.

Lim, M.T., Khan, S.A., Sepehrnoori, K., and Pope, G.A. 1992. Simulation of Carbon Dioxide Flooding Using Horizontal Wells. Paper presented at the SPE Annual Technical Conference and Exhibition, Washington, D.C., 4-7 October.

Litvak, M.L. 1994. New Procedure for Phase-Equilibrium Computations in Compositional Reservoir Simulators. *SPE Advanced Technology Series* 2(2): 113-121.

Liu, J., Delshad, M., Pope, G.A., Sepehrnoori, K. 1994. Application of Higher-Order Flux-Limited Methods in Compositional Simulation. *Transport in Porous Media* 16(1): 1-29.

Lohrenz, J., Bray, B.G., and Clark, C.R. 1964. Calculating Viscosities of Reservoir Fluids From Their Compositions. *Journal of Petroleum Technology* 16(10): 1171-1176.

Lucia, A., Miller, D.C., and Kumar, A. 1985. Thermodynamically Consistent Quasi-Newton Formulae. *AIChE Journal* 31(8): 1381-1388.

McDonald, C.M. and Floudas, C.A. 1995. Global Optimization for the Phase Stability Problem. *AIChE Journal* 41(7): 1798-1814.

McDonald, C.M. and Floudas, C.A. 1997. GLOPEQ: A New Computational Tool for the Phase and Chemical Equilibrium Problem. *Computers and Chemical Engineering* 21(1): 1-23.

Mehra, R.K., Heidemann, R.A., and Aziz, K. 1982. Computation of Multiphase Equilibrium for Compositional Simulation. *SPE Journal* 22(1): 61-68.

Mehra, R.K., Heidemann, R.A., and Aziz, K. 1983. Accelerated Successive Substitution Algorithm. *Canadian Journal of Chemical Engineering* 61(4): 590-596.

Metcalfe, R.S. and Yarborough, L. 1979. The Effect of Phase Equilibria on the CO_2 Displacement Mechanism. *SPE Journal* 19(4): 242-252.

Michelsen, M.L. 1982a. The Isothermal Flash Problem. Part I. Stability. *Fluid Phase Equilibria* 9(1): 1-19.

Michelsen, M.L. 1982b. The Isothermal Flash Problem. Part II. Phase-Split Calculation. *Fluid Phase Equilibria* 9(1): 21-40.

Michelsen, M.L. 1986. Simplified Flash Calculations for Cubic Equations of State. *Industrial and Engineering Chemistry Process Design and Development* 25(1): 184-188.

Michelsen, M.L. 1993. Phase Equilibrium Calculations. What is Easy and What is Difficult? *Computers & Chemical Engineering* 17(5/6): 431-439.

Michelsen, M.L. 1994. Calculation of Multiphase Equilibrium. *Computers & Chemical Engineering* 18(7): 545-550.

Michelsen, M.L. 1998. Speeding Up the Two-Phase PT-Flash, With Applications for Calculation of Miscible Displacement. *Fluid Phase Equilibria* 143(1-2): 1-12.

Michelsen, M.L. and Heidemann, R.A. 1988. Calculation of Tri-Critical Points. *Fluid Phase Equilibria* 39(1): 53-74.

Michelsen, M.L. and Mollerup, J.M. 2004. *Thermodynamic Models: Fundamentals & Computational Aspects.* Tie-Line Publications.

Miller, M.M. and Luks, K.D. 1989. Observations on the Multiphase Equilibria Behavior of CO_2-Rich and Ethane-Rich Mixtures. *Fluid Phase Equilibria* 44(3): 295-304.

Mohanty, K.K., Masino Jr., W.H., Ma, T.D., and Nash, L.J. 1995. Role of Three-Hydrocarbon-Phase Flow in a Gas-Displacement Process. *SPE Reservoir Engineering* 10(3): 214-221.

Moulds, T.P., McGuire, P.L., Jerauld, G.R., Lee, S.-T., and Solano, R. 2005. Pt. McIntyre: A Case Study of Gas Enrichment Above MME. *SPE Reservoir Evaluation and Engineering* 8(3): 182-188.

Müller, D. and Marquardt, W. 1997. Dynamic Multiple-Phase Flash Simulation: Global Stability Analysis Versus Quick Phase Determination. *Computers and Chemical Engineering* 21: S817-S822.

Mushrif, S.H. 2004. *Determining Equation of State Binary Interaction Parameters Using K- and L-Points.* Master thesis, the University of Saskatchewan, Saskatoon, Canada.

Mushrif, S.H. and Phoenix, A.V. 2008. Effect of Peng-Robinson Binary Interaction Parameters on the Predicted Multiphase Behavior of Selected Binary Systems. *Industrial and Engineering Chemistry Research* 47(16): 6280-6288.

Nagarajan, N.R., Cullick, A.S., and Griewank, A. 1991. New Strategy for Phase Equilibrium and Critical Point Calculations by Thermodynamic Energy Analysis. Part I. Stability Analysis and Flash. *Fluid Phase Equilibria* 62(3): 191-210.

Negahban, S. and Kremesec Jr., V.J. 1992. Development and Validation of Equation-of-State Fluid Descriptions for CO_2/Reservoir-Oil Systems. *SPE Reservoir Engineering* 7(3): 363-368.

Nelson, P.A. 1987. Rapid Phase Determination in Multiple-Phase Flash Calculations. *Computers & Chemical Engineering* 11(6): 581-591.

Nghiem, L.X., Aziz, K., and Li, Y.K. 1983. A Robust Iterative Method for Flash Calculations Using the Soave-Redlich-Kwong or the Peng-Robinson Equation of State. *SPE Journal* 23(3): 521-530.

Nghiem, L.X. and Heidemann, R.A. 1982. General Acceleration Procedure for Multiphase Flash Calculation With Application to Oil-Gas-Water Systems. Paper presented at the 2nd European Symposium on Enhanced Oil Recovery, Paris, France, 8-10 November.

Nghiem, L.X. and Li, Y.K. 1984. Computation of Multiphase Equilibrium Phenomena With an Equation of State. *Fluid Phase Equilibria* 17(1): 77-95.

Nghiem, L.X. and Li, Y.K. 1986. Effect of Phase Behavior on CO_2 Displacement Efficiency at Low Temperatures: Model Studies With an Equation of State. *SPE Reservoir Engineering* 1(4): 414-422.

Nichita, D.V., Broseta, D., and de Hemptinne, J.-C. 2006. Multiphase Equilibrium Calculation Using Reduced Variables. *Fluid Phase Equilibria* 246(1-2): 15-27.

Nichita, D.V., Gomez, S., and Luna, E. 2002a. Multiphase Equilibria Calculation by Direct Minimization of Gibbs Free Energy With a Global Optimization Method. *Computers and Chemical Engineering* 26(12): 1703-1724.

Nichita, D.V., Gomez, S., and Luna, E. 2002b. Phase Stability Analysis With Cubic Equations of State by Using a Global Optimization Method. *Fluid Phase Equilibria* 194-197: 411-437.

Ohanomah, M.O. and Thompson, D.W. 1984. Computation of Multicomponent Phase Equilibria-Part I. Vapor-Liquid Equilibria. *Computers and Chemical Engineering* 8(3/4): 147-156.

Orr Jr., F.M. 2007. *Theory of Gas Injection Processes.* Tie-Line Publications, Holte, Denmark.

Orr Jr., F.M. and Jensen, C.M. 1984. Interpretation of Pressure-Composition Phase Diagrams for CO_2/Crude-Oil Systems. *SPE Journal* 24(5): 485-497.

Orr Jr., F.M. and Jessen, K. 2007. An Analysis of the Vanishing Interfacial Tension Technique for Determination of Minimum Miscibility Pressure. *Fluid Phase Equilibria* 255(2): 99-109.

Orr Jr., F.M., Silva, M.K., and Lien, C.L. 1983. Equilibrium Phase Compositions of CO_2/Crude Oil Mixtures-Part 2: Comparison of Continuous Multiple-Contact and Slim-Tube Displacement Tests. *SPE Journal* 23(2): 281-291.

Orr Jr., F.M., Yu, A.D., and Lien, C.L. 1981. Phase Behavior of CO_2 and Crude Oil in Low-Temperature Reservoirs. *SPE Journal* 21(4): 480-492.

Pan, H. and Firoozabadi, A. 1998. Complex Multiphase Equilibrium Calculations by Direct Minimization of Gibbs Free Energy by Use of Simulated Annealing. *SPE Reservoir Engineering* 1(1): 36-41.

Pan, H. and Firoozabadi, A. 2003. Fast and Robust Algorithm for Compositional Modeling: Part II-Two-Phase Flash Computations. *SPE Journal* 8(4): 380-391.

Pedersen, K.S., Blilie, A.L., and Meisingset, K.K. 1992. *PVT* Calculations on Petroleum Reservoir Fluids Using Measured and Estimated Compositional Data for the Plus Fraction. *Industrial and Engineering Chemistry Research* 31(5): 1378-1384.

Pedersen, K.S. and Christensen, P.L. 2007. *Phase Behavior of Petroleum Reservoir Fluids.* CRC Press, Boca Raton, Florida.

Pedersen, K.S., Milter, J., and Sørensen, H. 2004. Cubic Equations of State Applied to HT/TP and Highly Aromatic Fluids. *SPE Journal* 9(2): 186-192.

Pedersen, K.S, Thomassen, P., and Fredenslund, A. 1984a. Thermodynamics of Petroleum Mixtures Containing Heavy Hydrocarbons. 1. Phase Envelope Calculations by Use of the Soave-Redlich-Kwong Equation of State. *Industrial and Engineering Chemistry Process Design and Development* 23(1): 163-170.

Pedersen, K.S, Thomassen, P., and Fredenslund, A. 1984b. Thermodynamics of Petroleum Mixtures Containing Heavy Hydrocarbons. 2. Flash and *PVT* Calculations With the SRK Equation of State. *Industrial and Engineering Chemistry Process Design and Development* 23(3): 566-573.

Pedersen, K.S., Thomassen, P., and Fredenslund, A. 1985. Thermodynamics of Petroleum Mixtures Containing Heavy Hydrocarbons. 3. Efficient Flash Calculation Procedures Using the SRK Equation of State. *Industrial and Engineering Chemistry Process Design and Development* 24(4): 948-954.

Peng, D.-Y. and Robinson, D.B. 1976a. A New Two-Constant Equation of State. *Industrial & Engineering Chemistry Fundamentals* 15(1), 59-64.

Peng. D.-Y. and Robinson, D.B. 1976b. Two and Three Phase Equilibrium Calculations for Systems Containing Water. *Canadian Journal of Chemical Engineering* 54(6): 595-599.

Perschke, D.R. 1988. *Equation of State Phase Behavior Modeling for Compositional Simulation.* PhD dissertation, the University of Texas at Austin, Austin, Texas.

Perschke, D.R., Chang, Y.-B., Pope, G.A., and Sepehrnoori, K. 1989. Comparison of Phase Behavior Algorithms for an Equation-of-State Compositional Simulator. Paper SPE 19443 available from SPE, Richardson, Texas.

Pontious, S.B. and Tham, M.J. 1978. North Cross (Devonian) Unit CO_2 Flood-Review of Flood Performance and Numerical Simulation Model. *Journal of Petroleum Technology* 30(12): 1706-1714.

Prigogine, I. and Defay, R. 1954. *Chemical Thermodynamics.* (translated by Everett, D.H.) Longmans, London.

PVTsim version 17.3.0 Calsep A/S, Lyngby, Denmark.

Rachford, Jr., H.H. and Rice, J.D. 1952. Procedure for Use of Electronic Digital Computers in Calculating Flash Vaporization Hydrocarbon Equilibrium. *Petroleum Transactions*, AIME 195, 327-328.

Rasmussen, C.P., Krejbjerg, K., Michelsen, M.L., and Bjurstrøm, K.E. 2006. Increasing the Computational Speed of Flash Calculations With Applications for Compositional, Transient Simulations. *SPE Reservoir Evaluation and Engineering* 9(1): 32-28.

Riazi, M.R. and Daubert, T.E. 1980. Simplify Property Predictions. *Hydrocarbon Processing* 59(3): 115-116.

Rowlinson, J.S. and Freeman, P.I. 1961. Lower Critical Solution Points in Hydrocarbon Mixtures. *Pure and Applied Chemistry* 2(1-2): 329-334.

Sandler, S.I. 1985. Generalized van der Waals Partition Function. I. Basic Theory. *Fluid Phase Equilibria* 19(3): 233-257.

Sandler, S.I. 2006. *Chemical, Biochemical, and Engineering Thermodynamics*, fourth edition. John Wiley & Sons, Inc.

Sandler, S.I. and Prausnitz, J.M. 1982. Molecular Thermodynamics for Chemical Process Design: Applications of Generalized van der Waals Theory. Paper presented at CIESC/AIChE Joint Meeting of Chemical Engineering, Beijing, China.

Schneider, G. 1968. Phase Equilibria in Binary Fluid Systems of Hydrocarbons With Carbon Dioxide, Water and Methane. *Chemical Engineering Progress Symposium Series* 64: 9-15.

Scott, R.L. and van Konynenburg, P.H. 1970. van der Waals and Related Models for Hydrocarbon Mixtures. *Discussions of the Faraday Society* 49: 87-97.

Shanno, D.F. 1970. Conditioning of Quasi-Newton Methods for Function Minimization. *Mathematics of Computation* 24(111): 647-656.

Shelton, J.L. and Yarborough, L. 1977. Multiple Phase Behavior in Porous Media During CO_2 or Rich-Gas Flooding. *Journal of Petroleum Technology* 29(9):1171-1178.

Smith, J.M., van Ness, H.C., and Abbott, M.M. 2005. *Introduction to Chemical Engineering Thermodynamics*, seventh edition. McGraw-Hill, NY.

Spee, M. and Schneider, G.M. 1991. Fluid Phase Equilibrium Studies on Binary and Ternary Mixtures of Carbon Dioxide With Hexadecane, 1-Dodecanol, 1,8-Octanediol and Dotriacontane at 393.2 K and at Pressures up to 100 MPa. *Fluid Phase Equilibria* 65: 263-274.

Stalkup, F.I. 1978. Carbon Dioxide Miscible Flooding: Past, Present, and Outlook for the Future. *Journal of Petroleum Technology* 30(8): 1102-1112.

Stenby, E.H. and Wang, P. 1993. Noniterative Phase Equilibrium Calculation in Compositional Reservoir Simulation. Paper presented at the SPE Annual Technical Conference and Exhibition, Houston, Texas, 3-6 October.

Stewart, W.C. and Nielsen, R.F. 1953. Phase Equilibria for Mixtures of Carbon Dioxide and Several Normal Saturated Hydrocarbons. *Pennsylvania State College-Engineering Experiment Station-Bulletin* 62: 19-29.

Strang, G. 2006. *Linear Algebra and Its Applications*, fourth edition. Thomson Brooks/Cole.

Sun, A.C. and Seider, W.D. 1995. Homotopy-Continuation Method for Stability Analysis in the Global Minimization of the Gibbs Free Energy. *Fluid Phase Equilibria* 103(2): 213-249.

Teh, Y.S. and Rangaiah, G.P. 2002. A Study of Equation-Solving and Gibbs Free Energy Minimization Methods for Phase Equilibrium Calculations. *Chemical Engineering Research and Design* 80(7): 745-759.

Trangenstein, J.A. 1985. Minimization of Gibbs Free Energy in Compositional Reservoir Simulation. Paper presented at the SPE Reservoir Simulation Symposium, Dallas, Texas, 10-13 February.

Trangenstein, J.A. 1987. Customized Minimization Techniques for Phase Equilibrium Computations in Reservoir Simulation. *Chemical Engineering Science* 42(12): 2847-2863.

Turek, E.A., Metcalfe, R.S., and Fishback, R.E. 1988. Phase Behavior of Several CO_2/West Texas-Reservoir-Oil Systems. *SPE Reservoir Engineering* 3(2): 505-516.

UTCOMP version 3.8. 2003. The University of Texas at Austin, Austin, Texas.

Uzunov, D.I. 1993. *Introduction to the Theory of Critical Phenomena.* World Scientific Publishing, Farrer Road, Singapore.

van der Waals, J.D. 1873. *On the Continuity of the Gaseous and Liquid States.* Edited and With an Introduction by Rowlinson, J.S. (1988) Dover Publications, Inc., New York.

van Konynenburg, P.H. 1968. *Critical Lines and Phase Equilibria in Binary Mixtures.* PhD dissertation, the University of California, Los Angeles, California.

van Konynenburg, P.H. and Scott, R.L. 1980. Critical Lines and Phase Equilibria in Binary van der Waals Mixtures. *Philosophical Transactions of the Royal Society of London. Series A, Mathematical and Physical Sciences* 298(1442): 495-540.

van Pelt, A. 1992. *Critical Phenomena in Binary Fluid Mixtures. Classification of Phase Equilibria With the Simplified-Perturbed-Hard-Chain Theory*. PhD dissertation, Delft University of Technology, Rotterdam, Netherlands.

Varotsis, N. 1989. A Robust Prediction Method for Rapid Phase-Behavior Calculations. *SPE Reservoir Engineering* 4(2): 237-243.

Vera, J.H. and Prausnitz, J.M. 1972. Generalized van der Waals Theory for Dense Fluids. *The Chemical Engineering Journal* 3: 1-13.

Voskov, D.V. and Tchelepi, H.A. 2008. Tie-Simplex Based Framework for General Multi-Phase Thermodynamic Equilibrium Computations. Paper presented at the 11th European Conference on the Mathematics of Oil Recovery, Bergen, Norway, 8-11 September.

Wagner, J.R., McCaffrey, D.S., and Kohn, J.P. 1968. Partial Miscibility Phenomena in the Ternary System Ethane-*n*-Hexadecane-*n*-Eicosane. *Journal of Chemical and Engineering Data* 13(1): 22-24.

Wang, P. and Barker, J.W. 1995. Comparison of Flash Calculations in Compositional Reservoir Simulation. Paper presented at the SPE Annual Technical Conference and Exhibition, Dallas, Texas, 22-25 October.

Wang, P. and Stenby, E.H. 1994. Non-Iterative Flash Calculation Algorithm in Compositional Reservoir Simulation. *Fluid Phase Equilibria* 95: 93-108.

Wang, X. and Strycker, A. 2000. Evaluation of CO_2 Injection With Three Hydrocarbon Phases. Paper presented at the International Oil and Gas Conference and Exhibition in China, Beijing, China, 7-10 November.

Wang, P., Yotov, I., Wheeler, M., Arbogast, T., Dawson, C., Parashar, M., and Sepehrnoori, K. 1997. A New Generation EOS Compositional Reservoir Simulator: Part I-Formulation and Discretization. Paper presented at the SPE Reservoir Simulation Symposium, Dallas, Texas, 8-11 June.

Warren, J.H. and Adewumi, M.A. 1993. Polynomial Objective Functions for Flash Calculations: Binary, Ternary, and Quaternary Systems. *Industrial and Engineering Chemistry Research* 32(7): 1528-1530.

Whitson, C.H. and Michelsen, M.L. 1989. The Negative Flash. *Fluid Phase Equilibria* 53, 51-71.

Whitson, C.H. and Torp, S.B. 1983. Evaluating Constant-Volume Depletion Data. *Journal of Petroleum Technology* 35(3): 610-620.

Widom, B. 1973. Tricritical Points in Three- and Four-Component Fluid Mixtures. *The Journal of Physical Chemistry* 77(18): 2196-2200.

Wilson, G. 1969. A Modified Redlich-Kwong Equation of State, Application to General Physical Data Calculations. Paper presented at AIChE 65th National Meeting, Cleveland, Ohio, 4-7 May.

Winzinger, R., Brink, J.L, Patel, K.S., Davenport, C.B., Patel, Y.R., and Thakur, G.C. 1991. Design of a Major CO_2 Flood, North Ward Estes Field, Ward County, Texas. *SPE Reservoir Engineering* 6(1): 11-16.

Yang, Q. 2006. *Automatic Development of Global Phase Diagrams for Binary Systems in Pressure-Temperature Space.* Master thesis, the University of Saskatchewan, Saskatoon, Canada.

Yellig, W.F. and Metcalfe, R.S. 1980. Determination and Prediction of CO_2 Minimum Miscibility Pressures. *Journal of Petroleum Technology* 32(1): 160-168.

Young, L.C. 1991. Full-Field Compositional Modeling on Vector Processors. *SPE Reservoir Engineering* 6(1): 107-114.

Young, L.C. and Stephenson, R.E. 1983. A Generalized Compositional Approach for Reservoir Simulation. *SPE Journal* 23(4): 727-742.

Yuan, H. and Johns, R.T. 2005. Simplified Method for Calculation of Minimum Miscibility Pressure of Enrichment. *SPE Journal* 10(4): 416-425.

VITA

Ryosuke Okuno was born in Okayama, Japan on October 20th, 1974, the second son of Kohei Okuno and Misako Okuno. Ryosuke Okuno attended Okayama High School, Okayama, Japan. In 1994, he entered the University of Tokyo, Tokyo, Japan, where he received the degree of Bachelor of Engineering in 1998 and the degree of Master of Engineering in 2000, both in Geosystem Engineering. During the following years, he was employed as a reservoir engineer at Japan Petroleum Exploration Co., Ltd. (JAPEX), Tokyo, Japan. In January, 2006, he entered the Graduate School in Petroleum and Geosystems Engineering at the University of Texas at Austin to study for his PhD degree on a scholarship from JAPEX and JOGMEC (Japan Oil, Gas and Metals National Corporation).

Permanent address: 1-13-25 Kojimakarakoto
Kurashiki-Shi, Okayama 711-0904
Japan

This dissertation was typed by the author.